DEBONDING FAILURE IN FRP-STRENGTHENED RC BEAMS: PREDICTION AND SUPPRESSION

FU BING

Ph.D

The Hong Kong Polytechnic University

2016

The Hong Kong Polytechnic University

Department of Civil and Environmental Engineering

DEBONDING FAILURE IN FRP-STRENGTHENED RC BEAMS: PREDICTION AND SUPPRESSION

FU BING

A Thesis Submitted in Partial Fulfilment of the Requirements for the Degree of Doctor of Philosophy

July 2015

To My Family

CERTIFICATE OF ORIGINALITY

I hereby declare that this thesis is my own work and that, to the best of my knowledge and belief, it reproduces no material previously published or written, nor material that has been accepted for the award of any other degree or diploma, except for where due acknowledgement has been made in the text.

_____(Signed)

_____FU Bing_____(Name of student)

ABSTRACT

Flexural strengthening of reinforced concrete (RC) beams by bonding a fibre-reinforced polymer (FRP) plate/sheet onto their tension face (i.e. FRP-plated RC beams) is now widely accepted in practice. Such an FRP-plated RC beam often fails by debonding of various forms, including intermediate crack (IC) debonding and plate-end concrete cover separation. The former initiates at a major flexural/flexural-shear crack and propagates in the direction of decreasing moment; while the latter initiates at the critical end of the FRP soffit plate and propagates at the level of steel tension reinforcement in the direction of increasing moment. Despite extensive existing research on these debonding failure modes, two major knowledge deficiencies still remain: (1) the effect of load distribution on IC debonding; (2) the effect of FRP U-jackets in suppressing debonding failures. This thesis presents a systematic research project aimed at addressing these two issues.

Following an introduction to the PhD research project and an extensive review of existing related research, an experimental study on IC debonding under different load distributions is presented. Five full-scale FRP-plated RC beams in two series were tested, with Series I addressing the effect of shear span and Series II addressing the effect of load uniformity. All five test beams

failed by IC debonding, and the maximum moment in the beam at IC debonding (i.e. debonding moment) was found to increase as the load uniformity increased; the recorded increases in the debonding moment due to these two factors were up to about 20%. Following the experimental study, a finite element (FE) approach recently developed by the author's group was augmented with a novel displacement control technique and verified using the test results to produce reliable simulations of IC debonding under different load distributions. An FE parametric study was then conducted to extrapolate the test results. Existing IC debonding strength models applicable to different loading conditions were then assessed using both the test data and the numerical results, indicating the need for a more accurate IC debonding strength model.

Attention was next shifted to the effect of FRP U-jackets on both IC debonding and concrete cover separation failures. Two series of tests on FRP-plated RC beams with vertical FRP U-jackets and inclined FRP U-jackets respectively were conducted to investigate their effect on IC debonding. The test results indicated that inclined FRP U-jackets performed much better than vertical ones and were capable of improving both the strength and ductility of the beam significantly. An experimental study on the use of FRP U-jackets of different forms to mitigate concrete cover separation then followed, in which ten full-scale FRP-plated RC beams were tested. Both

the ultimate load and the ductility of the beam were found to be significantly enhanced by the U-jackets. Among the forms of U-jackets explored, those inclined at 45^{o} were found to be the most effective. Finally, an approach for the design of FRP U-jackets for mitigating concrete cover separation was developed based on the 'concrete tooth' concept and verified using the test results obtained in the present research project.

ACKNOWLEDGMENTS

I first wish to express my deepest thanks to my supervisor, Prof. Jin-Guang Teng, for accepting me as one of his PhD students five years ago; for illuminating my research vision with kindness and patience and for continuously encouraging me throughout the PhD study. I feel privileged to have conducted my PhD study under his supervision. I am indebted to Prof. Jin-Guang Teng as he has tried his best to train me to become a successful researcher although there is still a long way to go for me.

I am grateful to my two co-supervisors, Drs Guang-Ming Chen and Tao Yu for their valuable guidance and help. Special thanks are due to Dr. Guang-Ming Chen for his valuable time spent in revising parts of the thesis and for hid kind help during my stay at Guangdong University of Technology for many of the tests presented in the thesis. Many thanks are due to Profs. Li-Juan Li and Yong-Chang Guo for their kind help provided during my stay at Guangdong University of Technology. I also would like to express my sincere thanks to Prof. Jian-Fei Chen of Queen's University Belfast for providing me with much valuable advice on my research work and for his kind help during my visit to Queen's. I am also very grateful to Drs Lik Lam and Jian-Guo Dai for their invaluable suggestions and kind help especially at the

beginning of my PhD study.

I would like to thank The Hong Kong Polytechnic University for providing me with a good study environment and abundant research resources to conduct the PhD study. Thanks also go to Guangdong University of Technology, where I conducted the experiments presented in Chapters 3 and 7 of this thesis, and Queen's University Belfast for accepting me as a visiting PhD student and providing me with a good study environment.

Sincere thanks also go to all the members of our research group for their friendship and helpful discussions, including but not limited to Drs Shi-Shun Zhang, Qiong-Guan Xiao, Bing Zhang, Wan-Yang Gao, Yu-Lei Bai, Messrs. Jun-Liang Zhao, Guan Lin, Jun-Jie Zeng, Xue-Fei Nie, Yi-Nan Yang, Qing-Kai Wang, Xiao-Liang Fang, Pan Zhang, Jie-Kai Zhou and Jiong-Yi Zhu as well as Mses. Pan Xie, Ji-Ji Wang, Jing-Yun Wu and Zi-Hao Wang.

My sincere thanks also go to my friends and colleagues in and beyond the Department of Civil and Environmental Engineering of The Hong Kong Polytechnic University, especially Drs Feng-Chen An, Bo Li, Gao Li, Yu-Ming Hong, Xiao-Fan Lai and Messrs Yu-Yang Liu, Zi-You Wang and Shuai-Yin Zhu as well as Ms Si Peng. Without them, it would have been more of a struggle to go through the difficult time of the PhD study.

Last but most importantly, I would like to give my heartfelt gratitude to my parents, for their unconditional love, support and encouragement. I also wish to express my thanks to my wife, Jing Zhao, for her constant understanding, love and encouragement. It is her who shared the most difficult time with me. I have been away from hometown for more than 10 years, and have been unable to fulfil my family responsibility. Many other family members, especially my brother Xiao-Fan Fu, my sister Long-Long Fu and my uncle Sun-An Yuan have helped shoulder my family responsibility. I am greatly indebted to them, and my gratitude to them cannot be described by words. It is to them that this thesis is dedicated.

CONTENTS

CERTIFICATE OF ORIGINALITY.....I

ABSTRACT..... II

ACKNOWLEDGMENTS..... V

LIST OF TABLES XVIII

LIST OF FIGURES XXI

NOTATION.....XXVII

CHAPTER 1 INTRODUCTION..... 1

1.1 GENERAL 1

1.2 DEBONDING FAILURES IN FRP-PLATED RC BEAMS 3

1.3 PREDICTION OF DEBONDING FAILURES 6

1.4 SUPPRESSION OF DEBONDING FAILURES 8

1.5 RESEARCH OBJECTIVES AND OUTILINE OF THIS THESIS .. 10

1.6 REFERENCES 17

1.7 FIGURES 25

CHAPTER 2 LITERATURE REVIEW 27

2.1 INTRODUCTION 27

2.2 BOND BEHAVIOUR OF FRP-TO-CONCRETE INTERFACES 28

2.2.1 Bond tests.....29

2.2.1.1 FES Double-shear tests.....30

2.2.1.2 NES Double-shear tests.....32

2.2.1.3 FES Single-shear tests.....33

2.2.1.4 NES Single-shear tests 34

2.2.1.5 Beam tests and modified beam tests.....36

2.2.2 Finite element analysis.....38

2.2.2.1 Perfect-bonding approach.....38

2.2.2.2 Interface approach.....41

2.2.3 Local bond-slip models.....43

2.2.4 Analytical investigations.....53

2.2.5 Bond strength models 56

2.2.5.1 Empitical models.....57

2.2.5.2 Semi-empitical models 58

2.2.5.3 Fracture mechanics based models.....58

2.3 IC DEBONDING FAILURES 63

2.3.1 Tests on IC debonding without anchorage measures 64

2.3.2 FE modelling of IC debonding 64

2.3.2.1 Modelling of concrete cracking 68

2.3.2.2 Modelling of bond of interfaces 69

2.3.3 IC debonding strength models 70

2.3.3.1 Models modified from a bond strength model for FRP-to-concrete bonded joints 71

2.3.3.2 Models based on interfacial shear stress distribution 75

2.3.3.3 Empirical models derived from a regression analysis of test results 78

2.3.3.4 Deficiencies of existing IC debonding strength models 79

2.3.4 Suppression of IC debonding 80

2.4 SUPPRESSION OF CONCRETE COVER SEPARATION 83

2.5 CONCLUDING REMARKS 88

2.6 REFERENCES 90

2.7 FIGURE 107

CHAPTER 3EFFECT OF LOAD DISTRIBUTION ON IC DEBONDING: EXPERIMENTAL STUDY 109

3.1 INTRODUCTION 109

3.2 EXPERIMENTAL PROGRAMME 110

3.2.1 Specimen design 110

3.2.2 Specimen preparation 112
3.2.3 Material properties 112
3.2.4 Testing and instrumentation 113
3.3 TEST RESULTS AND DISCUSSIONS 115
3.3.1 General 115
3.3.2 Tests of Series I 116
3.3.3 Tests of Series II 118
3.4 CONCLUSIONS 121
3.5 REFERENCES 124
3.6 TABLES AND FIGURES 126
APPENDIX 3.1 WET LAYUP PROCEDURE FOR THE BONDING OF CARBON FIBRE SHEETS 143
CHAPTER 4 EFFECT OF LOAD DISTRIBUTION ON IC DEBONDING: FINITE ELEMENT STUDY 153
4.1 INTRODUCTION 153
4.2 FE APPROACH 155
4.2.1 General 156
4.2.2 Modelling of concrete 156
4.2.3 Modelling of bond behaviour 160
4.2.4 Solution strategy 161

4.2.5 Loading scheme 162

4.2.5.1Imaginary physical model 162

4.2.5.2Verification of loading scheme 165

4.3 VERIFICATION OF THE AUGMENTEDFE APPROACH 166

4.3.1 Specimens of Chapter 3 of the present thesis 167

4.3.1.1Verification for two-point loading 169

4.3.1.2Verification for four- or eight-point loading 172

4.3.2 Specimens of Pan et al. (2009) 175

4.3.3 Specimens of Mazzotti and Savoia (2009) 177

4.3.3.1Series TN4 178

4.3.3.2Series TN8 179

4.3.3.2Exclusion of Specimen TN3 181

4.4 PARAMETRIC STUDY 182

4.4.1 Effect of concrete strength 183

4.4.2 Effect of yield stress of steel tension bars 185

4.4.3 Effect of amount of steel tension bars 185

4.4.4 Effect of thickness of FRP plate 186

4.4.5 Effect of width of FRP plate 187

4.4.6 Effect of span-to-depth ratio 187

4.5 CONCLUSIONS 188

4.6 REFERENCES 190

4.7 TABLES AND FIGURES 192

CHAPTER 5 EVALUATION OF IC DEBONDING STRENGTH MODELSTHAT CATER FOR DIFFERENT LOAD DISTRIBUTIONS..... 215

5.1 INTRODUCTION 215

5.2 EXISTING IC DEBONDING STRENGTH MODELS.....216

5.2.1 *fib*'s (2001) approach.....216

5.2.2 Chen et al.'s (2006) model.....219

5.2.3 Rosenboom and Rizkalla's (2008) model.....223

5.3 SECTION ANALYSIS 225

5.4 COMPARISONS BETWEEN STRENGTH MODELS' PREDICTIONS AND TEST RESULTS.....230

5.5 COMPARISONS BETWEEN STRENGTH MODELS' PREDICTIONS AND FE RESULTS 232

5.6 CONCLUSIONS.....236

5.7 REFERENCES 238

5.8 TABLES AND FIGURES.....240

CHAPTER 6 EFFECT OF FRP U-JACKETS ON IC DEBONDINGFAILURE 255

6.1 INTRODUCTION 255
6.2 EXISTING TESTS 256
6.3 EXPERIMENTAL PROGRAMME 258
6.3.1 Specimen design 258
6.3.2 Specimen preparation 262
6.3.3 Material properties 263
6.3.4 Test procedure and instrumentation 264
6.4 TEST RESULTS OF SERIES I 265
6.4.1 Failure modes and load-deflection responses 265
6.4.2 Cracking behaviour 268
6.4.3 Strain distributions over the FRP soffit plate 269
6.4.4 Strains in U-jackets and parallel side strips 270
6.5 TEST RESULTS OF SERIES II 271
6.5.1 Failure modes and load-deflection responses 271
6.5.2 Cracking behaviour 273
6.5.3 Strain distributions over the FRP soffit plate 274
6.5.4 Effects of U-jackets 274
6.6 CONCLUSIONS 276
6.7 REFERENCES 279
6.8 TABLES AND FIGURES 281

CHAPTER 7 MITIGATION OF CONCRETE COVER SEPARATION USING FRP U-JACKETS 305

7.1 INTRODUCTION 305

7.2 EXPERIMENTAL PROGRAMME 306

7.2.1 Specimen design 306

7.2.2 Specimen preparation 309

7.2.3 Material properties 310

7.2.4 Test set-up and instrumentation 311

7.3 TEST RESULTS AND DISCUSSIONS 312

7.3.1 General 312

7.3.2 Mechanism of concrete cover separation 313

7.3.3 Mitigation effects of vertical FRP U-jackets 315

7.3.4 Mitigation effects of inclined FRP U-jackets 319

7.3.5 Tests of Series-II 322

7.4 CONCLUSIONS 324

7.5 REFERENCES 328

7.6 TABLES AND FIGURES 331

CHAPTER 8 DESIGN OF FRP U-JACKETS TO MITIGATE CONCRETE COVER SEPARATION FAILURE.. 347

8.1 INTRODUCTION 347

8.2 CONCRETE COVER SEPARATION FAILURE 348
8.3 DATA OF TESTS WITH VERTICAL U-JACKETS 350
8.4 EXISTING PROVISIONS FOR DESIGN OF VERTICAL FRP U-JACKET 351
8.4.1 ACI guideline 352
8.4.2 Concrete Society guideline 353
8.4.3 Chinese National Standard (GB-50608) 354
8.4.4 Evaluation of existing provisions 355
8.5 DESIGN OF VERTICAL FRP U-JACKETS 356
8.5.1 Design approach 356
8.5.2 Evaluation of the proposed approach 362
8.6 DESIGN OF INCLINED FRP U-JACKETS 363
8.6.1 General 363
8.6.2 Design approach 364
8.6.3 Evaluation of the proposed approach 367
8.7 CONCLUSIONS 368
8.8 REFERENCES 371
8.9 TABLES AND FIGURES 374

CHAPTER 9 CONCLUSIONS 385

9.1 INTRODUCTION 385

9.2 EFFECT OF LOAD DISTIBUTION ON IC DEBONDING 387

9.3 EFFECT OF FRP U-JACKETS ON BOTH IC DEBONDING AND CONCRETE COVER SEPARATION 389

9.4 FUTURE RESEARCH.....392

9.5 REFERENCES 396

LIST OF TABLES

Table 3.1 Material properties of steel and FRP 126

Table 3.2 Summary of test results 127

Table 4.1 Geometrical and Material Properties of Specimens failing by IC debonding under different loading distributions 192

Table 4.2 Examined values of the main factors in the parametric study 194

Table 4.3 Key results of specimens with different concrete strengths 194

Table 4.4 Key results of specimens with different yield stresses of steel tension bars 195

Table 4.5 Key results of specimens with different amounts of steel tension bars.... 195

Table 4.6 Key results of specimens with different numbers of layer of the FRP sheet 196

Table 4.7 Key results of specimens with different widths of the FRP plate 196

Table 4.8 Key results of specimens with different span-to-depth ratios of beams... 197

Table 5.1 Geometrical and material properties of Specimens failing by IC debonding under different loading distributions 240

Table 5.2 Comparisons between predictions of IC debonding models and test data for beams under different loading distributions 241

Table 5.3 Comparison between predictions of IC debonding models and FE predicted results for specimens with varied concrete strengths 242

Table 5.4 Comparison between predictions of IC debonding models and FE predicted results for specimens with varied yield strengths of tension steel bars..243

Table 5.5 Comparison between predictions of IC debonding models and FE predicted results for specimens with varied in amount of tension steel bars.....243

Table5.6 Comparison between predictions of IC debonding models and FE predicted results for specimens with varied number of layer of the FRP sheet.....244

Table 5.7 Comparison between predictions of IC debonding models and FE predicted results for specimens with varied width of the FRP plate 244

Table 5.8 Comparison between predictions of IC debonding models and FE predicted results for specimens with varied span-to-height ratio of beams.....246

Table 6.1 Geometrical and material properties of beam specimens with FRP U-jackets for mitigating IC debonding.....281

Table 6.2 Material properties of steel and FRP 283

Table 6.3 Summary of test results of Series I.....283

Table 6.4 Summary of test results of Series II 284

Table 7.1 Material properties of steel and FRP 331

Table 7.2 Summary of test results 332

Table 8.1 Geometrical and material properties of beams with vertical FRP U-jackets 374

Table 8.2 Evaluation of existing design approaches for beams with vertical FRP U-jackets 377

Table 8.3 Evaluation of the proposed approach for beams with vertical FRP U-jackets 378

LIST OF FIGURES

Figure 1.1 Dry fibre sheets for wet lay-up applications [from Zhang (2011)].....25

Figure 1.2 Debonding failure modes of FRP-plated RC beams [from Teng et al. (2003)] 25

Figure 2.1 Bond tests of different types: (a) Far-end supported (FES) double-shear test; (b) Near-end supported (NES) double-shear test; (c) Far-end supported (FES) single-shear test; (d) Near-end supported (NES) single-shear test; (e) Beam test; (f) Modified beam test [from Chen et al. (2001)] 107

Figure 3.1 Geometry of test specimens.....128

Figure 3.2 Loading patterns of Series I specimens.....128

Figure 3.3 Loading patterns of Series II specimens 129

Figure 3.4 Shear force and bending moment diagrams for Series II specimens 130

Figure 3.5 Experimental set-ups for specimens under multi-point loading 131

Figure 3.6 Loads from loading jacks 132

Figure 3.7 Positions of LVDTs and strain gauges on concrete and steel bars.....133

Figure 3.8 Installation of LVDTs.....133

Figure 3.9 Positions of strain gauges on the soffit plate 134

Figure 3.10 Crack width measurement 134

Figure 3.11 Moment-deflection curves of beams under different loading distributions 135

Figure 3.12 Strain distributions at failure of specimens in Series I.....136

Figure 3.13 Failure modes and crack patterns of test beams 139

Figure 3.14 Development of critical crack and adjacent crack in specimens of Series

I 140

Figure 3.15 Strain distributions at failure in specimens of Series II 141

Figure 3.16 Development of critical crack and adjacent crack in specimens of Series II 142

Figure A3.1.1 Procedure for installinga wet lay-up FRP strengthening system 148

Figure A3.1.2 Profiling the concrete surface with a jet gun 148

Figure A3.1.3 Mixing of primer or resin 149

Figure A3.1.4 Application of primer 149

Figure A3.1.5 Distributing resin onto the fibre sheet 150

Figure A3.1.6 Slowly moving the roller to fully saturate the fibre sheet and force out excessive resin and entrapped air 150

Figure A3.1.7 Application of successive layers of fibre sheets 151

Figure 4.1 Definition of tensile damage 196

Figure 4.2 Imaginary whiffle tree system 196

Figure 4.3 Mesh of the beam 197

Figure 4.4 Applied load-time curves at each loading point 197

Figure4.5 FE predicted versus test moment-displacement curves for Series I specimens 198

Figure 4.6 FE predicted versus test crack pattern at failure for specimen LP2SP1000 199

Figure 4.7 FE predicted and test moment-crack width curves for typical cracks for specimen LP2SP1000 200

Figure 4.8 FE predicted and test FRP distributions at different load levels for specimen LP2SP1000 200

Figure 4.9 FE predicted versus test moment-deflection curves for Series II specimens 201

Figure 4.10 FE-predicted versus test crack patterns at failure 203

Figure 4.11 FE predicted and test FRP strain distributions at different load levels for specimens LP4SP1000 and LP8SP1000.....204

Figure 4.12 Moment-displacement curves for specimens in Pan et al. (2009) 205

Figure 4.13 FE crack patterns at ultimate failure for specimens in Pan et al. (2009) 206

Figure 4.14 FRP strains at ultimate load for specimens in Pan et al. (2009) 207

Figure 4.15 Moment-displacement curves for Series TN4 in Mazzotti and Savoia (2009).....207

Figure 4.16 FE crack patterns at ultimate failure for Series TN4 in Mazzotti and Savoia (2009) 208

Figure 4.17 FRP strains at ultimate load for Series TN4 in Mazzotti and Savoia (2009) 209

Figure 4.18 Moment-displacement curves for Series TN8 in Mazzotti and Savoia (2009).....209

Figure 4.19 FE crack patterns at ultimate failure for Series TN8 in Mazzotti and Savoia (2009) 210

Figure 4.20 FRP strains at ultimate load for Series TN8 in Mazzotti and Savoia (2009) 211

Figure 4.21 Comparison of moment-displacement curves for Specimens TN3-LP8 and TN8-LP8 in Mazzotti and Savoia (2009) 211

Figure 5.1 Intermediate crack debonding in FRP-plated RC beams [from Teng et al. (2006)] 246

Figure 5.2 FRP-to-concrete bonded joint model between two adjacent cracks [from Teng et al. (2006)] 246

Figure 5.3 Flow chart for the prediction of IC debonding strength 247

Figure 5.4 Section analysis predicted versus FE predicted FRP strain distributions 249

Figure 5.5 IC debonding strength model predicted versus test debonding strength 251

Figure 5.6 Prediction from *fib* (2001) model 253

Figure 5.7 Prediction from Chen et al. (2006) model 253

Figure 5.8 Predictions from Rosenboom and Rizkalla (2008) model 255

Figure 6.1 Geometries of control beams (all dimensions in mm) 285

Figure 6.2 FRP U-jacket layouts (all dimensions in mm) 287

Figure 6.3 Positions of LVDTs and strain gauges on steel tension bars 288

Figure 6.4 Positions of strain gauges on the soffit plate of control specimens 288

Figure 6.5 Load-deflection curves of specimens in Series I 289

Figure 6.6 Failure modes of specimens in Series I 291

Figure 6.7 Crack patterns at failure of specimens in Series I 293

Figure 6.8 Strain distributionsover the FRP soffit plate of specimens in Series I ... 295

Figure 6.9 Strain distributions over U-jacket or side strip of specimens in Series I 297

Figure 6.10 Load-deflection curves of specimens in Series II 297

Figure 6.11 Failure modes of specimens in Series II 299

Figure 6.12 Crack patterns at failure of specimens in Series II 301

Figure 6.13 Strain distributionsover the FRP soffit plate of specimens in Series II 303

Figure 6.14 Strain distributionsover U-jackets of specimens in Series II 304

Figure 7.1 Dimensions of specimens 334

Figure 7.2 Layout of FRP U-jackets in specimens 334

Figure 7.3 Positions of LVDTs and strain gauges on steel bars and concrete.....335

Figure 7.4 Positions of strain gauges on FRP soffit plate 335

Figure 7.5 Positions of strain gauges on FRP U-jackets.....336

Figure 7.6 Load-deflection curves of all specimens 336

Figure 7.7 Failure modes of control specimens.....337

Figure 7.8 Load-deflection curves of control specimens.....337

Figure 7.9 Details of the failure end 338

Figure 7.10 Strain distribution over the FRP soffit plate of Specimen CB at different load levels 338

Figure 7.11 Simplified process of concrete cover separation.....339

Figure 7.12 Load-deflection curves of beams with different vertical U-jackets 339

Figure 7.13 Strain distributions over the FRP soffit plate of Specimen VIL1W60 at selected load levels 340

Figure 7.14a Strain distributions over the FRP U-jacket of Specimen V1L1W60 at selected load levels 340

Figure 7.14b Crack pattern of Specimen V1L1W60 341

Figure 7.15 Strain distributions over the vertical FRP U-jacket at failure.....341

Figure 7.16 Failure modes of specimens with inclined FRP U-jackets in Series I ..342

Figure 7.17 Load-deflection curves of beams with different inclined U-jackets 342

Figure 7.18 Strain distributions over the FRP soffit plate of Specimen I1L1W120 at selected load levels 343

Figure 7.19 Strain distributions over the FRP U-jacket of Specimen I1L1W120 at selected load levels 343

Figure 7.20 Strain distributions over the inclined FRP U-jacket of specimens at failure..... 344

Figure 7.21 Load-deflection curves of beams with vertical and inclined U-jackets of the same width 344

Figure 7.22 Failure mode of Specimen I1L1W120b..... 345

Figure 7.23 Failure mode of Specimen I1L1W120b..... 345

Figure 8.1 Concrete cover separation: illustration of failure process..... 380

Figure 8.2 Comparison between provision predictions and results of tests with a vertical FRP U-jacket 382

Figure 8.3 Illustration of design model for a vertical U-jacket..... 383

Figure 8.4 Illustration of design model for an inclined U-jacket..... 383

NOTATION

a : distance from support to section of maximum moment in a beam

a_0 : coefficient in Lu et al.'s (2005b) bond strength model.

A_1, B_1 coefficients in the precise model in Lu et al.'s (2005) bond slip model

A_c, A_p : cross-sectional areas of concrete block and FRP plate, respectively

A_s : total area of steel tension bars

$A_{t,eff}$: effective area of concrete in tension

A_{uf}, A_{tf} : cross-sectional areas of FRP U-jackets and FRP soffit plate, respectively

b_c : width of concrete member (i.e. width of concrete block in an FRP-to-concrete bonded joint or width of concrete beam)

b_f : width of FRP plate

b_{f0} : constant in Eq. 2.2d

b_{uf} : width of FRP U-jacket

c_1, c_2 : coefficients in Dai and Ueda's (2003) bond-slip model

c_3 : coefficient in Dai et al.'s (2005) bond-slip model

c_4 : coefficient in Baky et al.'s (2012) bond-slip model

c_f : constant in Eq. 2.17b and Eq. 2.20d, and is set to be 0.204

C' : Horizontal distance from centerline of the inclined U-jacket to centre of rotation

d : degradation parameter

d_a : size of maximum aggregate

d_c : depth of concrete cover

D^{el} : elastic stiffness

D_0^{el} : initial elastic stiffness

d_{uf} : distance from FRP U-jacket curtailment to centre of steel

tension bars

E_f, E_c: elastic modulis of FRP plate and concrete, respectively

E_{i0} : initial elastic modulus of FRP-to-concrete interface

E_{uf} : elastic modulus of FRP U-jacket(s)

f_c : cylinder compressive strength of concrete

f_t : tensile strength of concrete

$F_{t,db}$: tensile force in FRP soffit plate at critical crack at beam failure

f_{tf}: stress of FRP soffit plate at rupture

$F_{u,db}$: total tensile force of U-jacket at debonding

$F_{x,ufrp}$, $F_{y,ufrp}$ Horizontal and vertical components of force resisted by an inclined U-jacket

G_f : interfacial fracture energy of FRP-to-concrete interface

G_f^q : interfacial fracture energy of FRP-to-concrete interface for the ascending branch of bond-slip response

G_F : tensile fracture energy of concrete

G_p, G_a, G_c : elastic shear moduli of FRP plate, adhesive and concrete, respectively

h_a : reference depth, taken to be 2.5-3.0 times the maximum aggregate size in Eq. 2.2e

h_{eff} : thickness of interfacial layer, and is set to be 3-5 times the maximum aggregate size in Eq. 2.10d

K_0 : initial stiffness of bond-slip model

K_a : axial stiffness of adhesive

L : shear span of beam

L_d : distance from loading point to end of FRP soffit plate in Lu et al.'s (2007) model

L_{ef} : effective bond length of FRP plate

L_f : bond length of FRP plate

M_{db} : moment resistance of beam at IC debonding

M_{rad} : moment induced by radial stresses from wedge effect

$M_{u,p}$: maximum moment of beam at beam failure

M_y : moment resistance of beam at yielding of steel tension bars

n_{uf} : number of layers of FRP U-jacket

P_1, P_2 : tensile forces at ends of FRP plate ($P_1 \geq P_2$), respectively

$P_{1,u}$: tensile force at complete debonding of FRP plate

s : slip between FRP and concrete

s_1 : slip between FRP and concrete corresponding at maximum local bond shear stress

s_2 : slip between FRP and concrete at complete release local bond shear stress

s_e : elastic component of s_1

$S_{cr,RC}$: mean crack spacing of un-strengthened RC beam

S_{cr} : mean crack spacing of FRP-plated RC beam

t_f : thickness of FRP plate

t_{uf} : thickness of FRP U-jacket

w_{cr} : crack opening displacement at complete release of concrete stress

w_t : crack opening displacement

W_{uf} : width of FRP U-jacket

x_y : distance from support to location of first yielding steel tension bars

α : coefficient in simplified model of Lu et al.'s (2005) bond slip model

$\alpha_1, \alpha_2, \alpha_3$: constants in precise model of Lu et al. (2005) and suggested to be 1.50, 0.0195 and 0.308 respectively.

a_u : effective bond length in Chen et al.'s (2007) bond strength model

α_σ : ratio between stresses of FRP plate at the critical crack and the adjacent crack

β : ratio between forces at the two ends of an FRP plate.

β_L : factor representing effect of bond length

β_w : factor reflecting effect of width ratio between FRP plate and concrete substrate

β_σ : factor representing effect of plate stress ratio between adjacent crack and critical crack

λ : coefficient in Chen et al.'s (2007) bond strength model.

γ_1, γ_2 : coefficient in Chen et al.' (2006) model and Lu et al.'s (2005) model, respectively.

δ : constant in strength model of Chen et al. (2006; 2007)

ε: compressive strain of concrete

ε_{fy} : strain of FRP plate at yielding of steel tension bars

ε_{ic} : strain of FRP plate at IC debonding

ε_p : concrete strain at peak compressive stress

ε_t : total tensile strain of concrete

ε_t^{el} : elastic tensile strain of concrete

ε_{ue} : effective strain of FRP U-jacket

ε_{uf} : rupture strain of FRP U-jacket(s)

θ : angle between U-jacket and beam axis

$\rho_{f,eff}$: ratio between area of FRP plate and effective area of concrete in tension

σ : stress of concrete

σ_{ic} : tensile stress of FRP plate at IC debonding

σ_p : maximum compressive stress of concrete

σ_t : tensile stress of concrete

$\sigma_{tf,max}$: maximum stress in FRP soffit plate

τ : Local shear bond stress between FRP and concrete

τ_{max} : maximum local shear bond stress between FRP and concrete

τ_{res} : residual local shear bond stress between FRP and concrete

τ_u : average shear bond stress between FRP and concrete

τ_{wmax} : maximum interfacial shear stress along an FRP-to-concrete interface

CHAPTER 1

INTRODUCTION

1.1 GENERAL

Concrete structures all over the world have been facing severe deterioration problems, and a large number of them are functionally obsolete or structurally deficient. In terms of cost effectiveness, extending the service life of these deteriorated structures by strengthening or repair, in most cases, is a better option than reconstructing them. Therefore, the need to strengthen or repair these concrete structures to satisfy the prescribed performance requirements of the ultimate as well as serviceability states has been increasing. It was reported in 2005 that 26.3% of the bridges in the United States were structurally deficient or functionally obsolete, and needed to be strengthened or repaired (US Bureau 2006). Annual cost amounting to about USD 9.4 billion (i.e. HK$ 72.9 billion) for the next 20 years would be needed to eliminate the problem with the bridges in the United States (Hamilton et al. 2009). Both mainland China and Hong Kong are no exceptions to this problem. For example, in

Guangdong province, more than 2000 deficient bridges needed strengthening or repair in 2002 (Liu et al. 2002).

Strengthening of concrete structures using fibre-reinforced polymer (FRP) composites has been among the most attractive strengthening techniques, and has been widely used (Teng et al. 2002; Hollaway and Teng 2008). Its popularity can be attributed to many superior properties of the bonded FRP system, such as excellent corrosion resistance and ease of installation. In terms of the embedded fibres, FRP products available in the strengthening market can be classified into carbon-fibre-reinforced polymer (CFRP), glass-fibre-reinforced polymer (GFRP), aramid-fibre-reinforced polymer (AFRP) and basalt-fibre-reinforced polymer (BFRP) (Figure 1.1). These FRP products can be pre-fabricated or formed in-situ via a wet layup process.

Externally bonding an FRP plate onto the tension face of concrete beams for flexural strengthening, which leads to FRP-plated RC beams, is one of the main applications of the FRP materials in the construction industry. Such an FRP-plated RC beam often fails by premature debonding of the FRP soffit plate from the concrete substrate, which initiates at the toes of flexural/flexural-shear cracks in the mid-span region (i.e. intermediate crack debonding, and referred to as IC debonding hereafter) or at the critical end of the FRP soffit plate (i.e. plate end debonding) (Smith and Teng 2002a). Premature debonding failures often occurs with the maximum strain of the FRP soffit plate (i.e. debonding strain) being much lower than the FRP tensile rupture strain (e.g. at only 30-40% of the FRP tensile rupture strain), thus limiting

utilization of the FRP material (Sebastian 2001; Kalfat et al. 2013). To ensure the safety of FRP-plated RC beams, design guidelines often impose conservative limits of the FRP tensile strain.

A large amount of research on debonding failures of FRP-plated RC beams has been undertaken (Sebastian 2001; Buyukozturk et al. 2004; Hollaway and Teng 2008; Teng and Chen 2009), and leads to a significant advancement on the knowledge of debonding failures in FRP-plated RC beams. However there are still two major knowledge deficiencies as discussed later. Simply-supported beams are assumed in all discussions in the thesis unless otherwise indicated. It should be emphasized that research on simply-supported FRP-plated beams can be adapted for use in the design of other FRP-plated RC beams as has been discussed in Teng et al. (2002).

1.2 DEBONDING FAILURES IN FRP-PLATED RC BEAMS

FRP-plated RC beams are vulnerable to FRP debonding failures of various forms, and their load-carrying capacity is often controlled by these debonding failures. These debonding failures can be classified into two major categories depending on the location of debonding initiation: (1) intermediate crack (IC) debonding, which initiates at a flexural/flexure-shear crack in the high moment region (e.g. mid-span of a simply-supported beam), and then propagates along the direction of moment decreasing (Wu and Niu 2000; Teng et al. 2003; Lu et al. 2007), and (2) plate end debonding, which initiates at or near one of the ends of the FRP soffit plate, and then

propagates towards the direction of moment increasing (e.g. mid-span of a simply-supported beam) along the level of steel-to-concrete interface or FRP-to-concrete interface (Malek et al. 1998; Smith and Teng 2002a, 2002b; Yao and Teng 2007; Teng and Yao 2007). Plate end debonding failures can be further divided into critical diagonal crack (CDC) debonding, plate end interfacial debonding or concrete cover separation. Concrete cover separation is much more common than the other two forms of plate end debonding. CDC debonding only occurs when the shear strength of the beam is not sufficient and plate end interfacial debonding only occurs when the FRP plate is far narrower than the beam soffit.

IC debonding (Figure 1.2) generally occurs in the surface layer of concrete of about 2-5 mm beneath the adhesive layer (Lu et al. 2005a, 2007), if an appropriate bonding adhesive is used and the bonding of the FRP plate is conducted following a standard procedure. This observation means that the IC debonding strength is highly dependent on the concrete strength, which has been included in the existing strength models against IC debonding. In addition, IC debonding has a close relationship with concrete cracking of the beam. Prior to concrete cracking, the bonded FRP plate together with the concrete and internal steel reinforcements carries the tensile force induced by the moment on the section. Once the concrete cracks, the tensile force, which was resisted by the concrete, is then released and partially transferred to the FRP plate, resulting in an abrupt increase in the FRP strain and fluctuation in the interfacial shear stress near the crack. With further increases of the applied load, the tensile stress of the FRP plate as well as the interfacial shear stress at the FRP-to-

concrete interface also increases. When the FRP stress or the interfacial shear stress of the FRP-to-concrete interface reaches a critical value, IC debonding occurs and propagates along the direction of moment decreasing, resulting in the beam failure. In addition, IC debonding propagates covering multi cracks and its behaviour can be affected by the interaction of adjacent cracks.

Concrete cover separation (Figure 1.2), being the most common type of plate end debonding failure, initiates at/near the critical end of the FRP tension plate, and propagates along the level of steel tension bars towards the mid-span. The mechanism of concrete cover separation is complex and is related to many factors, including the concrete cover thickness, the moment and shear force at the soffit plate end, the size and number of steel tension bars, and the use of mechanical anchors (Raoof and Hassanen 2000; Smith and Teng 2003; Teng and Yao 2007; Yao and Teng 2007). In particular, the distance between the plate end and the adjacent support, which determines the relative importance between the shear force and the moment of the section at the soffit plate end, plays a significant role in concrete cover separation failure (Smith and Teng 2003; Teng and Yao 2007). In addition, Zhang and Teng (2014) recently showed that the radial stresses resulting from slips between the steel tension and the surrounding concrete play an important role in the process of concrete cover separation failure.

Plate end debonding of other two forms (i.e. CDC debonding and plate end interfacial debonding) rarely occurs, and is outside the scope of this thesis. Readers

can refer to Smith and Teng (2003), Yao and Teng (2007) and Teng and Yao (2007) for further details.

1.3 PREDICTION OF DEBONDING FAILURES

In the design of an FRP-plated RC beam, the risk of occurrence of either IC debonding or concrete cover separation should be considered to determine the load carrying capacity of the beam. In order to achieve this goal, extensive research has been carried out to propose various strength models for different debonding failure modes (Oehlers 1992; Jansze1997; Raoof and Zhang 1997; Ahmed and van Gemert 1999; Raoof and Hassanen 2000; Wu and Niu 2000; Smith and Teng 2003; Teng et al. 2003, Lu et al. 2007; Teng and Yao 2007; Wu and Niu 2007; Rosenboom and Rizkalla 2008; Said and Wu 2008).

Some of the IC debonding strength models limit the maximum strain of the FRP soffit plate to a certain value to avoid the occurrence of IC debonding; while others determine the occurrence of IC debonding by comparing the difference in the tensile stress or force in the FRP plate with the maximum allowable ones. In terms of the ways to derive the models, they can be generally categorized into three types: (1) empirical models based on a regression analysis of test results; (2) models modified from a bond strength model for FRP-to-concrete bonded joints; (3) models derived from the shear stress distribution of FRP-to-concrete interfaces.

The IC debonding mechanism is believed to be similar to that of FRP-to-concrete bonded joints; as a result some IC debonding strength models were modified directly from a bond strength model with or without consideration of the interaction between cracks (Teng et al. 2003; Chen et al. 2007; ACI 440.2R-08 2008). The single-shear test on an FRP-to-concrete bonded joint, in which one of the FRP plate ends is subjected to tension, is often used to investigate the bond performance of an FRP plate bonded to concrete substrate. Many bond strength models have been proposed (Holzenkampfer 1994; Tanaka 1996; Hiroyuki and Wu 1997; Maeda et al. 1997; van Gemert 1997; Khalifa et al. 1998; Bizindavyi and Neale 1999; Yuan and Wu 1999; Chen and Teng 2001; Lu et al. 2005b; Chen et al. 2007).Some early IC debonding strength models were modified directly from these bond strength models (*fib* 2001; Teng et al. 2003; CNR-DT 200/2004 2004; ACI 440.2R-08 2008). They implied that IC debonding is driven by the widening of a single major crack and no interaction between adjacent cracks is considered in the model. However in the IC debonding failure process, multiple cracks in the beam are generally involved. Analytical solutions for an FRP-to-concrete bonded joint in which both ends of the FRP plate are subjected to tension produced by Teng et al. (2006) and Chen et al. (2007) have indicated that the interaction between adjacent cracks can significantly affect the debonding process and bond strength of FRP (Teng et al. 2006; Chen et al. 2007). Chen et al. (2006) have extended Teng et al.'s (2003) model to account for such an effect, thus leading to a model that has the potential to account for the effect of load distribution (hence crack pattern) on IC debonding.

In an IC debonding strength model of the second type, an interfacial shear stress block is assumed, and IC debonding is assumed to occur once the maximum interfacial shear stress reaches a critical value. This critical value can be empirically derived by regression analysis of the large number of laboratory tests available in the published literature, without clear reference to the failure mechanism.

Many strength models against concrete cover separation have been developed based on different assumptions of its failure mechanisms. Some researchers believed that concrete cover separation is triggered by lack of shear strength. As a result, some shear capacity-based models (Oehlers1992; Jansze 1997; Ahmed and van Gemert 1999; Smith and Teng 2003) have been proposed. In other studies, the so-called concrete tooth models were proposed based on the following experimental observation: the concrete cover between the major crack near the FRP plate end and its adjacent major crack behaves like a tooth, which can be treated as a cantilever beam. The authors of these studies suggested that concrete cover separation occurs when the combination of normal and shear stresses near the FRP plate tensile stress at the root of the 'tooth' that exceeds the tensile strength of concrete (Raoof and Zhang 1997; Raoof and Hassanen 2000).

1.4 SUPPRESSION OF DEBONDING FAILURES

Premature debonding failures limit the utilization of expensive FRP materials; for example, the maximum FRP strain at debonding failure in an FRP-plated RC beam,

in some cases, is only about 30% of the rupture strain of the FRP material (Kalfat et al. 2013). Moreover concrete cover separation often occurs prior to the yielding of the tension steel bars and in a brittle form with little advance warning. Effective and economical options to suppress debonding failures, especially concrete cover separation, are desirable for more confident use of the FRP material for flexural strengthening of RC elements.

Due to the ease of installation and compatibility (e.g. corrosion resistance) with the FRP material bonded to the beam soffit, FRP U-jackets with fibres in the transverse direction (i.e. perpendicular to the beam axis) have been commonly recommended by design guidelines (e.g. CNR-DT 200/2004 2004; ACI 440.2R-08 2008; Concrete Society 2012; GB-50608 2010) to reduce the risk and brittleness of debonding failure. Existing experimental studies (e.g. Smith and Teng 2003; Pimanmas and Pornpongsaroj 2004; Pham and Al-Mahaidi 2006) have confirmed the effectiveness of U-jacket anchorage in enhancing concrete cover separation resistance and ductility. A systematic study on the effect on concrete cover separation however is needed for proposing a design method to suppress concrete cover separation failure. Contrary to the effect of FRP U-jackets on concrete cover separation, the findings from a very small number of studies (e.g. Leung 2006; Kotynia et al. 2008; Rosenboom and Rizkalla 2008) on the effect of U-jackets on IC debonding are contradictory and need to be further clarified.

U-jackets used for end anchorage of FRP soffit plates can be expected to play the following roles: (1) to resist the interfacial peeling (normal) stress between the concrete and the FRP; (2) to constrain the development of a critical flexural-shear crack at the ends of the FRP tension plate or a major crack at the level of the steel tension reinforcement. Therefore, U-jacket anchorage can be expected to be beneficial in resisting both concrete cover separation and IC debonding.

1.5 RESEARCH OBJECTIVES AND OUTILINE OF THIS THESIS

Two major deficiencies still exist in the current knowledge about debonding failures of FRP-plated RC beams as can be seen from the detailed literature review presented in Chapter 2. The first major deficiency is that the effect of load distribution on IC debonding has been widely neglected by almost all the existing IC debonding strength models and design guidelines; although it may be significant. Most tests on FRP-plated RC beams are subjected to one- or two-point loads (i.e. three- or four-point bending). These loading distributions have been used primarily for their ease of application in laboratory testing. In reality, other load distributions [e.g. uniformly distributed load (UDL)] are often encountered. The limited existing research on the effect of load distribution on IC debonding strength has indicated that this effect can be significant but has provided little guidance on how this effect can be considered in a design procedure.

The second major deficiency is that the effect of FRP U-jackets for suppressing debonding failures has only been fragmentally investigated, and their real effect is far from clear. Although design guidelines commonly specify the use of FRP U-jackets for the suppression of concrete cover separation, the design provisions in these guidelines are empirical and preliminary, and have a very limited research basis. Moreover, the effect of U-jackets on IC debonding is far from clear and needs to be further clarified.

This PhD research project has therefore been carried out to correct these two major deficiencies to enhance our understanding of debonding mechanisms in the presence of U jackets and under different load distributions. The main objectives of the project were as follows:

(1) To investigate the effect of load distribution on IC debonding in FRP-plated RC beams;
(2) To develop an IC debonding strength model that considers the effects of load distribution;
(3) To investigate the effect of FRP U-jacket anchorage on IC debonding and concrete cover separation;
(4) To optimise the layout of U-jackets for end anchorage and propose a method for designing U-jackets to enhance the performance of FRP-plated RC beams.

Both experimental and numerical investigations have been carried out to fulfil the above objectives. These investigations are reported in the present PhD thesis as detailed below.

In Chapter 2, a comprehensive literature review on issues pertinent to this PhD research project is presented. It starts with a concise background on the application of FRP materials for flexural strengthening of RC members. Following some short opening remarks, a review of the bond behaviour of FRP-to-concrete interfaces, which plays a crucial role in controlling debonding failures of various models, is presented. Results of these studies form the basis for the development strength models against various debonding failures in FRP-plated RC beams. A review of research on IC debonding failure studies is presented following the review of the bond behaviour of FRP-to-concrete bonded joints. Research on the effect of FRP U-jackets on both IC debonding and concrete cover separation has also been reviewed. Although many studies including some popular guidelines suggest use of FRP U-jacketing to mitigate debonding failures of different forms, and to enhance the structural performance of FRP-plated RC beams, the existing experimental research on the effect of U-jacket anchorage has been fragmented, often studied as a side issue of a larger test programme. Moreover, conclusions on the effect of FRP U-jackets on IC debonding from different studies are somewhat contradicted. This comprehensive literature review reveals that further study on the two major knowledge deficiencies mentioned above is in need to develop a safe and economic design method against debonding failure in FRP-plated RC beams.

Chapter 3 presents an experimental programme on IC debonding failures under different load distributions. This experimental programme consisted of five full-scale FRP-plated RC beams of the same geometry: a cross-section of 200 mm by 450 mm and a clear span of 4000 mm. The first three beams (Series I) were used to study the effect of varying the shear span. They were subjected to two concentrated loads (i.e. four-point bending), and had shear spans of 1750 mm, 1250 mm and 1000 mm respectively. Series II was designed to investigate the effect of moment distribution. It also included three FRP-plated RC beams, sharing one specimen with Series I. The other two beams were subjected to four- and eight-point loading respectively. They all had the same effective shear span equal to 1000 mm. For the precise implementation of the designed loading conditions, the load at each loading point was directly applied by a hydraulic jack, and all hydraulic jacks were connected to a single, manually-operated pump to ensure simultaneous and equal loading for all jacks. All five test beams failed by IC debonding, and the maximum moment in the beam at IC debonding (i.e. debonding moment) was found to increase as the shear span decreases or the load uniformity increases; a total increase of about 20% in debonding moment due to a combination of these factors was recorded.

Chapter 4 is dedicated to the finite element analysis of IC debonding failures under different load distributions with the following objectives: (1) to verify the accuracy of the developed finite element approach; and (2) to gain in-depth understanding of the behaviour of the simulated specimens. In this chapter, a recent FE approach developed by Chen et al. (2011) was augmented with a novel displacement control

technique for multi-point loading to capture the full failure process of the simulated beams. This approach takes into account the following essential factors to achieve accurate predictions for IC debonding: (1) accurate constitutive modelling for concrete cracking; and (2) accurate modelling of bond behaviour between concrete and both steel bars and FRP. The displacement control technique for multi-point loading was implemented by using an imagery rigid beam system realized through constraint equations. The tests presented in Chapter 3, together with beams tested under different load distributions from two other independent sources (Pan et al. 2009; Mazzotti and Savoia 2009), were used to verify a finite element (FE) approach for modelling IC debonding under different load distributions. It was found that the augmented FE approach could produce very close predictions of test results in terms of not only the moment-deflection curves but also the cracking behaviour; that is, this FE approach is capable of accurate modelling of IC debonding in FRP-plated RC beams under different load distributions. An FE parametric study was then conducted to extrapolate the test results.

In Chapter 5, three existing IC debonding strength models [i.e., the second approach in *fib* (2001); Chen et al. (2006) and Rosenboom and Rizkalla (2008)] have the potential to predict the strength of IC debonding under different load distributions. They were assessed using both the available test data and the numerical results from the present research programme.

Chapter 6 presents two series of tests on FRP-plated RC beams with vertical FRP U-jackets or inclined FRP U-jackets to investigate the effect of these jackets on IC debonding strength. The first series of tests were conducted on beams with vertical FRP U-jackets to clarify the IC debonding mechanism in such beams, and to demonstrate the limited benefit of these U-jackets to IC debonding strength. The second series of tests were conducted on RC beams with inclined FRP U-jackets. Such inclined FRP U-jackets are shown to have the ability to improve the IC debonding strength significantly because they can restrain the widening of major cracks in the mid-span region; as a result, part of the tensile force in the FRP soffit plate can be transferred to these inclined jackets.

Chapter 7 presents the first systemic experimental study on the use of FRP U-jackets of different forms for mitigating concrete cover separation failure. Ten full-scale FRP-plated RC beams were tested. The test results show that both the ultimate load and the ductility of the beams were enhanced by the U-jackets. Among the forms of U-jackets explored, those inclined at 45^{o} are the most effective.

A new approach for the design of FRP U-jackets to mitigate concrete cover separation was presented in Chapter 8, which includes two design models: one for vertical FRP U-jackets and the other one for inclined FRP U-jackets. The approach was developed based on the concrete tooth concept, and was verified using the limited test data from the present research project. Although the approach was based

on a rigorous mechanism basis, data that are more reliable are needed to verify the design approach further.

Chapter 9 closes the thesis by summarising the conclusions drawn from the preceding chapters and elaborating on future research needs in the area.

1.6 REFERENCES

ACI 440.2R-08 (2008). *Guide for the design and construction of externally bonded FRP systems for strengthening concrete structures*, ACI Committee 440, American Concrete Institute, Farmington Hills, MI, USA.

Ahmed, O. and van Gemert, D. (1999). "Effect of longitudinal carbon fiber reinforced plastic laminates on shear capacity of reinforced concrete beams", *Proceedings of the Fourth International Symposium on Fiber Reinforced Polymer Reinforcement for Reinforced Concrete Structures*, Maryland, USA

Bizindavyi, L. and Neale, K.W. (1999). "Transfer lengths and bond strengths for composites bonded to concrete", *Journal of Composites for Construction*, ASCE, Vol. 3, No. 4, pp. 153-160.

Buyukozturk, O., Gunes, O. and Karaca, E. (2004). "Progress on understanding debonding problems in reinforced concrete and steel members strengthened using FRP composites", *Construction and Building Materials*, Vol. 18, No. 1, pp. 9-19.

Chen, G.M., Teng, J.G. and Chen, J.F. (2011). "Finite-element modeling of intermediate crack debonding in FRP-plated RC beams", *Journal of Composites for Construction*, ASCE, Vol. 15, No. 3, pp. 339-353.

Chen, J.F., Teng, J.G. and Yao, J. (2006). "Strength model for intermediate crack debonding in FRP-strengthened concrete members considering adjacent crack

interaction", *Proceedings, Third International Conference on FRP Composites in Civil Engineering* (CICE 2006), Miami, Florida, USA.

Chen, J.F., Yuan, H. and Teng, J.G. (2007). "Debonding failure along a softening FRP-to-concrete interface between two adjacent cracks in concrete members", *Engineering Structures*, Vol. 29, No. 2, pp. 259-270.

CNR DT 200/2004 (2004). *Guidelines for design, execution and control of strengthening interventions by means of fibre-reinforced composites – materials, reinforced concrete and prestressed concrete structures, masonry structures*, Advisory Committee on Technical Regulations for Constructions, National Research Council, Rome, Italy.

Concrete Society (2012). *Design guidance for strengthening concrete structures using fibre composite materials*, Concrete Society Technical Report No. 55, Crowthorne, UK.

fib (2001). *Externally bonded FRP reinforcement for RC structures*, International Federation for Structural Concrete, Lausanne, Switzerland.

GB-50608 (2010). *Technical code for infrastructure application of FRP composites*, China Planning Press, Beijing, China.

Hamilton, H.R., Benmokrane, B., Dolan, C.W. and Sprinkel, M.M. (2009). "Polymer Materials to Enhance Performance of Concrete in Civil Infrastructure", *Polymer Reviews*, Vol. 49, No. 1, pp. 1-24.

Hiroyuki, Y. and Wu, Z.S. (1997). "Analysis of debonding fracture properties of CFS strengthened member subject to tension", *Non-Metallic (FRP) Reinforcement for Concrete Structures, Proceedings of the 3rd International Symposium*, Japan Concrete Institute, Sapporo

Hollaway, L.C. and Teng, J.G. (eds.) (2008). *Strengthening and rehabilitation of civil infrastructures using fibre-reinforced polymer (FRP) composites*, Woodhead Publishing, Cambridge, U.K.

Holzenkämpfer, O. (1994). *Ingenieurmodelle des verbundes geklebter bewehrung fürbeton bauteile*, Dissertation,TU Braunschweig, Germany.

Jansze, W. (1997). *Strengthening of RC members in bending by externally bonded steel plates*, PhD thesis, Delft University of Technology, Delft, the Netherlands.

Kalfat, R., Al-Mahaidi, R. and Smith, S.T. (2013). "Anchorage devices used to improve the performance of reinforced concrete beams retrofitted with a FRP composites: State-of-the-art review", *Journal of Composites for Construction*, ASCE, Vol. 17, No. 1, pp. 14-33.

Khalifa, A., Gold, W.J., Nanni, A. and Aziz, A. (1998). "Contribution of externally bonded FRP to shear capacity of RC flexural members", *Journal of Composites for Construction*, ASCE, Vol. 2, No. 4, pp. 195–203.

Kotynia, R., Baky, H.A., Neale, K.W. and Ebead, U.A. (2008). "Flexural strengthening of RC beams with externally bonded CFRP systems: Test results

and 3D nonlinear FE analysis", *Journal of Composites for Construction*, ASCE, Vol. 12, No. 2, pp 190-201.

Leung, C.K.Y. (2006). "FRP debonding from a concrete substrate: Some recent findings against conventional belief", *Cement and Concrete Composites*, Vol. 28, No. 8, pp. 742-748.

Liu, H.P., He, Z.X. and Huang, P.Y. (2002). "The applications of FRP plates in repairing and strengthening bridges", *Guangdong Highway Communications*, Vol. 76, No.S1, pp. 148-151 (in Chinese).

Lu, X.Z., Ye, L.P., Teng, J.G. and Jiang, J.J. (2005a). "Meso-scale finite element model for FRP sheets/plates bonded to concrete", *Engineering Structures*, Vol. 27, No. 4, pp. 564-575.

Lu, X.Z., Teng, J.G., Ye, L.P. and Jiang, J.J. (2005b). "Bond-slip models for FRP sheets/plates bonded to concrete", *Engineering Structures*, Vol. 27, No. 6, pp. 920-937.

Lu, X.Z., Teng, J.G., Ye, L.P. and Jiang, J.J. (2007). "Intermediate crack debonding in FRP-strengthened RC beams: FE analysis and strength model", *Journal of Composites for Construction*, ASCE, Vol. 11, No. 2, pp. 161-174.

Maeda, T., Asano, Y., Sato, Y., Ueda, T., and Kakuta, Y. (1997). "A study on bond mechanism of carbon fiber sheet", *Non-Metallic (FRP) Reinforcement for*

Concrete Structures, Proceedings of the 3rd International Symposium, Japan Concrete Institute, Sapporo.

Malek, A.M., Saadatmanesh, H. and Ehsani, M.R. (1998). "Prediction of failure load of R/C beams strengthened with FRP plate due to stress concentration at the plate end", *ACI Structural Journal*, Vol. 95, No. 2,pp. 142-152.

Mazzotti, C. and Savoia, M. (2009). "Experimental tests on intermediate crack debonding failure in FRP-strengthened RC beams", *Advances in Structural Engineering*, Vol. 12, No. 5, pp. 701-713.

Oehlers, D.J. (1992). "Reinforced concrete beams with plates glued to their soffits", *Journal of Structural Engineering-ASCE*, Vol. 118, No. 8, pp. 2023-2028.

Pan, J.L., Chung, T.C.F. and Leung, C.K.Y. (2009). "FRP debonding from concrete beams under various load uniformities", *Advances in Structural Engineering*, Vol. 12, No. 6, pp.807-819.

Pham, H.B. and Al-Mahaidi, R. (2006). "Prediction models for debonding failure loads of carbon fiber reinforced polymer retrofitted reinforced concrete beams", *Journal of Composites for Construction*, ASCE, Vol. 10, No. 1, pp. 48-59.

Piamanmas, A. and Pornpongsaroj, P. (2004). "Peeling behaviour of reinforced concrete beams strengthened with CFRP plates under various end restraint conditions", *Magazine of Concrete Research*, Vol. 56, No. 2, pp. 73-81.

Raoof, M. and Hassanem, M.A.H. (2000). "Peeling failure of reinforced concrete

beams with fiber-reinforced plastic or steel plates glued to their soffits", *Proceedings of the Institution of Civil Engineers: Structures and Buildings*, Vol. 140, No. 3, pp. 291-305

Raoof, M. and Zhang, S. (1997). "An insight into the structural behavior of reinforced concrete beams with externally bonded plates", *Proceedings of the Institution of Civil Engineers: Structures and Buildings*, Vol. 122, No. 4, pp. 477-492

Rosenboom, O. and Rizkalla, S. (2008). "Modeling of IC debonding of FRP-strengthened concrete flexural members", *Journal of Composites for Construction*, ASCE, Vol. 12, No. 2, pp. 168-179.

Said, H. and Wu, Z.S. (2008). "Evaluating and proposing models of predicting IC debonding failure", *Journal of Composites for Construction*, ASCE, Vol. 12, No. 3, pp.284-299.

Sebastian, W.M. (2001). "Significance of mid span debonding failure in FRP-plated concrete beams", *Journal of Structural Engineering-ASCE*, Vol. 127, No. 7, pp. 792-798.

Smith, S.T. and Teng, J.G. (2002a). "FRP-strengthened RC beams. I: review of debonding strength models", *Engineering Structures*, Vol. 24, No. 4, pp. 385-395.

Smith, S.T. and Teng, J.G. (2002b). "FRP-strengthened RC beams. II: assessment of

debonding strength models", *Engineering Structures*, Vol. 24, No. 4, pp. 397-417.

Smith, S.T. and Teng, J.G. (2003). "Shear-bending interaction in debonding failures of FRP-plated RC beams", *Advances in Structural Engineering*, Vol. 6, No. 3, pp. 183–99.

Tanaka, T. (1996). "*Shear resisting mechanism of reinforced concrete beams with CFS as shear reinforcement*", Graduation thesis, Hokkaido University, Japan.

Teng, J.G. and Chen, J.F. (2009). "Mechanics of debonding in FRP-plated RC beams", *Proceedings of the Institution of Civil Engineers-Structures and Buildings*, Vol. 162, No. 5, pp. 335-345.

Teng, J.G., Chen, J.F., Smith, S.T. and Lam, L. (2002). *FRP-strengthened RC Structures*, West Sussex: Wiley.

Teng, J.G., Smith, S.T., Yao, J. and Chen, J.F. (2003). "Intermediate crack-induced debonding in RC beams and slabs", *Construction and Building Materials*, Vol. 17, No. 6-7, pp. 447-462.

Teng, J.G. and Yao, J. (2007). "Plate end debonding in FRP-plated RC beams—II: Strength model", *Engineering Structures*, Vol. 29, No. 10, pp. 2472–2486.

Teng, J.G., Yuan, H. and Chen, J.F. (2006). "FRP-to-concrete interfaces between two adjacent cracks: Theoretical model for debonding failure", *International Journal of Solids and Structures*, Vol. 43, No. 18-19, pp. 5750-5778.

US Bureau (2006). "*Statistical Abstract of the United States.120th ed",* Washington DC: USA Bureau of Statistics.

Wu, Z.S. and Niu, H.D. (2000). "Study on debonding failure load of RC beams strengthened with FRP sheets", *Journal of Structural Engineering*, JSCE,Vol. 46A, pp. 1431-1441.

Wu, Z.S. and Niu, H.D. (2007). "Prediction of crack-induced debonding failure in R/C structures flexurally strengthened with externally bonded FRP composites", *Doboku Gakkai Ronbunshun E*, Vol. 63, No. 4, pp. 620-639.

Yao, J. and Teng, J.G. (2007). "Plate end debonding in FRP-plated RC beams—I: Experiments", *Engineering Structures*, Vol. 29, No. 10, pp. 2457–2471.

Yuan, H., Wu, Z.S. and Yoshizawa, H. (2001). "Theoretical solutions on interfacial stress transfer of externally bonded steel/composite laminates", *Journal of Structural Mechanics and Earthquake Engineering,* JSCE, Vol. 18, No. 1, pp. 27-39.

Zhang, S.S. (2011). *Behaviour and Modelling of RC Beams Strengthened in Flexure with Near-surface Mounted FRP*, PhD Thesis, The Hong Kong Polytechnic University, Hong Kong, China.

Zhang, S.S. and Teng, J.G. (2014). "Finite element analysis of end cover separation in RC beams strengthened in flexure with FRP", *Engineering Structures*, Vol. 75, pp. 550-560.

1.7 FIGURES

(a) Carbon fibre sheets **(b) Glass fibre sheet**

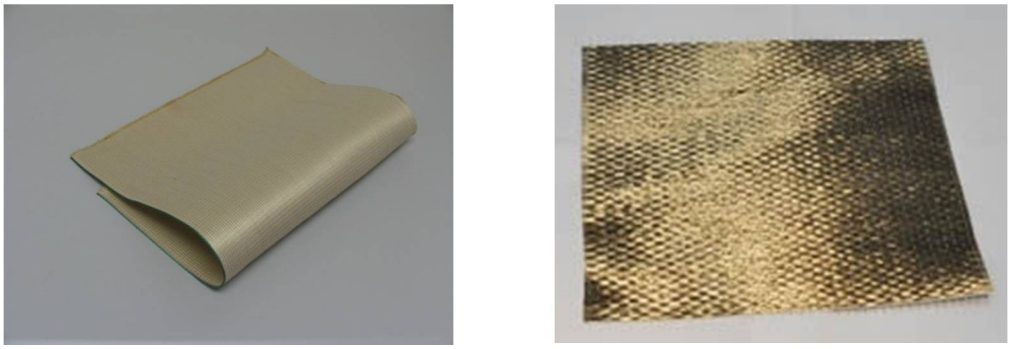

(c) Aramid fibre sheet **(d) Basalt fibre sheet**

Figure 1.1 Dry fibre sheets for wet lay-up applications [from Zhang (2011)]

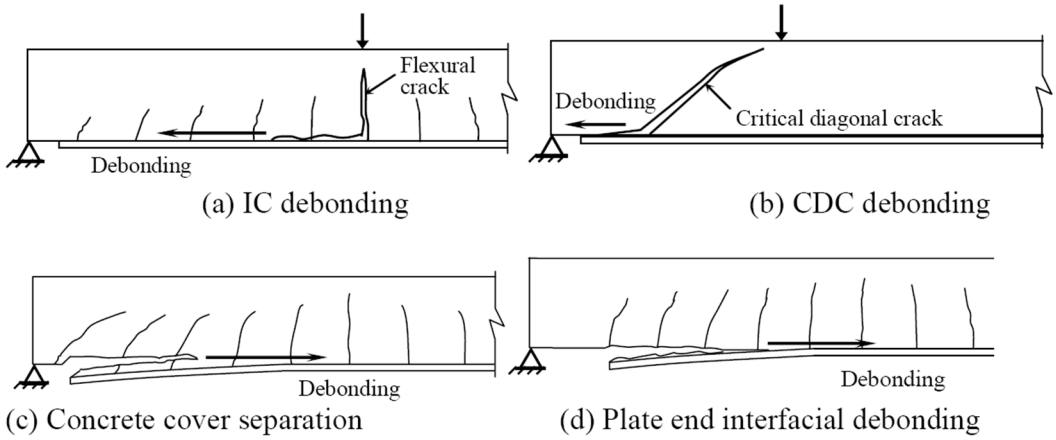

Figure 1.2 Debonding failure modes of FRP-plated RC beams [from Teng et al. (2003)]

CHAPTER 2

LITERATURE REVIEW

2.1 INTRODUCTION

This Chapter presents a comprehensive literature review on issues pertinent to the debonding failures in an FRP-plated RC beam. It starts with a review on studies on FRP-to-concrete bonded joints. The simple FRP-to-concrete bonded joints had been experimentally or numerically studied to investigate the debonding mechanism as well as to develop a bond strength model. It believed that the debonding mechanism in an FRP-to-concrete bonded joint was similar to that in an FRP-plated RC beams, and some debonding strength models for FRP-plated RC beams were therefore directly modified from a bond strength model for FRP-to-concrete bonded joint. A review on IC debonding failure, which is one of the most common failure modes of FRP-plated RC beams, is then followed. Research on the effect of FRP U-jackets on both IC debonding and concrete cover separation has also been reviewed. Research gaps in debonding failures in an FRP-plated RC beam, which are indicated by the present review, are briefly discussed to emphasize the necessity of the present

project.

2.2 BOND BEHAVIOUR OF FRP-TO-CONCRETE INTERFACES

Understanding of the bond behaviour between FRP and concrete is essential to study the mechanisms of various debonding failures of FRP-plated RC beams. It is believed that the stress states of the FRP-to-concrete interfaces of FRP-to-concrete bonded joints are similar to those in FRP-plated RC beams. In addition, tests on FRP-to-concrete bonded joints are much easier than direct testing on FRP-plated RC beams. Therefore, simple FRP-to-concrete bonded joints of different types as a direct and efficient way to investigate the bond behaviour between FRP and concrete have been widely studied for understanding the debonding failures in FRP-plated RC beams.

FRP-to-concrete bonded joints have been studed experimentally as well as theoretically (e.g. Taljsten 1997; Bizindavyi and Neale 1999; Chen and Teng 2001; Yuan et al. 2001; Yuan et al. 2004; Yao et al. 2005; Wu and Jiang 2013). The tests on FRP-to-concrete bonded joints have provided substantial direct information for understanding the bond behaviour between the FRP and concrete, and results of these tests formed a large database for the verification of theoretical models (e.g. FE approaches and bond strength models). FE analysis on FRP-to-concrete bonded joints using a verified FE approach could provide more detailed information on the debonding process of FRP-to-concrete bonded joints, and is therefore viewed as a efficient and convenient tool (e.g. Lu et al. 2005a; Lu et al. 2005b; Lu et al. 2006;

Baky et al. 2012; Tao and Chen 2015).

These theoretical and experimental studies finally lead to bond-slip models for FRP-to-concrete interfaces and bond strength models. The bond-slip models (e.g. Lu et al. 2005b; Baky et al. 2012) are essential for accurate FE modeling of an FRP-plated RC beam as well as analytical investigation into the debonding process in an FRP-to-concrete bonded joint. These bond strength models for FRP-to-concrete bonded joints (e.g. Holzenkampfer 1994; Tanaka 1996; Maeda et al. 1997; Neubauer and Rostasy 1997; van Gemert 1997; Yuan and Wu 1999; Niedermeier 2000; Chen and Teng 2001; Yuan et al. 2001) have been established by regressing test data of FRP-to-concrete bonded joints, or using a fracture mechanics theory with an appropriate bond-slip model for the FRP-to-concrete interfaces. These bond strength models for FRP-to-concrete bonded joints can be slightly modified to serve as a strength model against IC debonding in FRP-plated RC beams. These research works on FRP-to-concrete bonded joints are reviewed in the following sub-sections.

2.2.1 Bond tests

The existing tests on FRP-to-concrete bonded joints has been categorized by Yao et al. (2005) into five types: (1) far-end support (FES) double-shear tests (van Gemert 1980; Brosensand van Gemert 1997; Maeda et al. 1997; Pellegrino et al. 2008; Serbescu et al. 2013; Ko et al. 2014); (2) near-end support (NES) double-shear tests (Neubauer and Rostasy 1997, Schilde and Seim 2007, Biscaia et al. 2012); (3) FES single-shear tests (Chen et al. 2001); (4) NES single-shear tests and (5) beam tests as

shown in Figure 2.1. The first four types are also referred to as (1) double-shear pull tests; (2) double-shear push tests; (3) single-shear pull tests; and (4) single-shear push tests respectively (Chen et al. 2001, Chen and Teng 2001). The present thesis follows the category definition by Yao et al. (2005) for better clarity, as the plate in a bonded joint of all the four types is always directly subjected to a tension force and the joint can be referred to as a "pull" bonded test.

Among them, the FES double-shear test and the NES single-shear test are the most popular ones due to their ease of application. Test results of the bond behaviour are sensitive to testing methods, and different testing methods can lead to significantly different results (Horiguchi and Saeke 1997; Chen et al. 2001; Yuan et al. 2004). As a result, Yao et al. (2005) suggested the NES single-shear test as the standard test set-up for the development of a bond strength model and local bond-slip relationship although the FES double-shear test has also been recommended by Serbescu et al. (2013) and Ko et al. (2014).

2.2.1.1 FES Double-shear tests

The FES double-shear test has been widely accepted as one of the most popular testing methods for FRP (or steel)-to-concrete bonded joints (van Gemert 1980; Brosensand van Gemert 1997; Maeda et al. 1997; Pellegrino et al. 2008; Serbescu et al. 2013; Ko et al. 2014). In an FES double-shear test, two FRP plates are bonded onto the two opposite sides of the concrete block with one end of each of the two FRP plates being subjected to an equal tensile force. The forces on the FRP plates are

balanced by the force from a steel bar embedded into the concrete block or two strong steel plates onto the other two sides of the concrete block.

Maeda et al. (1997) conducted a series FES double-shear tests on FRP-to-concrete bonded joints. The effects of the thickness, bond length, and width of the FRP plate were examined. It was found that the bond strength did not increase significantly when the bond length of the FRP plate exceeded a certain value (e.g. 100 mm), and the width of the FRP plate had a significant influence on the averaged bond stress (= tensile force on the plate divided by the entire bond area).

Sixteen FES double-shear tests on FRP-to-concrete bonded joints were carried out by Pellegrino et al. (2008) to examine the effect of the rigidity of the FRP plate on the bond behaviour of FRP-to-concrete interfaces. Different types and cross-sectional areas of the FRP plate were used to cover a wide range of the FRP axial rigidity. Based on the test results, new expressions for the effective bond length and the both strength (i.e. the ultimate load of the bonded joint) were proposed, with the effect of the FRP axial rigidity taken into account.

Serbescu et al. (2013) presented the results of 20 small-scale double-shear tests for evaluating the bond performance between FRP and concrete. They suggested the FES double-shear test as the potential standard set-up for evaluating the bonding performance of FRP-to-concrete interfaces. The experimental variables considered are the concrete surface preparation as well as the FRP plate type, which differ in their width, thickness and elastic modulus. The concrete surfaces were prepared

using two different methods leading, to surface roughness of two different degrees. All the concrete blocks had the same dimensions: 400 mm in length and 150 mm in both height and width. The test results showed that the rougher surface, which was prepared using air blasting to remove the dust, led to a debonding failure with a thicker concrete layer attached to the FRP plate. As a result, this method of concrete surface preparation was suggested for use in such bond tests.

Another 18 FES double-shear tests on FRP-to-concrete bonded joints were carried out by Ko et al. (2014), which also formed part of the same iRRT as that conducted by Serbescu et al. (2013). This experimental program had the same experimental variables (i.e. types of FRP plates and concrete surface preparation methods) and specimens of the same dimensions as those of Serbescu et al. (2013). It is therefore reasonable that Ko et al. (2014) also suggested the use of the FES double-shear test as a standard approach for evaluating the bond characteristics of FRP-to-concrete interfaces. Based on the test results, Ko et al. (2014) proposed a local bond-slip model for FRP-to-concrete interfaces considering the characteristics of concrete, FRP and adhesive. This bond-slip model is further discussed in the review of bond-slip models given later in the chapter.

2.2.1.2 NES Double-shear tests

In a NES double-shear test, two FRP plates with one end being subjected to tension are bonded onto the two opposite sides of a concrete block. Different from a FES double-shear test, the forces in the FRP plates are balanced by the push force on the

concrete block, so the concrete block is loaded in compression. This test method has also been adopted by many researchers (e.g. Neubauer and Rostasy 1997; Schilde and Seim 2007; Biscaia et al. 2012).

Thirteen NES double-shear tests were carried out by Biscaia et al. (2012) to investigate the bond behaviour of FRP-to-concrete interfaces under different combinations of shear stress and normal stress. The experimental parameters examined are the concrete strength and the compressive stress perpendicularly exerted on the plane of the FRP plate. They reported that the compressive stress exerted on the FRP plate had a significant effect on the bond behaviour of FRP-to-concrete interfaces.

2.2.1.3 FES Single-shear tests

FES Single-shear tests on FRP-to-concrete bonded joints are a possible alternative to investigate the bond behaviour of FRP-to-concrete interfaces (Chen et al. 2001). In such a test, one FRP plate is bonded on one side of the concrete block and one end of the plate is under tension, which is balanced by the tensile force exerted on the concrete block. However no study has yet been found using such a set-up to investigate the bond behaviour of FRP-to-concrete interfaces.

2.2.1.4 NES Single-shear tests

The NES single-shear test is possibly the most popular set-up for the

FRP-to-concrete bonded joint to investigate the bond behaviour of FRP-to-concrete interfaces (Chajes et al. 1996; Bizindavyi and Neale 1999; Yao et al. 2005; Yao 2004; Sharma et al. 2006; Mazzotti et al. 2008; Bilotta et al. 2011; Toutanji et al. 2012; Wu and Jiang 2013). In such a test, one FRP plate is bonded onto one side of the bonded joint with one of two ends of the plate being subjected to tension, and the tensile force on the FRP plate is balanced by the compressive force on the concrete block, so the concrete block is loaded in compression.

Chajes et al. (1996) used the NES single-shear test to determine the bond characteristics of FRP-to-concrete interfaces. Their experimental program included the bond length, concrete surface preparation method, concrete strength, and type of adhesive as the test variables. It concluded that all the four test variables had significant effects on the bond behaviour of FRP-to-concrete interfaces. As the concrete strength increased, the bond strength increased. It was also demonstrated by this study that no further increase in the bond strength of the FRP plate could be achieved when the bond length of the FRP plate exceeded a specific value.

Two series of FRP-to-concrete bonded joints were tested by Bizindavyi and Neale (1999). The effects of the bonded length, type and thickness of the FRP plate on the bond behaviour of FRP-to-concrete interfaces were examined. The test results were compared with the predictions from their own theoretical study given in Bizindavyiand Neale (1999).The concept of the effective bond length of the FRP plate externally bonded to concrete was also highlighted by them.

Yao et al. (2005) and Yao (2004) reported the test results of 72 FRP-to-concrete bonded joints, and they used the NES single-shear test as their test method. Their test variables included the width of concrete block, the height of free concrete edge, and the width, bond length of the FRP plate and loading offset (i.e. the initial loading angle between the pull force and the top face of the concrete block). Among the examined test variables, the height of free concrete edge, which was defined as the height of concrete block minus the height of the region acted on by the compressive force, was first experimentally examined. The debonding mechanisms and processes of the FRP plate from concrete were reported in detail. In addition to the effect of bond length, the effects of FRP-to-concrete width ratio, loading offset and height of free concrete edge on the bond behaviour were emphasized.

Sharma et al. (2006) tested thirty six FRP-to-concrete bonded joints using the single shear push test rig. In this experimental program, the effects of the type and bond length of FRP plate were examined. It concluded that the tensile strength and bond length of the plate bonded to the concrete had critical effects on the bond behaviour of the FRP-to-concrete interface.

Eight FRP-to-concrete bonded joints were tested by Mazzotti et al. (2008) using the single-shear push test method to verify the bond-slip models of the FRP-to-concrete interface. The width and bond length of the FRP plate were the experimental variables examined in their study. The same research group modified the NES single-shear test, and used the modified test method to achieve a stable debonding process (Mazzotti et al. 2009). The stable debonding process was achieved by a steel

plate system, which clamped the free end of the FRP plate. In addition, a compressive force perpendicular to the plane of the FRP plate was applied through an actuator.

Thirty-four NES single-shear tests on FRP-to-concrete bonded joints were carried out by Bilotta et al. (2011). The effects of type, thickness, width and bond length of the FRP plate on the bond behaviour were investigated in the experimental program. The results of these thirty-four tests together with test data collected from other existing studies were used to calibrate the theoretical models for predicting the bond strength of an FRP plate bonded to concrete.

The above lists some of the most profound studies on this issue, however there are still many other studies on FRP-to-concrete bonded joints using the NES single-shear or FES double-shear bonded joint tests have been reported (e.g. Toutanji et al. 2012; Wu and Jiang 2013). The variables examined by these experimental programs primarily include the strength and width of the concrete block, as well as the type, thickness, width and bond length of the FRP plate.

2.2.1.5 Beam tests and modified beam tests

The beam test has also been adopted by some researchers to investigate the bond behaviour of FRP-to-concrete interfaces. This method has been preferred by some researchers as they thought that the variation of the shear force and moment of section along the beam is closer to that of an FRP-plated RC beam in practice.

(Miller and Nanni 1999; Pellegrino et al. 2008).

Miller and Nanni (1999) carried out three series of beam tests to quantify the bond characteristics of FRP-to-concrete interfaces. In their experimental study, the effects of thickness and bond length of the FRP plate and concrete strength were investigated. The authors concluded that the bond length of the FRP plate and concrete strength had marginal effects on the bond strength of the FRP plate. Their conclusions may be questionable as it has been well recognized that concrete strength has a significant effect on the bond strength of an FRP plate bonded onto concrete substrate, and the bond length of the plate can affect the bond strength significantly if the bond length does not exceed the effective bond length of the FRP plate.

Twenty-one beam tests were conducted by Pellegrino et al. (2008) to quantify the bond behaviour of the FRP-to-concrete interface. The type of FRP plate was its experimental variable. Based on these experimental results, new expressions for the bond characteristics of the FRP-to-concrete interface including the effective bond length, maximum local bond stress, local slip at the maximum local bond stress and local slip at complete debonding were proposed.

2.2.2 Finite element analysis

Finite element (FE) analysis has been often used to gain a fuller understanding of the fundamental mechanics of debonding of FRP from concrete in FRP-to-concrete

bonded joints. Existing FE approaches for this purpose can be categorized into:(a) the perfect bonding approach, in which the concrete elements are directly connected to the FRP elements by sharing nodes (Camata et al. 2004 ; Pham et al. 2006; Lu et al. 2005a; Lu et al. 2005b; Lu et al. 2006; Baky et al. 2012; Tao and Chen 2015); (b) the interface approach, in which the concrete elements are connected to the FRP elements via a group of interface elements (Ebead and Neale 2007; Diab and Wu 2007; Salomoni et al 2011). The interface approach requires the input of a bond-slip model for the FRP-to-concrete interface elements, which means that the interface approach is not a truly predictive approach (i.e. its predictions depend on the bond-slip model employed). These existing studies are reviewed as follows.

2.2.2.1 Perfect-bonding approach

In the perfect bonding approach, the elements representing the FRP plate (referred to as the FRP elements for brevity) is directly connected to the elements representing the concrete (referred to as the concrete elements for brevity) by sharing element nodes, and debonding of the FRP plate in FRP-to-concrete bonded joints is simulated by concrete cracking. If an appropriate constitutive model for concrete and an appropriate FE mesh are used, the perfect bonding model can predict the debonding behaviour closely. The method provides a powerful tool to gain in-depth understanding of debonding behaviour in FRP-to-concrete bonded joints. In particular, the method can be used to generate numerical results for the development of bond-slip models for the FRP-to-concrete interface (e.g. Lu et al. 2005a, 2005b; Baky et al. 2012).

Camata et al. (2004) and Pham et al. (2006), which are from the same group and used the same approach, carried out FE analyses on the debonding of FRP-to-concrete bonded joints using a combination of smeared and discrete crack approaches. The smeared crack model was used to define the cracking criterion and softening behaviour of concrete after cracking, and an additional interface crack model was used to define the behaviour of the interfaces between the opposite sides of a crack. They concluded that this approach had the ability to predict debonding in FRP-to-concrete bonded joints closely. However their approach required the predefinition of crack positions and re-meshing for cracking propagation, which means that the method is not a truly predictive method.

A meso-scale FE approach was proposed and used for developing bond-slip models for FRP-to-concrete interfaces by Lu et al. (2005a, 2005b). In these studies, small element sizes ranging from 0.25 mm to 0.50 mm were used to closely capture both the micro-cracking and the macro-cracking of concrete. The concrete elements were directly connected to those of the adjacent FRP plate without using any interface elements. Based on the modeling results, three bond-slip models of different levels of sophistication were proposed and have received wide recognition (e.g. Neale et al. 2006; Baky et al. 2007; Kotynia et al. 2008).

Lu et al. (2006) used three different smeared crack models to simulate debonding in an FRP-to-concrete bonded joint. In this study, the FRP elements shared nodes with their adjacent concrete elements, and the debonding of the FRP plate from the concrete substrate was simulated as cracking of the concrete elements adjacent to the

FRP plate. The smallest size of concrete elements employed in the study was 2 mm. It was found that a non-coaxial rotating smeared crack model could avoid the shear stress locking problem, which was encountered in FE analysis using other smeared crack models. The non-coaxial rotating smeared crack model was therefore found to perform the best in predicting the debonding behaviour. Detailed numerical results are presented in the paper for an in-depth understanding of the debonding process.

Pham and Al-Mahaidi (2006) developed an FE approach for modeling debonding in FRP-to-concrete bonded joints. A fine element size of about 2 mm was used for the elements near the bond-line. The concrete elements were directly connected to the FRP elements, and therefore debonding was simulated as concrete cracking. They concluded that predictions from their FE approach agreed well with the experimental results.

Baky et al. (2012) proposed a 3D meso-scale FE approach for establishing a new bond-slip model. The size of elements used adjacent to the bond-line was 0.5 mm. Due to the use of very fine elements, such a simulation imposed heavy demands on both computational power and data storage, and the authors resorted to the use of supercomputers and parallelization techniques. Concrete cracking was simulated using the microplane constitutive law, which was implemented as a user-defined subroutine in the general-purpose FE package ADINA. Based on FE results, a new bond-slip model, which considers the interaction between the interfacial normal stress and the local bond strength, was proposed.

Tao and Chen (2015) directly used the concrete damage plasticity model in the general-purpose FE package ABAQUS (ABAQUS 2004) to simulate debonding behaviour in FRP-to-concrete bonded joints. This approach is simple but robust, and can be easily implemented in ABAQUS without composing a complex user subroutine. Based on a mesh convergence study presented in Tao and Chen (2015), the size of concrete elements adjacent to the bond-line has a marginal effect on the predicted debonding behaviour when the size was smaller than 1.0 mm. As a result, in most of the FE simulations conducted by Tao and Chen (2015), 1.0 mm was used as the element size. Good agreement between FE predictions and test results was achieved, indicating the capability of this approach in accurately predicting the debonding behaviour of the FRP-to-concrete bonded joint.

2.2.2.2 Interface approach

The interface approach employs a layer of interface elements to connect the concrete elements to the FRP elements. A constitutive model for the interface element (i.e., a bond-slip model) is required as the input, and the accuracy of modeling depends on the bond-slip model used. Such an FE approach is not a truly predictive approach, but is still a useful tool for understanding the debonding process in FRP-to-concrete bonded joints.

Ebead and Neale (2007) developed an FE approach to investigate the interfacial behaviour of FRP-to-concrete interfaces. The sizes of the FRP and the concrete elements were chosen to be 0.25 mm to 0.50 mm. The concrete and the FRP plate

were simulated using plane stress elements and truss elements respectively; while the bond behaviour between the FRP plate and its adjacent concrete was simulated using interface elements with a bond-slip model. The FE approach provided predictions of the bond strength as well as the stress and the strain distributions over the FRP plate. The accuracy of the predictions highly depends on the choice of the bond-slip model for the interface elements; although they claimed that good agreement with test results was achieved in their studies.

Diab and Wu (2007) used FE analysis to investigate the long-term behaviour of FRP-to-concrete interfaces. In their approach, the concrete was simulated using four-node plain stress elements, and the FRP plate was modeled using two-node truss elements. The concrete elements were connected to the FRP elements through interface elements, whose constitutive behaviour was governed by a bond-slip model.

A 3D FE approach was developed by Salomoni et al. (2011) to investigate the debonding of FRP-to-concrete bonded joints. The Drucker-Prager model in ABQUS was adopted to simulate the behaviour of concrete, while the FRP plate was assumed to behave in a linear-elastic manner. The interfacial behaviour of FRP-to-concrete interfaces was simulated using a surface-to-surface contact approach, whose constitutive behaviour was governed by a bond-slip model.

2.2.3 Local bond-slip models

A reliable bond-slip model is of crucial importance for the FE modeling and analytical investigation of FRP-plated RC beams, and hence for understanding their debonding behaviour. Development of bond-slip models for FRP-to-concrete interfaces has therefore received intensive research attention and many bond-slip models have been proposed based on experimental or FE modeling results (Neubauer and Rostasy 1997; Brosens and van Gemert 1999; Nakaba et al. 2001; Savioa et al. 2004; Cao et al. 2007; Dai and Ueda 2003; Dai et al. 2005; Lu et al. 2005b; Baky et al. 2012; Ko et al. 2014). The most-widely accepted bond-slip models are reviewed as follows.

Neubauer and Rostasy's (1997)model

A bond-slip model for FRP-to-concrete interfaces with a linear ascending branch and a sudden drop was proposed by Neubauer and Rostasy (1997). Its expressions are given as follows:

$$\tau = \tau_{max}\left(\frac{s}{s_1}\right) \text{ if } s < s_1 \tag{2.1a}$$

$$\tau = 0 \text{ if } s > s_1 \tag{2.1b}$$

in which τ is the local shear bond stress between FRP and concrete; s is the slip between FRP and concrete; τ_{max} is the maximum local shear bond stress between FRP and concrete; s_1 is the slip between FRP and concrete corresponding to the maximum local shear bond stress. The maximum local bond stress, τ_{max}, is equal to $1.8f_t$; f_t is the tensile strength of concrete; while s_1 is equal to $0.224\beta_w^2$. The width ratio, β_w, can be determined using Eq. 2.1c:

$$\beta_w = \sqrt{\frac{1.06(2.0 - b_f/b_c)}{1.0 + b_f/400.0}} \quad (2.1c)$$

where b_f, b_c are the widths of the FRP plate and the concrete block respectively.

Brosens and van Gemert's (1999) model

A bilinear bond-slip model was proposed by Brosens and van Gemert (1999). The expressions of the bond-slip model are as follows:

$$\tau = \tau_{max}\left(\frac{s}{s_1}\right) \text{if} s < s_1 \quad (2.2a)$$

$$\tau = \tau_{max}\left(\frac{s_2 - s}{s_2 - s_1}\right) \text{if } s_1 < s < s_2 \quad (2.2b)$$

where s_2 is the slip between FRP and concrete corresponding to the local bond shear stress decreasing to zero (i.e. the slip between FRP and concrete at complete debonding of the FRP plate).The maximum bond stress, τ_{max}, is determined by

$$\tau_{max} = 1.8\beta_w f_t \quad (2.2c)$$

The width ratio, β_w, is defined by Eq. 2.2d.

$$\beta_w = \sqrt{\frac{1.5(2.0 - b_f/b_c)}{1.0 + b_f/b_{f0}}} \quad (2.2d)$$

b_{f0} is a constant and is taken to be 100.0 mm.

The slip between FRP and concrete corresponding to the maximum local bond shear stress, s_1, is defined as follows:

$$s_1 = 2.5\tau_{max}\left(\frac{t_f}{E_f} + \frac{h_a}{E_c}\right) \tag{2.2e}$$

in which t_f is the thickness of the FRP plate;h_a is the reference depth taken to be 2.5-3.0 times the maximum aggregate size; E_f and E_c are the elastic modulis of the FRP plate and the concrete respectively.

The ultimate local slip, s_2, is given by

$$s_2 = 2.0G_f/\tau_{max} \tag{2.2f}$$

where G_f is the interfacial fracture energy between FRP and concrete, and can be determined as follows:

$$G_f = 0.3\beta_w^2 f_t \tag{2.2g}$$

If the slip exceeds s_2; the bond stress, τ, decreases to zero.

Nakaba et al.'s (2001) model

A bond-slip model of the Popovics' type is presented in Nakaba et al. (2001). This model is expressed as follows:

$$\tau = \tau_{max}\left(\frac{s}{s_1}\right)\left[3.0/\left(2.0 + \left(\frac{s}{s_1}\right)^3\right)\right] \tag{2.3a}$$

The slip between FRP and concrete corresponding to the maximum local bond shear stress, s_1, is expressed as follows:

$$s_1 = 3.5f_c^{0.19} \tag{2.3b}$$

where $\boldsymbol{f_c}$ is the cylinder compressive strength of concrete.

Savioa et al.'s (2003) model

Savioa et al.'s (2003) model is also of the Popovics' type but with the coefficients being different from those used in Nakaba et al.'s (2001) model, and is given by

$$\tau = \tau_{max}\left(\frac{s}{s_1}\right)\left[2.86/\left(1.86+\left(\frac{s}{s_1}\right)^{2.86}\right)\right] \tag{2.4a}$$

The expression for s_1 in this model is the same as that in Nakaba et al.'s model.

Dai and Ueda's (2003) model

Dai and Ueda (2003) proposed a bond-slip model based on the FRP strain distributions of FRP-to-concrete bonded joints with a very soft adhesive layer. This model is given as follows:

$$\tau = \tau_{max}\left(\frac{s}{s_1}\right)^{0.575} \text{if} s < s_1 \tag{2.5a}$$

$$\tau = \tau_{max} e^{-c_2(s-s_1)} \text{if} s_1 < s \tag{2.5b}$$

in which τ_{max} is given by

$$\tau_{max} = \frac{-1.575c_1K_a + \sqrt{2.481c_1^2K_a^2 + 6.3c_1c_2^2K_aG_f}}{2c_2} \tag{2.5c}$$

The local slip corresponding to the maximum bond stress, s_1, is given as follows:

$$s_1 = \tau_{max}/(\alpha K_a) \tag{2.5d}$$

The coefficients, c_1 and c_2, are given by

$$c_1 = 0.028\left(E_f t_f/1000\right)^{0.254} \tag{2.5e}$$

$$c_2 = 0.0035K_a\left(E_f t_f/1000\right)^{0.34} \tag{2.5f}$$

in which K_a and $E_f t_f$ are the axial stiffness of the adhesive and the FRP respectively.

The interfacial fracture energy between FRP and concrete, G_f, is given by

$$G_f = 7.554K_a^{-0.449}(f_c)^{0.343} \tag{2.5g}$$

Dai et al.'s (2005) model

Dai et al. (2005) proposed another bond-slip model, in which the ascending and the descending branches are expressed using a single equation as follows:

$$\tau = 2c_3 G_f(e^{-c_3 s} - e^{-2c_3 s}) \tag{2.6a}$$

in which τ_{max} can be determined by the following equation:

$$\tau_{max} = 0.5c_3 G_f \tag{2.6b}$$

The local slip corresponding to the maximum bond stress, s_1, is given as follows:

$$s_1 = 0.693c_3 \tag{2.6c}$$

The coefficient, c_3, is given by

$$c_3 = 6.846\left(E_f t_f/1000\right)^{0.108}(K_a)^{0.833} \tag{2.6d}$$

The interfacial fracture energy between FRP and concrete, G_f, is given by

$$G_f = 0.446\left(E_f t_f/1000\right)^{0.023} K_a^{-0.352} (f_c)^{0.236} \quad (2.6e)$$

The precise model in Lu et al. (2007)

Lu et al. (2006) proposed three bond-slip models of different levels of sophistication based on results from meso-scale finite element analysis and test data. The precise model was established with a precise definition of the effective thickness of the concrete. This precise model is given as follows:

$$\tau = \tau_{max}\left(\sqrt{\frac{s}{s_1 A_1} + B_1^2} - B_1\right) \text{if} \quad s < s_1 \quad (2.7a)$$

$$\tau = \tau_{max} e^{-\alpha(s/s_1 - 1)} \text{if} s_1 < s \quad (2.7b)$$

in which $\tau_{max}$and s_1 and can be determined by Eq. 2.7c and 2.7d respectively.

$$\tau_{max} = \alpha_1 \beta_w f_t \quad (2.7c)$$

$$s_1 = \alpha_2 \beta_w f_t + s_e \quad (2.7d)$$

where s_e is the elastic component of $s_1$and is equal to τ_{max}/K_0; the width ratio factor, β_w, can be determined by Eq. 2.7e.

$$\beta_w = \sqrt{\left(2 - b_f/b_c\right)/\left(1 + b_f/b_c\right)} \quad (2.7e)$$

The coefficients A_1 and B_1 in Eqs.2.7a are determined by the following equations:

$$\mathrm{A}_1 = (s_1 - s_e)/s_1 \quad (2.7f)$$

$$B_1 = s_e/[2(s_1 - s_e)] \quad (2.7g)$$

The initial stiffness of the bond-slip model, K_0, is given by

$$K_0 = K_a K_c/(K_a + K_c) \tag{2.7h}$$

where $K_a = G_a/t_a$ and $K_c = G_c/t_c$. G_a and G_c are the elastic shear modulis of adhesive and concrete respectively; while t_a, and t_c are the thickness of adhesive and effective thickness of concrete respectively.

The coefficient, α, is given by

$$\alpha = \tau_{max} s_1/(G_f^a - G_f) \tag{2.7i}$$

in which G_f^a is the interfacial fracture energy between FRP and concrete of the ascending branch, and is given by

$$G_f^a = \tau_{max} s_1 \left[\frac{2\mathrm{A}_1}{3} \left(\frac{1 + \mathrm{A}_1 B_1^2}{\mathrm{A}_1} \right)^{\frac{3}{2}} - B_1 - \frac{2}{3} B_1^3 \mathrm{A}_1 \right] \tag{2.7g}$$

The interfacial fracture energy between FRP and concrete, G_f, is determined by Eq. 2.7k

$$G_f = \alpha_3 \beta_w^2 \sqrt{f_t} f(K_a) \tag{2.7k}$$

for normal adhesive layers with $\mathrm{K_a} \geq 2.5\ \mathrm{GPa/mm}$, the function, $f(K_a)$, is equal to 1.

The simplified model in Lu et al.'s (2007)

Lu et al. (2006) proposed a simplified bond-slip model by simplifying the precise model. In the simplified bond-slip model, the effective concrete thickness is not

included as a parameter. It was believed by the authors that the simplified model still has enough precision as the effective concrete thickness has only a marginal effect on the bond-slip curve. This model is expressed as follows:

$$\tau = \tau_{max}\sqrt{\frac{s}{s_1}} \text{ if } \quad s < s_1 \tag{2.8a}$$

$$\tau = \tau_{max} e^{-\alpha(s/s_1 - 1)} \text{ if } s_1 < s \tag{2.8b}$$

in which τ_{max} and , s_1 and can be determined by Eq. 2.8c and 2.8d respectively.

$$\tau_{max} = \alpha_1 \beta_w f_t \tag{2.8c}$$

$$s_1 = 0.0195 \beta_w f_t \tag{2.8d}$$

The expression for β_w is the same as that of the precision model, and is given by Eq.7e.

The concrete fracture energy, G_f, is determined by Eq. 2.8e.

$$G_f = 0.308 \beta_w^2 \sqrt{f_t} \tag{2.8e}$$

The coefficient, α, can be determined by

$$\alpha = \frac{1}{\left(\frac{G_f}{\tau_{max} s_1} - \frac{2}{3}\right)} \tag{2.8f}$$

The bilinear model in Lu et al.'s (2007)

Further simplifications were made by Lu et al. (2006) to propose a bilinear bond-slip model, which can be used to establish a design equation for the bond strength of the FRP plate bonded to concrete. This model is expressed as follows:

$$\tau = \tau_{max} \frac{s}{s_1} \text{ if } s < s_1 \quad (2.9a)$$

$$\tau = \tau_{max} \left(\frac{s_2 - s}{s_2 - s_1} \right) \text{ if } s_1 < s < s_2 \quad (2.9b)$$

$$\tau = 0 \text{ if } s > s_2 \quad (2.9c)$$

The slip between FRP and concrete corresponding to the local bond shear stress decreasing to zero, s_2, is determined by Eq. 2.9d

$$s_2 = 2G_f / \tau_{max} \quad (2.9d)$$

The expressions for parameters τ_{max}, s_1, and G_f are the same as those for the simplified model.

Baky et al.'s (2012) model

Based on a 3D meson-scale FE study, Baky et al. (2012) proposed a complicated bond-slip model, which considers the interaction between the interfacial normal stress and the local bond shear strength. This model is expressed by the following equations:

$$\tau = E_{i0} s + \left[\frac{\tau_{max} - E_{i0} s}{s_1^3} \right] s^3 \text{ if } s < s_1 \quad (2.10a)$$

$$\tau = \tau_{max} e^{-c_4 \left(\frac{s}{s_1} - 1 \right)} \text{ if } s_1 < s < s_2 \quad (2.10b)$$

$$\tau = \tau_{res} \text{ if } s > s_2 \quad (2.10c)$$

where τ_{res} is the residual shear stress of the FRP-to-concrete interface; E_0 is the initial elastic moduli of the FRP-to-concrete interface;

$$\frac{1}{E_{i0}} = \frac{t_p + h_{eff}}{G_p} + \frac{t_a}{G_a} \tag{2.10d}$$

in which G_p, and G_a are the shear moduli of the FRP plate and the adhesive layer respectively; t_p, and t_a are the thicknesses of the FRP plate and the adhesive layer respectively; h_{eff} is the thickness of the interfacial layer, and is set to be 3-5 times the maximum aggregate size.

$$s_1 = \tau_{max}\left[0.35\frac{t_p}{G_p} + 8.5\frac{t_a}{G_a} + \frac{3h_{eff}}{G_c}\right] \tag{2.10e}$$

$$s_2 = 4s_1 \tag{2.10f}$$

The maximum bond stress is defined as

$$\tau_{max} = \frac{2f_t}{-c_4 + \sqrt{c_4^2 + 4}} \tag{2.10g}$$

where $c_4 = \frac{\rho}{\lambda t_p}$, with$\lambda^2 = \left[\frac{G_a}{E_p t_p t_a}(1 + \eta\rho)\right]$, $\eta = \frac{E_p}{E_c}$ and $\rho = \frac{A_p}{A_c}$. A_c and A_p are the cross-sectional areas of the concrete block (equal to $b_p h_{eff}$) and FRP plate respectively.

$$\tau_{res} = 0.1\tau_{max} \tag{2.10h}$$

$$\alpha_1 = -\frac{0.9\tau_{max}s_1}{G_f^p} \tag{2.10i}$$

and

$$G_f^p = \tau_{max}^2\left[\frac{150}{G_c} - 0.405\left(\frac{t_p}{G_p} + \frac{t_a}{4.25G_a}\right)\right] \tag{2.10j}$$

Ko et al.'s bilinear model

A bilinear model was proposed by Ko et al. (2014), and is given as follows:

$$\tau = \tau_{max} \frac{s}{s_1} \text{ if } s < s_1 \quad (2.11a)$$

$$\tau = \tau_{max} \left(\frac{s_2 - s}{s_2 - s_1}\right) \text{ if } s_1 < s < s_2 \quad (2.11b)$$

$$\tau = 0 \text{ if } s > s_2 \quad (2.11c)$$

These expressions are the same as those of Lu et al. (2005b), but with different coefficients. τ_{max}, s_1 and s_2 can be are determined by Eq. 2.11d, 2.11e and 2.11f respectively.

$$\tau_{max} = 0.165 f_c \quad (2.11d)$$

$$s_1 = -0.001 f_c + 0.122 \quad (2.11e)$$

$$s_2 = -0.002 f_c + 0.302 \quad (2.11f)$$

2.2.4 Analytical investigations

Many researchers have employed nonlinear fracture mechanics to analytically investigate debonding in FRP-to-concrete bonded joints (Taljsten1997; Brosens and Van Gemert 1998; Yuan et al. 2001; Wu et al. 2002; Yuan et al. 2004; Teng et al. 2006; Chen et al. 2007; Wang and Zhang 2007; Chen and Qiao 2009; Wu et al. 2012). With the use of an appropriate bond-slip model, the bond strength, effective bond length, and interfacial shear stress distribution can all be obtained from the analytical investigation. These studies are reviewed as follows.

Brosensand Van Gemert (1998) used nonlinear fracture mechanics to analyse the debonding of FRP-to-concrete bonded joints. They made the following assumptions: a) all the materials are linear elastic; b) no bending is considered; c) the axial stresses of both the FRP plate and the concrete are uniformly distributed over the cross-section; d) a bilinear bond-slip model governs the FRP-to-concrete interface. Based on the analytical results, the expressions for both the bond strength and the effective bond length of FRP-to-concrete bonded joints at both the serviceability and ultimate limit states were established.

Yuan et al. (2001) analytically investigated the debonding of FRP-to-concrete bonded joints using nonlinear fracture mechanics, in which assumptions similar to those adopted by Brosens and Van Gemert (1998) were made. Four types of nonlinear bond-slip models were examined in the study. Expressions of the bond strength and the interfacial stress distribution were derived.

Wu et al. (2002) used nonlinear fracture mechanics to analytically examine the debonding behaviour of FRP-to-concrete bonded joints. In this study, both single-shear tests and FES single-shear tests were investigated. In addition, two different bond-slip models were employed to depict the bond constitutive behaviour of FRP-to-concrete interfaces. Expressions for the bond strength and distributions of the interfacial shear stress and the FRP plate stress were derived. It concluded that the bond strength of the FES single-shear test is larger than its counterpart of the NES single-shear test, and the difference in the bond strength between the two types of bonded joints becomes larger with a decrease in the ratio of the axial rigidity of

concrete to that of the FRP plate.

Yuan et al. (2004) presented a closed-form analytical solution for the full-range debonding response of FRP-to-concrete bonded joint, in which a bi-linear bond-slip model is used to depict the FRP-to-concrete interface. Distributions of the interfacial shear stress and the load-displacement response for different stages of the debonding process were derived and interpreted.

Teng et al. (2006) presented an analytical solution for FRP-to-concrete bonded joints, in which both ends of the FRP plate are subjected to tension, as an idealized model to investigate the debonding process of the FRP plate between two adjacent cracks. A bi-linear bond-slip model is employed this analytical solution. The distributions of the interfacial shear stress and the load-displacement response of the joint were derived in detail. Chen et al. (2007) simplified the solution for the same FRP-to-concrete bonded joints with using a linear-softening bond-slip model is used to allow a simple closed-form solution. As these solutions account for the interaction between two adjacent cracks, it is possible to use an IC debonding strength model based on these solutions to account for the effect of load distribution on IC debonding.

Wang and Zhang (2007) analytically investigated IC debonding using a nonlinear fracture mechanics approach. Different from analytical approaches reviewed above, this study directly analysed a beam segment instead of an FRP-to-concrete bonded joint. The governing equations were established using a rotational spring model at

the middle sections of cracks, and a simple bilinear bond-slip model was employed for the bond behaviour of FRP-to-concrete interfaces. Closed-form expressions for interfacial shear stresses at different loading states were presented in detail for understanding IC debonding in FRP-plated RC beams.

Chen and Qiao (2009) presented an analytical study on debonding between two adjacent cracks using an approach similar to that of Wang and Zhang (2009). The bond behaviour of FRP-to-concrete interfaces was characterized using a simple bilinear bond-slip model. Detailed information of the debonding process including the distributions of interfacial shear stress was given. The effect of the thickness of the adhesive on the debonding process was investigated through a parametric study.

The debonding process of FRP-to-concrete bonded joints with the FRP plate of different lengths was also analytically by Wu et al. (2012). The analytical solution given in Wu et al. (2012) is similar to that presented in Yuan et al. (2004), but with a different bond-slip model which can be expressed by one equation for different stages. The load-displacement response and the distributions of the interfacial shear stress were presented in detail.

2.2.5 Bond strength models

Many bond strength models have been proposed for predicting the strength of the FRP-to-concrete bonded joints (i.e. the ultimate tensile force acting on the FRP plate that can be resisted by the bonded joint). These models can be categorized into

empirical models (Hiroyuki and Wu 1997; Tanaka 1996; Maeda et al. 1997), semi-empirical models (van Gemert 1997; Khalifa et al. 1998) and fracture mechanics-based models (Holzenkampfer 1994; Neubauer and Rostasy 1997; Yuan and Wu 1999; Niedermeier 2000; Yuan et al. 2001). The fracture mechanics-based models are based on an analytical solution for the FRP-to-concrete bonded joints using the nonlinear fracture mechanics theory. The empirical models were proposed through regression analysis of test data, and the semi-empirical models were established using a combination of regression of test data and some simple rational assumptions. Altogether 16 bond strength models have been reviewed by Chen and Teng (2001) and Lu et al. (2005b); some later bond strength models are also included in the review given below.

2.2.5.1 Empirical models

An empirical model was proposed by Hiroyuki and Wu (1997) based on the results of double-shear tests on FRP-to-concrete bonded joints. This bond strength model is expressed in terms of the average bond shear stress at failure, τ_u, and the bond strength, P_u, can be determined by multiplying the average bond shear stress at failure, τ_u by the width, b_f, and bond length, L_f.

$$\tau_u = 5.88{L_f}^{-0.669} \tag{2.12a}$$

$$P_u = \tau_u b_f L_f \tag{2.12b}$$

Tanaka (1996) presented an empirical model, which is similar to Hiroyuki and Wu's model. The model is given by Eq. 2.13a and 2.13b.

$$\tau_u = 6.13 - ln\, L_f \tag{2.13a}$$

$$P_u = \tau_u b_f L_f \tag{2.13b}$$

Maeda et al. (1997) proposed a model which considers the effects of the effective bond length and the stiffness of the FRP plate. This model is given as follows.

$$\tau_u = 110.2 \times 10^{-6} E_f t_f \tag{2.14a}$$

$$P_u = \tau_u b_f L_{ef} \tag{2.14b}$$

where E_f and t_f are theelastic modulus and thickness of the FRP plate; $L_{ef}$is the effective bond length as given by Eq. 2.14c.

$$L_{ef} = e^{6.13 - 0.58 ln E_f t_f} \tag{2.14c}$$

It should be noted that the units of E_f and t_f are gigapascal and millimeter.

This model is more robust than those of Hiroyuki and Wu (1997) and Tanaka (1996), however this model does not cover cases for which $L_f < L_{eff}$.

2.2.5.2 Semi-empirical models

van Gemert (1997) assumed a triangular shear stress distribution over the FRP plate and proposed a bond strength model, which is expressed as follows:

$$P_u = 0.5 b_f L_f f_t \tag{2.15}$$

It is obvious that this model contradicts the now well-established concept of effective bond length for externally bonded FRP plates.

Khalifa et al. (1998) proposed a bond strength model by modifying Maeda et al.'s model to consider the effect of concrete strength. The average interfacial shear stress is expressed as a function of $(f_c)^{2/3}$, and can be determined using Eq. 2.16a.

$$\tau_u = 110.2 \times 10^{-6} E_f t_f (f_c/40)^{2/3} \tag{2.16}$$

The bond strength can be determined using Eq. 2.14c. This model has the same drawback as that of Maeda et al.'s model: it does not cover cases that the FRP plate length is smaller than its effective bond length.

2.2.5.3 Fracture mechanics based models

A fracture mechanics based models was proposed by Holzenkampfer (1994). This model is based on the analytical solution on the steel plate-to-concrete bonded joint, and can be expressed as follows:

$$P_u = b_f \sqrt{G_f E_f t_f} \tag{2.17a}$$

in which G_f is the interfacial fracture energy and is determined by Eq. 2.17b.

$$G_f = c_f f_t \tag{2.17b}$$

where c_f is a coefficient, and is equal to 0.204 mm, which is based on regression analysis results.

Neubauer and Rostasy(1997) modified Holzenkampter's (1994) model using nonlinear fracture mechanics to make it applicable to all cases of bond lengths. The

equations for the model are as follows:

$$P_u = 0.64\beta_w b_f \sqrt{f_t E_f t_f} \qquad \text{if } L_f \geq L_{ef} \tag{2.18a}$$

$$P_u = 0.64\beta_L \beta_w b_f \sqrt{f_t E_f t_f} \qquad \text{if } L_f < L_{ef} \tag{2.18b}$$

in which β_L is the factor related to the bond length of the FRP plate, and is given as follows:

$$\beta_L = \frac{L_f}{L_{ef}}\left(2 - \frac{L_f}{L_{ef}}\right) \tag{2.18c}$$

β_w is a factor reflecting the FRP-to-concrete width ratio, and is expressed as follows:

$$\beta_w = \sqrt{1.125\frac{2 - b_f/b_c}{1 + b_f/400}} \tag{2.18d}$$

Yuan and Wu (1999) and Yuan et al. (2001) analytically derived an expression for the bond strength using nonlinear fracture mechanics. This bond strength model is expressed as follows.

$$P_u = b_f \sqrt{\frac{2G_f E_f t_f}{1 + \beta_w}} \tag{2.19a}$$

The coefficient representing the effect of the FRP-to-concrete width ratio, β_w, can be determined by Eq. 2.19b.

$$\alpha_T = \frac{b_f E_f t_f}{b_c E_c t_c} \tag{2.19b}$$

Niedermeier (2000) modified the fracture mechanics based model proposed by Holzenkampfer (1994) so that it is applicable to all cases of bond lengths. This model

is expressed as follows:

$$P_u = 0.78 b_f \sqrt{2 G_f E_f t_f} \qquad \text{if } L_f \geq L_{ef} \tag{2.20a}$$

$$P_u = 0.78 \beta_L b_f \sqrt{G_f E_f t_f} \qquad \text{if } L_f < L_{ef} \tag{2.20b}$$

in which β_L is a coefficient related to the ratio between the bond length of the FRP plate to its effective bond length, and is given by Eq. 2.20c.

$$\beta_L = \frac{L_f}{L_{ef}}\left(2 - \frac{L_f}{L_{ef}}\right) \tag{2.20c}$$

The interfacial fracture energy, G_f, is determined by Eq. 2.20d.

$$G_f = c_f \beta_w^2 f_t \tag{2.20d}$$

in which c_f is a coefficient determined using a regression analysis on test data; β_w is a factor reflecting the FRP-to-concrete width ratio as given by Eq. 2.18d.

Chen and Teng (2001) developed a bond strength model using an existing fracture mechanics analysis in combination with experimental observations. The bond strength of this model is as follows:

$$P_u = 0.427 \beta_w \beta_L b_f L_{ef} \sqrt{f_c} \tag{2.21a}$$

in which β_w is a factor related to the effect of width ratio between the FRP plate and the concrete prism; β_L is a factor representing the effect of the bond length of the FRP plate. The effective bond length, L_{ef}, can be determined by the following equations

$$L_{ef} = \sqrt{\frac{E_f t_f}{\sqrt{f_c}}} \tag{2.21b}$$

$$\beta_w = \sqrt{\frac{2.25 - b_f/b_c}{1.25 + b_f/b_c}} \tag{2.21c}$$

$$\beta_L = 1 \qquad \text{if } L_f \geq L_{ef} \tag{2.21d}$$

$$\beta_L = sin\frac{\pi L_f}{2L_{eff}} \qquad \text{if } L_f < L_{ef} \tag{2.21e}$$

Lu et al. (2005b) re-examined an existing nonlinear fracture mechanics solution, and developed a bond strength model with its coefficients being derived using their own bond-slip model. The equations of the bond strength model are as follows:

$$P_u = b_f\sqrt{2G_f E_f t_f} \qquad \text{if } L_f \geq L_{ef} \tag{2.22a}$$

$$P_u = \beta_L b_f\sqrt{2G_f E_f t_f} \qquad \text{if } L_f < L_{ef} \tag{2.22b}$$

in which L_{ef} is given by

$$L_{ef} = a_0 + \frac{1}{2\lambda_1}\ln\frac{\lambda_1 + \lambda_2\tan(\lambda_2 a_0)}{\lambda_1 - \lambda_2\tan(\lambda_2 a_0)} \tag{2.22c}$$

where a_0, λ_1 andλ_2 can be determined by

$$a_0 = \frac{1}{\lambda_2}sin^{-1}\left(0.99\sqrt{\frac{s_2 - s_1}{s_2}}\right) \tag{2.22d}$$

$$\lambda_1 = \sqrt{\frac{\tau_{max}}{s_1 E_f t_f}} \tag{2.22e}$$

$$\lambda_2 = \sqrt{\frac{\tau_{max}}{(s_2 - s_1)E_f t_f}} \tag{2.22f}$$

τ_{max}, s_1 and G_f are given by Eqs 2.8c, 2.8d and 2.8e respectively.

Chen et al. (2007) analytically investigated the debonding of FRP-to-concrete

bonded joints, in which both ends of the FRP plate are subjected to tension. This analytical solution led to a new bond strength model (Chen et al. 2006), which takes into account the effect of interaction between two adjacent cracks. The bond strength model is expressed by the following equations:

$$P_{1,u} = \begin{cases} b_f \sqrt{2G_f E_f t_f}\,(1-\beta^2)^{-1/2} & \text{if} \quad L_f \geq a_u \\ b_f \sqrt{2G_f E_f t_f}\,\sin(\lambda L_f)\left[1-\beta\cos(\lambda L_f)\right]^{-1} & \text{if} \quad L_f < a_u \end{cases} \tag{2.23a}$$

where

$$\beta = \frac{P_2}{P_1} \tag{2.23b}$$

$$a_u = \frac{1}{\lambda}\arccos\beta \tag{2.23c}$$

$$\lambda^2 = \frac{\tau_{\max}{}^2}{2G_f}\frac{1}{E_f t_f} = \frac{\tau_{\max}}{s_1}\frac{1}{E_f t_f} \tag{2.23d}$$

where P_1, and P_2 are the tensile forces at the two ends of the FRP plate.

2.3 IC DEBONDING FAILURES

In a flexural strengthening application with the use of externally bonded FRP reinforcement, an FRP plate is adhesively bonded to the soffit of RC members. The FRP soffit plate resists the tensile force together with the internal steel reinforcement as well as the concrete. The force in the FRP soffit plate is transferred via the FRP-to-concrete interface. Such force transfer significantly relies on the bond of the FRP-to-concrete interfaces.

IC debonding, which initiates at the toe of flexural or flexural-shear cracks in a high moment region, then propagates along the direction of moment decreasing, impairs the integrity of FRP-plated RC beams, and often control the strength of FRP-plated RC beams. In design of such an FRP-plated RC beam, IC debonding should be considered, and IC debonding strength is often viewed as the beam strength. In order to investigate the mechanism and strength of IC debonding for design of an FRP-plated RC beam, numerous experimental and theoretical studies have been carried out (Teng et al. 2002; Lu et al. 2007; Hollaway and Teng 2008; Rosenboom and Rizkalla 2008a; Said and Wu 2008; Pan et al. 2009; Rusinowski and Taljsten 2009; Alfano et al. 2012). These studies on IC debonding in FRP-plate RC beams are reviewed as follows.

2.3.1 Tests on IC debonding without anchorage measures

A large number of tests have been carried out to investigate the IC debonding mechanisms. The majority of these experimental studies on IC debonding are carried out in the first two decades since FRP-plated RC beams have been studied. Results of these tests were collected in Lu et al. (2007) as well as Said and Wu (2008) to form a large database to verify the IC debonding strength models. In addition, these beams in tests were subjected to subjected to three- or four-point bending (one or two point loads) due to the ease of the application of one- or two-point loading; while load distribution of other forms (e.g. UDL) has been rarely used in laboratory tests (Hollaway and Teng 2008; Teng et al. 2002). However in reality UDL is more common than point loads, and different load distributions may lead to different IC

debonding processes. Therefore only the experimental studies published after Lu et al. (2007) and Said and Wu (2008) are examined herein and the very limited experimental work on IC debonding in FRP-plated RC beams under other load distributions is reviewed.

Rosenboom and Rizkalla (2008b) completed an experimental program in which six concrete bridge girders of 9.14 m in span were tested. Among the six girders, three were strengthened with procured CFRP plates, and two were strengthened using wet lay-up CFRP sheets. All the six beams failed by IC debonding, and the test results were used to verify an IC debonding strength model proposed by them.

Rusinowski and Taljsten (2009) presented laboratory tests on FRP-plated RC beams to investigate their IC debonding behaviour. The experimental variables included the concrete strength, type of FRP plate, and type and thickness of adhesive. All the beams had the same dimensions: 120 mm in width, 170 mm in height and 1900 mm in clear span. The cracking information was collected using optical equipment. Finally, test results were used to verify some of the existing IC debonding strength models.

Alfano et al. (2012) undertook an experimental program to investigate IC debonding in FRP-plated RC beams. In this experimental program, all the beams were tested under four-point bending, and the test variables were the type of internal reinforcement and beam geometry. The results of the beam tests were used to verify many existing IC debonding strength models and the popular design procedures.

Only two experimental studies presented IC debonding under other load distribution rather than under one- or two-point loading (Pan et al. 2007; Mazzotti and Savoia 2009). They are briefly described as follows:

Pan et al. (2007) tested six small-scale (150 mm x 200 mm x 1800 mm) RC beams under multi-point loading with limited strain measurements. Some of their beams failed by IC debonding, while others failed by concrete cover separation. In this study, the application of multi-point loading was realized using a waffle-tree loading system. However the differences between loads at different loading points could have been significant due to the existence of significant friction in the loading frame when the deflection of the specimen became large (Chung 2004). Therefore in order to eliminate the differences between loads at different loading points, Aprile and Feo (2007) applied multiple-point loading using a set-up different from that in Chung (2004) and Pan et al. (2009) and tested four small-scale (150 mm x 250 mm x 2000 mm) beams under 16-point loading. Aprile and Feo (2007) used a series of hydraulic jacks (a separate hydraulic jack for each loading point) to apply loading, and these hydraulic jacks were all connected to a single hydraulic pump to ensure equal loading from each jack.

Mazzotti and Savoia (2009) carried out a series of tests on FRP-plated RC beams under an eight-point loading condition, which was applied using a waffle-tree loading system. The test variables of this experimental program included the type of FRP plate, amount of FRP used, and amount of internal steel bars. All the beams had the same dimensions: 250 mm in width, 400 mm in height, and 3000 mm in clear

span. The results of the beam tests were used to verify the existing IC debonding strength models and existing design provisions.

2.3.2 FE modeling of IC debonding

FE modeling has been widely used to simulate IC debonding in FRP-plated RC beams. A summary of existing FE studies on IC debonding in FRP-plated RC beams is presented in this sub-section.

To accurately predict IC debonding in FRP-plated RC beams, an FE approach should consider the following three key components: (a) appropriate modeling of concrete cracking; (b) accurate modeling of the bond of FRP-to-concrete interface; (c) accurate modeling of the bond of steel-to-concrete interface (Chen et al. 2011). All the existing FE studies are categorized by the ways how to consider these three key elements, although none of the existing FE studies, with the exception of Chen at al. (2011), took into consideration all the three key elements.

2.3.2.1 Modeling of concrete cracking

For the modeling of concrete cracking, there are two distinct approaches: (1) discrete-crack approach; and (2) smeared-crack model (Lu et al. 2007; Chen et al. 2011). Both of them have been used to simulate IC debonding in FRP-plated RC beams. The discrete-crack approach traces crack propagation by continuous re-meshing, with the cracks being simulated by the boundaries of concrete elements.

The continuous re-meshing of the FE model during the propagation of cracks leads to a very high demand of computational power. Moreover, pre-definition of crack positions is required in the discrete-crack approach. As a result, the discrete-crack approach has only been used to investigate IC debonding resulting from one or several pre-defined cracks (Monti et al. 2003; Yang et al. 2003; Niu and Wu 2005).

The smeared-crack approach has been much more popular with researchers who are concerned with IC debonding in FRP-plated RC beams (Wong and Vecchio 2003; Wu and Yin 2003; Teng et al. 2004; Pham and Al-Mahaidi 2005; Coronado and Lopez 2006; Neale et al. 2006; Baky et al. 2007; Lu et al. 2007; Nour et al. 2007; Kotynia et al. 2008; Niu and Karbhari 2008; Chen et al. 2011). In this approach, concrete cracking is represented by the weakening of concrete properties. The assumptions in the smeared-crack approach do lead to the mesh sensitivity problem: results of the simulation with the smeared-crack approach are sensitive to choice the size of elements. In order to address the mesh sensitivity problem, the crack band model (Bazant and Planas 1998), which characterizes the constitutive model of concrete by the fracture energy and relates the tensile stress-strain curve of concrete to the size of concrete elements, has been widely used in modeling of FRP-plated RC beams (e.g. Lu et al. 2007; Chen et al. 2011).

2.3.2.2 Modeling of bond of interfaces

Appropriate modeling of both FRP-to-concrete and steel-to-concrete interfaces is essential for capturing the localization of slips at cracks for the accurate prediction of

IC debonding. Except Nour et al. (2007) and Coronado and Lopez (2006), who directly connected concrete element to FRP elements (i.e. perfect bonding) in their FE modeling, most existing studies considered slips between the FRP plate and the concrete using a bond-slip model. Among the many bond-slip models, Lu et al.'s(2005) model has received the widest acceptance for describing the bond behaviour of FRP-to-concrete interfaces (Teng et al. 2004; Neale et al. 2006; Lu et al. 2007; Baky et al. 2007; Kotynia et al. 2008). Pham and Al-Mahaidi (2005) and Niu and Karbhari (2008) used a bilinear model for the FRP-to-concrete interface. The parameters of the bilinear bond-slip model adopted by Pham and Al-Mahaidi (2005) and Niu and Karbhari (2008) were directly determined from tests on bonded joints, so these FE approaches were not yet truly predictive.

Most of existing studies on FE modeling of FRP-plated RC beams considered the bond behaviour of steel-to-concrete interface using either perfect bonding (i.e. directly connecting the concrete elements to steel elements) or tension stiffening concrete stress-strain model (i.e. directly connecting the concrete elements to steel elements and modifying the stress-strain model for concrete elements adjacent to consider the slip between concrete and steel tension bars) (Wong and Vecchio 2003; Teng et al. 2004; Pham and Al-Mahaidi 2005; Coronado and Lopez 2006; Neale et al. 2006; Lu et al. 2007; Baky et al. 2007; Nour et al. 2007; Kotynia et al. 2008). Both approaches shows to be inaccurate in predicting cracking behaviour (i.e. crack patterns and widths), thus leading to inaccurate prediction of IC debonding (Chen et al. 2011). Chen et al. (2011) considered the bond behaviour of both steel-to-concrete interface and FRP-to-concrete interface using interfacial elements cooperating

appropriate bond-slip models for them to connect the concrete elements and steel elements. Numerical results presented in Chen et al. (2011) shows that their approach has the ability to accurately predict both the crack pattern and crack width, thus accurately predicting IC debonding of FRP-plated RC beams.

2.3.3 IC debonding strength models

Many strength models for IC debonding in FRP-plated RC beams have been proposed for design use(Wu and Niu 2000; Teng et al. 2003a; Lu et al. 2007b; Wu and Niu 2007;Rosenboom and Rizkalla 2008a; Said and Wu 2008; Oehlers et al. 2011). Most of these strength models can be categorized into three types: (1) models modified from a bond strength model for FRP-concrete bonded joints (e.g. Teng et al. 2003); (2) models derived from a regression analysis of test results(e.g. Said and Wu 2008); (3) models based on the interfacial shear stress distribution between FRP and concrete in a beam(e.g. Lu et al. 2007;Rosenboom and Rizkalla 2008a; Oehlers et al. 2011).

2.3.3.1 Models modified from a bond strength model for FRP-to-concrete bonded joints

In some early studies, the IC debonding mechanism in FRP-plated RC beams was believed to be similar to that in an FRP-to-concrete bonded joint. Therefore, some IC debonding strength models were modified from a bond strength model for FRP-to-concrete bonded joints (e.g. Teng et al. 2003a). This approach is based on the

assumption that IC debonding of the FRP plate is primarily driven by the widening of a single major crack, any interaction between adjacent cracks is taken into consideration through empirical modification of the bond strength model. Recent studies have shown that the interaction between two adjacent major cracks may substantially affect the debonding process and hence the IC debonding strength, and should be explicitly accounted for in IC debonding strength models (Teng et al. 2006; Chen et al. 2007). For this reason, Chen et al.(2006) extended Teng et al.'s (2003) model to account for the interaction between two adjacent major cracks based on the analytical modeling of FRP debonding process in bonded joints subjected to tension at both ends of the bonded FRP plate(Teng et al. 2006; Chen et al. 2007).

Teng et al.'s (2003) model

Based on the similarity between IC debonding failure in FRP-plated RC beams and debonding failure in FRP-to-concrete bonded joints, Teng et al. (2003b) proposed an IC debonding strength model by modifying the bond strength model for FRP-to-concrete bonded joint proposed by Chen and Teng (2001). A design procedure against IC debonding was also applied with by Teng et al. (2003b), and is briefly presented as follows.

Step1: Determination of the plate stress or strain at IC debonding using Eq. 2.24a.

$$\sigma_{ic} = 0.48\beta_w\beta_l\sqrt{\frac{E_f\sqrt{f_c}}{t_f}} \tag{2.24a}$$

where

$$\beta_w = \sqrt{\frac{2 - b_f/b_c}{1 + b_f/b_c}} \tag{2.24b}$$

$$\beta_l = \begin{cases} 1, & \text{if} \quad L_f \geq L_{ef} \\ \sin\frac{\pi L_f}{2L_e}, & \text{if} \quad L_f < L_{ef} \end{cases} \tag{2.24c}$$

$$L_e = \sqrt{\frac{E_f t_f}{\sqrt{f_c}}} \tag{2.24d}$$

in which b_c and f_c are the width (mm) and the cylinder compressive strength (MPa) of the concrete block, respectively; b_f, t_f and E_f are the width (mm), thickness (mm) and elastic modulus (MPa) of the FRP plate, respectively; L_f and L_{ef} are the bond length (mm) and effective bond length (mm) of the FRP plate.

Step2: By comparing the debonding stress σ_{ic} with the tensile strength of the plate, the smaller value will be used in the section analysis to determine the ultimate moment $M_{u,p}$.

Step-3: The ultimate moment $M_{u,p}$ at the critical section is then determined by the section analysis.

Chen et al.'s (2006) model

This strength model was proposed by modifying the bond strength model presented in Chen et al. (2006), which accounts for the interaction between two adjacent cracks. This strength model therefore has the ability of considering the effect of load

distribution on IC debonding strength if crack spacings of FRP-plated beams under different load distributions are known. Some parameters used in this model were also calibrated with a significant database for tests on FRP-plated RC beams. The ultimate stress in the FRP plate at the critical major crack where debonding initiates is given by

$$\sigma_{ic} = \gamma_1 \beta_\sigma \beta_w \beta_L \sqrt{\frac{E_f \sqrt{f_c}}{t_f}} \tag{2.25a}$$

where f_c is the cylinder compressive strength of concrete; The coefficients β_σ, β_w and β_L reflect the effect of the ratio between the plate stresses at the adjacent crack and the critical crack α_σ, the effect of the width ratio between the FRP plate b_f and the concrete prism (the beam) b_c, and the effect of the bond length, respectively. They are defined by the following equations:

$$\beta_\sigma = \begin{cases} \dfrac{1}{\sqrt{1-\alpha_\sigma^2}}, & \text{if} L_f \geq L_{ef} \\ \dfrac{1}{1-\alpha_\sigma cos\frac{\pi L}{2L_{ef}}}, & \text{if} L_f < L_{ef} \end{cases} \tag{2.25b}$$

$$\beta_w = \begin{cases} \dfrac{b_f + 2\delta}{b_f}, & \text{if} \quad b_f + 2\delta < b_c \\ \dfrac{b_c}{b_f}, & \text{if} \quad b_f + 2\delta \geq b_c \end{cases} \tag{2.25c}$$

$$\beta_l = \begin{cases} 1, & \text{if} \quad L_f \geq L_{ef} \\ \sin\dfrac{\pi L_f}{2L_{ef}}, & \text{if} \quad L_f < L_{ef} \end{cases} \tag{2.25d}$$

where the effective bond length L_{ef} is given by

$$L_{ef} = \frac{2}{\pi}\sqrt{\frac{E_f t_f}{\sqrt{f_c}}}\arccos\alpha_\sigma \tag{2.25e}$$

This definition of the effective bond length reduces to that of Eq. 2.21b if the stress ratio is equal to zero. It should be emphasized that the stress ratio α_σ can be approximated by the ratio of moments at the adjacent cracked sections with sectional analysis.

ACI's (2008) model

The ACI design guide (ACI 440.2.R-08 2008) modified Teng et al.'s (2003)model discussed above through the calibration by a database for tests on FRP-plated RC beams that failed by IC debonding. The effect of width ratio between the FRP plate and the RC beam is ignored in this model. According to this model, the plate stress at IC debonding failure is given by the following equation:

$$\sigma_{ic} = 0.41\sqrt{\frac{E_f f_c}{t_f}} \tag{2.26}$$

2.3.3.2 Models based on the interfacial shear stress distribution

It is reasonable to expect that IC debonding of FRP plate from its concrete substrate occurs when the maximum interfacial shear stress attains a critical value. Some researchers have therefore proposed IC debonding strength models based on the various distributions of various interfacial shear stress from either experimental

observations or finite element analyses.

Lu et al.'s (2007) model

Lu et al. (2007) proposed an IC debonding strength model on the basis of an interfacial shear stress distribution from a series of finite element analyses. It was believed by the authors that the interfacial shear stresses in a FRP-plated RC beam were from two distinct sources: one directly caused by the shear force in the section and the other induced by the opening-up of the major flexural crack in an RC beam. The distribution of interfacial shear stress in this model is, therefore, represented by the superposition of two distinct triangular stress blocks. The accuracy of this strength model was verified by all the test results available to the authors from 77 FRP-plated RC beams. This model predicts that IC debonding occurs when the tensile stress in the FRP plate reaches the following value:

$$\sigma_{ic} = 0.114(4.41 - \gamma_2)\tau_{max}\sqrt{\frac{E_f}{t_f}} \tag{2.27a}$$

where E_f and t_f are the elastic modulus (MPa) and thickness (mm) of the bonded plate, respectively; $\gamma_2$is a factor which is defined by

$$\gamma_2 = 3.41\, L_{ef}/L_d \tag{2.27b}$$

in which L_d can be simply taken to be the distance from the loading point to the end of the soffit plate; the effective bond length, L_{ef},is given by following the equation (Yuan et al. 2004):

$$L_{ef} = \sqrt{\frac{4E_f t_f}{\tau_{max}/s_1}} = 0.228\sqrt{E_f t_f} \quad (2.27c)$$

τ_{max} is the maximum bond shear stress of the FRP-to-concrete interface and is approximated by the equation 2.27d.

$$\tau_{max} = 1.5\beta_w f_t \quad (2.27d)$$

where f_t is the tensile strength of concrete (MPa); and the width ratio,β_w, is defined by

$$\beta_w = \sqrt{\frac{2.25 - b_f/b_c}{1.25 + b_f/b_c}} \quad (2.27e)$$

Rosenboom and Rizkalla's (2008a) model

An analytical model for predicting IC debonding was proposed in by Rosenboom and Rizkalla(2008b), which was based on the characterization of the interfacial shear stress. In this approach, an iterative process is used for predicting IC debonding. The design procedure using this analytical model follows the following nine steps:

Step1: Determine the moment resistance at the initiation of yielding of tension steel bars,M_y, and the corresponding strain of the FRP plate, ε_{fy};

Step2: Set an initial value for the FRP strain at IC debonding, ε_{ic}, which should be larger thanε_{fy};

Step3: Calculate the nominal moment resistance of the section at IC debonding M_{db} with the assumed debonding strain in *Step2*;

Step4: Determine the maximum interfacial shear stress induced by the applied load, τ_{wmax}, using Eq.2.37

$$\tau_{wmax} = E_f t_f \frac{\varepsilon_{ic} - \varepsilon_{fy}}{a - x_y} \tag{2.28a}$$

where E_f is elastic modulus of the bonded plate; t_f is the thickness of the bonded plate; a is the distance from the support to the section with the maximum moment of the beam; x_y is the distance from the support to the location of first yielding of internal tensile steel, and is given by

$$x_y = \begin{cases} a\frac{M_y}{M_{db}}, & \text{for } 3- \text{or } 4- \text{point bending} \\ -\frac{L^2}{8M_{db}}\left(-\frac{4M_{db}}{L} + \sqrt{\left(\frac{4M_{db}}{L}\right)^2 - 16\left(\frac{M_{db}}{L^2}\right)M_y}\right), & \text{for UDL} \end{cases} \tag{2.28b}$$

where L is the shear span of the beam; $M_{db}$is the maximum moment of the beam at IC debonding failure; while $M_y$is the maximum moment of the beam at the initial yielding of the steel tension bars.

Step 5: Determine the maximum interfacial shear stress induced by stress concentration, τ_{scmax} by the following equation

$$\tau_{scmax} = 3\left(1.1 - \frac{M_y}{M_{db}}\right)\sqrt{f_c'} \tag{2.28c}$$

Step 6: Calculate the total maximum interfacial shear stress τ_i by superposing τ_{wmax} and τ_{scmax};

Step 7: Adjust the IC debonding strain ε_{ic} until τ_i is equal to the critical value $\tau_{cmax} = 1.8\left(0.63\left(f_c\right)^{0.5}\right)$;

Step 8: Calculate the maximum strain in the FRP by Eq. 2.40.

$$\varepsilon_{cmax} = \varepsilon_{ic} + 0.114\frac{\tau_{scmax}}{\sqrt{E_f t_f}} \leq \varepsilon_u \tag{2.28d}$$

Step 9: If the maximum strain of FRP ε_{cmax} is greater than ε_u, the member is deemed to fail by modes the tensile rupture of the FRP soffit plate and its moment resistance can be calculated by sectional analysis accordingly.

2.3.3.3 Empirical models derived from a regression analysis of test results

Due to the complexity of the IC debonding mechanism, some researchers proposed IC debonding strength models by a simple regression analysis of results of laboratory tests on FRP-plated RC beams under three- or four-point bending (e.g. Said and Wu 2008).

Said and Wu's model

Said and Wu (2008) proposed a simple model for predicting IC debonding failure in FRP-plated RC beams based on a statistical analysis of test results without any clarification of the debonding mechanism. IC debonding is predicted to occur when the FRP strain reaches the critical value defined by the following equation:

$$\varepsilon_{ic} = 0.23(f_c)^{0.2}/\left(E_f t_f\right)^{0.35} \quad (2.29)$$

2.3.3.4 Deficiencies of existing IC debonding strength models

As mentioned above, the mechanism of IC debonding as well as the debonding strength of FRP-plated RC beams under common loading conditions in practice (UDL or UDL plus point loads) may be significantly different from that under 3- or 4-point bending. Therefore, the existing IC debonding strength models, which have been established based on research on beams in 3- or 4-point bending, generally need to be modified for use in the practical design of FRP-plated RC beams.

An IC debonding strength model based on a bond strength model must account for the interaction of adjacent cracks properly if it is to provide accurate predictions for IC debonding for all common loading conditions. The model proposed by Chen et al. (2006) is a promising model of this type, and can be improved by using information of crack patterns and moment and shear force distributions in FRP-plated RC beams under different load distributions. For an IC debonding strength model of the second type, the distribution of interfacial shear stress naturally needs to be modified in accordance with the loading condition. The performance of such a model is determined by the performance of the shear stress distribution, which in turn depends strongly on the crack pattern and distribution of moment and shear force in a beam, and hence the load distribution. The simplified stress blocks of existing models of the second type were derived for beams in 3- or 4-point bending and are unlikely to be accurate (although possibly conservative) for other load distributions. It is obvious

that the accuracy of an IC debonding strength model of the third type depends on the test data, and only a limited amount of test data is available on FRP-plated RC beams under load distributions other than 3- or 4-point bending. It is therefore clear that further research is needed to clarify the debonding mechanism of FRP-plated RC beams under different loading conditions and to develop more accurate IC debonding strength models.

2.3.4 Suppression of IC debonding

To improve the utilization of expensive FRP materials, many studies have been conducted to seek possible methods to suppress or delay premature debonding failures (Duthinh and Starnes 2001; Orton et al. 2008; Wu and Huang 2008; Ebead 2011). Mechanical anchors (e.g. fibre anchors; steel clamps) installed along the FRP soffit plate as additional anchorage measures have been found to be effective in improving the debonding strength (Lam and Teng 2001; Orton et al. 2008;Wu and Huang 2008; Zhang et al., 2012; Zhang and Smith, 2012; Ebead, 2011). However, the presence of such anchors makes the process of bonding the FRP plate much more complicated. Drilling holes in concrete for installing the anchors may induce concrete damage and spalling as well as damage to the internal steel bars. Moreover, metallic anchors may suffer from corrosion. As a result, both metallic and fiber anchors have not yet been widely used in practice.

To mitigate debonding in FRP-plated RC beams, the use of FRP U-jackets with the fibres oriented perpendicular to the beam axis are an attractive choice for engineers

due to ease of installation and excellent corrosion resistance, and has therefore been commonly recommended by design guidelines (e.g. fib 2001; ACI-440 2008;GB50608 2010). Despite the fact mentioned above, only a very small number of studies (e.g. Leung 2006; Kotynia et al. 2008; Rosenboom and Rizkalla 2008b) have been conducted on the effect of U-jackets on IC debonding. Moreover, the findings from these studies are somewhat contradictory, and do not provide a sufficient basis to support the current provisions in design guidelines. Results from one beam in Brena et al. (2003) indicated that the IC debonding strength can be significantly increased by the installation of additional FRP U-jackets. However others found that there was only a marginal benefit from FRP U-jackets on the IC debonding strength, especially for these with U-jackets only at plate ends. Leung (2006) found that the locations of U-jackets played a significant role in enhancing the IC debonding strength.

As mentioned above, only a limited number of tests on FRP-plated RC beams with U-jackets for improving the IC debonding strength have been conducted, and somewhat contradictory findings have arisen from these tests.

Compared with the control specimen (i.e., specimen strengthened with an FRP soffit plate only), the increase in the load-carrying capacity of specimens due to the use of FRP U-jackets ranged from-6% to 18%. The percentage increase depends on the amount, layout and positions of the FRP U-jackets as well as the properties of the FRP-plated RC beam. In Brena et al. (2003), three of the four beams failed by FRP plate rupture instead of debonding in their counterparts. In specimen C3 in Brena et

al. (2003), a significant increase in the load-carrying capacity of about 18% was achieved by bonding 6 vertical FRP U-jackets distributed over the beam. As a result, Brena et al. (2003) concluded that debonding of the FRP soffit plate could be delayed or in some cases suppressed by bonding vertical FRP U-jackets along the shear span. Similar statements can also be found in Leung (2006). However, three other beams from the same resource showed negligible changes (from -6% to 2%) in the load-carrying capacity although similar vertical FRP U-jackets as these in specimen C3 were used. The strains in the FRP plate at debonding failure were not significantly increased, and the strong constraint provided by the vertical FRP jackets probably had a detrimental effect on the rupture of the FRP soffit plate.

Other researchers found that vertical FRP U-jackets had a marginal effect in improving the IC debonding strength, especially when the U-jackets were only installed at plate ends (Matthys2000;Rosenboom and Rizkalla 2008b; Kotynia et al. 2008). Kotynial et al. (2008) conducted two series of tests on full-scale beams to investigate the effect of vertical FRP U-jackets on mitigating IC debonding. Increases of 6%-9% in the load-carrying capacity were achieved by using FRP U-jackets, even with continuously spaced U-jackets. Rosenboom and Rizkalla (2008b) also concluded that vertical CFRP U-jackets placed throughout the girder length could increase the load-carrying capacity and the tensile strain of the FRP soffit plate at IC debonding failure by as much as 20% and about 9%, respectively. Matthys (2000) however showed that the increase in the load-carrying capacity by bonding vertical FRP U-jackets was just about -1% in his tests and could be neglected.

As indicated by the review above, existing findings from previous studies on the effect of vertical FRP U-jackets on increasing the IC debonding strength are somewhat contradictory. In some cases, the failure mode of the beam shifted from IC debonding to tensile rupture of the FRP soffit plate, however, without a significant increase in the load-carrying capacity. This phenomenon is attributed to the combined effect of two factors: (1) the U-jackets lead to a small reduction of the ultimate load by tensile rupture of the FRP plate by restraining the moments of the FRP plate; (2) the IC debonding strength is increased above the reduced tensile rupture strength of the beam.

2.4 SUPPRESSION OF CONCRETE COVER SEPARATION

Concrete cover separation is the most common type of the plate end debonding, which initiates at/near the critical end of the FRP tension plate, and then propagates along the steel tension bar-concrete interface towards the beam mid-span. The mechanism of concrete cover separation is complex and is affected by many factors, such as the concrete cover thickness, the moment and the shear force at the plate end, the size and number of internal steel bars, and the use of mechanical anchors (Yao and Teng 2007; Teng and Yao 2007; Raoof and Hassanen 2000). With an increase in the thickness of the concrete cover, the cover separation failure strength of an FRP-plated RC beam decreases (Yao and Teng 2007; Teng and Yao 2007). Not only the shear force but also the moment at the plate end significantly affects the occurrence of concrete cover separation (Smith and Teng 2002a and 2002b; Yao and Teng 2007; Teng and Yao 2007). An FRP-plated RC beam is more likely to fail by

concrete cover separation if the moment at the plate end is higher. Many design guidelines suggest to extend the FRP plate ends to the adjacent supports as closely as possible (ACI 440.2R 2008; Concrete Society 2012). However, the size of the columns supporting the beam is finite and can be large, which means that the FRP plate ends are still at section that are subjected to a significant sagging moment if a simply-supported beam is considered. As the size and the number of internal steel tension bars increase, the likelihood of concrete cover separation also increases for two reasons: (1) the clear concrete width at the level of steel tension bars decreases; (2) significant radial stresses are generated by the steel tension bars (Zhang 2011; Zhang and Teng 2014). All these factors make concrete cover separation a common failure mode of FRP-plated RC beams. Concrete cover separation often occurs in a very brittle manner, and may sometimes occur prior to the yielding of steel tension bars. The prevention of concrete cover separation failure is therefore not only of crucial importance in achieving a more efficient utilization of the expensive FRP material but also in ensuring a more ductile failure process for an FRP-plated RC beam.

Therefore, the development of simple and effective plate-end anchorage measures to prevent cover separation failure is of great interest to the practical application of the FRP flexural strengthening technique. Plate end anchorage with bolts was initially used to mitigate/suppress concrete cover separation failure in RC beams strengthened with externally bonded steel plates (Hussain et al. 1995). Plate end anchorage with bolts or clamping was also found to be effective to improve the concrete cover separation strength of FRP-plated RC beams, especially for cases with a low shear

span/depth ratio. In addition, such end anchorage measures have been recommended for all cases as a means to reduce the brittleness of cover separation failure (Garden and Hollaway 1998; Buyle-Bodin and David 2004). The use of steel U-jacket has also been demonstrated to be beneficial in suppressing concrete cover separation (Ritchie et al., 1991). However steel end anchorage devices are generally difficult to install and have poor corrosion resistance.

The use of bonded FRP U-jackets to suppress cover separation failure is therefore more attractive than other options in terms of ease of application: the same strengthening material is used and the installation procedure is simple. A number of studies have thus explored the effectiveness of FRP U-jackets in mitigating or suppressing concrete cover separation failure in FRP-plated RC beams (Demakos and Koutsoukos 2003; Smith and Teng 2003; Buyle-Bodin and David 2004; Pimanmas and Pornpongsaroj 2004; Pham and Al-Mahaidi 2006; Kalfat et al. 2013; Grelle and Sneed 2013). Its effectiveness can be attributed to the ability of vertical FRP U-jackets to resist the interfacial peeling (normal) stress between the concrete and the FRP tension plate and to constrain the development of a major horizontal crack at the level of the steel tension reinforcement. Smith and Teng(2002a and 2002b) used vertical FRP U-jackets with the FRP tension plate being wrapped with or outside the FRP U-jackets to effectively postpone concrete cover separation. Similar enhancements in the load-carrying capacity by bonding different arrangements of FRP U-jackets (i.e. with the FRP tension plate being wrapped by or outside the FRP U-jackets) were achieved, which indicates that constraining the horizontal crack at the level of the steel tension reinforcement play an important role

in mitigating or suppressing concrete cover separation failure. The extent of enhancement in the load-carrying capacity depends on not only the arrangement of the FRP U-jackets but also the difference between the concrete cover separation strength and the strength controlled by other failure modes. A 34% increase in the load-carrying capacity was achieved by installing FRP U-jackets at the ends of the FRP tension plate in the study by Buyle-Bodin and David (2004). Similar FRP U-jackets were adopted in Ceroni (2010), which however led to failure by FRP rupture instead of concrete cover separation with a marginal improvement in the load-carrying capacity.

Inclined FRP U-jackets at ends of the FRP tension plate have been demonstrated as a promising measure to postpone/suppress concrete cover separation failure (Piamanmas and Porpongsaroj 2004; Kalfat et al. 2013). The force in the FRP tension plate can be effectively transferred to the inclined FRP U-jackets, thus postponing/suppressing concrete cover separation. In addition to use of vertical U-jackets, Piamanmas and Porpongsaroj (2004) also used X-shaped U-jackets as well as L-shaped U-jackets to successfully suppress concrete cover separation so that concrete crushing became the governing failure mode with an increase in the load-carrying capacity of up to 20%.

Although plate end anchorage measures have been investigated to postpone/suppress concrete cover separation to achieve more efficient utilization of the FRP material and a more ductile failure process for FRP-plated RC beams, most of the existing studies were conducted with the mitigation of concrete cover separation using FRP

U-jackets as a secondary issue; furthermore, all these tests were conducted on small-scale beams. In addition, in the existing research, the mitigation of concrete cover separation has not been clearly separated from the mitigation of IC debonding, which has caused some confusion on the effect of end anchorage. No systematic study has previously been focused on the optimal design/layout of these U-jackets, and its underlying mechanism has not been clearly understood.

The use of end anchorage to suppress concrete cover separation has been commonly recommended by design guidelines (CNR-DT 200/2004 2004; ACI 440.2R 2008; GB-50608 2010 and Concrete Society 2012). The ACI guideline(ACI 440.2R 2008) includes a provision for the design of FRP U-jacket anchorage for preventing concrete cover separation, based on the requirement that the transverse force resisted by the U-jackets is equal to the force from the longitudinal FRP reinforcement at failure. This rule was based on the test results of only three beam specimens (Reed et al. 2005). In the Concrete Society guideline (Concrete Society 2012), an equation similar in form but different in coefficients from that employed in ACI guideline is employed to determine the total area of vertical FRP U-jackets. The Chinese national standard (GB50608 2010) specifies the use of FRP U-jackets as plate-end anchorage that meets a prescriptive detailing requirement to avoid the occurrence of concrete cover separation. These design provisions have been established without a rigorous basis, and need to be more fully validated and/or improved. A much more rigorous approach is thus needed.

2.5 CONCLUDING REMARKS

This chapter presents a review of existing studies on debonding failures in FRP-plated RC beams, covering the bond behaviour of the FRP-to-concrete interface, intermediate crack (IC) debonding, and concrete cover separation. This review has indicated that a great deal of research on debonding failures of FRP-plated RC beams has been carried out leading to a substantial body of knowledge on the subject and the development of relevant design methods for FRP-plated RC beams.

Two major deficiencies, however, still exist in the current knowledge about debonding failures and in the methods to design against debonding in existing design guidelines. The first major deficiency is that almost all existing research is for RC beams subjected to one or two point loads (i.e. three- or four-point bending). These loading conditions have been used primarily for convenience of laboratory testing. In reality, a uniformly-distributed load (UDL) is much more common and other loading conditions are also often encountered. The limited existing research on the effect of load distribution on IC debonding strength has clearly indicated that this effect can be very significant, but this existing research is far from adequate to provide useful guidance on how this effect can be captured in a design procedure. The second major deficiency is that although design guidelines specify the use of U-jackets for the suppression of plate end debonding, the design provisions in these guidelines are rather empirical and preliminary, and have a very limited research basis. The reliability of these provisions is highly uncertain; some can be very conservative while others can be highly unsafe.

To address the two major deficiencies in existing knowledge, the author has undertaken a systematic study on the effect of load distribution on IC debonding strength and on the use of FRP U-jackets of different forms for mitigating concrete cover separation failure in FRP-plated RC beams. Both experimental and FE studies were carried out as part of the PhD research program, with the ultimate aim being the development of a better understanding of these issues and then the formulation of reliable design methods. These studies will be presented in the subsequent chapters of the thesis.

2.6 REFERENCES

ABAQUS (2004). *ABAQUS 6.5 user's manual*, ABAQUS, Inc., Providence, RI.

ACI 440.2R-08 (2008). *Guide for the design and construction of externally bonded FRP Systems for Strengthening Concrete Structures*, ACI Committee 440, American Concrete Institute, Farmington Hills, MI, USA.

Alfano, G., DeCicco, F. and Prota, A. (2012). "Intermediate debonding failure of RC beams retrofitted in flexure with FRP: Experimental results versus prediction of codes of practice", *Journal of Composites for Construction*, ASCE, Vol.16, No. 2, pp. 185-195.

Aprile, A. and Feo, L. (2007). "Concrete cover rip-off of R/C beams strengthened with FRP composites", *Composites Part B-Engineering*, Vol. 38, No. 5-6,pp. 759-771.

Baky, H.A., Ebead, U.A. and Neale, K.W. (2007). "Flexural and interfacial behaviour of FRP-strengthened reinforced concrete beams", *Journal of Composites for Construction*, ASCE, Vol. 11, No.6, pp. 629–639.

Baky, H.A., Ebead, U.A. and Neale, K.W. (2012). "Nonlinear micromechanics-based bond-slip model for FRP/concrete interfaces", *Engineering Structures*, Vol. 39, pp. 11-23.

Bazant, Z.P. and Planas, J. (1998). *Fracture and size effect in concrete and other quasi brittle materials*, CRC Press, Boca Raton.

Bilotta, A., Di Ludovico, M. and Nigro, E. (2011). "FRP-to-concrete interface debonding: Experimental calibration of a capacity model", *Composites Part B-Engineering*, Vol. 42, No. 6,pp. 1539-1553.

Biscaia, H.C., Chastre, C. and Silva, M.A.G. (2012). "Double shear tests to evaluate the bond strength between GFRP/concrete elements", *Composite Structures*, Vol. 94, No. 2,pp. 681-694.

Bizindavyi, L. and Neale, K.W (1999). "Transfer lengths and bond strengths for composites bonded to concrete", *Journal of Composites for Construction*, ASCE, Vol. 3, No. 4, pp. 153-160.

Brena, S.F., Bramblett, R.M., Wood, S.L. and Kreger, M.E. (2003). "Increasing flexural capacity of reinforced concrete beams using carbon fiber-reinforced polymer composites", *ACI Structural Journal*, Vol. 100, No. 1, pp. 36-46.

Brosens, K. and van Gemert, D. (1997). "Anchoring stresses between concrete and carbon fibre reinforced laminates", *Non-Metallic (FRP) Reinforcement for Concrete Structures, Proceedings of the 3rd International Symposium*, Japan Concrete Institute, Sapporo, Vol. 1, pp. 271–278.

Buyle-Bodin, F. and David, E. (2004). "Use of carbon fibre textile to control premature failure of reinforced concrete beams strengthened with bonded CFRP plates", *Journal of industrial textiles*, Vol. 33, No. 3, pp. 145-157.

Camata, G., Spacone, E., Al-Mahaidi, R. and Saouma, V. (2004). "Analysis of test specimens for cohesive near-bond failure of fiber-reinforced polymer-plated

concrete", *Journal of Composites for Construction*, ASCE, Vol. 8, No. 6, pp.528-538.

Cao, S.Y., Chen, J.F., Pan, J.W. and Sun, N. (2007). "ESPI measurement of bond-slip relationships of FRP-concrete interface", *Journal of Composites for Construction*, ASCE, Vol. 11, No. 2,pp. 149-160.

Chajes, M.J., Finch, W.W., Januszka, T.F. and Thomson, T.A. (1996). "Bond and force transfer of composite material plates bonded to concrete", *ACI Structural Journal*, Vol. 93, No. 2,pp. 208-217.

Chen, G.M., Teng, J.G. and Chen, J.F. (2011). "Finite-element modeling of intermediate crack debonding in FRP-plated RC beams", *Journal of Composites for Construction*, ASCE, Vol. 15, No. 3, pp. 339-353.

Chen, J.F. and Teng, J.G. (2001). "Anchorage strength models for FRP and steel plates bonded to concrete", *Journal of Structural Engineering,* ASCE, Vol. 127, No. 7, pp. 784-791.

Chen, J.F., Teng, J.G. and Yao, J. (2006). "Strength model for intermediate crack debonding in FRP-strengthened concrete members considering adjacent crack interaction", *Proceedings of Third International Conference on FRP Composites in Civil Engineering (CICE 2006)*, Miami, Florida, USA, pp. 67-70.

Chen, J.F., Yang, Z.J. and Holt, G.D. (2001). "FRP or steel plate-to-concrete bonded joints: effect of test methods on experimental bond strength", *Steel and Composite Structures*, Vol. 1, No.2, pp. 231–244.

Chen, J.F., Yuan, H. and Teng, J.G. (2007). "Debonding failure along a softening FRP-to-concrete interface between two adjacent cracks in concrete members", *Engineering Structures*, Vol. 29, No. 2, pp. 259-270.

CNR DT 200/2004 (2004). *Guidelines for design, execution and control of strengthening interventions by means of fibre-reinforced composites – materials, reinforced concrete and prestressed concrete structures, masonry structures*, Advisory Committee on Technical Regulations for Constructions, National Research Council, Rome, Italy.

Concrete Society (2012). *Design guidance for strengthening concrete structures using fibre composite materials*, Concrete Society Technical Report No. 55, Crowthorne, UK.

Coronado, C.A. and Lopez, M.M. (2006). "Sensitivity analysis of reinforced concrete beams strengthened with FRP laminates", *Cement and Concrete Composites*, Vol. 28, No. 1, pp. 102–114.

Dai, J.G. and Ueda, T. (2003). "Local bond stress slip relations for FRP sheets-concrete interfaces", *Proceedings of 6th International Symposium on FRP Reinforcement for Concrete Structures*, World Scientific Publications, Singapore, pp. 143–152.

Dai, J.G., Ueda, T. and Sato, Y. (2005). "Development of the nonlinear bond stress-slip model of fiber reinforced plastics sheet-concrete interfaces with a simple method", *Journal of Composites for Construction*, ASCE, Vol. 9, No. 1, pp. 52-62.

De Lorenzis, L., Miller, B. and Nanni, A. (2001). “Bond of fiber-reinforced polymer laminates to concrete”, *ACI Materials Journal*, Vol. 98, No. 3,pp. 256-264.

Demakos, C. and Koutsoukos, D. (2003). “Effective Strengthening of Reinforced Concrete Beams with Anchored FRPs”, Recent Advances in Composite Materials. Springer.

Diab, H. and Wu, Z.S. (2007). “Nonlinear constitutive model for time-dependent behaviour of FRP-concrete interface”, *Composites Science and Technology*,Vol. 67, No. (11-12),pp. 2323-2333.

Duthinh, D. and Starnes, M. (2001). “Strengthening of reinforced concrete beams with carbon FRP”, *Composites in Construction*, Lisse, the Netherlands, pp. 493-498.

Ebead, U.A. and Neale, K.W. (2007). “Mechanics of fibre-reinforced polymer-concrete interfaces”, *Canadian Journal of Civil Engineering*, Vol. 34, No. 3,pp. 367-377.

Ebead, U. (2011). “Hybrid externally bonded/mechanically fastened fiber-reinforced polymer for RC beam strengthening”, *ACI Structural Journal*, Vol. 108, No. 6, pp. 669-678.

fib (2001). *Externally bonded FRP reinforcement for RC structures*, International Federation for Structural Concrete, Lausanne, Switzerland.

Garden, H.N. and Hollaway, L.C. (1998). “An experimental study of the influence of

plate end anchorage of carbon fibre composite plates used to strengthen reinforced concrete beams", *Composite Structures*, Vol. 42, No. 2, pp. 175-188.

GB-50608 (2010). *Technical code for infrastructure application of FRP composites*, China Planning Press, Beijing, China.

Grelle, S.V. and Sneed, L.H. (2013). "Review of anchorage systems for externally bonded FRP laminates". *International Journal of Concrete Structures and Materials*, Vol. 7, No. 1, pp.17-33.

Hamilton, H.R., Benmokrane, B., Dolan, C.W. and Sprinkel, M.M. (2009). "Polymer materials to enhance performance of concrete in civil infrastructure", *Polymer Reviews*, Vol. 49, No. 1, pp. 1-24.

Hiroyuki, Y. and Wu, Z.S. (1997). "Analysis of debonding fracture properties of CFS strengthened member subject to tension", *Non-Metallic (FRP) Reinforcement for Concrete Structures, Proceedings of the 3rd International Symposium*, Japan Concrete Institute, Sapporo, Vol. 1, pp. 287

Hollaway, L.C. and Teng, J.G. (2008). *Strengthening and rehabilitation of civil infrastructures usingfibre-reinforced polymer (FRP) composites*, Woodhead Publishing Limited, Cambridge, U.K.

Holzenkämpfer, O. (1994). *Ingenieurmodelle des verbundes geklebter bewehrung für betonbauteile*, Dissertation,TU Braunschweig, Germany.

Hussain, M., Sharif, A., Basunbul, I. A., Baluch, M.H. and Alsulaimani, G.J. (1995). "Flexural behavior of precracked reinforced-concrete beams strengthened externally by steel plates", *ACI Structural Journal*, Vol. 92, No. 1, pp. 14-22.

Kalfat, R., Al-Mahaidi, R. and Smith, S.T. (2013). "Anchorage devices used to improve the performance of reinforced concrete beams retrofitted with FRP composites: state-of-the-art review", *Journal of Composites for Construction*, ASCE, Vol. 17, No. 1, pp. 14-33.

Khalifa, A., Gold, W.J., Nanni, A., Aziz, A. (1998). "Contribution of externally bonded FRP to shear capacity of RC flexural members", *Journal of Composites for Construction*, ASCE, Vol. 2, No.4, pp. 195–203.

Ko, H., Matthys, S., Palmieri, A. and Sato, Y. (2014). "Development of a simplified bond stress-slip model for bonded FRP-concrete interfaces", *Construction and Building Materials*, Vol. 68, pp. 142-157.

Kotynia, R., Baky, H.A., Neale, K.W. and Ebead, U.A. (2008). "Flexural strengthening of RC beams with externally bonded CFRP systems: Test results and 3D nonlinear FE analysis", *Journal of Composites for Construction*, ASCE, Vol. 12, No. 2, pp. 190-201.

Lam, L. and Teng, J.G. (2001). "Strength of RC cantilever slabs bonded with GFRP strips", *Journal of Composites for Construction*, ASCE, Vol. 5, No. 4, pp. 221-227.

Leung, C.K.Y. (2006). "FRP debonding from a concrete substrate: Some recent findings against conventional belief", *Cement and Concrete Composites*, Vol. 28, No. 8, pp. 742-748.

Lu, X.Z., Jiang, J.J., Teng, J.G. and Ye, L.P. (2006). "Finite element simulation of

debonding in FRP-to-concrete bonded joints", *Construction and Building Materials*, Vol. 20, No. 6,pp. 412-424.

Lu, X.Z., Teng, J.G., Ye, L.P. and Jiang, J.J. (2007). "Intermediate crack debonding in FRP-strengthened RC beams: FE analysis and strength model", *Journal of Composites for Construction*, ASCE, Vol. 11, pp. 161-174.

Lu, X.Z., Ye, L.P., Teng, J.G. and Jiang, J.J. (2005a). "Meso-scale finite element model for FRP sheets/plates bonded to concrete", *Engineering Structures*, Vol. 27, No. 4, pp. 564-575.

Lu, X.Z., Teng, J.G., Ye, L.P. and Jiang, J.J. (2005b). "Bond-slip models for FRP sheets/plates bonded to concrete", *Engineering Structures*, Vol. 27, No. 6, pp. 920-937.

Maeda, T., Asano, Y., Sato, Y., Ueda, T., and Kakuta, Y. (1997). "A study on bond mechanism of carbon fiber sheet", *Non-Metallic (FRP) Reinforcement for Concrete Structures, Proceedings of the 3rd International Symposium*, Japan Concrete Institute, Sapporo, Vol. 1, pp. 279–285.

Malek, A.M., Saadatmanesh, H. and Ehsani, M.R. (1998). "Prediction of failure load of R/C beams strengthened with FRP plate due to stress concentration at the plate end", *ACI Structural Journal*, Vol. 95, No. 2, pp. 142-152.

Matthys, S. (2001). *Structural behaviour and design of concrete members strengthened with externally bonded FRP reinforcement*, Doctoral thesis, University of Ghent, Belgium.

Mazzotti, C., Savoia, M. and Ferracuti, B. (2008). "An experimental study on delamination of FRP plates bonded to concrete", *Construction and Building Materials*, Vol. 22, No. 7,pp. 1409-1421.

Monti, G., Renzelli, M., and Luciani, P. (2003). "FRP adhesion in uncracked and cracked concrete zones", *Proceedings of 6th International Symposium on FRP Reinforcement for Concrete Structures*, World Scientific, Singapore, pp. 183–192.

Nakaba, K., Toshiyuki, K., Tomoki, F., Hiroyuki, Y. (2001). "Bond behaviour between fiber-reinforced polymer laminates and concrete", *ACI Structural Journal*, Vol. 98, No. 3, pp. 359–367.

Neale, K.W., Ebead, U.A., Baky, H.M.A., Elsayed, W.E., and Godat, A. (2006). "Analysis of the load-deformation behaviour and debonding for FRP-strengthened concrete structures", *Advances of Structural Engineering*, Vol. 9, No. 6, pp. 751–763.

Neubauer, U., and Rostásy, F.S. (1997). "Design aspects of concrete structures strengthened with externally bonded CFRP plates", *Proceedings of the 7th International Conference on Structures Faults and Repairs*, ECS Publications, Edinburgh, Scotland, Vol. 2, pp. 109–118.

Neubauer, U., Rostasy, F.S. (1999). "Bond failure of concrete fiber reinforced polymer plates at inclined cracks-experiments and fracture mechanics model", *Proceedings of 4th International Symposium on Fiber Reinforced Polymer Reinforcement for reinforced Concrete Structures*, SP-188, ACI, Farmington Hills (MI), 369–382.

Niedermeier, R. (2000). *Envelope line of tensile forces while using externally bonded*

reinforcement, Ph.D. thesis, TU München, Germany (in German).

Niu, H.D., and Wu, Z.S. (2005). "Numerical analysis of debonding mechanisms in FRP-strengthened RC beams", *Computer-Aided Civil and Infrastructure Engineering*, Vol. 20, No. 5, pp. 354–368.

Nour, A., Massicotte, B., Yildiz, E., and Koval, V. (2007). "Finite element modelling of concrete structures reinforced with internal and external fibre-reinforced polymers", *Canadian Journal of Civil Engineering*, Vol. 34, No. 3, pp. 340–354.

Oehlers, D.J., Ali, M.S.M., Haskett, M., Lucas, W., Muhamad, R. and Visintin, P. (2011). "FRP-reinforced concrete beams: unified approach based on IC theory", *Journal of Composites for Construction*, ASCE, Vol. 15, No. 3, pp. 293-303.

Orton, S.L., Jirsa, J.O. and Bayrak, O. (2008). "Design considerations of carbon fiber anchors", *Journal of Composites for Construction*, ASCE, Vol. 12, No. 6, pp. 608-616.

Pan, J.L., Chung, C.F. and Leung, C.K.Y. (2009). "FRP debonding from concrete beams under various load uniformities", *Advances in Structural Engineering*, Vol. 12, No. 6, pp. 807-819.

Pellegrino, C., Tinazzi, D. and Modena, C. (2008). "Experimental study on bond behaviour between concrete and FRP reinforcement", *Journal of Composites for Construction*, ASCE, Vol. 12, No. 2,pp. 180-189.

Piamanmas, A. and Pornpongsaroj, P. (2004). "Peeling behaviour of reinforced concrete beams strengthened with CFRP plates under various end restraint

conditions", *Magazine of Concrete Research*, Vol. 56, No. 2, pp. 73-81.

Pham, H.B., and Al-Mahaidi, R. (2005). "Finite element modelling of RC beams retrofitted with CFRP fabrics", *Proceedings of 7th International Symposium on Fiber-Reinforced (FRP) Polymer Reinforcement for Concrete Structures (ACI Symposium Publication 230)*, Kansas City, MO, pp. 499–513.

Pham, H.B. and Al-Mahaidi, R. (2006). "Prediction models for debonding failure loads of carbon fiber reinforced polymer retrofitted reinforced concrete beams", *Journal of Composites for Construction*, ASCE, Vol. 10, No. 1,pp. 48-59.

Qiao, P.Z. and Chen, F.L. (2008). "An improved adhesively bonded bi-material beam model for plated beams", *Engineering Structures*, Vol. 30, No. 7,pp. 1949-1957.

Raoof, M. and Hassanen, M.A.H. (2000). "Peeling failure of reinforced concrete beams with fibre-reinforced plastic or steel plates glued to their soffits", *Proceedings of the Institution of Civil Engineers-Structures and Buildings*, Vol. 140, No. 3, pp.291-305.

Rosenboom, O. and Rizkalla, S.H. (2008a). "Modeling of IC debonding of FRP-strengthened concrete flexural members", *Journal of Composites for Construction*, ASCE, Vol. 12, No. 2, pp. 168-179.

Rosenboom, O. and Rizkalla, S.H. (2008b). "Experimental study of intermediate crack debonding in fiber-reinforced polymer strengthened beams", *ACI Structural Journal*, Vol. 105, No. 1, pp. 41-50.

Rusinowski, P. and Taljsten, B. (2009). “Intermediate crack induced debonding in concrete beams strengthened with CFRP plates - an experimental study”, *Advances in Structural Engineering*, Vol. 12, No. 6,pp. 793-806.

Said, H. and Wu, Z.S. (2008). “Evaluating and proposing models of predicting IC debonding failure”, *Journal of Composites for Construction*, ASCE, Vol. 12, No. 3, pp. 284-299.

Salomoni, V., Mazzucco, G., Pellegrino, C. and Majorana, C. (2011).“Three-dimensional modelling of bond behaviour between concrete and FRP reinforcement”, *Engineering Computations*, Vol. 28, No. 1-2,pp. 5-29.

Savioa, M., Farracuti, B. and Mazzotti, C. (2003). “Non-linear bond–slip law for FRP-concrete interface”, Proceedings of 6th International Symposium on FRP Reinforcement for Concrete Structures, World Scientific Publications, Singapore, pp. 163–172

Schilde, K. and Seim, W. (2007). “Experimental and numerical investigations of bond between CFRP and concrete”, *Construction and Building Materials*, Vol. 21, No. 4, pp. 709-726.

Sebastian, W.M. (2001). “Significance of midspan debonding failure in FRP-plated concrete beams”, *Journal of Structural Engineering-ASCE*, Vol. 127, No. 7, pp. 792-798.

Serbescu, A., Guadagnini, M. and Pilakoutas, K. (2013). “Standardised double-shear test for determining bond of FRP to concrete and corresponding model

development", *Composites Part B-Engineering*, Vol. 55, pp. 277-297.

Sharma, S.K., Ali, M.S.M., Goldar, D. and Sikdar, P.K. (2006)."Plate-concrete interfacial bond strength of FRP and metallic plated concrete specimens", *Composites Part B-Engineering*, Vol. 37, No. 1,pp. 54-63.

Smith, S.T. and Teng, J.G. (2002a). "FRP-strengthened RC beams. I: review of debonding strength models", *Engineering Structures*, Vol. 24, No. 4, pp. 385-395.

Smith, S.T. and Teng, J.G. (2002b). "FRP-strengthened RC beams. II: assessment of debonding strength models", *Engineering Structures*, Vol. 24, No. 5, pp. 397-417.

Smith, S.T. and Teng, J.G. (2003). "Shear-bending interaction in debonding failures of FRP-plated RC beams", *Advances in Structural Engineering*, Vol. 6, No. 3, pp. 183–99.

Taljsten, B. (1997). "Defining anchor lengths of steel and CFRP plates bonded to concrete", *International Journal of Adhesion and Adhesives*, Vol. 17, No. 4, pp. 319-327.

Tanaka, T. (1996).*Shear resisting mechanism of reinforced concrete beams with CFS as shear reinforcement*, Graduation thesis, Hokkaido University, Japan.

Tao, Y. and Chen, J.F. (2015). "Concrete damage plasticity model for modeling FRP-to-concrete bond behaviour", *Journal of Composites for Construction*,

ASCE, Vol. 19, No. 1.

Teng, J.G., Chen, J.F., Smith, S.T. and Lam, L. (2002). *FRP-strengthened RC Structures*, West Sussex: Wiley.

Teng, J.G., Lu, X.Z., Ye, L.P., and Jiang, J.J. (2004). "Recent research on intermediate crack-induced debonding in FRP-strengthened RC beams", P*roceedings of 4th International Conference on Advanced Composite Materials in Bridges and Structures*, ACMBS IV, Calgary, Alberta, Canada.

Teng, J.G., Yuan, H. and Chen, J.F. (2006). "FRP-to-concrete interfaces between two adjacent cracks: Theoretical model for debonding failure", *International Journal of Solids and Structures*, Vol. 43, No. 18-19, pp. 5750-5778.

Teng, J.G., Smith, S.T., Yao, J. and Chen, J.F. (2003). "Intermediate crack-induced debonding in RC beams and slabs", *Construction and Building Materials*, Vol. 17, No. 6-7, pp. 447-462.

Teng, J.G. and Yao, J. (2007). "Plate end debonding in FRP-plated RC beams - II: Strength model", *Engineering Structures*, Vol. 29, No. 10, pp. 2472-2486.

Toutanji, H., Han, M. and Ghorbel, E. (2012). "Interfacial bond strength characteristics of FRP and RC substrate", *Journal of Composites for Construction,* ASCE, Vol. 16, No. 1, pp. 35-46.

Wu, Y.F. and Huang, Y. (2008). "Hybrid bonding of FRP to reinforced concrete structures", *Journal of Composites for Construction*, ASCE, Vol. 12, No. 3, pp.

266-273.

van Gemert, D. (1980). “Force transfer in epoxy-bonded steel-concrete joints”, *International Journal of Adhesion and Adhesives*, Vol. 1, No. 2, pp. 67–72.

Wang, J. and Zhang, C. (2008). “Nonlinear fracture mechanics of flexural-shear crack induced debonding of FRP strengthened concrete beams”, *International Journal of Solids and Structures*, Vol. 45, No. 10,pp. 2916-2936.

Wong, R.S.Y., and Vecchio, F.J. (2003). “Towards modeling of reinforced concrete members with externally bonded fiber-reinforced polymer composites”, *ACI Structural Journal*, Vol. 100, No. 1, pp. 47–55.

Wu, Y.F. and Jiang, C. (2013). “Quantification of bond-slip relationship for externally bonded FRP-to-concrete joints”, *Journal of Composites for Construction*, ASCE, Vol. 17, No. 5, pp. 673-686.

Wu, Y.F., Xu, X.S., Sun, J.B. and Jiang, C. (2012). “Analytical solution for the bond strength of externally bonded reinforcement”, *Composite Structures,* Vol. 94, No. 11, pp. 3232-3239.

Wu, Y.F., Yan, J.H., Zhou, Y.W. and Xiao, Y. (2010). “Ultimate strength of reinforced concrete beams retrofitted with hybrid bonded fiber-reinforced polymer”, *ACI Structural Journal*, Vol. 107, No. 4, pp. 251-460.

Wu, Z.S. and Niu, H.D. (2000). “Study on debonding failure load of RC beams strengthened with FRP sheets”, *Journal of Structural Engineering-ASCE*, Vol.

46A, pp. 1431-1441.

Wu, Z.S., Yuan, H. and Niu, H.D. (2002). "Stress transfer and fracture propagation in different kinds of adhesive joints", *Journal of Engineering Mechanics-ASCE*, Vol. 128, No. 5, pp. 562-573.

Wu, Z.S., and Yin, J. (2003). "Fracture behaviours of FRP-strengthened concrete structures", *Engineering Fracture Mechanics*, Vol. 70, No. 10, pp. 1339–1355.

Wu, Z.S. and Niu, H.D. (2007). "Prediction of crack-induced debonding failure in R/C structures flexurally strengthened with externally bonded FRP composites", *JSCE Journal of Materials, Concrete Structures and Pavements*, Vol. 63, No. 4, pp. 620–639

Yang, Z.J., Chen, J.F., and Proverbs, D. (2003). "Finite element modelling of concrete cover separation failure in FRP plated RC beams", *Construction and Building Materials*, Vol. 17, No. 1, pp. 3–13.

Yao J. (2004). *Debonding failures in reinforced concrete structures strengthened with externally bonded FRP sheets/plates*, Ph.D. thesis, Hong Kong Polytechnic University, Hong Kong.

Yao, J. and Teng, J.G. (2007). "Plate end debonding in FRP-plated RC beams - I: Experiments", *Engineering Structures*, Vol. 29, No. 10, pp. 2457-2471.

Yao, J., Teng, J.G. and Chen, J.F. (2005). "Experimental study on FRP-to-concrete bonded joints", *Composites Part B-Engineering*, Vol. 36, No. 2, pp. 99-113.

Yuan, H., Teng, J.G., Seracino, R., Wu, Z.S. and Yao, J. (2004). "Full-range behaviour of FRP-to-concrete bonded joints", *Engineering Structures*, Vol. 26, No. 5, pp. 553-565.

Yuan, H., Wu, Z.S. and Yoshizawa, H. (2001). "Theoretical solutions on interfacial stress transfer of externally bonded steel/composite laminates", *Journal of Structural Mechanics and Earthquake Engineering,* JSCE, Vol. 18, No. 1, pp. 27-39.

Zhang, H.W. and Smith, S.T. (2012). "FRP-to-concrete joint assemblages anchored with multiple FRP anchors", *Composite Structures*, Vol. 94, No. 2, pp. 403-414.

Zhang, H.W., Smith, S.T. and Kim, S.J. (2012). "Optimisation of carbon and glass FRP anchor design", *Construction and Building Materials*, Vol. 32, pp. 1-12.

Zhang, S.S. (2011). *Behaviour and Modelling of RC Beams Strengthened in Flexure with Near-surface Mounted FRP*, PhD Thesis, The Hong Kong Polytechnic University, Hong Kong, China.

Zhang, S.S. and Teng, J.G. (2014). "Finite element analysis of end cover separation in RC beams strengthened in flexure with FRP", *Engineering Structures*, Vol. 75, pp. 550-560.

2.7 FIGURE

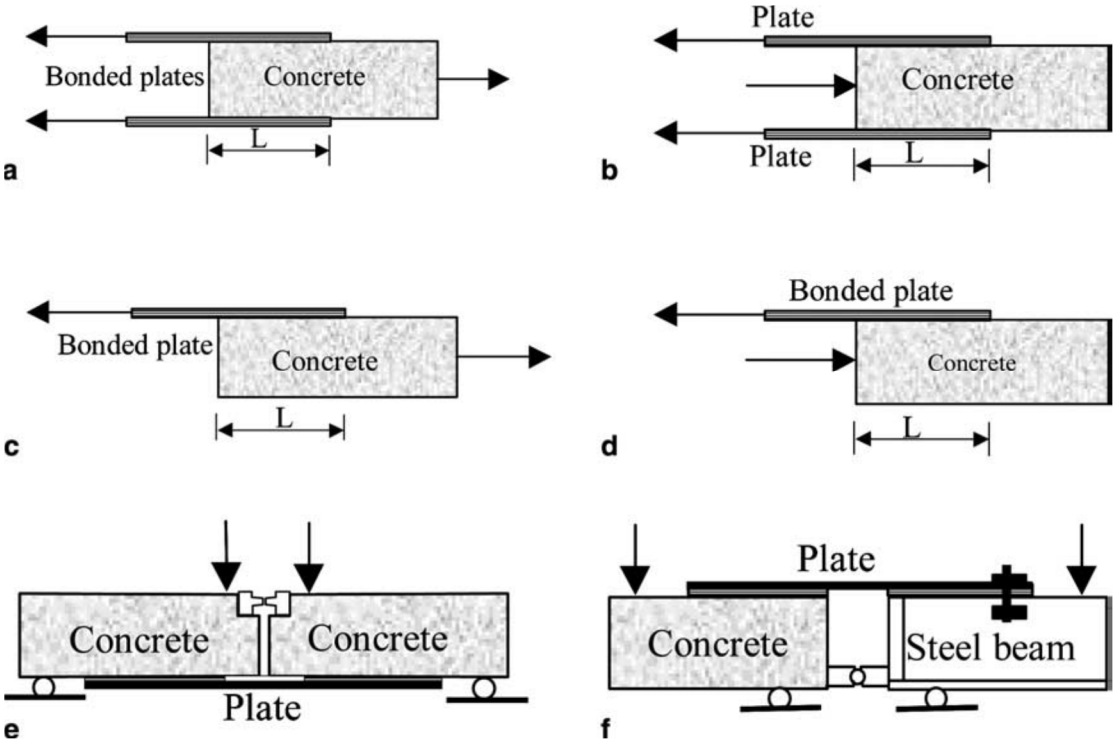

Figure 2.1 Bond tests of different types: (a) Far-end supported (FES) double-shear test; (b) Near-end supported (NES) double-shear test; (c) Far-end supported (FES) single-shear test; (d) Near-end supported (NES) single-shear test; (e) Beam test; (f) Modified beam test [from Chen et al. (2001)]

CHAPTER 3

EFFECT OF LOAD DISTRIBUTION ON IC DEBONDING: EXPERIMENTAL STUDY

3.1 INTRODUCTION

As mentioned in Chapter 2, the effect of load distribution on IC debonding has been largely neglected by existing experimental and FE investigations on FRP-plated RC beams. Only two experimental studies have investigated IC debonding under other one- or two-point loading (Mazzotti and Savoia 2009; Pan et al. 2009), and most of these experimental studies are under one- and two-point loading (i.e. three- and four-point bending) for ease of laboratory realization. Accordingly, only these tested plated RC beams under one- or two-point loading was analyzed using the finite element modelling. In reality, the UDL is much more common and other loading conditions are often encountered. Different load distributions result in different distributions of shear force and moment in the beam, and therefore may significantly affect IC debonding behaviour in FRP-plated RC beams. Due to the lack of research on the effect of load distribution on IC debonding, most of the current IC debonding

strength models are unsuitable for loading conditions other than one- or two-point loading.

Against the above background, this chapter presents an experimental study on full-scale FRP-plated RC beams under different loading distributions. The study was undertaken with the following objectives: (a) to gain a better understanding of the effect of load distribution on IC debonding; (b) to provide reliable test results for future use in developing an IC debonding model capable of considering the effect of load distribution.

3.2 EXPERIMENTAL PROGRAMME

3.2.1 Specimen design

The experimental programme consisted of five full-scale FRP-plated RC beams of the same geometry: a cross-section of 200 mm in width by 450 mm in height and a clear span of 4000 mm (Figure 3.1). The beams were under-reinforced as follows: two 16 mm steel tension bars and two 16 mm steel compression bars. To avoid shear failure prior to IC debonding, 8 mm stirrups at 100 mm centre-to-centre spacing were used as the steel shear reinforcement. A wet layup FRP plate formed from three layers of unidirectional carbon fibre sheets and epoxy was bonded to each RC beam. These FRP plates all had the same nominal dimensions: 100 mm wide, 0.999 mm thick and 3800 mm long. Although the FRP plates all had the same nominal width, the actual widths achieved were different due to the wet layup process. As the actual width dictates the width of the FRP-to-concrete interface, which affects the debonding behaviour, the actual width of each FRP plate was measured at a number

of locations after testing using the debonded plate, and the average is recorded in Table 3.1.

The load distribution, which can result in different distributions of shear force and bending moment, was the only experimental variable investigated. Series I, which consisted of three beams under two-point loading and covering different shear spans, was used to investigate the effect of varying the shear span on IC debonding. All three beams were subjected to two concentrated loads (i.e. four-point bending) but had shear spans of 1750 mm, 1250 mm and 1000 mm respectively (Figure 3.2). According to their shear spans, these three beams were named LP2SP1750, LP2SP1250, and LP2SP1000, respectively. The number following the letters 'LP' indicates the number of loading points while 'SP' denotes the effective shear span of the beam.

Series II was designed to investigate the effect of load uniformity on IC debonding in FRP-plated RC beams. It included three FRP-plated RC beams; sharing Specimen LP2SP1000 with Series I (i.e. five beams were tested in the two series). The other two beams, denoted as LP4SP1000 and LP8SP1000, were subjected to four- and eight-point loading respectively. They all had the same effective shear span, which is equal to 1000 mm. The loading patterns and the corresponding shear force and bending moment diagrams are shown in Figures 3.3 and 3.4. Figure 3.4 indicates that the differences in the distributions of shear force and bending moment between eight-point loading and UDL are small. It is believed that the difference in debonding behaviour of beams under eight-point loading and UDL is also small. The eight-point loading condition was thus used to represent the UDL condition due to the difficulty

in accommodating more loading points in the test set-up.

3.2.2 Specimen preparation

All five full-scale RC beams were cast with one batch of commercial concrete following the standard casting practice. In the first week of curing, the specimens were sprayed with water and covered with a plastic film to ensure that the specimens were under a moist condition and had enough water for the hydration of cement. After that, the specimens were cured under a normal indoor condition. The tension face of the specimens after about 28 days' curing was roughened using a jet gun driven by compressed air with a pressure of about 0.7 MPa and left to dry for at least one day. It was then cleaned using compressed air, followed by the application of primer. Unidirectional fibre sheets together with the bonding epoxy were then applied layer by layer within the open time of the epoxy adhesive (one hour for the present epoxy adhesive). The wet lay-up FRP plate was left to cure for at least seven days to achieve its full strength. The detailed bonding procedure for wet layup FRP plates can be found in Appendix 3.1.

3.2.3 Material properties

The specimens were prepared with the same commercial concrete to ensure consistent properties for all the beams. For each beam, three 150 mm x 300 mm cylinder specimens were prepared using the same concrete as the beams and were tested following a British Standard (BS EN 12390-3 2009) on the same day when the beam was tested. The results of the three cylinder specimens were averaged to obtain

the cylinder compressive strength of concrete.

Two different types of steel bars were used in the test beams: 8 mm steel bars for shear reinforcement and 16 mm steel bars for longitudinal reinforcement (both compression and tension steel bars). The average yield stress, ultimate stress and elastic modulus from three tensile tests for each type of steel bar are listed in Table 3.1 (BS EN ISO 6892-1 2009). Unfortunately, the steel elastic modulus is believed to have been overestimated as slips between the steel bar and the extensometer may have existed and have led to underestimation of strains. An elastic modulus of 200 GPa is suggested to be used in numerical simulations or sectional analysis. The tensile strength and elastic modulus of the FRP material were averaged from the test results of six flat FRP coupons following the ASTM standards (ASTM D3039/D3039M-08 2008; ASTM D7565/D7565M-10 2010), and are also listed in Table 3.1.

3.2.4 Testing and instrumentation

The test set-ups for Specimen LP4SP1000 and Specimen LP8SP1000 are shown in Figures 3.5a and 3.5b. A waffle-tree system has been widely used to apply multiple point loads simultaneously. The two existing experimental studies on debonding failures under different load distributions (Mazzotti and Savoia 2009;Pan et al. 2009) adopted the waffle-tree system for 2-, 4- and 8-point loading. However, as mentioned by Chung (2004), it is difficult to ensure same load at all loading points when load distribution is achieved using such a waffle-tree system; this problem was indeed observed in a trial test conducted by the author's research group prior to the present experimental programme.

To overcome the problem with a waffle-tree system, a loading set-up similar to that employed by Aprile and Feo (2007) was used in the present experimental programme. This loading set-up included individual jacks at different loading points, which were connected to a single manually-operated pump to ensure the same load from each jack. A load cell was installed under each loading jack to monitor the precise load from the jack. Figures 3.6a and 3.6b give the loads at different loading jacks of Specimens LP4SP1000 and LP8SP1000, which indicated that the desired equal loading at different points was closely achieved with the overall difference between different loads within 2 %.

Five Linear Variable Differential Transformers (LVDTs) were uniformly distributed along the beam, with two at the supports, one at mid-span, and two between the supports and the mid-span, to measure deflections of different locations of the beam (Figure 3.7). The LVDTs were connected to the supporting bases, which had the same displacements as that of the ground so that the readings of LVDTs were measured using the same reference base (Figure 3.8).

Many strain gauges of 80 mm or 20 mm in gauge length were used to measure the strains of either compression concrete or the FRP plate. One strain gauge of 80 mm in gauge length was attached to the extreme compression fibre of concrete at mid-span, and a large number of strain gauges of 20 mm as shown in Figure 3.9were installed onto the FRP plate. The spacing of the strain gauges on the FRP plate was 125 mm except for the three strain gauges near the plate end, which had smaller spacings of either 55 mm or 75 mm to monitor the large variation of FRP strain in this region. All test data, including loads, displacements, and strains were collected

using an automatic data logger.

The crack information (pattern and widths) was carefully measured and recorded during testing to interpret debonding behaviour and for future use in verifying some existing IC debonding strength models. The crack widths of most major cracks were measured using an optic digital camera (Figure 3.10a), which automatically read crack widths. A part, which is an optic digital camera and is connected to the processing centre via a data wire, is handed by the operator, and put on the position of crack to be measured. The crack can be automatically captured by the digital camera and the width of the measured crack can be automatically recorded with a figure. An example for the measurement of crack width using this instrument is given in Figure 3.10b. The positions for crack width measurements were marked when the crack widths were measured for the first time for reference in the subsequent crack width measurements at other load levels. The positions were generally at the level of the steel tension bars instead of at a position very close to the beam soffit, as some spacing was needed to accommodate the measurement instrument.

3.3 TEST RESULTS AND DISCUSSIONS

3.3.1 General

A summary of the key experimental results of all five full-scale beam tests is given in Table 3.2, including the moment at mid-span, deflection at mid-span, maximum FRP strain in the FRP plate, and maximum crack width at mid-span at the initiation of concrete cracking, steel yielding and beam failure. The concrete strains at the compression face of the beam at beam failure are also given in Table 3.2, which are

far below the concrete crushing strain. All five specimens failed by IC debonding of the FRP plate, but the ultimate loads, crack patterns and locations of debonding initiation (i.e. debonding of the FRP soffit plate within a small part of the bonded interface) differed in each case. An increase of about 20% in the total ultimate load was achieved by increasing the load uniformity from two-point to eight-point loading together with shortening of the shear span from 1750 mm to 1000 mm. The debonding behaviour of the specimen under four-point or eight-point loading is different from that of specimens under two-point loading. In all the specimens under two-point loading, debonding was initiated at a crack under one of the loading points and propagated along the direction of decreasing moment. Under four-point or eight-point loading, debonding initiated at a significant crack closer to the mid-span than that in Specimen LP2SP1000. More specifically, the locations of debonding initiation in Specimens LP2SP1000, LP4SP1000 and LP8SP1000 are 1032 mm, 1197 mm, and 1873 mm from one of the supports, respectively.

3.3.2 Tests of Series I

The three beams of Series I was tested under two-point loading to investigate the effect of shear span on IC debonding. The moment-deflection curves are compared in Figure 3.11a. It is demonstrated that the ultimate load slightly increases with a reduction of the shear span. The maximum moment in the beam at debonding (debonding moment) for a shear span of 1000 mm is 144.0 kN.m, which is 4.3% and 9.0% higher than those for shear spans of 1250 mm and 1750 mm, respectively. The deflection at mid-span at debonding failure increases significantly from 20.5 mm in Specimen LP2SP1750, to 25.8 mm in Specimen LP2SP1250, and to 29.9 mm in

Specimen LP21000. The elastic stiffness of the beam reduces as the shear span increases. The yield loads of Specimens LP2SP1750, LP2SP1250 and LP2SP1000 are about 108 kN, 110 kN and 115 kN respectively. It however was expected that all the specimens in Series I had the same yield load as the load at steel yielding should be primarily controlled by the steel yield stress and steel tension bars of the same batch were used in these specimens.

The FRP strain distributions at failure of specimens in Series I are given in Figure 3.12. The maximum FRP strain of each specimen increases from 5970 $\mu\varepsilon$ in Specimen LP2SP1750, to 6810 $\mu\varepsilon$ in Specimen LP2SP1250 and 6675 $\mu\varepsilon$ in Specimen LP2SP1000. As shown in Figure 3.12, the FRP strain distribution is almost proportional to the moment distribution of the specimens. Fluctuations of FRP strains occur at positions of major cracks. Crack initiation of all beams in Series I occurred at about the same load level of 34.5 kN.m in moment at mid-span (i.e. $\mathrm{M_{mid-span}} \approx$ 34.5 kN.m). The crack patterns at failure with the corresponding failure modes of beams are given in Figure 3.13, which indicates that the number of significant cracks increases from 29 in Specimen LP2SP1750 to 33 in Specimen LP2SP1250, and to 34 in Specimen LP2SP1000. The flexural/shear-flexural cracks become more distributed with a decrease of shear span, and the distance between the closest significant crack and the adjacent support decreases from 614 mm in Specimen LP2SP1750, to 415 mm in Specimen LP2SP1250, and to 242 mm in Specimen LP2SP1000. The mean crack spacing increases from 96.7 mm in Specimen LP2SP1750 to 97.5 mm in Specimen LP2SP1250 and103.5 mm in Specimen LP2SP1000.The debonding process of the FRP soffit plate in all three beams in Series I initiated at a significant crack (referred to as the 'critical crack' here after) and then propagated along the

direction of decreasing moment. The critical cracks of the beams were at one of the loading points, and specifically their distances from the left support were 2227 mm in Specimen LP2SP1750, 2703 mm in Specimen LP2SP1250 and 1023 mm in Specimen LP2SP1000. Development of both the critical crack and its adjacent crack in the decreasing moment direction has a significant influence on the FRP plate debonding failure. The spacings between the critical crack and its adjacent crack were 88 mm, 98 mm, and 121 mm in Specimens LP2SP1750, LP2SP1250 and LP2SP1000, respectively. Figure 3.14shows the development in width of both the critical crack and its adjacent crack. The critical crack developed rapidly when its width reached about 0.3 mm at the mid-span moment of about 110.0 kN.m, and the yielding of tension steel bars started. However, at the same time, the width of the adjacent crack increased almost linearly with the moment.

3.3.3 Tests of Series II

The three specimens in Series II had the same effective shear span of 1000 mm but different numbers of loading points (Figure 3.2). Series II shared Specimen LP2SP1000 with Series I. They were designed to investigate the effect of load distribution (hence shear and moment distributions) on IC debonding failure. The chosen effective shear span is equal to that of the same beam under UDL, which is common in practice. To ensure equal loads from all loading jacks, a series of individual hydraulic jacks were connected to a single manually-operated pump. The precise load from each jack was monitored by a load cell and dully considered in interpretation. Figures3.6a and 3.6b give loads from all jacks for Specimens LP4SP1000 and LP8SP1000, which were under 4- and 8-point loading respectively.

Both of these figures indicate differences of less than 3% between the loads from different jacks, which confirm the accuracy of the loading system.

The moment-deflection curves of specimens in Series II are given in Figure 3.11b. All three beams failed by IC debonding; their failure modes and corresponding crack patterns at failure are shown in Figure 3.13. As the number of loading points increases, the debonding moment increases from 144.0 kN.m for Specimen LP2SP1000, to 151.0 kN.m for Specimen LP4SP1000, and to 156.7 kN.m for Specimen LP8SP1000. At the same time, the mid-span deflection at debonding failure slightly decreases from 29.9 mm for Specimen LP2SP1000, to 29.4 mm for Specimen LP4SP1000, and to 28.8 mm for Specimen LP8SP1000.The moment-deflection curves of the three specimens are close to each other before the initiation of concrete cracking at about 38.0 kN.m. After concrete cracking, the curve of Specimen LP2SP1000 deviates from those of the other two specimens gradually and shows a slightly softer response.

The FRP strain distributions at failure of specimens in series II are given in Figure 3.15. In general, the FRP strain distribution is proportional to the corresponding moment distribution. The maximum FRP strain of each specimen at failure increases from 6675 $\mu\varepsilon$ in Specimen LP2SP1000 to 6773 $\mu\varepsilon$ in Specimen LP4SP1000 and 6845 $\mu\varepsilon$ in Specimen LP8SP1000. Although the maximum FRP strain in Specimen LP2SP1000 is slightly smaller than those of Specimens LP4SP1000 and LP8SP1000, the strains in the region close to the adjacent support are larger than those in Specimens LP4SP1000 and LP8SP1000. It also should be noted here that fluctuations of FRP strains occur at positions of major cracks, such as the position of

525 mm from the left support in Specimen LP2SP1000.

As mentioned above, the crack pattern and crack development are dependent on the distribution of moment in a beam (Figure 3.13). When the three specimens of Series II were subjected to about the same maximum moment, the larger moments in the shear span of Specimen LP2SP1000 induced more intensive cracking with smaller crack spacings; that is, 34 major cracks existed in Specimen LP2SP1000, but31 and 32 major cracks existed in Specimens LP4SP1000 and LP8SP1000, respectively. IC debonding initiated at a significant crack (i.e. the critical crack) and was always influenced by its adjacent crack.

In this series of tests, the position of the critical crack varied with the load distribution, with the distances of the critical cracks from its adjacent support being 1196 mm, 1196 mm and 1873mm in Specimens LP2SP1000, LP4SP1000 and LP8SP1000 respectively. The distance between the adjacent crack and the critical crack increases from 121 mm in Specimen LP2SP1000, to 157 mm in Specimen LP4SP1000 and 148 mm in Specimen LP8SP1000. The development of the critical crack and its adjacent crack are given in the Figure 3.16. All the critical cracks occurred at an early stage of loading. After the initiation of FRP debonding, the crack width increased dramatically until the completed bonding of the FRP plate. During the entire debonding process, the adjacent crack was always narrower than the critical crack as the adjacent crack was at a location of lower moment. Although the critical crack appeared almost directly under the loading point in all specimens, which was simultaneously subjected to the maximum moment and the maximum shear force in the beam, the critical cracks in the specimens under 4- and 8-point

loading were wider than those in the specimen under 2-point loading were. The widths of most of the major cracks increased linearly with the increase of load. However, some major cracks experienced a dramatic increase in width at the load of about 110.0 kN.m, which is due to the local debonding of FRP plate adjacent to these cracks.

3.4 CONCLUSIONS

This chapter has presented an experimental study on the effect of load distribution on IC debonding, in which five full-scale RC beams strengthened in flexure with a wet layup FRP soffit plate were carefully designed and tested. For the precise implementation of the designed loading conditions, the load at each loading point was directly applied by a hydraulic jack, and all hydraulic jacks were connected to a single manually-operated pump to ensure simultaneous and equal loading for all jacks.

All five test beams failed by IC debonding. However, the IC debonding behaviours of FRP-plated RC beams under different loading conditions are different from each other. Under four-point or eight-point loading, debonding initiated at a crack closer to the mid-span compared to their counterpart under two-point loading. More specifically, the locations of debonding initiation in Specimens LP2SP1000, LP4SP1000, LP8SP1000 were respectively 1032mm, 1196mm, and 1873mm from the nearer support.

An increase of about 9% in the maximum moment in the beam at IC debonding (i.e. debonding moment) was achieved by increasing the load uniformity from two-point

loading to eight-point loading. The increase in the debonding strain (i.e. maximum strain of the FRP soffit plate at debonding) was expected to be larger than the increase in the debonding moment. However the monitored debonding strain increased only by about 3% when the load uniformity increased from two-point loading to eight-point loading. This may be because the existence of cracks in concrete made it difficult to capture the actual maximum strain in the FRP soffit plate at debonding using strain gauges although a larger number of strain gauges were used. This means that the existing IC debonding strength models based on beams in three- or four- point bending can be slightly conservative for use in the design of beams under more uniform loading such as uniformly distributed loading. Therefore, it is desirable to include the benefit of load uniformity in an IC debonding strength model in the future, if this benefit can be accurately predicted. More research is thus needed for the precise quantification of this benefit to enable more economical use of the expensive FRP materials.

An increase of about another 9% in the debonding moment was obtained when the shear span of the beam decreased from 1750 mm to 1000 mm. However, it is uncertain whether this increase was only due to the shear span decrease as the different beams had different yield moments although these yield moments were expected to be the same. Further research on this effect undertaken using reliable FE modelling will be presented in Chapter 4.

The cracking behaviour of the test beams (e.g. crack pattern and crack development) was dependent on the distribution of moment in the beam and had a significant effect on the IC debonding process. Beams under two-point loading tended to have a more

intensive crack pattern than beams under four- or eight-point loading when they were subjected to similar maximum moments. This is because a beam under two-point loading has larger moments in the shear spans than that under four- or eight-point loading. In addition, the critical crack in the beam under 2-point loading at failure was narrower than its counterparts were under 4- and 8-point loading.

It should be noted that the above conclusions were drawn based on the results of a small number of test specimens. A more extensive study of the issues (e.g. through reliable FE modelling) will be presented in Chapter 4.

3.5 REFERENCES

Aprile, A. and L. Feo (2007). "Concrete cover rip-off of R/C beams strengthened with FRP composites", *Composites Part B-Engineering*, Vol.38, No. 5-6, pp.759-771.

ASTM D3039/D3039M-08 (2008). S*tandard test method for tensile properties of polymer matrix composite materials*, ASTM International, West Conshohocken, Philadelphia (PA).

ASTM D7565/D7565M-10 (2010). *Standard test method for determining tensile properties of fiber reinforced polymer matrix composites used for strengthening of civil structures*, ASTM International, West Conshohocken, Philadelphia, PA.

BS EN 12390-3 (2009). *Testing hardened concrete. Part 3: Compressive strength of test specimens*, The British Standards Institute, London, UK.

BS EN ISO 6892-1 (2009). *Metallic materials —Tensile testing Part 1: Method of test at ambient temperature*, The British Standards Institute, London, UK.

Chung, C.F. (2004). *Flexural strengthening of beams with FRP under various loading configurations*, M.Phil. thesis, Hong Kong University of Science and Technology, Hong Kong.

Mazzotti, C. and Savoia, M. (2009). "Experimental tests on intermediate crack debonding failure in FRP-strengthened RC beams", *Advances in Structural Engineering*, Vol. 12, No. 5, pp.701-713.

Pan, J.L., Chung, T.C.F. and Leung, C.K.Y. (2009). “FRP debonding from concrete beams under various load uniformities”, *Advances in Structural Engineering*, Vol. 12, No.6, pp.807-819.

3.6 TABLES AND FIGURES

Table 3.1 Material properties of steel and FRP

Martial	Yield stress, f_y (MPa)	Ultimate stress, f_u (MPa)	Elastic modulus, E (GPa)
8 mm bars	374	486	225*
16 mm bars	431	569	228*
FRP	/	3800	242

*Note: The steel elastic moduli were obtained from extensometer readings and are believed to have overestimated the actual values. An elastic modulus of 200 GPa was used in numerical simulations in the present research programme.

Table 3.2 Summary of test results

Specimen		LP2SP1750	LP2SP1250	LP2SP1000	LP4SP1000	LP8SP1000
Width of the FRP plate (mm)		111.0	112.1	109.8	109.9	110.2
Cylinder compressive strength of concrete (MPa)		47.0	47.1	48.2	48.5	48.5
Initiation of concrete cracking	Maximum moment of the beam (kN.m)	38.2	35.9	35.4	37.0	38.7
	Displacement at mid-span (mm)	1.78	1.88	1.86	1.82	1.83
	Maximum strain of the soffit plate($\mu\varepsilon$)	792	646	478	514	508
	Critical crack width (mm)	0.05	0.07	0.05	0.03	0.03
Initiation of yielding of steel tension bars	Maximum moment of the beam (kN.m)	108.1	110.0	115.2	115.4	115.3
	Displacement at mid-span (mm)	12.0	15.0	16.4	16.0	14.6
	Maximum strain of the soffit plate ($\mu\varepsilon$)	3531	3944	3453	3752	3155
	Critical crack width (mm)	0.12	0.36	0.23	0.30	0.33
Beam failure	Maximum moment of the beam (kN.m)	132.2	138.1	143.6	151.1	156.7
	Displacement at mid-span (mm)	20.4	25.8	30.0	29.4	28.6
	Maximum strain of the soffit plate ($\mu\varepsilon$)	5970	6810	6675	6773	6839
	Critical crack width (mm)	/	0.56	/	/	/
	Concrete strain ($\mu\varepsilon$)	-1724	-1538	-1307	-1808	-1759
Failure mode		IC debonding	IC debonding	IC debonding	IC debonding	IC debonding

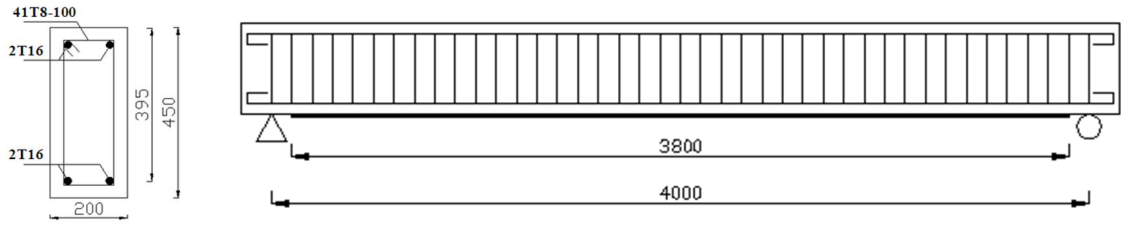

Figure 3.1 Geometry of test specimens

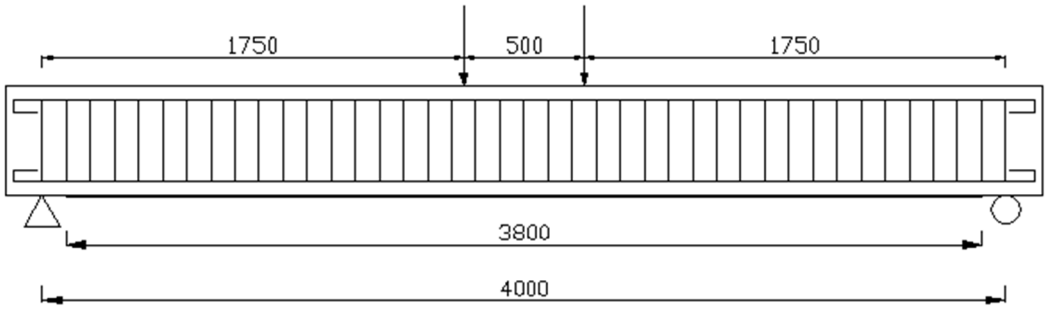

(a) Loading pattern of Specimen LP2SP1750

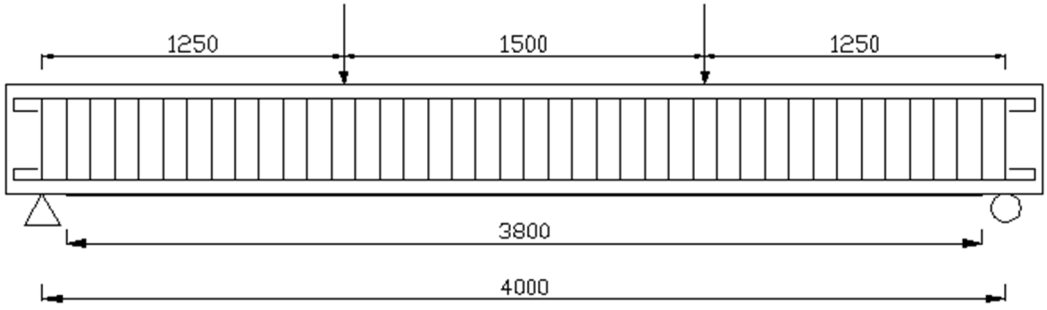

(b) Loading pattern of Specimen LP2SP1250

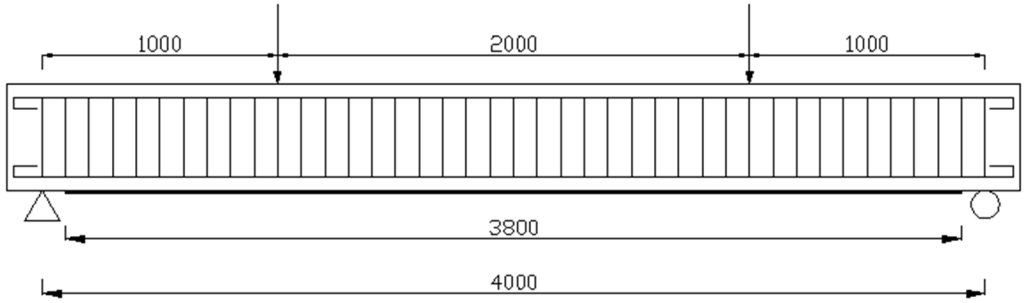

(c) Loading pattern of Specimen LP2SP1000

Figure 3.2 Loading patterns of Series I specimens

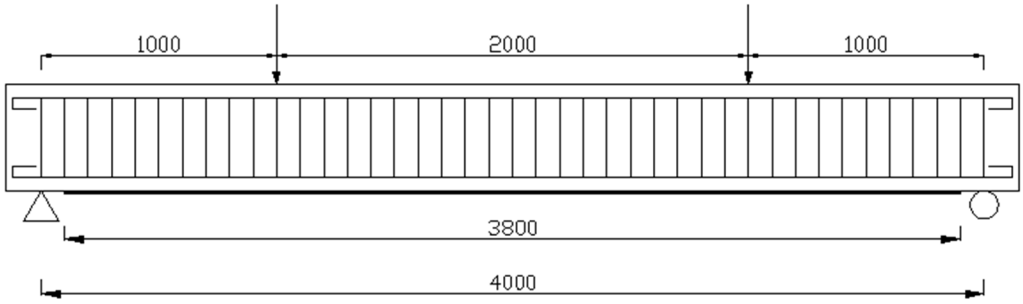

(a) Loading pattern of Specimen LP2SP1000

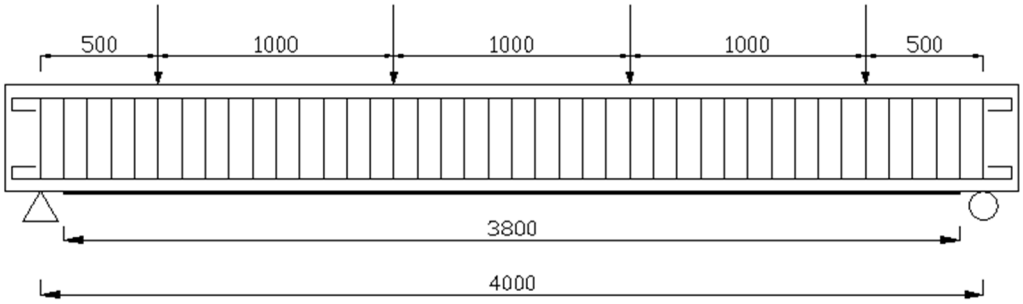

(b) Loading pattern of Specimen LP4SP1000

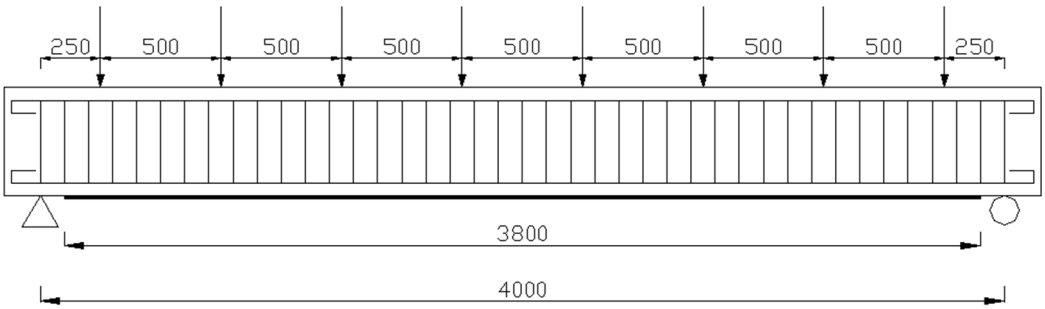

(c) Loading pattern of Specimen LP8SP1000

Figure 3.3 Loading patterns of Series II specimens

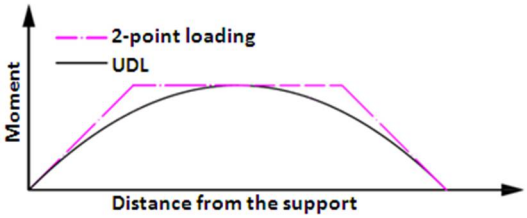

Bending moment diagram for Specimen LP2SP1000

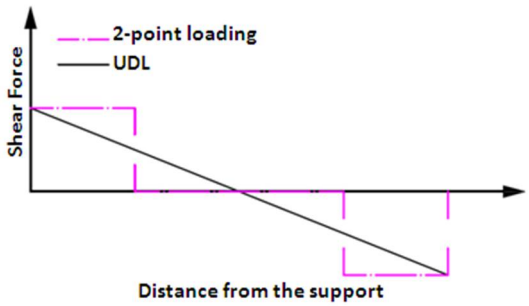

Shear force diagram for Specimen LP2SP1000

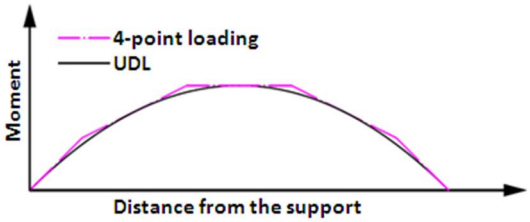

Bending moment diagram for Specimen LP4SP1000

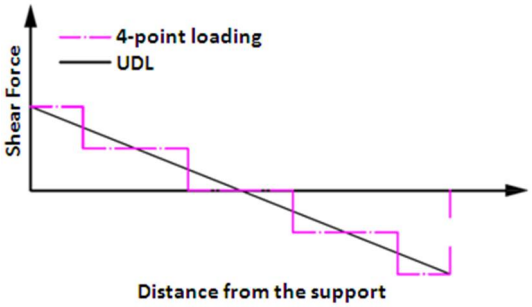

Shear force diagram for Specimen LP4SP1000

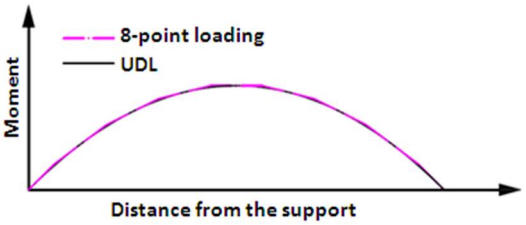

Bending moment diagram for Specimen LP8SP1000

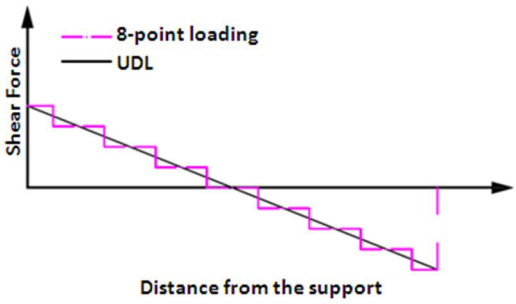

Shear force diagram for Specimen LP8SP1000

Figure 3.4 Shear force and bending moment diagrams for Series II specimens

(a) Specimen LP4SP1000 under four-point loading

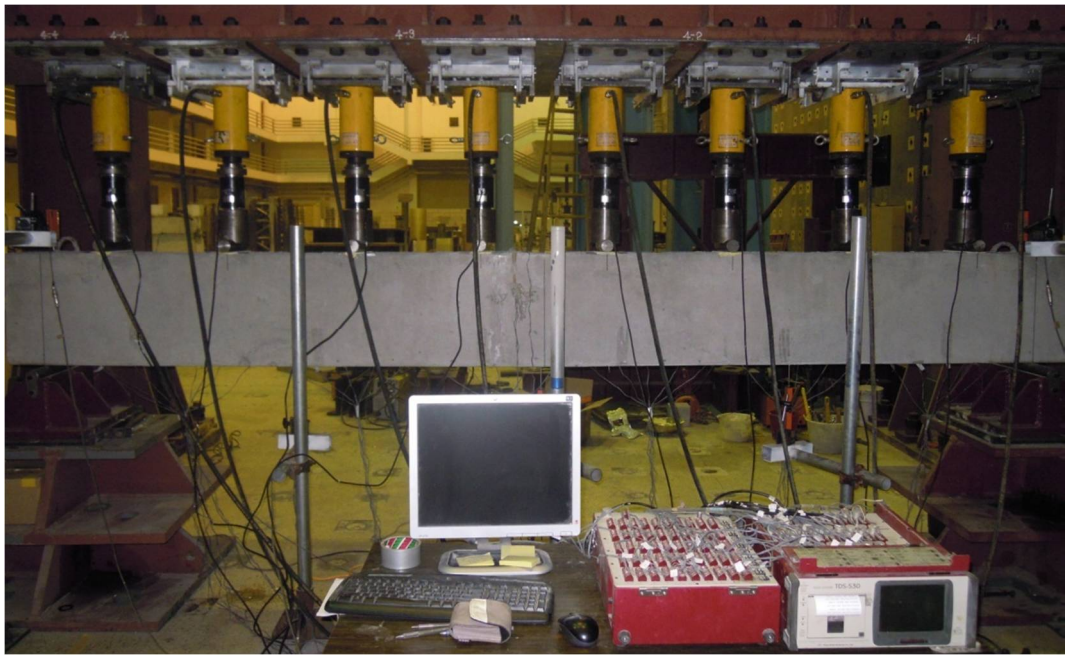

(b) Specimen LP8SP1000 under eight-point loading

Figure 3.5 Experimental set-ups for specimens under multi-point loading

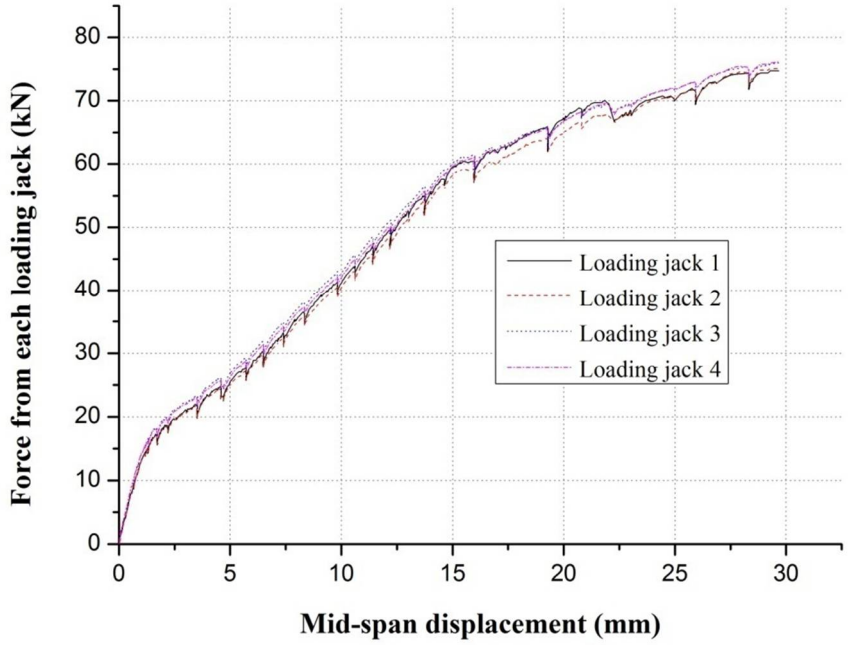

(a) Specimen LP4SP100

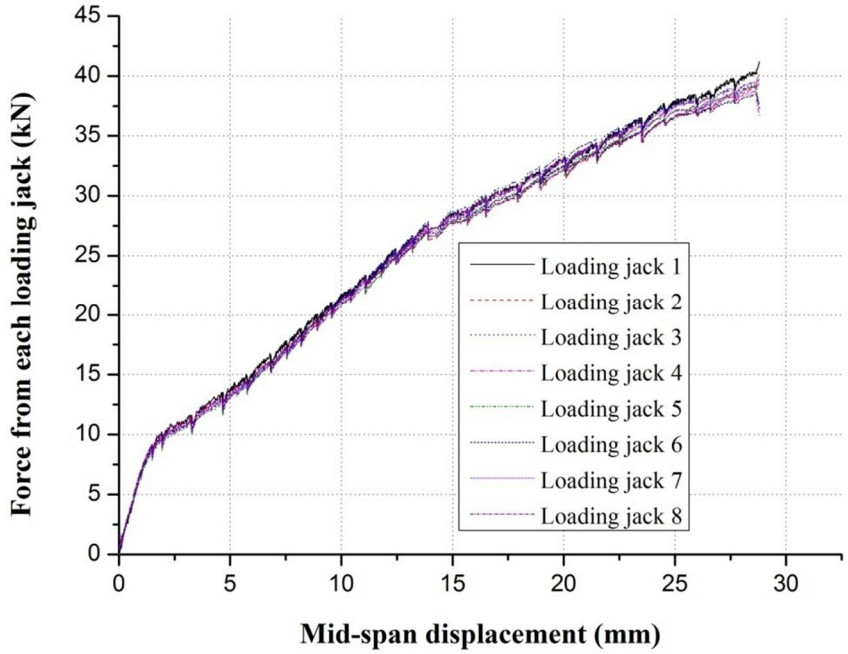

(b) Specimen LP8SP1000

Figure 3.6 Loads from loading jacks

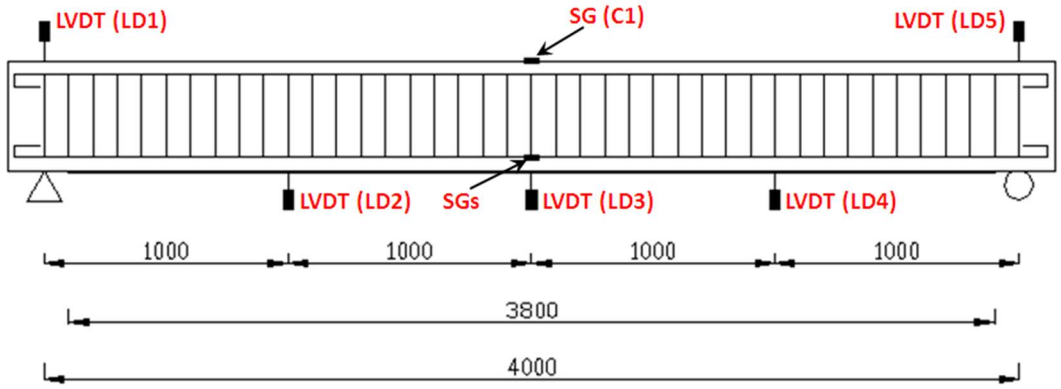

Figure 3.7 Positions of LVDTs and strain gauges on concrete and steel bars

Figure 3.8 Installation of LVDTs

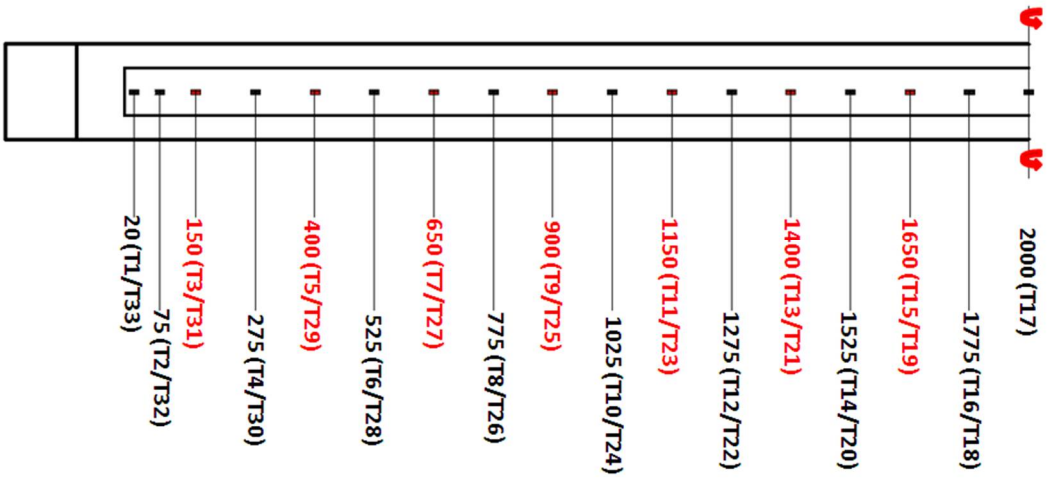

Figure 3.9 Positions of strain gauges on the soffit plate

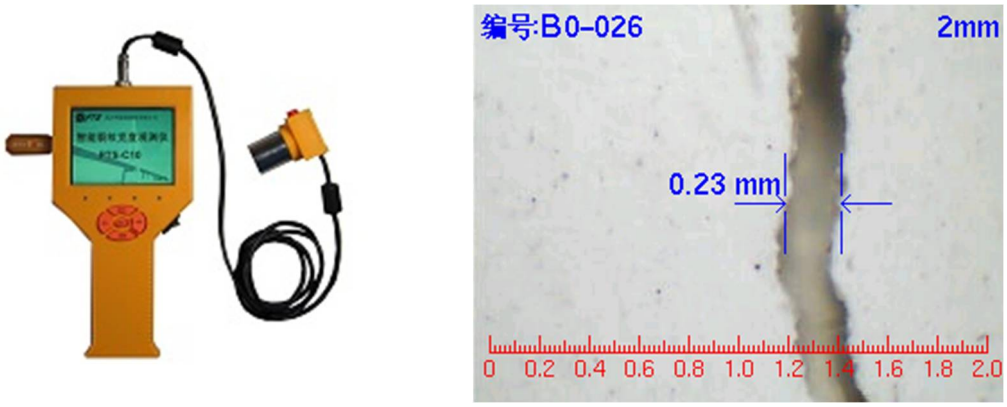

(a) Measurement device (b) Measurement example

Figure 3.10 Crack width measurement

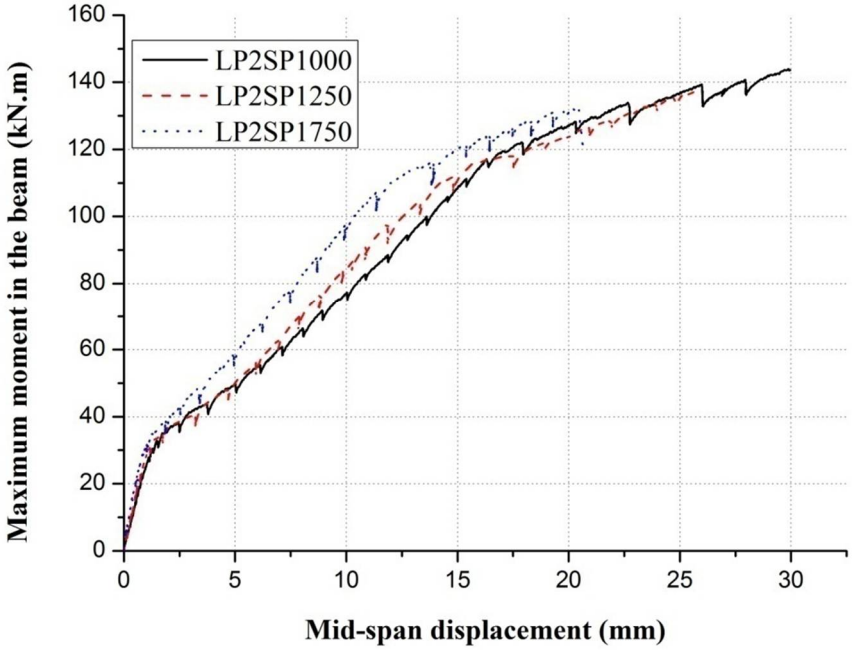

(a) Series I: effect of the sear span

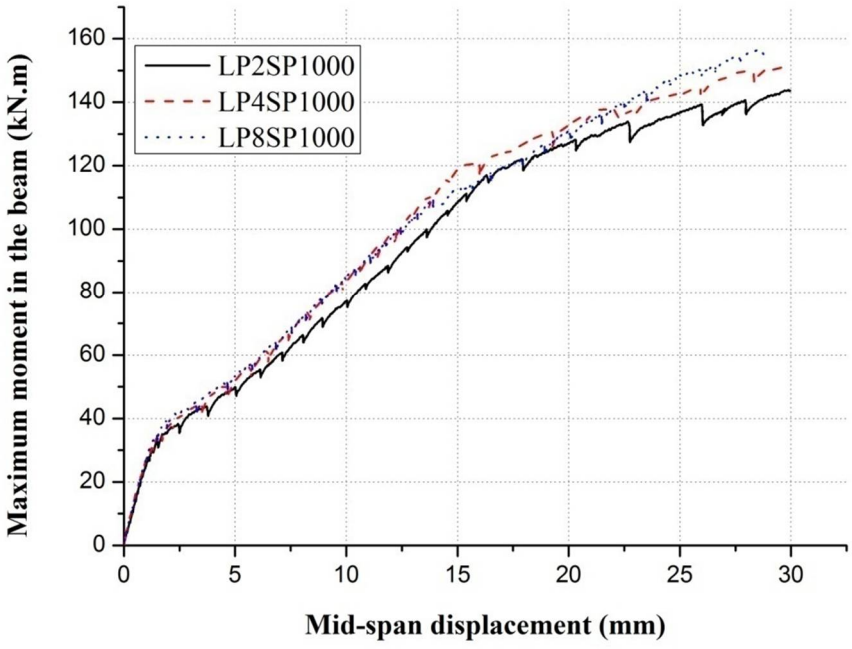

(b) Series II: effect of the load uniformity

Figure 3.11 Moment-deflection curves of beams under different loading distributions

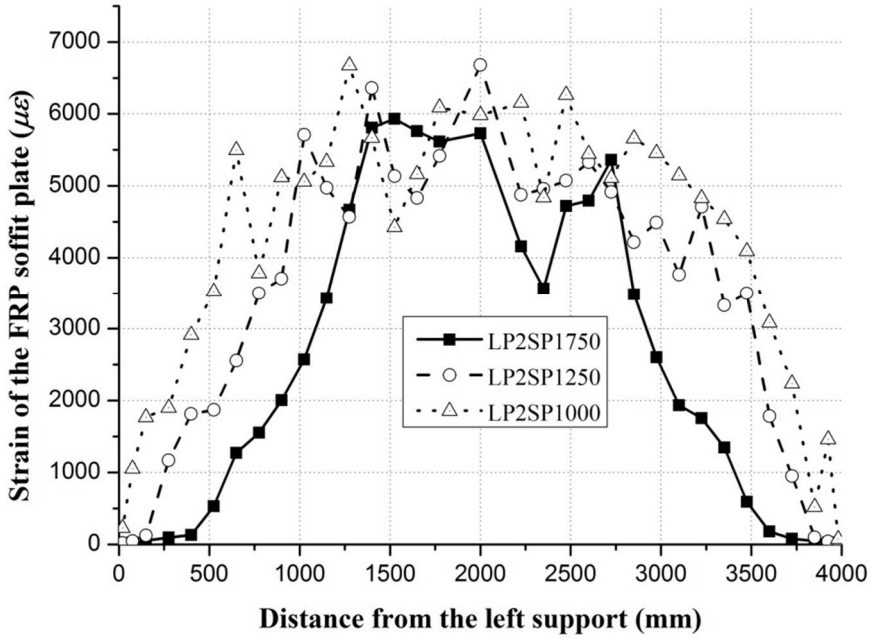

Figure 3.12 Strain distributions at failure of specimens in Series I

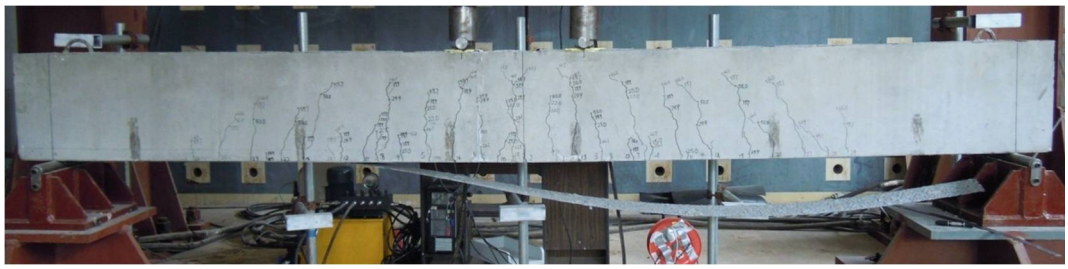

(a1) Failure mode of Specimen LP2SP1750

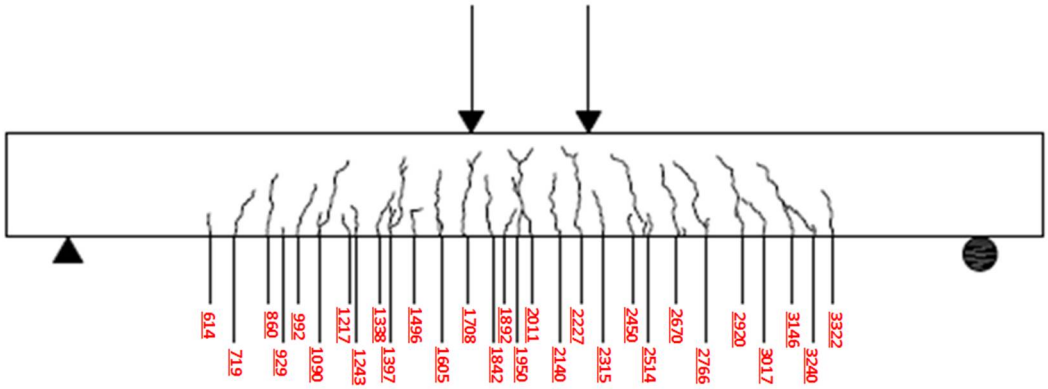

(a2) Crack pattern of Specimen LP2SP1750

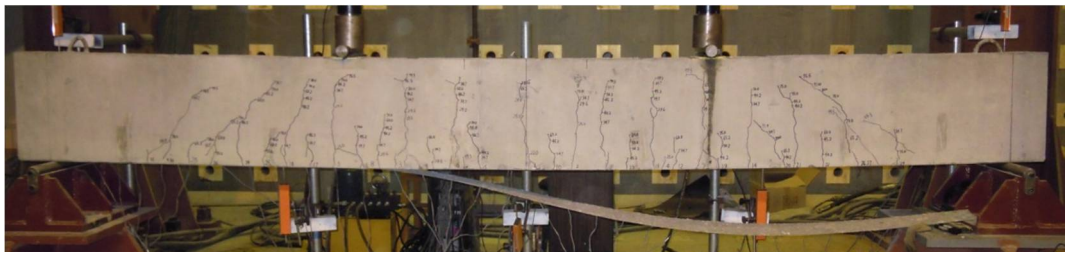

(b1) Failure mode of Specimen LP2SP1250

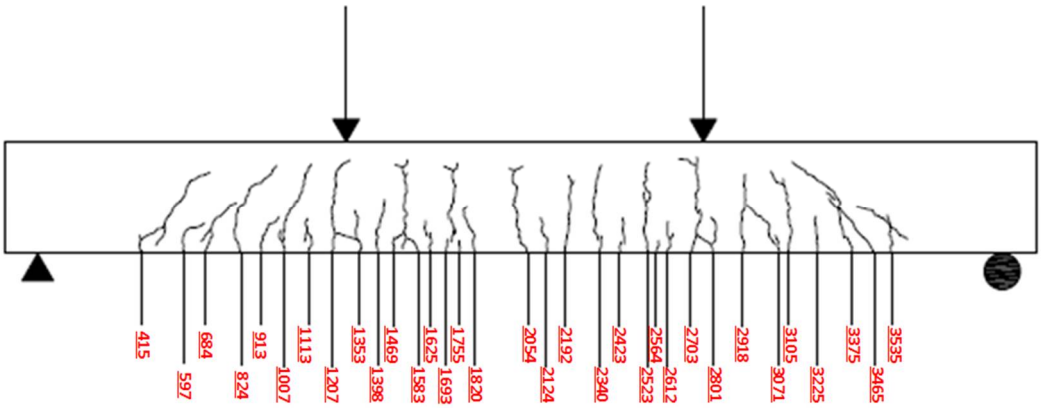

(b2) Crack pattern of Specimen LP2SP1250

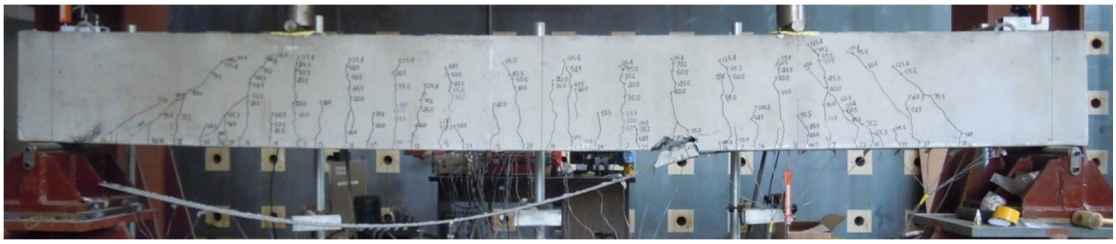

(c1) Failure mode of Specimen LP2SP1000

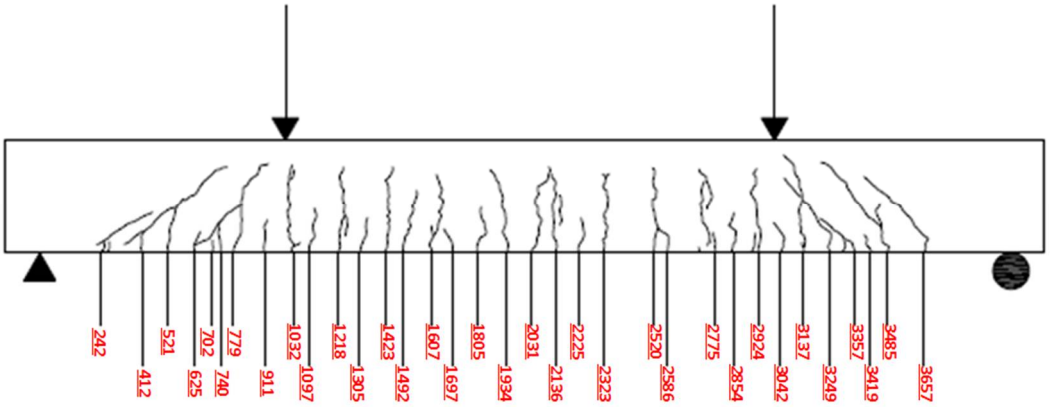

(c2) Crack pattern of Specimen LP2SP1000

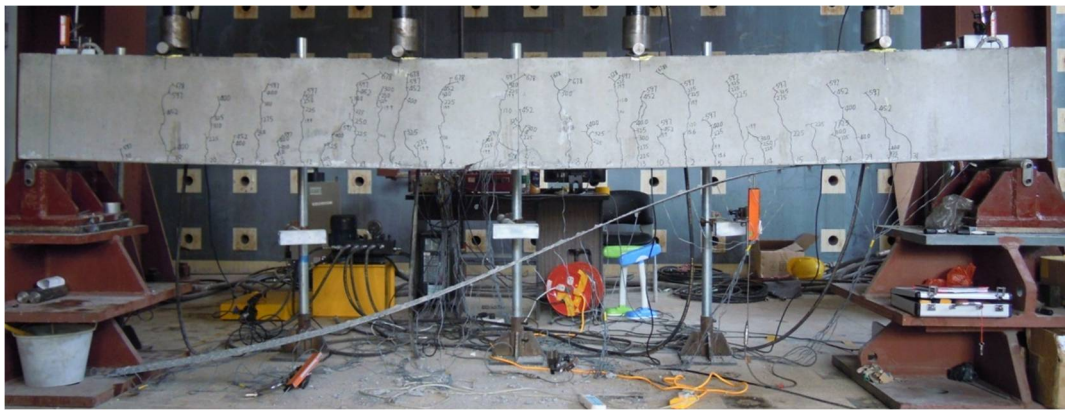

(d1) Failure mode of Specimen LP4SP1000

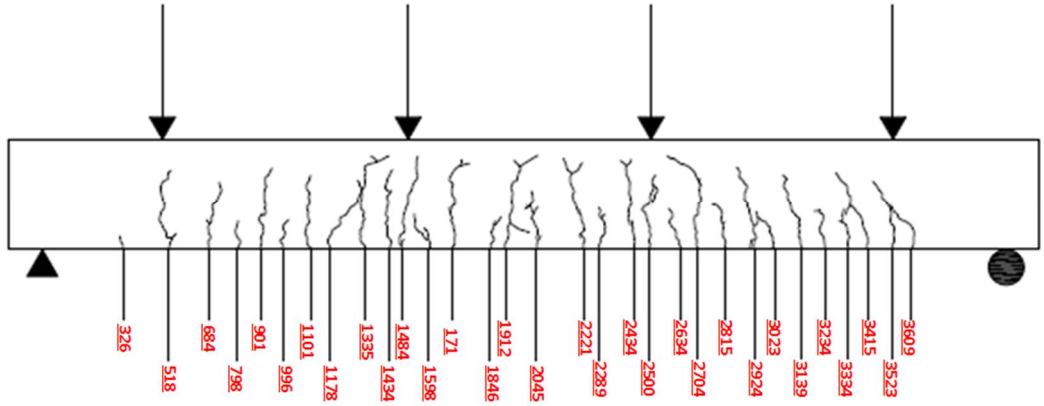

(d2) Crack pattern of Specimen LP4SP1000

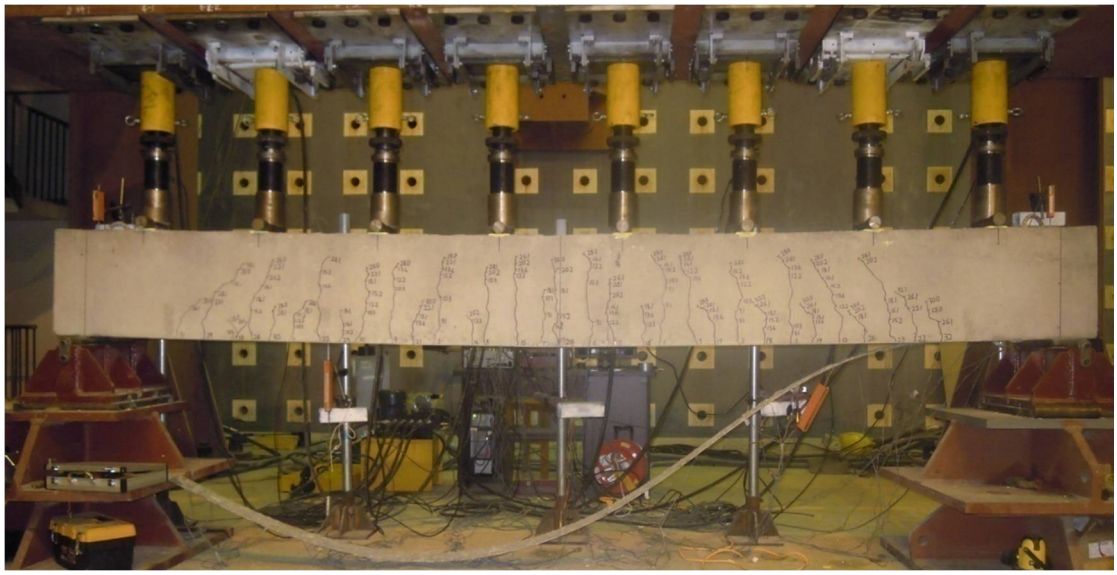

(e1) Failure mode of Specimen LP8SP1000

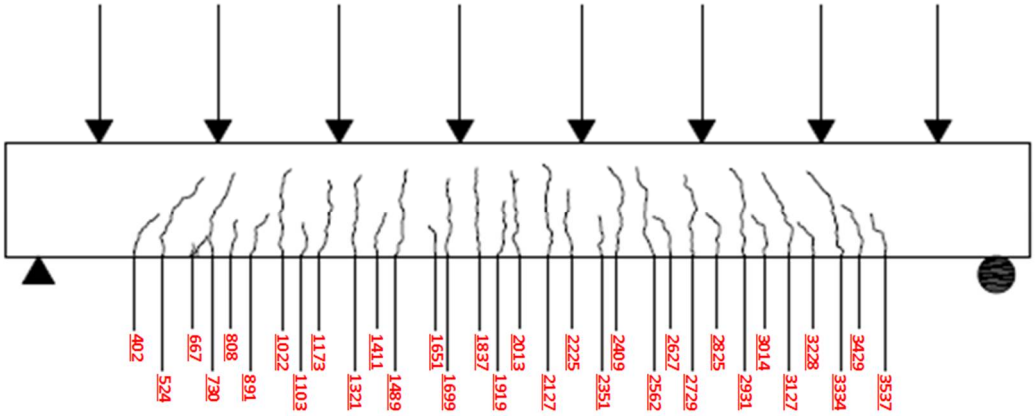

(e2) Crack pattern of Specimen LP8SP1000

Figure 3.13 Failure modes and crack patterns of test beams

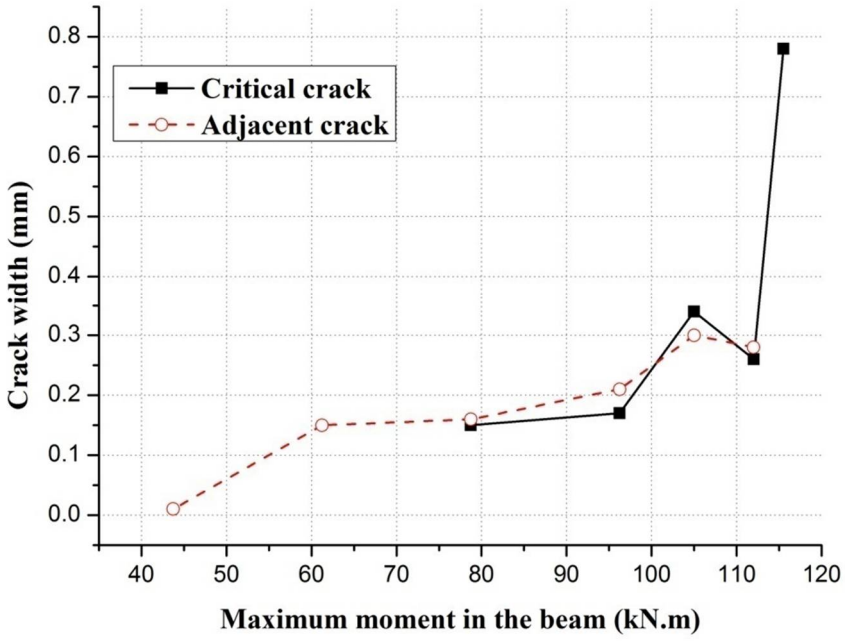

(a) Development of critical crack and adjacent crack in Specimen LP2SP1750

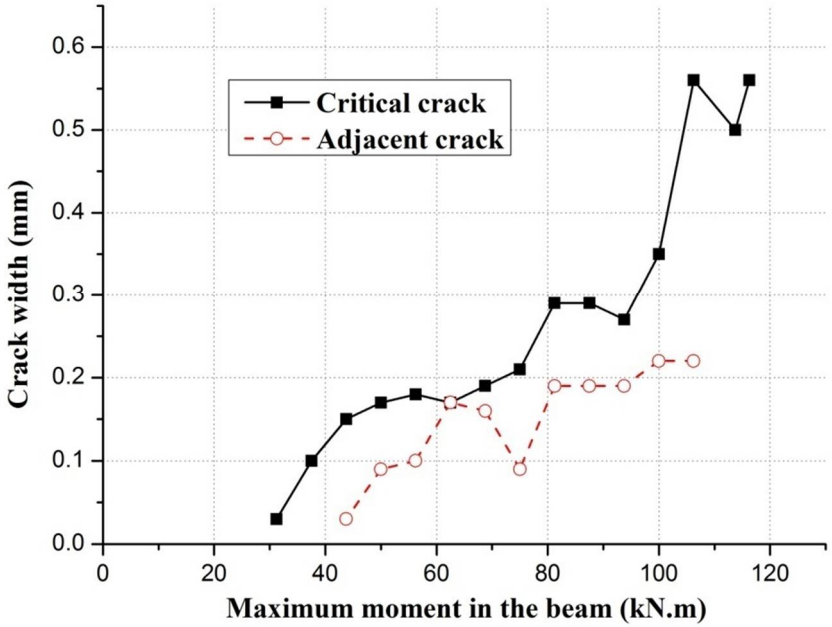

(b) Development of critical crack and adjacent crack in Specimen LP2SP1250

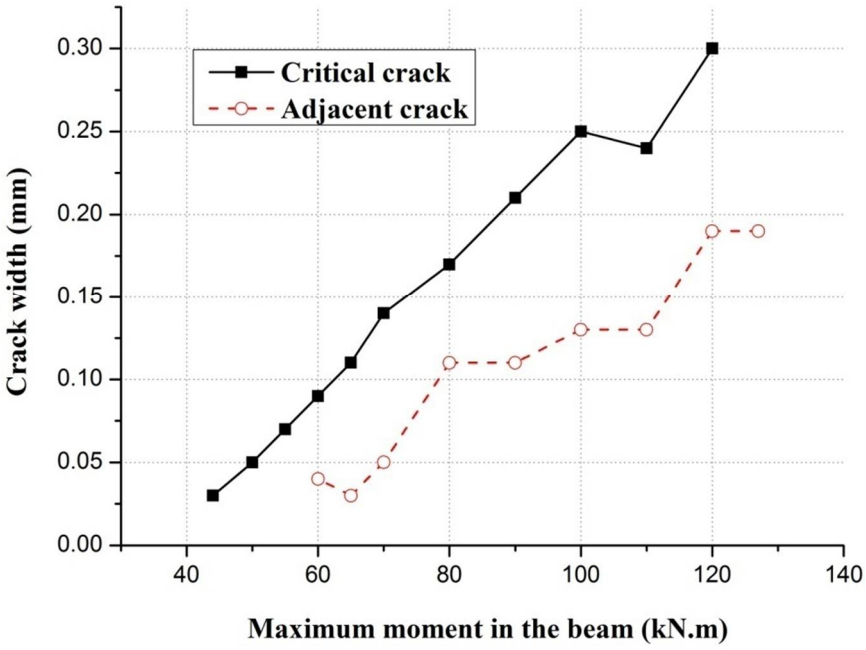

(c) Development of critical crack and adjacent crack in Specimen LP2SP1000

Figure 3.14 Development of critical crack and adjacent crack in specimens of Series I

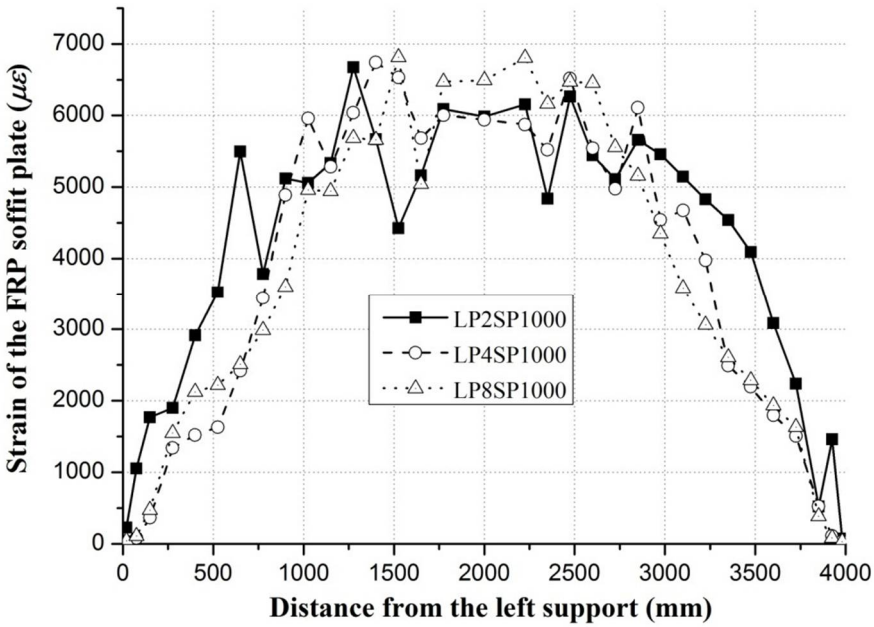

Figure 3.15 Strain distributions at failure in specimens of Series II

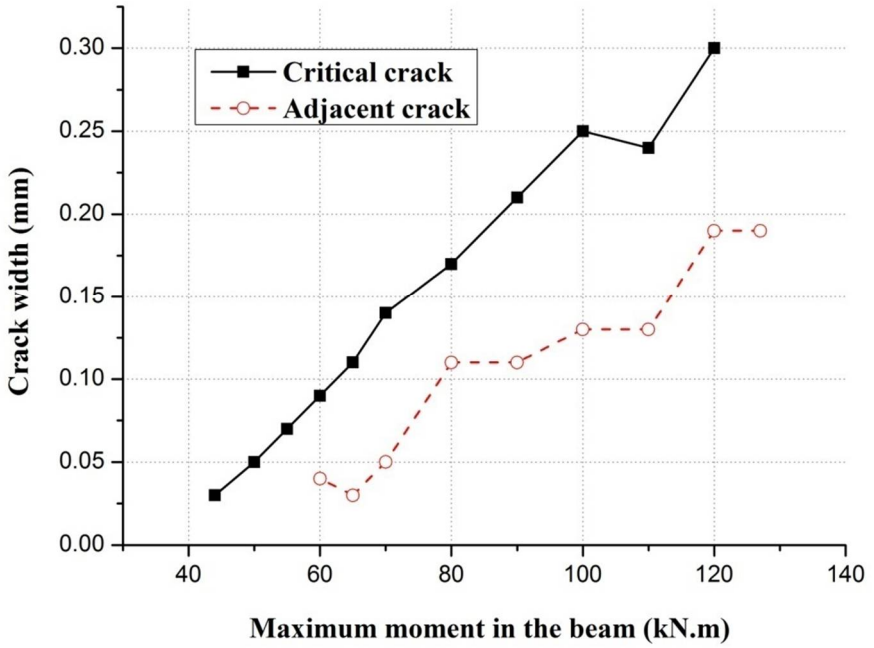

(a) Development of critical crack and adjacent crack in Specimen LP2SP1000

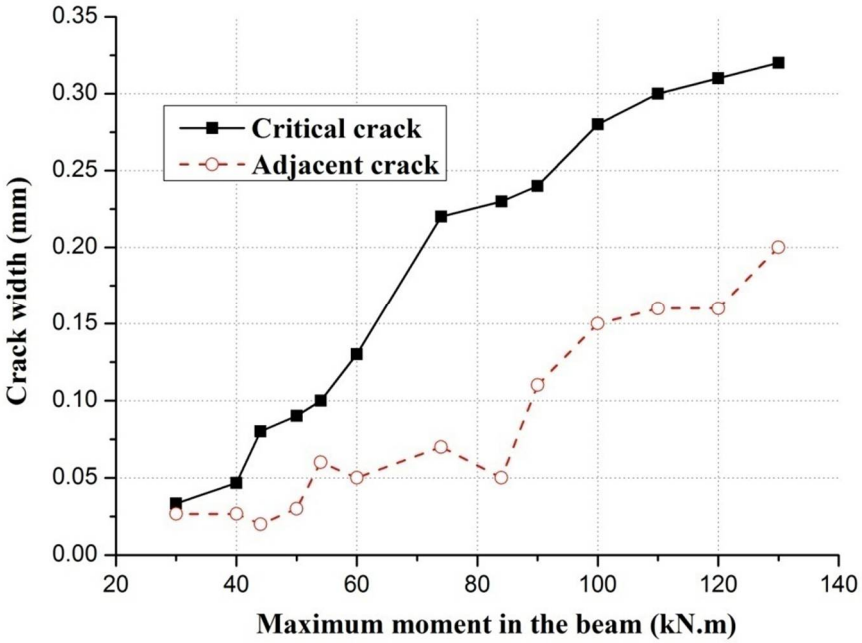

(b) Development of critical crack and adjacent crack in Specimen LP4SP1000

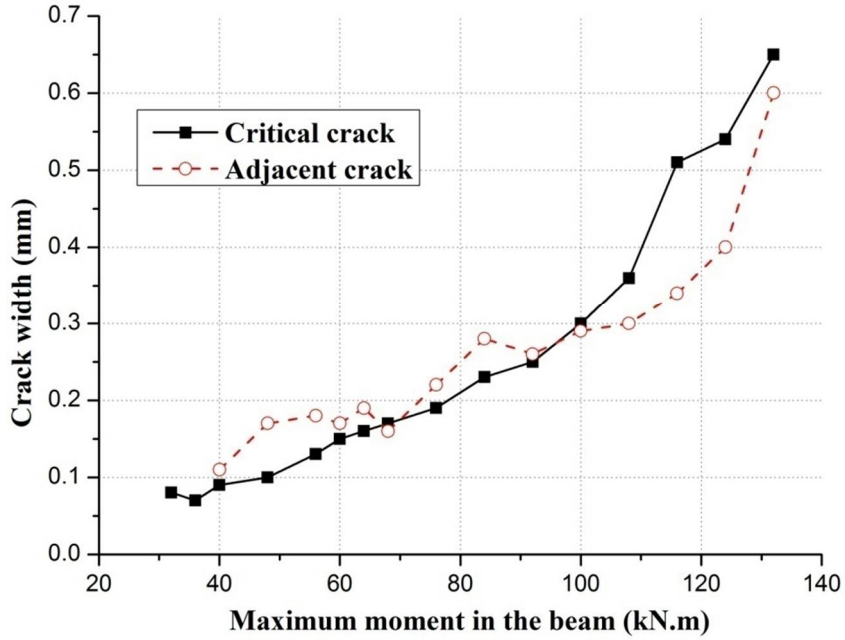

(c) Development of critical crack and adjacent crack in Specimen LP8SP1000

Figure 3.16 Development of critical crack and adjacent crack in specimens of Series II

APPENDIX 3.1

WET-LAYUP PROCEDURE FOR THE BONDING OF CARBON FIBRE SHEETS

A reliable bond between FRP and concrete is essential to achieve the prescribed performance of FRP-plated RC beams. In order to achieve such a reliable bond, the bonding procedure (wet-layup procedure) for fibre sheets to form FRP plates must be conducted following a standard process. In this appendix, the bonding process for fibre sheets to form FRP plates, which was adopted based on trials in the present research programme as well as procedures suggested in guidelines (ACI 440R-08 2008; TR55 2010) is presented in this appendix.

The wet-layup procedure to form FRP plates must be carried out by a competent contractor and follow a proper process to ensure that the application of a wet layup FRP system is carried out in a manner that assures high quality adhesion of epoxy. This procedure includes the preparation of concrete surface, application of primer to concrete substrate, wet layup of FRP system, and curing of impregnating resin

(Figure A3.1.1). Each of the steps is described in detail as follows.

The installation of wet layup FRP plates requires unique equipment, which includes a jet gun for profiling the concrete surface, a high-pressure water jet used for cleaning the concrete surface after its profiling, a high-pressure air jet for removing dust and loose particles before the application of primer, an electronic mixer for mixing the two-part resin, a brush for distributing the resin onto the concrete surface and the fibre sheets, and rollers to evenly distribute the resin over the fibre sheets. All equipment should be cleaned immediately after use using a suitable solvent, or the cured materials should be mechanically removed. Protective equipment (e.g. coveralls, masks and gloves) should be used during the whole procedure of applying the wet layup FRP system to protect the personnel for installation of FRPs. All these equipment for applying the wet layup FRP system should be prepared in sufficient quantity in advance to ensure the continuity of installation of the wet layup system.

Step 1a: ***Preparation of concrete surface***

Concrete surface preparation of a good quality is the prerequisite to achieve a reliable bond between FRP and concrete. The concrete surface for bonding of FRPs should be freshly prepared and loose or unsound materials should be removed from the concrete surface. Surface imperfections (e.g. concave surfaces, inside corners, obstructions and embedded objects) should be addressed. Small voids in surface should be first exposed during surface preparation and then be filled with primer.

Surface preparation can be accomplished using a jet gun driven by compressed air with a pressure of about 0.7 MPa as shown in Figure A3.1.2. After profiling the concrete surface using the jet gun, the dust and loose materials on the concrete surface should be removed using high pressure water, and then the prepared concrete surface should be left to dry in a dry condition for at least one day.

Step 1b: ***Cutting of the fibre sheet into desired dimensions***

Before beginning the wet layup process, fibre sheets of desired dimensions should be cut from larger fibre sheets. Cutting of fibre sheets should be done with care to avoid damaging the fibres.

Step 2: Application of primer

Before applying the primer, dust as well as loose materials must be removed from the concrete surface to protect the primer from these contaminants. In the tests of the present research project, the primer was formed in two parts with a mixing ratio of approximately 100: 34.5 by weight. These two parts after being poured into a clean container must be mixed for a short period (at least for the primer used in the tests of the present research project) at low speed (i.e. max. 600 rpm) (Figure A1.3). During the mixing of primer, aeration should be avoided. The primer should then be uniformly distributed using a brush to the concrete surface for bonding the fibre sheets prescribed by the manufacturer (Figure A3.1.4). The placement of the fibre sheets should be conducted within the open hour of the primer. In the tests of the

present research project, the wet layup process had to be completed in its open hour of the primer, which was specified by the manufacturer.

Step 3: Wet layup FRP systems

Wet layup FRP systems can be applied by hand with a brush to ensure that the fibre sheets are properly impregnated with the epoxy resin (i.e. adhesive). Two-thirds of the expected amount of resin should be applied on the side of the fibre sheet to be in touch with the concrete surface and the concrete surface itself for bonding of the FRP sheets before placing the fibre sheet (Figure A3.1.5). The other one-third of the expected amount of resin should then be uniformly distributed onto the other side of the fibre sheet. A roller should be used to roll over the fibre sheet to achieve full saturation of the fibre sheet with resin and to force out any trapped air and excess amount of resin (Figure A3.1.6). Successive layers should be applied repeating the above procedure and should be placed within the open time of adhesive or otherwise after complete curing of the resin (Figures A3.1.7). If previous layers are cured, preparation for interlayer surface (e.g. light sanding or solvent application) may be required.

The straightness of fibre material (i.e. the fibre orientation be less than five degree) should be ensured by being handled with care, as the intended direction of fibre alignment can cause a substantial reduction in strength and modulus.

Step 4: Resin curing

After application, the newly installed wet layup FRP plates must be protected for at least 24 hours from rain or water of any kind. Ambient-cure resins can take several days to reach full cure. However the exactly time for resin curing is highly dependent on the temperature. Temperature variations can affect the resin curing time.

REFERENCES

ACI 440.2R-08 (2008). *Guide for the Design and Construction of Externally Bonded FRP Systems for Strengthening Concrete Structures*, ACI Committee 440, American Concrete Institute, Farmington Hills, MI, USA.

Concrete Society (2012). *Design guidance for strengthening concrete structures using fibre composite materials*, Concrete Society Technical Report No. 55, Crowthorne, UK.

FIGURES

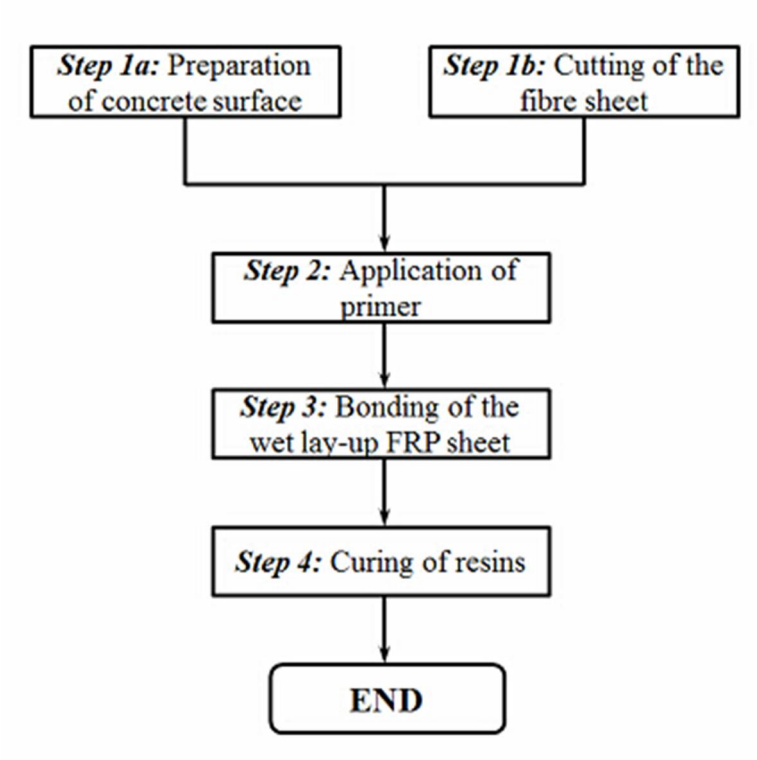

Figure A3.1.1 Procedure of bonding a wet layup FRP sheet

Figure A3.1.2 Profiling the concrete surface with a jet gun

Figure A3.1.3 Mixing of primer or resin

Figure A3.1.4 Application of primer

Figure A3.1.5 Distributing resin onto the fibre sheet

Figure A3.1.6 Slowly moving the roller to saturate the fibre sheet fully and force out excessive resin and trapped air

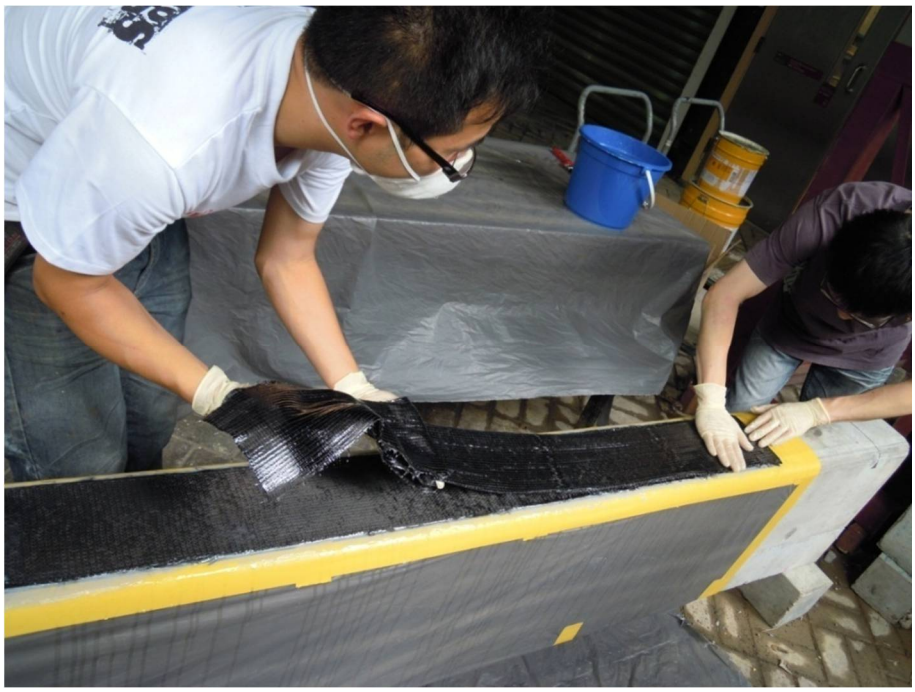

Figure A3.1.7 Application of successive layers of fibre sheets

CHAPTER 4

EFFECT OF LOAD DISTRIBUTION ON IC DEBONDING: FINITE ELEMENT STUDY

4.1 INTRODUCTION

Although tailor-made laboratory experiments can be conducted to investigate the behaviour of intermediate crack (IC) debonding for different load distributions as demonstrated in Chapter 3, finite element (FE) analysis provides a more convenient way to investigate the behaviour of IC debonding for different load distributions. This is because in an FE analysis, different load distributions [e.g. uniformly distributed load (UDL)] can be easily applied and the effects of various other factors (such as beam size and steel reinforcement ratio) can be easily investigated with much less cost compared to an experimental study. This chapter presents an FE investigation into the effect of load distribution on IC debonding.

For the FE analysis of IC debonding, Chen et al. (2011) developed an FE approach capable of accurately predicting not only the IC debonding failure but also the

full-range failure process of the FRP-plated RC beam. This FE approach takes the following factors into account to predict IC debonding accurately: (1) a proper constitutive model for cracked concrete; and (2) proper modelling of bond behaviour between concrete and, both steel bars and FRP. Accurate modelling of these factors is essential for the accurate simulation of IC debonding behaviour in FRP-plated RC beams. Furthermore, the approach adopts a dynamic solution method (Chen 2010), which can effectively avoid convergence problems originating from concrete cracking and different forms of interfacial debonding (between concrete and FRP/steel reinforcement). Teng et al. (2010) extended the FE approach of Chen et al. (2011) to predict IC debonding of FRP-plated RC beams under different load distributions. Although the FE analysis of Teng et al. (2010) was shown to provide close predictions of the test results (only small-scale beam specimens were available then), a load control solution scheme was adopted in the FE analysis. It has been well established that a load control solution scheme has its limitation in overcoming the limit load (Clarke and Hancock 1990). If a dynamic solution method such as that used in Chen (2010) is employed with a load control scheme, the analysis may overcome the limit load; however, as the solution process is usually associated with snap-through effects, a significant dynamic effect may arise upon IC debonding failure, which, if not carefully controlled, may lead to overshooting of the ultimate load. Against the above background, Chen et al.'s (2011) approach has been augmented in the present study by using a novel displacement control scheme to capture the whole debonding process of FRP-plated RC beams especially for multi-point loading (i.e. number of loading points > 2). This displacement-based load control method for multi-point loading was achieved using an imaginary rigid beam

system with constraint equations (ABAQUS 2004).

In the remainder of this chapter, the validity of the displacement-based load control method is first demonstrated using a numerical example. The augmented FE approach is then verified using the tests presented in Chapter 3 together with existing tests from the literature. The verification indicates that the augmented FE approach is capable of accurately simulating IC debonding of FRP-plated RC beams under different load distributions. A parametric study is then presented to examine the effects of various other factors on IC debonding, and the numerical results from the parametric study can be used to supplement the limited test data for the evaluation of the accuracy of existing IC debonding strength models for different load distributions.

4.2 FE APPROACH

4.2.1 General

As mentioned above, in the FE approach of Chen et al. (2011), three key factors (e.g. modelling of cracked concrete, FRP-to-concrete interfaces, and steel bar-to-concrete interfaces) were appropriately considered to capture localized flexural cracks to achieve accurate prediction of IC debonding in FRP-plated RC beams. A novel displacement-based load control technique to cater to multi-point loading (i.e. number of loading points > 2) is adopted in the augmented FE approach of the present chapter, and is used together with the three key factors considered in Chen et

al.'s (2011) model for accurately predicting IC debonding in FRP-plated RC beams under different load distributions. As with Chen et al. (2011), the dynamic solution method of Chen (2010) is used to overcome convergence problems originating from the concrete cracking and different forms of interfacial debonding (between concrete and FRP/steel reinforcement). The whole FE approach is briefly presented next in this section [more details can be found in Chen (2010) and Chen et al. (2011)] but in the part on the displacement-based load control method, a much more detailed description is given for ease of understanding by the reader.

This FE approach was implemented in the general purpose FE package ABAQUS (2004).The concrete was simulated using plane stress elements (element CPS4 in ABAQUS), and both steel bars and the FRP soffit plate were represented by truss elements (element T2D2 in ABAQUS). Bond between the concrete and both the steel bars and the FRP plate was simulated using cohesive elements (element COH2D4 in ABAQUS).The constitutive models for different components of FRP-plated RC beams are briefly reported in the following sub-sections while more details can be found in Chen et al. (2011).

4.2.2 Modelling of concrete

Accurate modelling of the behaviour of cracked concrete is one of the essential parts for the accurate modelling of IC debonding in FRP-plated RC beams (Chen et al. 2011). In the present study, the accurate modelling of the concrete cracking behaviour was realized via the crack band model (Bazant and Planas 1998) in which

the opening of concrete cracks is controlled by the fracture energy of concrete to overcome the mesh sensitivity problem associated with the conventional smeared crack model (Rots 1988). With this approach, a stress-cracking displacement response instead of a stress-strain response is used to characterize the cracking behaviour of the concrete to allay the mesh sensitivity problem in ABAQUS [see Lubliner et al. (1989) and Lee (1996) for more details].

The following equation for the stress-strain behaviour of concrete under uniaxial compression proposed by Saenz (Eq. 4.1) used the CDPM of ABAQUS to model the compression-dominated behaviour of concrete:

$$\sigma = \frac{\alpha\varepsilon}{1 + \left[\left(\alpha\varepsilon_p/\sigma_p\right) - 2\right]\left(\varepsilon/\varepsilon_p\right) + \left(\varepsilon/\varepsilon_p\right)^2} \tag{4.1}$$

where σ_p is set to be equal to the cylinder compressive strength of concrete f_c; ε_p is the concrete strain when the concrete reaches its compressive strength and is set to be equal to 0.002; α is the initial elastic modulus of concrete and can be approximated from the concrete compressive strength [e.g. $E_c = 4730\sqrt{f_c^{'}}$ in ACI (2008)].

For cracked concrete under uniaxial tension, the tension-softening curve following the initial linearly elastic branch can be represented using the following equation proposed by Hordijk (1991):

$$\frac{\sigma_t}{f_t} = \left[1 + \left(c_1 \frac{w_t}{w_{cr}}\right)^3\right] e^{\left(-c_2 \frac{w_t}{w_{cr}}\right)} - \frac{w_t}{w_{cr}}(1 + c_1^3) e^{(-c_2)} \quad (4.2a)$$

$$w_{cr} = 5.14 \frac{G_F}{f_t} \quad (4.2b)$$

where w_t is the crack opening displacement; w_{cr} is the crack opening displacement at the complete release of concrete stress; G_F is the concrete fracture energy (i.e. the area covered by the strain-stress curve of concrete under uniaxial tension); c_1 and c_2 are constants determined from tensile tests of concrete and are set to be 3.0 and 6.93 respectively, for normal concrete. f_t and G_F can be estimated from the cylinder compressive strength based on the equations in CEB-FIP (1993), if no specific tests are provided for the determination of values of these two parameters.

$$f_t = 1.4 \left(\frac{f_c - 8}{10}\right)^{(2/3)}, \qquad \text{MPa} \quad (4.3)$$

$$G_F = (0.0469 d_a^2 - 0.5 d_a + 26) \left(\frac{f_c}{10}\right)^{0.7}, \qquad \text{Nm/m}^2 \quad (4.4)$$

where d_a represents the maximum aggregate size, which can be assumed to be 20 mm if no test data is available.

In this FE approach, the degradation of elastic stiffness of concrete, *d*, as cracks widen is assumed to be isotropic and defined by Eq. 4.5

$$D^{el} = (1 - d) D_0^{el} \qquad 0 \le d \le 1 \quad (4.5)$$

where d is the degradation parameter; D^{el} is the elastic stiffness; D_0^{el} is the initial

elastic stiffness. The damage propagation in uniaxial tension is defined using a user-defined damage curve for the damage parameter, *d,* given by Eq. 4.9.

After the cracking of concrete, its behaviour can be described by the following relationships. The cracking strain of concrete is defined as

$$\varepsilon_t^{cr} = \varepsilon_t - \varepsilon_t^{el} \tag{4.6}$$

in which ε_t is the total strain of concrete; ε_t^{el} is the elastic strain of concrete.For damaged concrete with plasticity, the plastic strain, ε_t^{pl}, is defined by the following equation.

$$\varepsilon_t^{pl} = \varepsilon_t - \varepsilon_{t,d}^{el} \tag{4.7}$$

where $\varepsilon_{t,d}^{el}$ is the elastic damage strain as illustrated in Figure 4.1 and defined by Eq. 4.8.

$$\varepsilon_{t,d}^{el} = \frac{\sigma_t}{(1-d_t)E_c} \tag{4.8}$$

In the present FE approach, the plastic strain, ε_t^{pl}, is assumed to be zero; based on this assumption the tensile damage parameter (d_t) can be expressed in terms of the cracking strain (ε_t^{cr}) or crack opening displacement (w_t) by Eqs 4.9a and 4.9b respectively [see Chen et al. (2011) for details].

$$d_t = \frac{\varepsilon_t^{cr}}{(\varepsilon_t^{cr} + \sigma_t/E_c)} \tag{4.9a}$$

$$d_t = \frac{w_t}{[w_t + (h_c\sigma_t)/E_c]} \tag{4.9b}$$

The damage evolution curve can be obtained based on the preceding definition of

stress vs. cracking strain/crack opening displacement curve (Eq. 4.2) provided as input for ABAQUS.

4.2.3 Modelling of bond behaviour

The bond behaviour between concrete and both internal steel bars and external FRP reinforcement is simulated using cohesive elements (e.g. element COH2D4 in ABAQUS) based on proper bond-slip models. For the modelling of behaviour of FRP-to-concrete interfaces, three bond-slip models of different levels of sophistication have been proposed by Lu et al. (2005) based primarily on a meso-scale finite element study of FRP-to-concrete bonded joints. Their 'simplified model' is adopted in the present FE approach and is given by the following equations:

$$\tau = \tau_{max}\sqrt{s/s_0} \qquad for\ 0 \le s \le s_0 \tag{4.10a}$$

$$\tau = \tau_{max} e^{-\alpha(s/s_0 - 1)} \qquad for\ s > s_0 \tag{4.10b}$$

where τ_{max} is the maximum interfacial shear stress and is equal to $\alpha_1 \beta_w f_t$; the slip at the maximum interfacial shear stress $s_0 = 0.0195 \beta_w f_t$; the interfacial fracture energy $G_f = 0.308 \beta_w^2 \sqrt{f_t}$, in which the width ratio β_w is equal to $\sqrt{\frac{2 - b_f/b_c}{1 + b_f/b_c}}$ and α_1 is set to be 1.5 determined from data regression by Lu et al. (2005).

The modelling of bond behaviour of steel bars also plays a key role in predicting crack patterns of FRP-plated RC beams; it thus also significantly affects the prediction of IC debonding strength [see Chen et al. (2011) for details]. In the present

study, the bond-slip model for steel-to-concrete interfaces in CEB-FIP (1993) is used, which is given by:

$$\tau = \tau_{max}\left(s/s_0\right)^{\alpha} \qquad for\ 0 \le s \le s_0 \qquad (4.11a)$$

$$\tau = \tau_{max} \qquad for\ s_0 \le s \le s_1 \qquad (4.11b)$$

$$\tau = \tau_{max} - \left(\tau_{max} - \tau_f\right)\left(\frac{s - s_2}{s_3 - s_2}\right) \qquad for\ s_1 \le s \le s_2 \qquad (4.11c)$$

$$\tau = \tau_f \qquad for\ s_2 \le s \qquad (4.11d)$$

where $\alpha = 0.4$ (deformed bar), 0.5 (plain bar); s_1=s_2=0.6 mm; s_3=1.0 mm (deformed bar); s_1=s_2= s_3=0.1 mm (plain bar).

4.2.4 Solution strategy

Modelling of debonding problems in FRP-plated RC beams involves severe nonlinearity as a result of concrete cracking and FRP debonding. Convergence difficulties often a rise from concrete cracking and different forms of interfacial debonding [see Chen (2010) for more explanations]. In order to solve the convergence problem, a dynamic solution method (Chen 2010) based on an implicit time integration method, namely the Hilber-Hughes-Taylor α method (Hilber 1976), is adopted. A salient feature of this dynamic solution method is that the convergence difficulties arising from concrete cracking and interfacial debonding can be effectively overcome without compromising the accuracy of the numerical predictions due to the implicit nature (i.e. iterations in each load step ensure satisfactory accuracy) of the adopted time integration method [i.e. the HHT-α method (Hilber 1976)], as demonstrated by Chen (2010).

In an FE analysis, a load control scheme usually has difficulties in surpassing the limit load; as a result, a displacement control scheme is used to obtain structural responses with a load limit (Clarke and Hancock 1990). The displacement control scheme can be easily used to apply load to loading points of a simply-supported beam under three-point bending or four-point bending by taking advantage of symmetry (i.e. one loading point is involved), as demonstrated in Chen (2010) and Chen et al. (2011). However, the displacement control scheme can hardly be used to simultaneously apply loads with prescribed magnitudes to the loading points of abeam subjected to multi-point loading (i.e. number of loading points >2) due to the difficulty in identifying the relationship between displacements of different points during the loading process. In the present study, a novel displacement control scheme was proposed for exerting the required loads at multiple loading points (i.e. number of loading points >2) by applying the technique of constraint equations in ABAQUS (2004).

The idea of using constraint equations to apply multi-point loading is developed based on an assumed physical model detailed next. The accuracy of using the constraint equations to apply multi-point loading is demonstrated by a typical multi-point loading case in the next sub-section.

4.2.5 Loading scheme

4.2.5.1 Imaginary physical model

In a practical test, a whiffle-tree system is often used to apply multi-point loading although the accuracy of such a system in applying a prescribed load distribution can be compromised by the adverse effects of the lateral friction between the loading heads and the loaded structural member, which prevents the load-transferring rigid beams from free rotations (Pan et al. 2009). Theoretically, the accurate application of the prescribed loads can be achieved using the whiffle-tree system if the adverse effects from the lateral friction can be removed. The mechanism of the whiffle-tree system is therefore used to derive the constraint equations for multi-point loading. The typical whiffle-tree system shown in Figure 4.2 is used to illustrate how the constraint equations for the displacement of three loading points (e.g. P1, P2 and P3) can be derived; these constraint equations can then be extended to general cases including uniformly distributed loading (UDL) based on the same principle.

The derivation is based on moment equilibrium. In this whiffle-tress system, the load is directly applied at point 5 (e.g. P5) and transferred to the beam through points P1, P2, and P3 through the use of two rigid beams(namely rigid beam 1 and rigid beam 2 in Figure 4.2). To derive the required constraint equations, two additional assumptions are made: (1) no lateral friction exists; and (2) only small movements exist at loading points. The relationship among the displacements of the loading points, which relies on the relationship of forces at different points, can be established through moment equilibrium. Assuming that the forces at different loading points are so related that $F_1 : F_2 : F_3 = k_1 : k_2 : k_3$, the relationship among the displacements of loading points can be derived by utilizing equilibrium equations of the rigid beams. Here F_1, F_2 and F_3 are forces at the loading points P1, P2 and P3

respectively while k_1, k_2 and k_3 are constants used to prescribe the relationship among loads.

The equilibrium equations of rigid beam 1 are:

$$F_2 + F_3 + (-F_4) = 0 \tag{4.12}$$

$$F_2 \times L_2 - F_3 \times L_3 = 0 \tag{4.13}$$

where L_2 and L_3 are the lengths of lever arm for $F_2$and F_3 , respectively. The lever arms in Eqs 4.12 and 4.13 can be expressed as functions of displacements of the rigid beams:

$$L_2 = (u_2^y - u_4^y)/\tan(\theta) \tag{4.14}$$

$$L_3 = (u_4^y - u_3^y)/\tan(\theta) \tag{4.15}$$

in which θ is the rotation of rigid beam 1 from the horizontal axis; andu_2^y, u_3^y and u_4^y are the vertical displacements of rigid beam 1 at points P2, P3, and P4 respectively.

Substituting Eqs 4.14 and 4.15into Eq. 4.13 results in

$$F_2 \times (u_2^y - u_4^y) - F_3 \times (u_4^y - u_3^y) = 0 \tag{4.16}$$

As a result, the following vertical displacement relationship is obtained:

$$k_2 u_2^y + k_3 u_3^y = (k_2 + k_3) u_4^y \tag{4.17}$$

In the same way, the displacement relationship for points related to rigid beam 2 is as

follows:

$$k_1 u_1^y + (k_2 + k_3) u_4^y = (k_1 + k_2 + k_3) u_5^y \quad (4.18)$$

Substituting Eq.4.17 into Eq. 4.18 results in Eq. 4.19, thus eliminating the term u_4^y.

$$k_1 u_1^y + k_2 u_2^y + k_3 u_3^y = (k_1 + k_2 + k_3) u_5^y \quad (4.19)$$

For the general case of an N-point loading condition, if the force ratios $F_1 : F_2 : \cdots : F_n = k_1 : k_2 : \cdots : k_n$ are prescribed, the following displacement relationship should be imposed:

$$k_1 u_1^y + k_2 u_2^y + \cdots + k_n u_n^y = (k_1 + k_2 + \cdots + k_n) u_{n+1}^y \quad (4.20)$$

4.2.5.2 Verification of loading scheme

As explained above, simultaneous loading at different points can be numerically implemented according to Eq. 4.20 in the FE analysis. This equation is validated herein using a typical RC beam under 16-point loading. The dimensions of the beam are taken from Pan et al. (2009), and are as follows: the width, height and clear span of the beam are 150 mm, 200 mm, and 1800 mm, respectively. Two high yield steel bars of 10 mm in diameter and another two high yield steel bars of 8 mm in diameter are used as the tension steel bars and compression steel bars, respectively. Steel stirrups of 12 mm in diameter, at 80 mm centre-to-centre spacing are used as the shear reinforcement. Moreover, a 150 mm×1650 mm CFRP soffit plate is used to strengthen the beam. However, all components of the beam are assumed to be linearly elastic for the sake of computational efficiency. The elastic moduli of

concrete, steel bars and FRP plate are32.9 GPa, 235 GPa, and 202 GPa respectively according to the test data. By taking advantage of symmetry, only half of the beam with eight loading points was included in the FE analysis.

In order to achieve simultaneous, equal loading at the eight loading points, Eq. 4.21needs to be used.

$$u_1^y + u_2^y + u_3^y + u_4^y + u_5^y + u_6^y + u_7^y + u_8^y = 8u_9^y \qquad (4.21)$$

in which u_i^y $(1 \le i \le 8)$is the vertical displacement at loading point i;$u_9^y$is the vertical displacement of the reference point, at which the prescribed displacement is imposed. To minimize the initial dynamic effect induced by the loading scheme, the displacement at the reference point was applied as a conic curve with time.

Figure 4.4 gives the loads achieved at different loading points during the FE simulation as a result of the prescribed displacement at the reference point and the constraint imposed by Eq. 4.21. The predicted load-time curves for all the loading points coincide, which demonstrates the validity of the proposed scheme.

4.3 VERIFICATION OF THE AUGMENTEDFE APPROACH

Only two series of tests on FRP-plated RC beams under multi-point loading to investigate IC debonding have been found in the existing literature (Mazzotti and Savoia2009; Pan et al. 2009). Some of the tests in Mazzotti and Savoia (2009) and

Pan et al. (2009) together with the tests presented in Chapter 3 are used to verify the augmented FE approach. Three beams (e.g. D2-P2-L2, D3-P4-L2, and D4-P8-L2) were selected from Pan et al. (2009) as all these beams failed by IC debonding and were under different load distributions. In these beams, the only variable was the load distribution (e.g. two-point loading for beam D2-P2-L2, four-point loading for beam D2-P2-L4, and eight-point loading for beam D2-P2-L8).These three beams are re-examined herein although they were previously simulated by Teng et al. (2010) using a force control technique for the loading process. A series of tests were conducted under the eight-point loading condition by Mazzotti and Savoia (2009). Two specimens, which failed by IC debonding, were selected for the verification of the FE approach; while the test results of the other specimens may be unreliable as demonstrated in the next section. In addition, the other loading conditions (e.g. two- and four-point loading) with the loading positions as indicated in Table 4.1 were also employed. The key information of the geometrical and material properties of specimens in both Mazzotti and Savoia (2009) and Pan et al. (2009) is given in Table 4.1.All five specimens from Chapter 3 of the present research project failed by IC debonding and were simulated using the augmented FE approach to verify its accuracy.

4.3.1 Specimens of Chapter 3 of the present research project

All five full-scale specimens of Chapter 3 of the present thesis had the same dimensions: a cross-section of 200 mm x 450 mm and a clear span of 4000 mm. The beams were under-reinforced with two tension steel bars and two compression steel

bars, both 16 mm in diameter (see Chapter 3 for details). To avoid shear failure prior to IC debonding, steel stirrups with a diameter of 8 mm at a centre-to-centre spacing of 100 mm were used as the steel shear reinforcement. All five beams were strengthened in flexure by bonding an FRP plate to the soffit of the beam following the wet lay-up process. The FRP plates had the same nominal dimensions: 100 mm wide, 0.999 mm thick and 3800 mm long. The material properties of concrete, steel and FRP can be found in Tables 3.2 and 3.3 of Chapter 3.

The five beams were divided into two series: Series I was conducted to investigate the effect of varying the shear span, and Series II was used to examine the effect of load uniformity on debonding behaviour. The three beams in Series I were subjected to two concentrated loads (e.g. under four-point bending), and had shear spans of 1000 mm, 1250 mm and 1750 mm respectively. They were denoted as LP2SP1750, LP2SP1250, and LP2SP1000, respectively. In Series II, Specimen LP2SP1000 of Series I served as the reference beam; two other beams, namely LP4SP1000 and LP8SP1000, were subjected to four- and eight-point loading respectively. The three beams in Series II had the same effective shear span of 1000 mm. The loading schemes of Series II can be found in Figure 3.3 in Chapter 3.

Only half of each beam was simulated considering the symmetry of these beams about the mid-span, and symmetry boundary conditions were applied to the centre-line of the beam. The results of a mesh convergence study conducted by Teng et al. (2010) showed that the predicted load-displacement curves, cracking behaviour and FRP debonding strains change only slightly if the maximum size of elements are

less than 20 mm. The maximum size of 10 mm was therefore chosen for the elements of concrete and matching sizes were adopted for the elements of other components (e.g. steel bars, FRP, and the interfaces between concrete and steel reinforcement/FRP) of beams. The total number of elements used was about 12500.

4.3.1.1 Verification for two-point loading

The verification work carried out by Chen et al. (2011) has demonstrated that the FE approach has the capability to predict IC debonding under two-point loading accurately. Figure 4.5 shows a comparison between the FE predicted and test mid-span moment-deflection curves for specimens LP2SP1000, LP2SP1250, and LPSP1750. Like the test moment-deflection curves, the three key points representing the initiation of concrete cracking, the yielding of tension steel, and FRP debonding, respectively can be easily identified on the predicted moment-deflection curves. The predicted ultimate mid-span moments of LP2SP1000, LP2SP1250, and LP2SP1750 are 142.2 kN.m, 143.2kN.m, and 143.6 kN.m, while the corresponding values of tests are 143.6 kN.m, 138.1 kN.m and 132.2 kN.m, respectively. The predicted mid-span deflections at IC debonding are 26.8 mm, 26.3 mm and 20.0 mm respectively for specimens LP2SP1000, LP2SP1250, and LP2SP1750, close to the corresponding test values of 30.0 mm, 26.0 mm and 21.0 mm. For Specimen LP2SP1000, the three key points from FE analysis are very close to the corresponding test points. However, for Specimens LP2SP1250 and LP2SP1750, the predicted moments for steel yielding (yield moments) are higher than the corresponding test values, with differences around 15% and 9% respectively.

The yield moments (i.e. the maximum moment in the beam at the yielding of steel tension bars) of Specimens LP2SP1750, LP2SP1250 and LP2SP1000 from tests are about 108 kN.m, 110 kN.m and 115 kN.m respectively (Figure 4.5). It however was expected that all the specimens in Series I would have the same yield moment, as the moment at steel yielding should be primarily controlled by the steel yield stress and the steel tension bars of the same batch were used in these specimens. The yield stresses of the steel tension bars in Specimens LP2SP1750, LP2SP1250 and LP2SP1000 may be different, despite the fact that the steel tension bars were from one batch. As a result, the differences in the yield stress of the steel tension bars may primarily result in the differences in the maximum moment of the beam at debonding. According to FE modelling, all the specimens in Series I had the same yield moment of about 115 kN.m. The differences among the predicted IC debonding moments of Specimens LP2SP1750, LP2SP1250 and LP2SP1000 are within 2kN.m. The numerical results indicate that the effect of the shear span on IC debonding may be marginal and could be neglected.

The FE-predicted crack pattern of Specimen LP2SP1000 is compared with that from the test in Figure 4.6. It can be seen that the FE approach provides a very close prediction of the experimental crack pattern although minor differences exist. In particular, it can be seen that16 significant cracks with their crack tips located higher than 1/5 the beam height are predicted by FE analysis compared to the 14 test-observed significant cracks. The numerically-predicted significant crack closest to the support occurs at the position of about 300 mm from the support, while its test counterpart is at the position of 343 mm from the support. The FE critical crack

spacing (i.e. the crack spacing between the critical crack, where IC debonding initiates, and its adjacent crack in the shear span) is about 110 mm, which is just slightly smaller than the critical crack spacing of 112 mm determined from the experimental crack pattern.

Comparisons of widths of several typical cracks of Specimen LP2SP1000 between FE predictions and test results are given in Figure 4.7. These typical cracks are the critical crack, the crack adjacent to the critical crack (adjacent crack) and the crack near the mid-span. The critical crack is the crack where IC debonding initiates, and often near the loading point for beams under 1- or 2-point loading. The critical cracks are at 779 mm and 880 mm from the left support in the test and the FE simulation, respectively. The adjacent crack in the test is at 625 mm from the left support while its numerical counterpart is at 670 mm from the support. In the test, a novel device using a hand-held HD camera to calculate crack widths automatically was used to measure the width of visible cracks. The crack width was measured at the height of steel tension bars instead of the FRP plate to leave enough space to accommodate the device for measuring crack widths. Therefore, the numerical crack widths of the three typical cracks were obtained at the level of steel tension bars. The predicted width of the critical crack is about 0.04 mm, which is larger than its experimental counterpart when the maximum moment of the beam is slightly smaller than about 70 kN.m; the difference between the numerical and the experimental results decreases as the maximum moment of the beam increases, and they reach the same value when the maximum moment of the beam reaches 80kN.m. In addition, the widths of the critical crack from both the numerical and the experimental results

increase abruptly due to the yielding of steel tension bars. The predicted value for the width of the adjacent crack is smaller than the test result with the average difference being about 0.04 mm. Very close predictions are achieved for the width of the crack near mid-span with the difference being about 0.02 mm before the maximum moment of the beam of 100.0 kN.m and about 0.15 mm afterwards. Considering the complexity of concrete cracking and the limitations of the crack-measurement device, it can be concluded that crack widths of Specimen LP2SP1000 are well predicted by the FE approach.

Figure 4.8 shows the comparison of FRP strains at different load levels between numerical and experimental results. The predicted maximum FRP strains are 2106 $\mu\varepsilon$, 3409 $\mu\varepsilon$, and 5407 $\mu\varepsilon$ respectively for the applied moments of 80.0 kN.m, 120 kN.m, and 140 kN.m, which are close to their test counterparts of 2148$\mu\varepsilon$, 3819 $\mu\varepsilon$, and 5828 $\mu\varepsilon$.The variations of FRP strains as a result of concrete cracks along the length of FRP plate at different load levels are accurately captured by the FE approach; that is, the FE approach provides good predictions of the experimental FRP strain distributions, implying the ability of the FE approach to predict FRP strains accurately at different loading stages as well as the cracking behaviour of FRP-plated beams.

4.3.1.2 Verification for four- or eight-point loading

The detailed FE results for Specimens LP4SP1000 and LP8SP1000, which were tested under four- and eight-point loading respectively, are given in this section to

demonstrate the ability of the FE approach to predict accurately IC debonding for different load distributions. The predicted moment-deflection curves, cracking behaviour and FRP strains at different load levels are compared next.

Figure 4.9 shows that the FE-predicted moment-deflection curves for specimens in Series II are close to their test counterparts. In particular, the predicted failure moments for Specimens LP4SP1000 and LP8SP1000 are 156.3 kN.m and 160.0 kN.m respectively, which differ from the corresponding test values by only 3.5% and 2.1% respectively. The predicted mid-span deflections at IC debonding failure are 29.8 mm and 30.4 mm for Specimens LP4SP1000 and LP8SP1000 respectively, which are close to their corresponding test values of 29.7 mm and 28.8 mm. After concrete cracking, the FE-predicted moment-deflection curves are slightly stiffer than their test counterparts are.

Figure 4.10 shows the comparison of crack patterns at IC debonding failure. The numbers of significant cracks predicted by FE analysis are 17 and 18 for Specimens LP4SP1000 and LP8SP1000 respectively, which are close to the 16significant cracks observed in tests for LP4SP1000 and LP8SP1000. FRP debonding is predicted to initiate at 1190 mm and 1690 mm from the support for Specimens LP4SP1000 and LP8SP1000 respectively, which is similar to the test observation that the critical cracks were at1296 mm and1591 mm from the support for these two beams respectively. The spacings between the critical crack and the adjacent crack are110 mm and153 mm for LP4SP1000 and LP8SP1000 respectively, which are close to the corresponding experimental crack spacings of 111 mm and 138 mm. Despite the

complexity of concrete cracking and difficulty with the accurate measurement of crack widths, it can be concluded that the numerically predicted widths of the critical crack, its adjacent crack and the crack nearest to mid-span match their test values well.

Figure 4.11 shows the comparison of FRP strains at different load levels between numerical and experimental results for Specimens LP4SP1000 and LP8SP1000. The predicted maximum FRP strains of Specimen LP4SP1000 are 2010$\mu\varepsilon$, 3440$\mu\varepsilon$, and 6260$\mu\varepsilon$ respectively for the applied moments of 80.0 kN.m, 120 kN.m, and 148 kN.m, which are close to their test counterparts of 2035$\mu\varepsilon$, 3750$\mu\varepsilon$, and 6516$\mu\varepsilon$.The predicted maximum FRP strains of Specimen LP8SP1000 are 2090$\mu\varepsilon$, 3320$\mu\varepsilon$, and 6530$\mu\varepsilon$respectively for the applied moments of 80.0 kN.m, 120 kN.m, and 152 kN.m, which are close to their test counterparts of 2222$\mu\varepsilon$, 3843$\mu\varepsilon$, and 6281$\mu\varepsilon$.Variations of FRP strains as a result of concrete cracks along the length of FRP plate at different load levels are accurately captured by the FE approach. That is, the FE approach provides good predictions of the experimental FRP strain distributions, demonstrating the ability of the FE approach to predict FRP strains accurately at different loading stages as well as the cracking behaviour of FRP-plated beams.

The comparison between numerical results and experimental results presented above demonstrate that the FE approach is also capable of accurately predicting IC debonding of full-size FRP-plated beams under different load uniformity[the capability of the FE approach in accurately predicting the effect of load distribution on IC debonding of FRP-plated RC beams of small size was already shown byTeng

et al. (2010)].As the limited number of tests has indicated that an increase in load uniformity can significantly increase the IC debonding strength, this issue should be considered in design. In order to understand the effect of load uniformity on IC debonding further, a parametric study was conducted as part of the present study and is presented later.

4.3.2 Specimens of Pan et al. (2009)

Three beams tested by Pan et al. (2009) are re-examined herein using the results from the augmented FE approach. These three beams (e.g. D2-P2-L2, D3-P4-L2, and D4-P8-L2) were selected as they all failed by IC debonding and were subjected to different load distributions. In these beams, the only variable is the load distribution (e.g. two-point loading for D2-P2-L2, four-point loading for D2-P2-L4, and eight-point loading for D2-P2-L8). The loads were applied by a waffle-tree system. All three beams had a clear span of 1800 mm, a width of 150 mm and a height of 200 mm. Two high yield steel bars of 10 mm and 8 mm in diameter were used as the tension steel bars and compression bars, respectively. Twelve mm stirrups at an 80 mm centre-to-centre spacing were employed to ensure that the shear strength would be much higher than its flexural strength. Moreover, a 150 mm×1650 mm CFRP soffit plate was used to strengthen these beams. The key properties of each component in these FRP strengthened RC beams are listed in Table 4.1.

In the FE modelling of these beams, only half of each beam was simulated considering the symmetry nature of these beams about mid-span. Ten mm was chosen as the maximum size of concrete elements on the basis of a mesh convergence study, and elements of matching sizes were used to represent the other components such as the FRP plate and the steel bars.

All three simulated beams were predicted by the FE approach to fail by IC debonding. Figure 4.12 shows that the FE-predicted maximum moment-mid-span displacement curves are in good agreement with the test results for all three beams, which were tested under different load distributions. The predicted maximum moments at debonding of beams D2-P2-L2, D3-P4-L2 and D4-P8-L2 are 25.0, 28.7 and 28.9 kN.m, respectively, which are close to corresponding test results of 25.8, 29.4 and 30.72 kN.m, with the differences being only 3.2%, 2.4% and 6.3%, respectively. The predicted mid-span displacements at debonding failure are also close to the test values, with the differences being 8.8%, 4.5% and 3.8% for beams D2-P2-L2, D3-P4-L2 and D4-P8-L2, respectively. In addition, good agreement for the maximum moment vs. mid-span displacement is observed. The predicted crack patterns at failure (in Figure 4.13) match the test results very well. All these accurate predictions demonstrate the good capacity of the FE approach in capturing the important conditions of IC debonding of FRP-strengthened RC beams under different load distributions.

Both the test and the numerical results indicate that the ultimate moment of the strengthened beams increases significantly with an increase in load uniformity. The predicted crack patterns are also directly affected by the load distribution. The cracks become more distributed as the load uniformity increases, which results in more similar stresses at two adjacent cracks, thus inducing a significant increase in the IC debonding strain. This phenomenon is clearly illustrated by Figure 4.14, where the predicted FRP strain distributions at 95% of the debonding load are given. As the loading point number increases from 2 to 8, the strain of the FRP increases from $8820\mu\varepsilon$ to $11700\mu\varepsilon$.

4.3.3 Specimens of Mazzotti and Savoia (2009)

Several beams were tested by Mazzotti and Savoia (2009) to investigate IC debonding in FRP-strengthened RC beams under UDL, which was approximated using eight-point loading in the tests. Two typical specimens were selected for the verification of the augmented FE approach for accurately predicting IC debonding under different load distributions; the other specimens (e.g. Specimen TN3) were excluded, as experimental errors may have existed in these tests. As an example, the experimental errors of Specimen TN3 can be demonstrated by comparing its test results with those of Specimen TN8 and FE results. In addition, other loading conditions [i.e. two- and four-point loading similar to those in Pan et al. (2009)] were

also employed to investigate the effect of load distribution on IC debonding. The position of each loading point together with geometrical and mechanical properties of the specimens is given in Table 4.1.

4.3.3.1 Series TN4

Specimen TN4 in Mazzotti and Savoia (2009) had a span of 3200 mm (clear span of 3000 mm), a width of 250 mm and a height of 400 mm. Five 14 mm steel bars and two 12 mm steel bars were used as tension and compression bars, respectively. A CFRP plate of 250 mm in width and 0.260 mm in nominal thickness was used for flexural strengthening. In addition, sufficient shear steel reinforcement was employed to avoid premature shear failure. Specimen TN4 was tested under eight-point loading and is denoted as TN4-LP8 for the remainder of this chapter. Two- and four-point loading were also employed in the simulation with these numerical specimens being denoted as TN4-LP2 and TN4-LP4 respectively.

Only half of each specimen was simulated by taking advantage of the symmetry nature of these specimens about mid-span. The maximum size of concrete elements was chosen to be 10 mm, and matching element sizes were adopted for modelling the FRP soffit plate and the steel bars. The FE results are presented in the same fashion as that for the beams in Pan et al. (2009).

Specimen TN4-LP8 failed by IC debonding as observed in the test. The predicted maximum moment is almost the same with the test value, with a difference of 1% (Figure 4.15). However, the difference in mid-span deflection at failure, being about 15%, is larger than that in the test. The difference in the moment-deflection curve between the FE predictions and the test results becomes significant after the initiation of concrete cracking.

The cracks become more distributed as the load uniformity increases (Figure 4.16). In this series of simulated beams, the maximum moment at debonding increases from 223.1 kN.m to 237.4 kN.m, when the number of loading points increases from two to eight. In addition, the debonding strain also increases when the load becomes more distributed (e.g. 10400 με, 11700 με, and 12900 με for two-point loading, four-point loading and eight-point loading, respectively), which is believed to be the result of a more distributed crack pattern under more uniformly distributed loading (Figure 4.17).

4.3.3.2 Series TN8

Details of the geometric and mechanical properties of SpecimenTN8in Mazzotti and Savoia (2009) are given in Table 4.1.Specimen TN8 is different from Specimen TN4-LP8 in the amount of steel tension bars. Like Series TN4, two- and four-point

loading were also considered in the FE simulations with the names of the numerical specimens TN8-LP2 and TN8-LP4 respectively. The FE modelling information including the types and sizes of elements used is the same as that for TN4-LP8. The predicted maximum moment-mid-span displacement curves are given in conjunction with the test results of Specimen TN8 under 8-point loading.

Specimen TN8-LP8 was predicted by FE analysis to fail by IC debonding as observed in the test. As shown in Figure 4.18, the moment-displacement curve of Specimen TN8-LP8 is accurately predicted by the FE approach. The predicted maximum moment and mid-span displacement at debonding are almost the same as the corresponding test results, with small differences of 0.7% and 3.3%, respectively.

Figures 4.18-4.20 clearly show that the load distribution has a significant effect on IC debonding behaviour in FRP-plated RC beams. With an increase in load uniformity, both the debonding strength and ductility of the plated beam increase. In this series of beams, the maximum moment and mid-span displacement increase from 148.4 kN.m and 22.4 mm to 166.9 kN.m and 29.2 mm, when the number of loading points increases from two to eight. The crack pattern becomes more distributed as the load uniformity increases (Figure 4.19).

4.3.3.3 Exclusion of Specimen TN3

Specimen TN3 (i.e. or TN3-LP8 to follow the naming convention in the present section) has the same geometrical and material properties as Specimen TN8-LP8 except that an FRP soffit plate of a higher axial stiffness was used in TN3-LP8. The FRP soffit plate of Specimen TN3-LP8 is 1.2 mm in thickness, 100 mm in width, and 195 GP in elastic moduli, with the axial stiffness being 23400 kN while the soffit plate of Specimen TN8-LP8 is 0.26 mm in thickness, 250 mm in width, and 290 GP inelastic moduli, with the axial stiffness being 18850 kN, which is slightly smaller than that of Specimen TN3-LP8.

Due to an FRP plate with a higher axial stiffness, it is logical that the moments at the initiation of concrete cracking and tension steel yielding of Specimen TN3-LP8 are higher than the corresponding values of Specimen TN8-LP8.Such features are successfully predicted by the FE analysis (Figure 4.21).However, the test values of Specimen TN3-LP8 for these moments are much lower than the corresponding test values of Specimen TN8-LP8. As it is easy to predict the behaviour of an RC beam before the yielding of steel tension bars, it is believed that the experimental results of Specimen TN3-LP8 may not be reliable. The experimental errors may have arisen from considerable difficulty with the application of eight-point loading.

4.4 PARAMETRIC STUDY

As demonstrated in the section above, the effect of load distribution on IC debonding is significant, and the FE approach has the ability to capture this effect. Due to the limited number of studies on the subject, there is still a lack of understanding of the mechanism of IC debonding in FRP-plated RC beams under different load distributions. For this reason, a parametric study on the effect of load distribution on IC debonding was conducted and the results are presented in this section.

The parametric study examined a number of major factors affecting the IC debonding strength, including concrete strength, yield stress and amount of steel tension bars, width and thickness of the FRP soffit plate, and depth-to-span ratio of the beam. Each factor was examined at a minimum of three values covering a wide range. Details of the parametric values are given in the following sub-sections (Table 4.2). In addition, two typical load distributions (e.g. two-point loading and uniformly distributed loading) were investigated for each case.

In the parametric study, the name of each numerical specimen is a combination of letters and numbers with their meaning as explained next. A specimen name starts with either 'LP2' or 'UDL' to denote the load distribution (e.g. LP2=two-point loading; UDL=uniformly distributed loading), followed by two capital letters representing the factor being examined. For example, 'CS', 'BY', 'BS', 'FL', 'FW' and 'DS' stand for concrete strength, yield stress, amount of steel tension bars, number of FRP layers, width of FRP plate, and span-to-depth ratio, respectively. The

specimen name ends with a number indicating the value of the second factor; for example, Specimen LP2CS30is a specimen under two-point loading with the concrete strength being 30 MPa, while Specimen UDLCS30 denotes a specimen under uniformly distributed loading with the concrete strength being 30MPa.LP2FL2 and UDLBS316 are respectively specimens under two-point loading with a two-layer FRP plate (e.g.0.666 mm in total nominal thickness) and under uniformly distributed loading with three 16 mm steel tension bars.

4.4.1 Effect of concrete strength

Four cylinder concrete compressive strengths (20 MPa, 30 MPa, 40 MPa and 50 MPa) were considered to investigate the effect of concrete strength. The two typical loading conditions (e.g. two-point loading and uniformly distributed loading) were considered. For ease of description in the following sub-sections, Specimens LP2CS30 and UDLCS30 are referred to as the reference specimens having the same geometric and material properties (the reference beam). In the remainder of this section, each of the beam specimens has the same geometrical and material properties as the reference beam as detailed below except for the parameter being investigated. The reference beam has the following geometrical and material properties: a clear span of 4000 mm and an overall depth of 450 mm. The beam is reinforced by two 16mm steel tension bars and two 16 mm steel compression bars, and is heavily reinforced in shear with 10 mm steel stirrups at a centre-to-centre spacing of 100 mm to avoid shear failure. The FRP soffit plate has the same nominal dimensions: 150 mm wide, 0.999 mm thick (i.e. three plies x 0.333 mm), and 3800

mm long. The yield stress of steel bars is 400 MPa and the concrete cylinder strength is 40 MPa. The reference specimen has a different name in a different group to follow consistent naming of specimens in each group.

Table 4.3 gives the key results of the specimens with different concrete strengths. The percentage increases in the maximum moment and the maximum FRP strain in the beam at debonding (also referred to as the debonding moment and the debonding strain) are in the range of 6.5% to 12.5% and the range of 9.9% to 18.5% respectively when the loading condition changes from two-point loading to uniformly distributed loading. Specimen LP2CS20 fails by IC debonding with the debonding moment being 116.67 kN.m and the debonding strain being 3920 $\mu\varepsilon$ while SpecimenUDLCS20 fails by IC debonding with the debonding moment and the debonding strain being 124.31 kN.m and 4310 $\mu\varepsilon$, respectively. When the concrete strengths are 20 MPa, 30 MPa, 40 MPa and 50 MPa, the increases in debonding moment and debonding strain are 6.5% and 9.9%, 7.1% and 11.0%, 11.1% and 18.5%, and 12.5% and 18.4%, respectively. The effect of load distribution becomes more significant for specimens with a higher concrete strength, possibly because the contribution of the FRP soffit plate to the load carrying capacity of the beam is affected by the crack bebaviour, thus by the load distribution, and become larger when the concrete strength increases.

4.4.2 Effect of yield stress of steel tension bars

Four yield stresses, namely 250 MPa, 300 MPa, 400 MPa and 500 MPa were

considered in the parametric study. As for the concrete strength, two load conditions (e.g. two-point loading and uniformly distributed loading), were investigated in the parametric study.

Table 4.4 gives the key results of specimens with different yield stresses of steel tension bars. The percentage increases in the maximum moment and the maximum FRP strain in the beam at debonding are in the range of 6.2% to 12.9% and the range of 9.6% to 21.9% respectively when the loading condition changes from two-point loading to uniformly distributed loading. The debonding moment and the debonding strain of Specimen UDLBY250 are higher than those of Specimen LP2BY250 by 12.9% and 21.9% respectively. The increases in debonding moment and debonding strain are respectively10.9% and 8.4% for the yield stress of 300 MPa, and respectively 6.2% and 9.6% for the yield stress of 500 MPa. It can be concluded that the effect of load distribution is more significant in a specimen with a lower yield stress of steel tension bars, may due to the fact that the ratio of the contribution of the FRP plate to the load carrying capacity, which can be easily affected by the load distribution, increases with the decrease in the yield stress of steel tension bars.

4.4.3 Effect of amount of steel tension bars

Three steel tension reinforcement scenarios, namely two 10 mm bars (i.e., 0.17% in the volume ratio of the steel tension bar), two 16 mm bars (i.e., 0.45% in the volume ratio of the steel tension bar) and three 16 mm bars (i.e., 0.45% in the volume ratio of the steel tension bar), were considered in the parametric study.

Table 4.5 gives the key results of the specimens with different scenarios of steel tension bars. The percentage increases in the maximum moment and the maximum FRP strain in the beam at debonding are in the range of 6.0% to 12.9% and the range of 11.0% to 15.6% respectively when the loading condition changes from two-point loading to uniformly distributed loading. The debonding moment and the debonding strain of Specimen UDLBS210 are larger than those of Specimen LP2BS210 by 12.9% and 15.6% respectively. For specimens with three 16 mm bars, the debonding moment and the debonding strain increase by 6.0% and 13.2% respectively, as the loading condition changes from two-point loading to uniformly distributed loading. It can be concluded that the effect of load distribution becomes less significant in a specimen with a larger amount of steel tension bars.

4.4.4 Effect of thickness of FRP plate

Three FRP plate thicknesses (expressed in terms of number of layers), namely two, three and four layers of FRP, were considered in the parametric study.

Table 4.6 gives the key results of specimens with FRP plates of different numbers of layers. The percentage increases in the maximum moment and the maximum FRP strain in the beam at debonding are in the range of 9.2% to 9.6% and about 15.0 % respectively when the loading condition changes from two-point loading to uniformly distributed loading. The debonding moment and the debonding strain of Specimen UDLFL2 are larger than those of Specimen LP2FL2 by 9.2% and 15.5% respectively. For specimens with a four-layer FRP plate, the debonding moment and

the debonding strain increase by 9.6 % and 15.0% respectively as the loading condition changes from two-point loading to uniformly distributed loading. This shows that the FRP plate thickness has a slight influence on the effect of load distribution in terms of the percentage increase in the debonding moment and the debonding strain.

4.4.5 Effect of width of FRP plate

Three FRP plate widths, namely 100 mm, 150 mm and 200 mm, were considered in the parametric study.

Table 4.7 gives the key results of specimens with different FRP plate widths. The percentage increases in the maximum moment and the maximum FRP strain in the beam at debonding are in the range of 10.8% to 16.6% and the range of 23.1% to 28.4% respectively when the loading condition changes from two-point loading to uniformly distributed loading. The debonding moment and the debonding strain of Specimen UDLFW100 are larger than SpecimenLP2FW100 by 10.8% and 23.1% respectively. For the specimens with an FRP plate width of 200 mm, the debonding moment and the debonding strain increase by 16.6 % and 28.4% respectively as the loading condition changes from two-point loading to uniformly distributed loading. It can be concluded that the effect of load distribution is more significant in a specimen with a wider FRP plate.

4.4.6 Effect of span-to-depth ratio

Three beam heights of 450 mm, 350 mm and 250 mm were considered in the parametric study (all the beams have the same clear span of 4000 mm). The span-to-depth ratios of the beams are 8.9, 11.4 and 16 respectively (approximately indicated by 'DS9', 'DS11' and 'DS16' in specimen names).

Table 4.8 gives the key results of specimens with different span-to-depth ratios. The percentage increases in the maximum moment and the maximum FRP strain in the beam at debonding are in the range of 7.1% to 28.3% and the range of 11.0% to 65.8% respectively when the loading condition changes from two-point loading to uniformly distributed loading. The debonding moment and the debonding strain of Specimen UDLDS11 are larger than those of Specimen LP2DS11 by 12.2% and 23.8% respectively. For specimens of 250 mm in height, the debonding moment and debonding strain increase by 28.3% and 65.8% respectively, as the loading condition changes from two-point loading to uniformly distributed loading. It can be concluded that the effect of load distribution is much more significant in a specimen with a higher span-to-depth ratio.

4.5 CONCLUSIONS

In this chapter, a novel displacement control-based loading scheme was proposed to augment the FE approach of Chen et al. (2011) for the modelling of IC debonding failure in FRP-plated RC beams under various load distributions. This chapter first presented a verification study of the FE approach in predicting IC debonding for different load distributions using the full-scale beam test results presented in Chapter

3 together with existing test results from two other studies found in the open literature. A parametric study was then presented to investigate the effects of a number of significant factors, including concrete strength, yield stress and amount of steel tension bars, thickness of FRP plate, width of FRP plate, and span-to-depth ratio of the beam on the behaviour of IC debonding. The following conclusions can be drawn based on the numerical results and the discussions presented in this Chapter:

(1) Using the proposed displacement control-based loading scheme, the FE approach is capable of accurately predicting the IC debonding failure of FRP-plated RC beams under different load distributions; in particular, the load-displacement responses, crack patterns, crack widths and FRP strains can all be well predicted by the FE approach;

(2) Results from the parametric study conducted with the verified FE approach showed that the load distribution can significantly affect the behaviour of IC debonding, and the effect of load distribution depends on a number of significant factors such as concrete strength, yield stress and amount of steel tension bars, width of FRP plate, and beam span-to-depth ratio, but the thickness of FRP plate has little effect on the IC debonding behaviour.

4.6 REFERENCES

ABAQUS (2004). *ABAQUS 6.5 user's manual*, ABAQUS, Inc., Providence, RI.

Bazant, Z.P. and Planas, J. (1998). *Fracture and size effect in concrete and other quasi brittle materials*, CRC Press, Boca Raton.

CEB-FIP (1993). *CEB-FIP model code 90*, Thomas Telford, London.

Chen, G.M. (2010). *Behaviour and strengthen of RC beams shear-strengthened with externally bonded FRP reinforcement*, PhD Thesis, The Hong Kong Polytechnic University, Hong Kong, China.

Chen, G.M., Teng, J.G. and Chen, J.F. (2011). "Finite-element modeling of intermediate crack debonding in FRP-plated RC beams", *Journal of Composites for Construction*, ASCE, Vol. 15, No. 3, pp. 339-353.

Chen, J.F., Teng, J.G. and Yao, J. (2006). "Strength model for intermediate crack debonding in FRP-strengthened concrete members considering adjacent crack interaction", *Proceedings of Third International Conference on FRP Composites in Civil Engineering (CICE 2006)*, Miami, Florida, USA, pp. 67-70.

Clarke M.J., Hancock G.J. (1990). "A study of incremental interactive strategies for nonlinear analysis", *International Journal for Numerical Methods in Engineering*.Vol. 29, pp.1365-91.

Lee, J. and Fenves, G.L. (1998). "Plastic-damage model for cyclic loading of concrete structures", *Journal of Engineering Mechanics*, Vol. 124, No.8, pp.

892–900.

Lu, X.Z., Teng, J.G., Ye, L.P. and Jiang, J.J. (2007). "Intermediate crack debonding in FRP-strengthened RC beams: FE analysis and strength model", *Journal of Composites for Construction*, ASCE, Vol. 11, pp. 161-174.

Lubliner, J., Oliver, J., Oller, S. and Oñate, E. (1989). "A plastic-damage model for concrete", *International Journal of Solids and Structures*, Vol. 25, No.3, pp. 229-326.

Pan, J.L., Chung, T.C.F. and Leung, C.K.Y. (2009). "FRP debonding from concrete beams under various load uniformities", *Advances in Structural Engineering*, Vol.12, No.6, pp. 807-819.

Rots, J. G. (1988). *Computational modeling of concrete fracture*, PhD thesis, Delft University of Technology.

Teng, J.G., Chen, G.M. and Chen, J.F. (2010). "Effect of load distribution on IC debonding in FRP-plated RC beams", *Proceedings, Fifth International Conference on FRP Composites in Civil Engineering (CICE 2010)*, Beijing, China, CD ROM.

4.7 TABLES AND FIGURES

Table 4.1 Geometrical and Material Properties of Specimens failing by IC debonding under different loading distributions

Sources		Mazzotti and Savoia (2009)							Pan et al. (2009)		
Specimen name		TN3-LP8	TN4-LP2	TN4-LP4	TN4-LP8	TN8-LP2	TN8-LP4	TN8-LP8	D2-P2-l2	D3-P4-l2	D4-P8-l2
$f_c^{'}$		45.5	48.0#			44.5#			59.0		
Dimensions	L	1500	3000			3000			1800		
	b_c	250	250			250			150		
	h_c/d	400/370	400/370			400/370			200/163		
Steel bars	f_{yt}	3Y14/550	5Y14/550			3Y14/550			2Y10/550		
	f_{yc}	2Y12/550	2Y12/550			2Y12/550			2Y8/550		
	Stirrups	Y10@90+Y10@200 (deformed, double legs)							Y12@80		
	f_{yv}	550							550		
	E_s	200							202		
FRP plate	Type	Protruded FRP Plate	Wet lay-up FRP plate			Wet lay-up FRP plate			Wet lay-up FRP plate		
	$n \times t_f$	1 × 1.2	2 x 0.13			2 x 0.13			2 x 0.11		
	b_f	100	250			250			150		

	L_f	2800	2800			2800			1650		
	f_f	3100	3900			3900			4200		
	E_f	195	290			290			235		
Loading points	*LP1*	340	1280	620	340	1280	620	340	787.5	337.5	112.5
	LP2	620	--	1280	620	--	1280	620	--	787.5	337.5
	LP3	1000	--	--	1000	--	--	1000	--	--	562.5
	LP4	1280	--	--	1280	--	--	1280	--	--	787.5

#converted from cube compressive strength of concrete using $f_c^{'} = 0.8f_{cu}$; $f_c^{'}$ =cylinder compressive strength of concrete, in MPa; *L,* b_c, $h_c$and *d*= clear span , width, height and *e*ffective depth of specimen, respectively, all in mm; f_{yt}, f_{yc}, and f_{yv}=yielding strength of tension bars, compression bars and stirrup respectively, all in MPa; E_s= Young's modulus of steel bars; $n \times t_f$= no. of plies and thickness of each ply of FRP sheets or plates; b_f, L_f, E_f= width, length and Young's modulus of FRP plate, and in mm, mm and GPa respectively;*LP1, LP2, LP3* and *LP4* are the positions of loading points from the left support, in mm.

Table 4.2 Examined values of the main factors in the parametric study

	Case-I	Case-II	Case-III	Case-IV
Concrete strength (MPa)	20	30	**40**	50
Yield stress of steel tension bars (MPa)	250	300	**400**	500
Amount of steel tension bars	2T10	**2T16**	3T16	
Thickness of FRP plate (mm)	2 X 0.33	**3 X 0.33**	4 X 0.33	
Width of FRP plate (mm)	100	**150**	200	
Span-to-depth ratio	**8.89**	11.43	16	

Note: numbers in bold are the values of parameters for the benchmark beam

Table 4.3 Key results of specimens with different concrete strengths

		Debonding Moment (kN.m)	Maximum FRP strain at debonding ($\mu\varepsilon$)	Critical crack spacing(mm) #1	Debonding initiation position
CS20	LP2	116.67	3920	170	710
	UDL	124.31	4310	210	1580
	Percentage Increase	6.5%	9.9%	--	--
CS30	LP2	134.72	4900	100	970
	UDL	144.31	5440	150	1180
	Percentage increase	7.1%	11.0%	--	--
CS40	LP2	151.53	5890	90	1000
	UDL	168.30	6980	130	840
	Percentage increase	11.1%	18.5%	--	--
CS50	LP2	166.80	6830	80	920
	UDL	187.73	8090	120	1150
	Increase ratio	12.5%	18.4%	--	--

Note: #1: Critical crack spacing is the spacing between the critical crack and the adjacent crack.

Table 4.4 Key results of specimens with different yield stresses of steel tension bars

		Debonding Moment (kN.m)	Maximum FRP strain at debonding ($\mu\varepsilon$)	Critical crack spacing (mm) #1	Debonding initiation position
BY250	LP2	87.27	3100	170	960
	UDL	98.59	3780	230	1580
	Increase ratio	12.9%	21.9%	--	--
BY300	LP2	98.4	3700	150	960
	UDL	109.16	4010	200	1580
	Increase ratio	10.9%	8.4%	--	--
BY400	LP2	151.53	5890	90	1000
	UDL	168.30	6980	130	840
	Increase ratio	11.1%	18.5%	--	--
BY500	LP2	155.40	5440	80	960
	UDL	165.07	5960	130	1140
	Increase ratio	6.2%	9.6%	--	--

Note: #1 Critical crack spacing is the spacing between the critical crack and the adjacent crack.

Table 4.5 Key results of specimens with different amounts of steel tension bars

		Debonding Moment (kN.m)	Maximum FRP strain at debonding ($\mu\varepsilon$)	Critical crack spacing(mm) #1	Debonding initiation position
BS210	LP2	85.16	3850	170	840
	UDL	96.11	4450	250	1500
	Increase ratio	12.9%	15.6%	--	--
BS216	LP2	151.53	5890	90	1000
	UDL	168.30	6980	130	840
	Increase ratio	11.1%	18.5%	--	--
BS316	LP2	156.13	4540	80	960
	UDL	165.42	5140	160	1520
	Increase ratio	6.0%	13.2%	--	--

Note: #1 Critical crack spacing is the spacing between the critical crack and the adjacent crack.

Table 4.6 Key results of specimens with different numbers of layer of FRP sheet

		Debonding Moment (kN.m)	Maximum FRP strain at debonding ($\mu\varepsilon$)	Critical crack spacing(mm) #1	Debonding initiation position
FL2	LP2	113.12	5240	100	720
	UDL	123.52	6050	150	1220
	Increase ratio	9.2%	15.5%	--	--
FL3	LP2	151.53	5890	90	1000
	UDL	168.30	6980	130	840
	Increase ratio	11.1%	18.5%	--	--
FL4	LP2	139.43	3990	100	960
	UDL	152.83	4590	150	1260
	Increase ratio	9.6%	15.0%	--	--

Note: #1 Critical crack spacing is the spacing between the critical crack and the adjacent crack.

Table 4.7 Key results of specimens with different widths of the FRP plate

		Debonding Moment (kN.m)	Maximum FRP strain at debonding ($\mu\varepsilon$)	Critical crack spacing(mm) #1	Debonding initiation position
FW100	LP2	94.54	3290	170	880
	UDL	104.78	4050	180	1500
	Increase ratio	10.8%	23.1%	--	--
FW150	LP2	151.53	5890	90	1000
	UDL	168.30	6980	130	840
	Increase ratio	11.1%	18.5%	--	--
FW200	LP2	163.03	5190	80	700
	UDL	190.02	6663	100	780
	Increase ratio	16.6%	28.4%	--	--

Note: #1 Critical crack spacing is the spacing between the critical crack and the adjacent crack.

Table 4.8 Key results of specimens with different span-to-depth ratios of beams

		Debonding Moment (kN.m)	Maximum FRP strain at debonding ($\mu\varepsilon$)	Critical crack spacing(mm) #1	Debonding initiation position
DS09	LP2	94.54	3290	170	880
	UDL	104.78	4050	180	1500
	Increase ratio	10.8%	23.1%	--	--
DS11	LP2	98.17	4530	110	1030
	UDL	110.19	5610	170	1070
	Increase ratio	12.2%	23.8%	--	--
DS16	LP2	70.77	4590	110	800
	UDL	90.79	7610	120	1100
	Increase ratio	28.3%	65.8%	--	--

Note: #1 Critical crack spacing is the spacing between the critical crack and the adjacent crack.

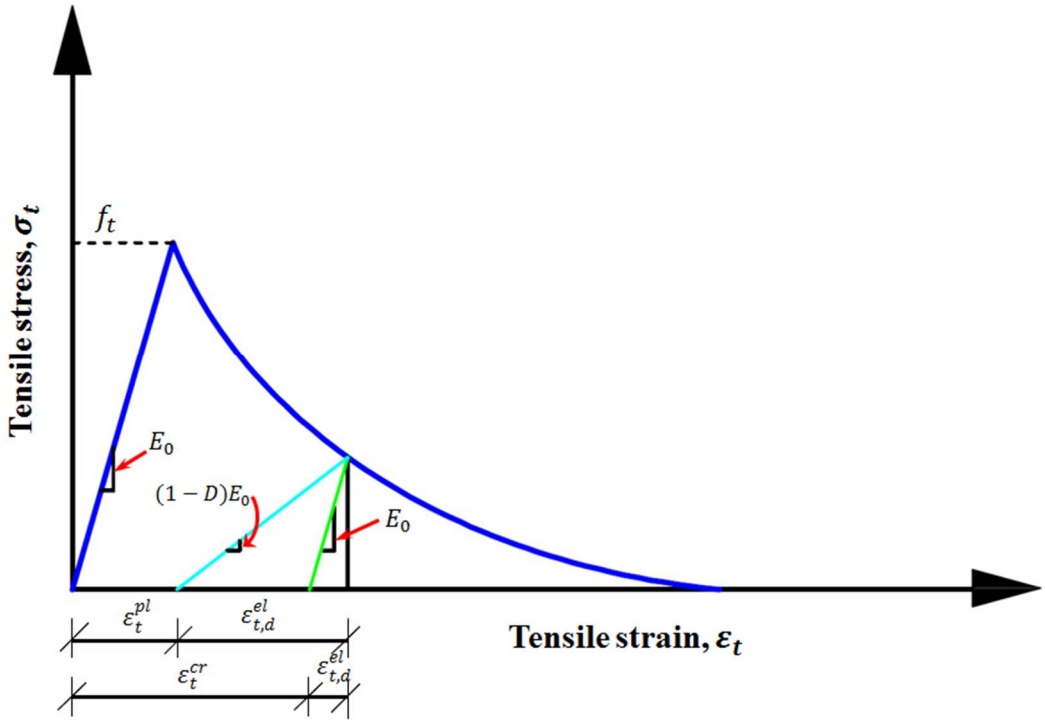

Figure 4.1 Definition of tensile damage

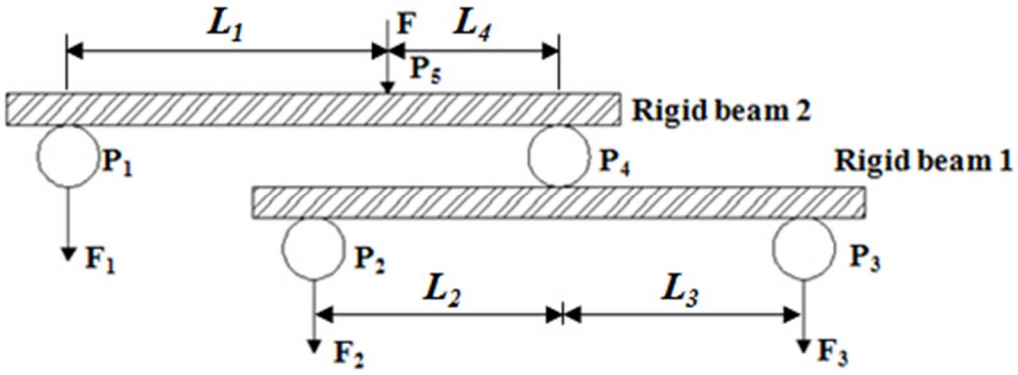

Figure 4.2 Imaginary whiffle-tree system

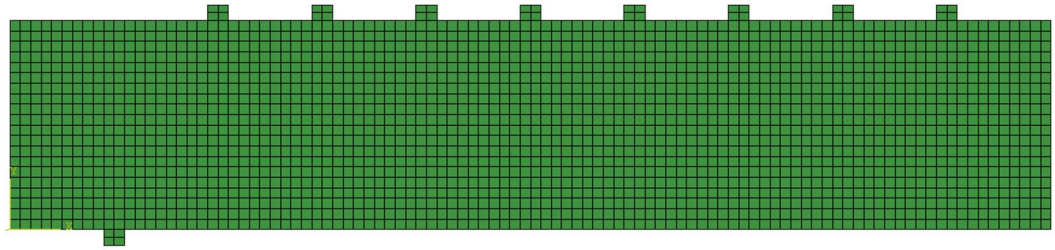

Figure 4.3 Mesh of the beam

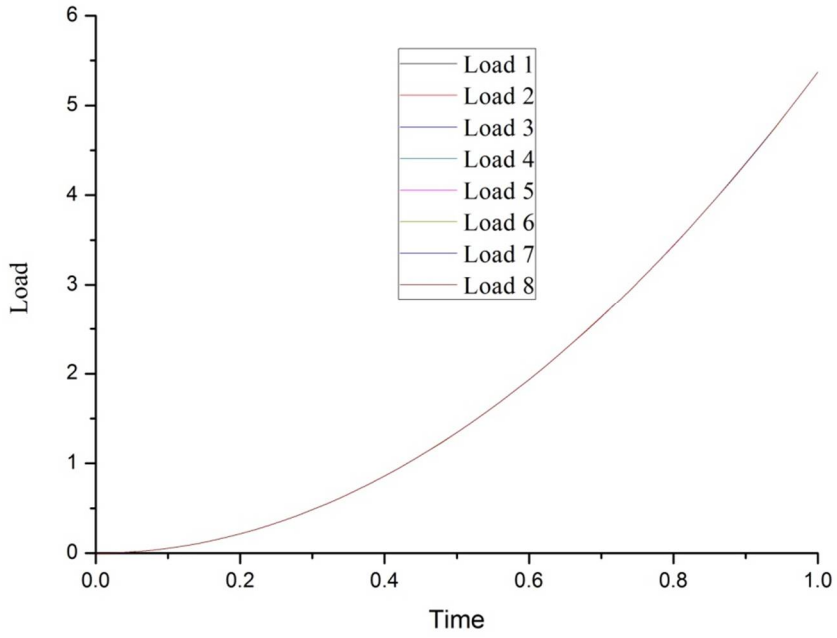

Figure 4.4 Applied load-time curves at each loading point

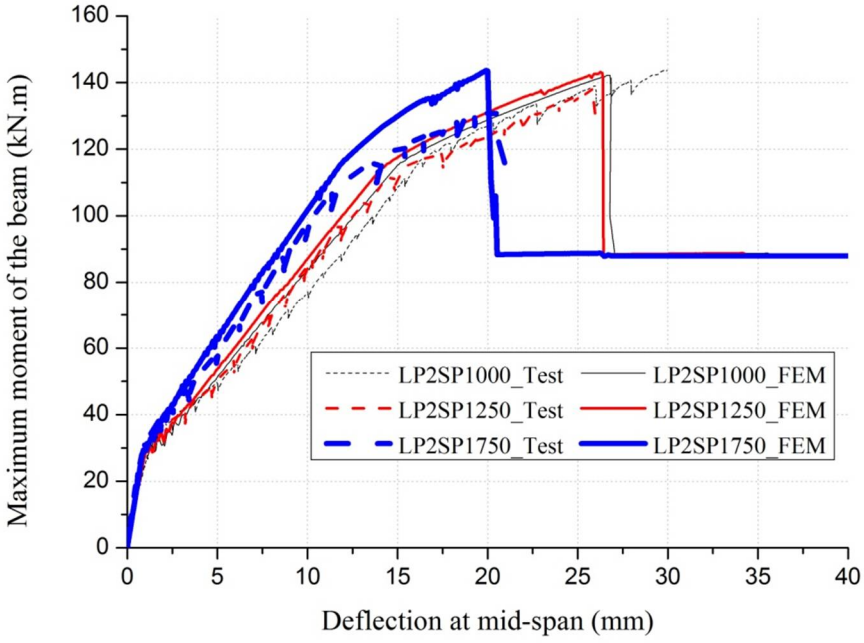

Figure 4.5 FE predicted versus test moment-displacement curves for Series I specimens

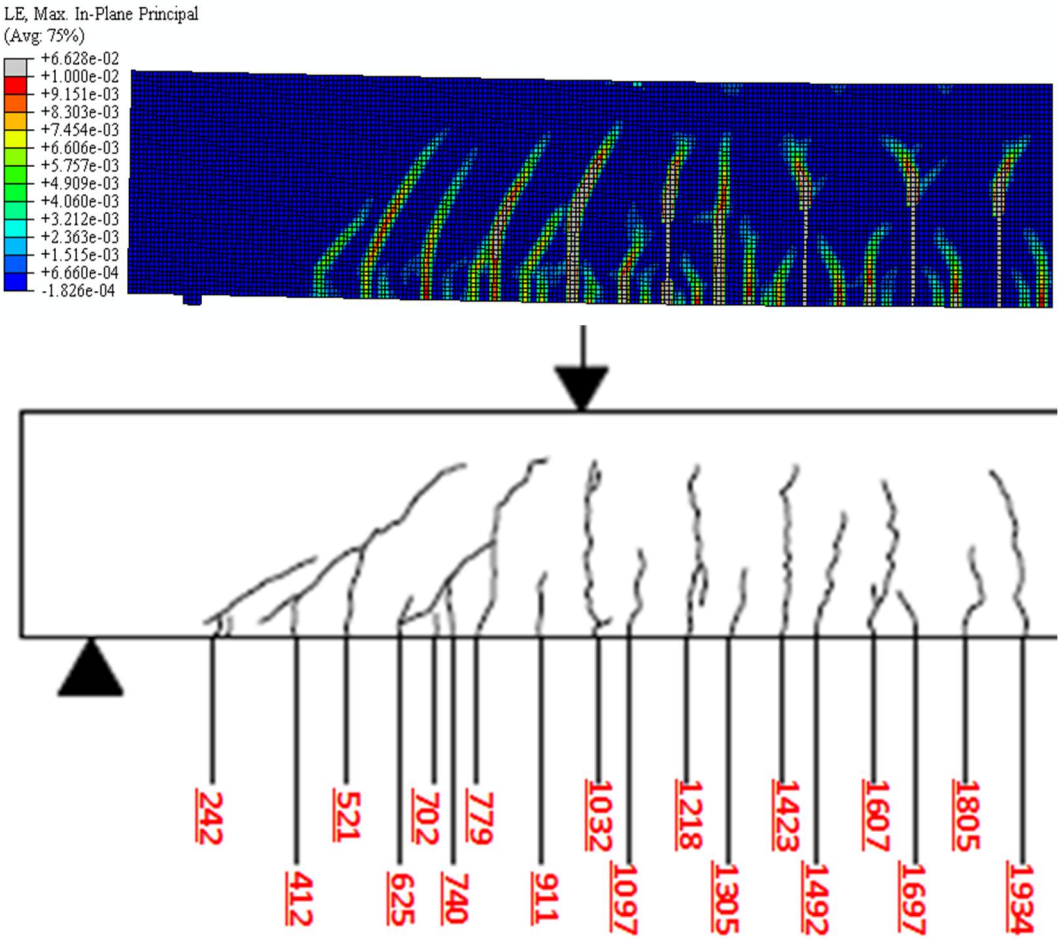

Figure 4.6 FE predicted versus test crack pattern at failure for Specimen LP2SP1000

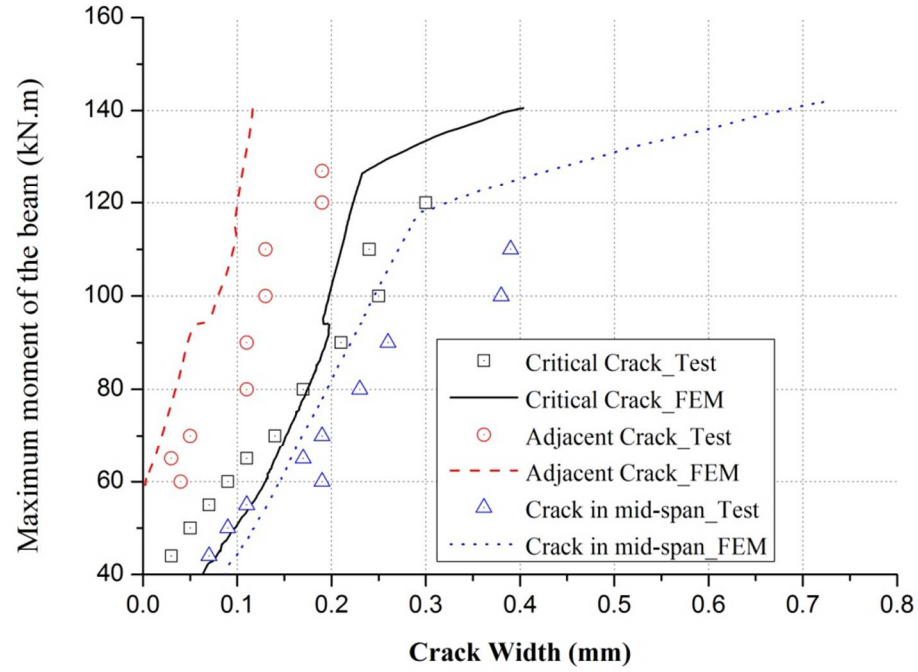

Figure 4.7 FE predicted and test moment-crack width curves for typical cracks of Specimen LP2SP1000

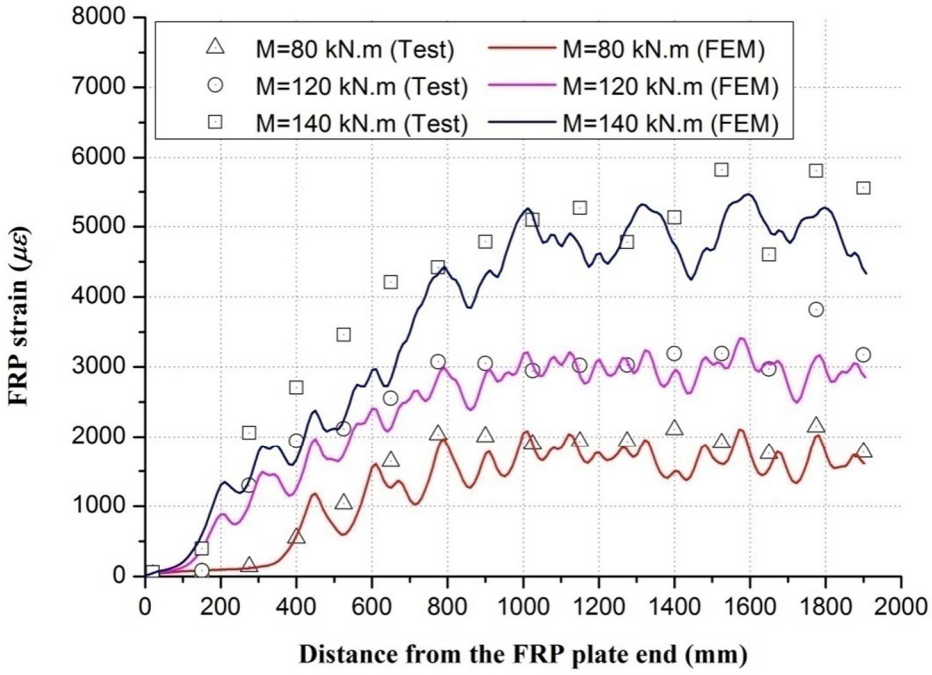

Figure 4.8 FE predicted and test FRP strain distributions at different load levels for Specimen LP2SP1000

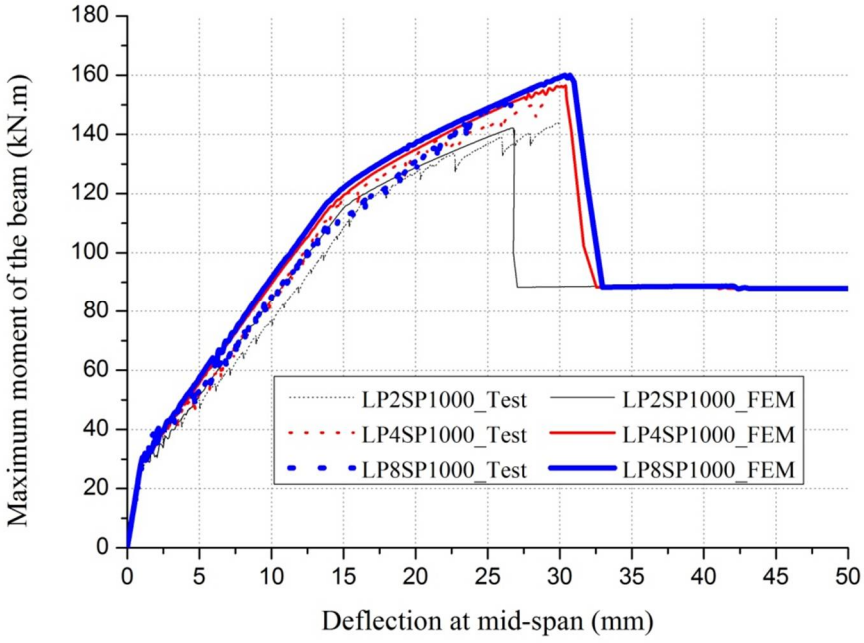

Figure 4.9 FE predicted versus test moment-deflection curves for Series II specimens

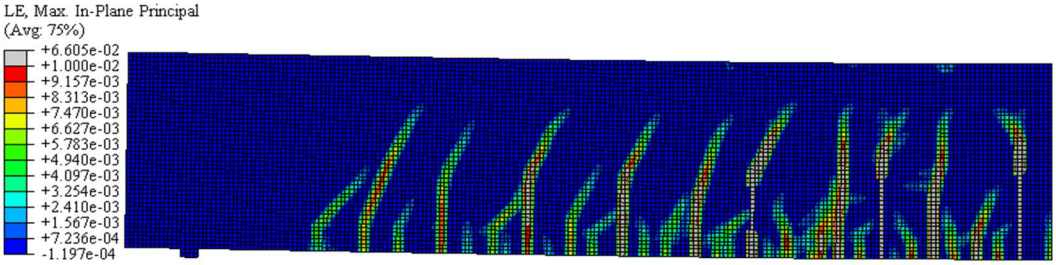

(a) LP4SP1000-FEM

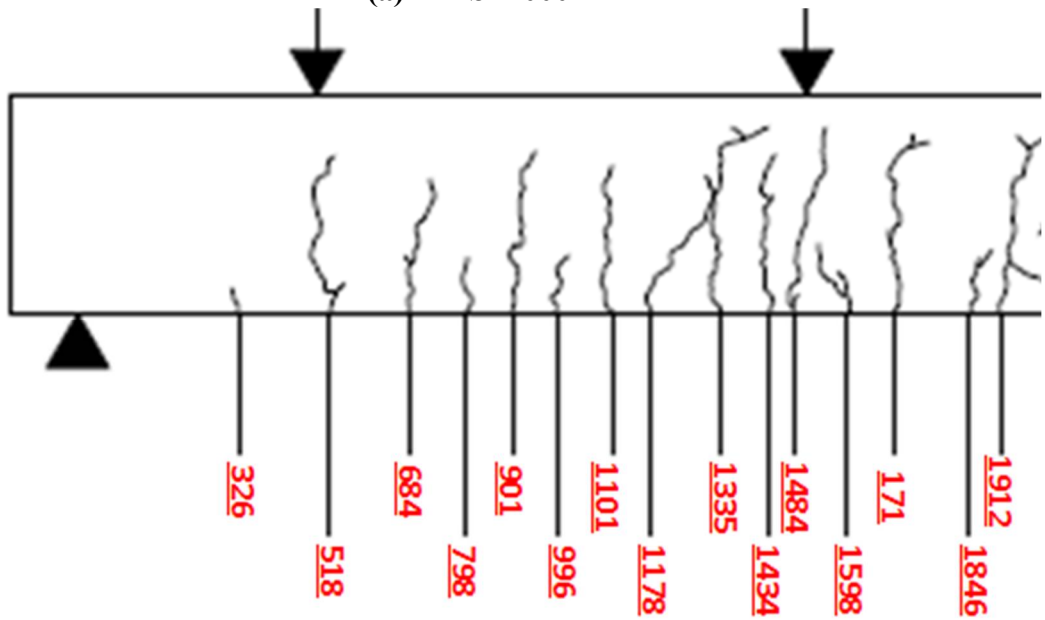

(b) LP4SP1000-Test

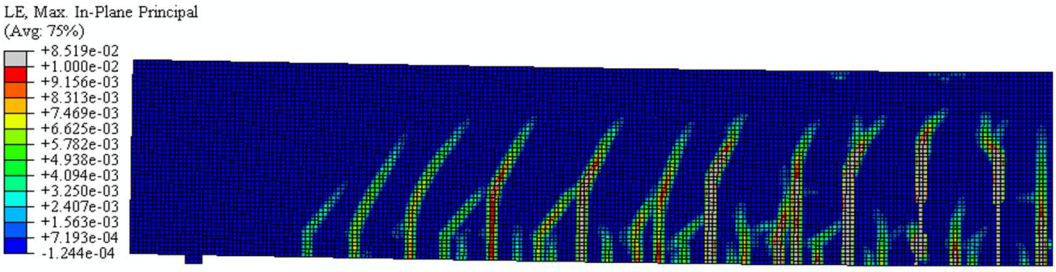

(c) LP8SP1000-FEM

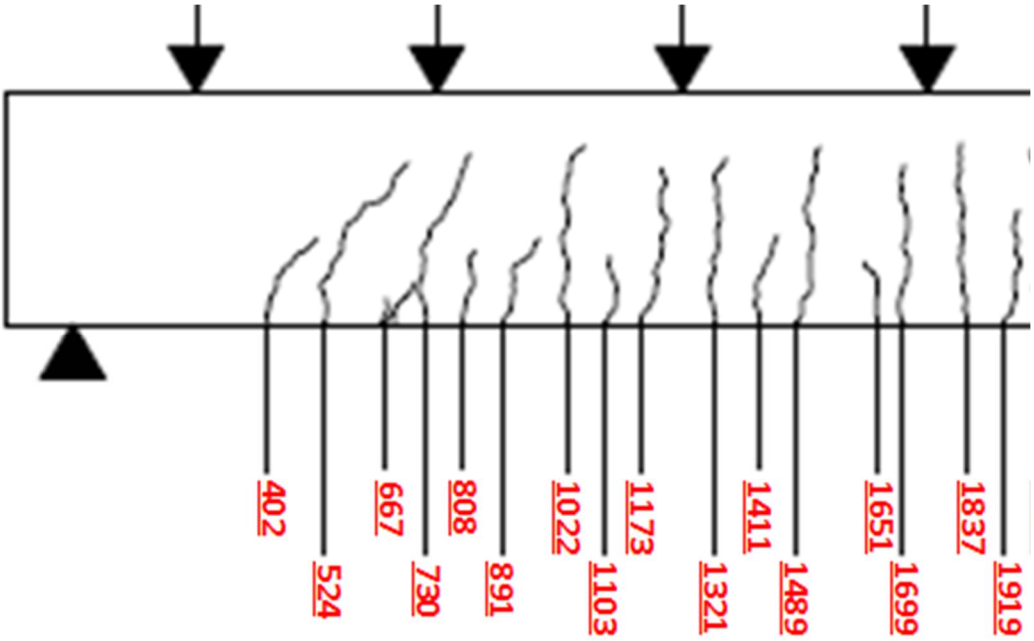

(d) LP8SP1000-Test

Figure 4.10 FE-predicted versus test crack patterns at failure

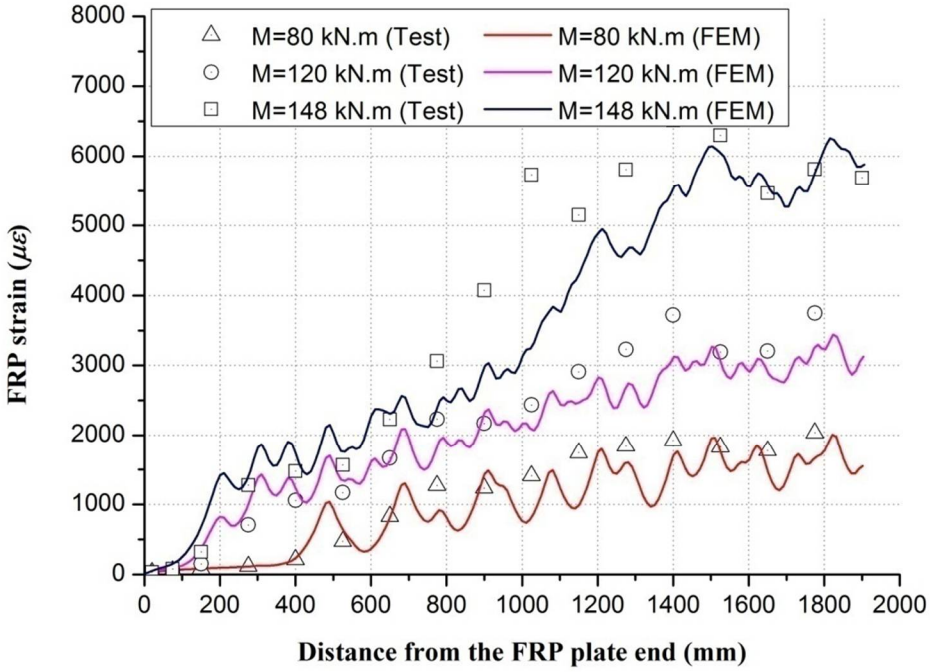

(a) Specimen LP4SP1000

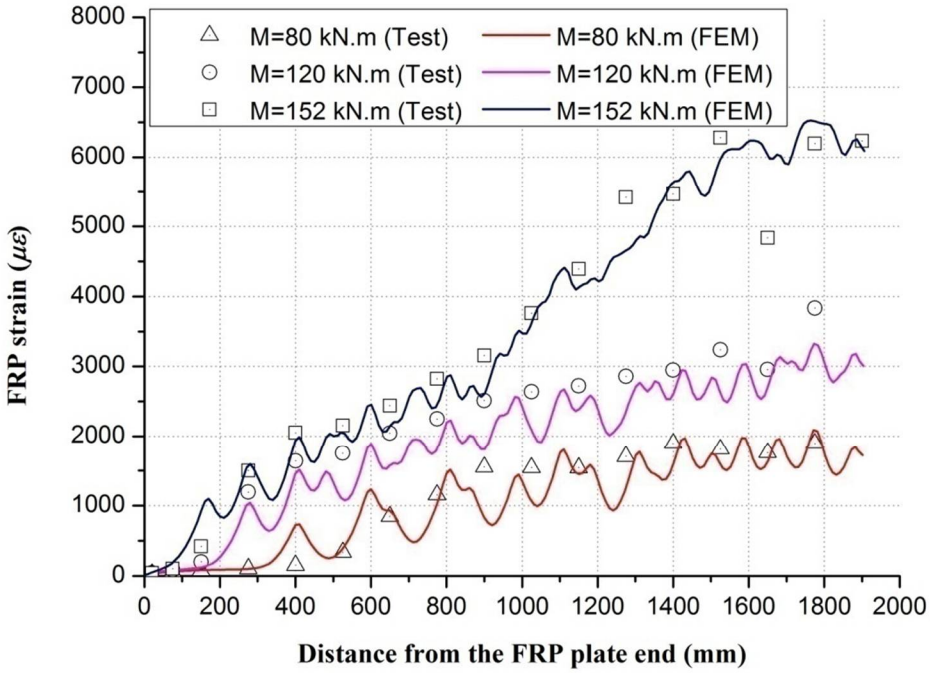

(b) Specimen LP8SP1000

Figure 4.11 FE predicted and test FRP strain distributions at different load levels for Specimens LP4SP1000 and LP8SP1000

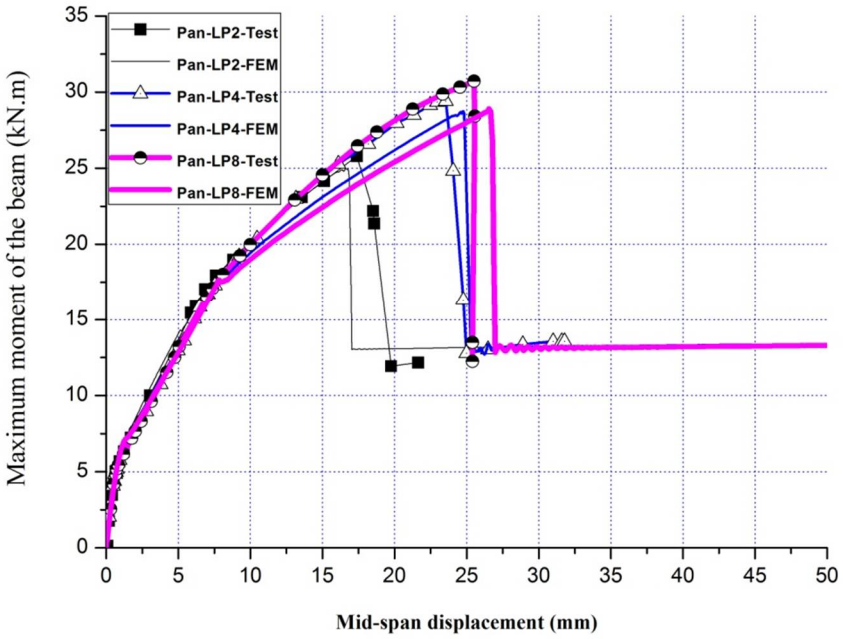

Figure 4.12 Moment-displacement curves for specimens in Pan et al. (2009)

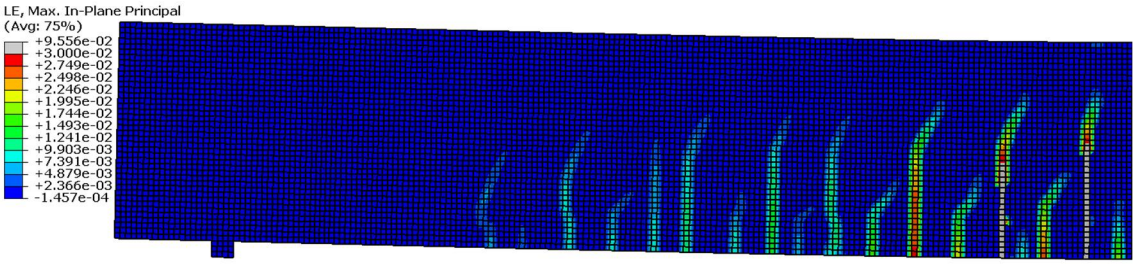

(a) D2-P2-L2

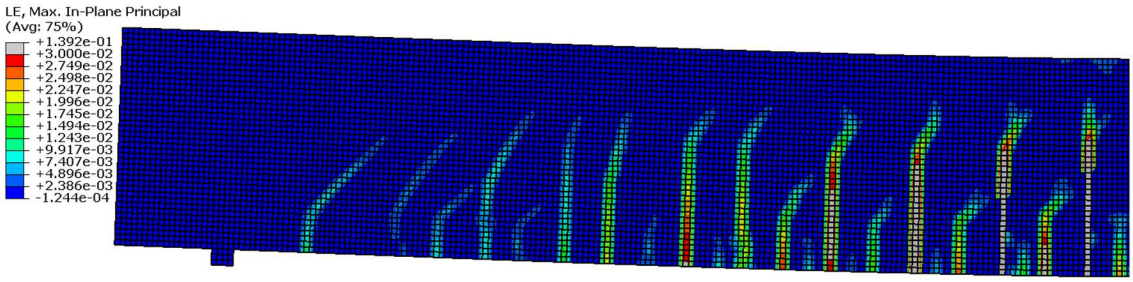

(b) D3-P4-L2

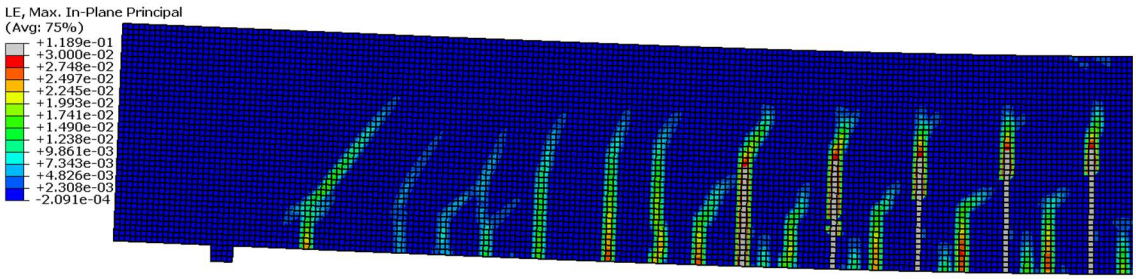

(c) D4-P8-L2

Figure 4.13 FE crack patterns at ultimate failure for specimens in Pan et al. (2009)

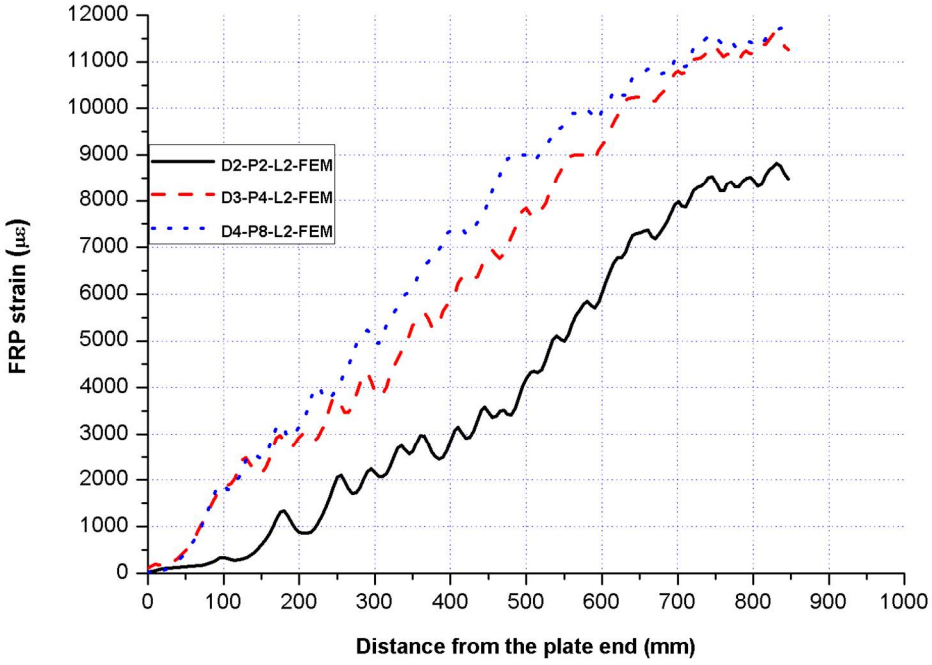

Figure 4.14 FRP strains at ultimate load for Specimens in Pan et al. (2009)

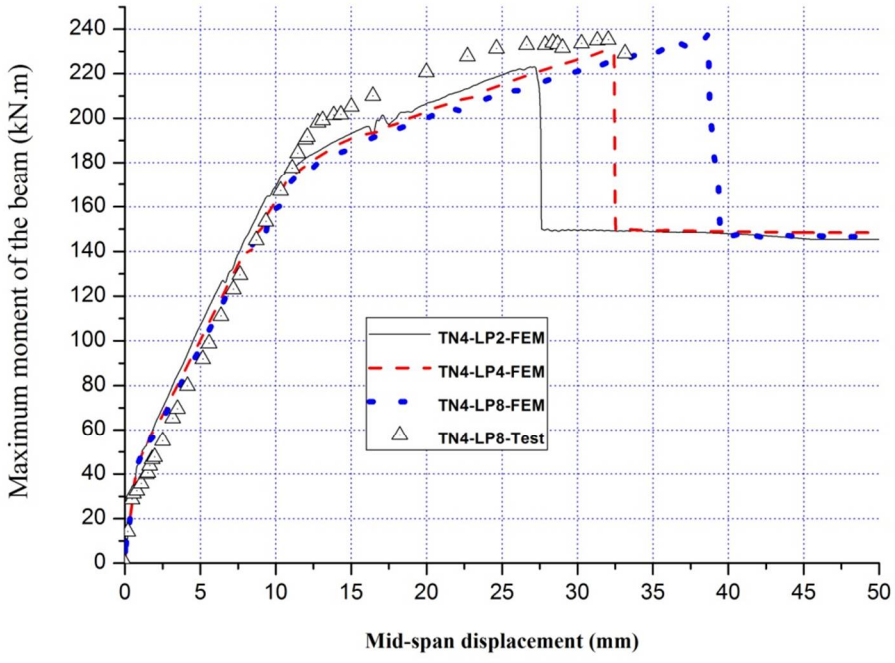

Figure 4.15 Moment-displacement curves for Series TN4 in Mazzotti and Savoia (2009)

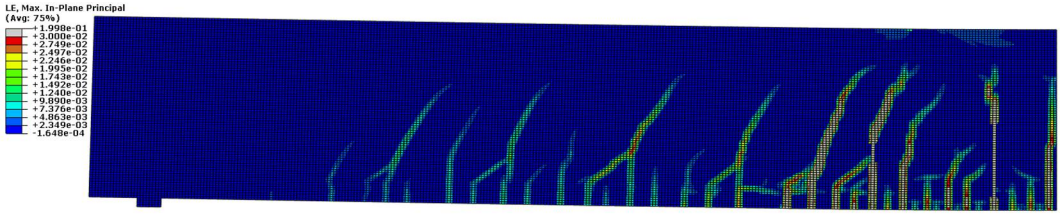

(a) TN4-LP2

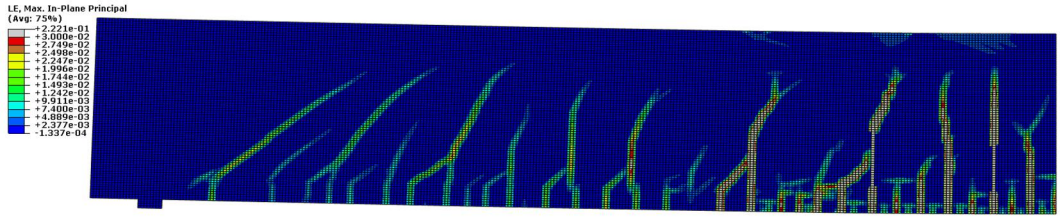

(b) TN4-LP4

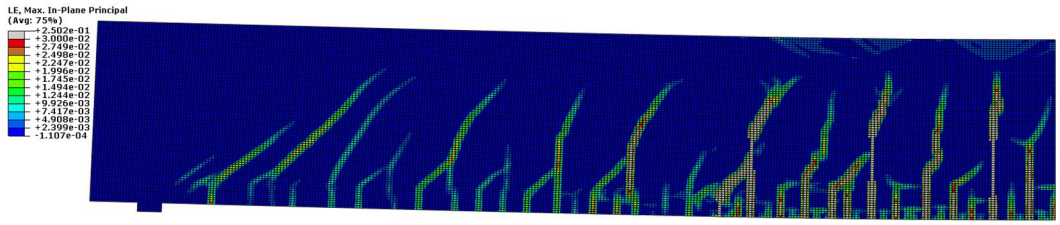

(c) TN4-LP8

Figure 4.16 FE crack patterns ultimate failure for Series TN4 in Mazzotti and Savoia (2009)

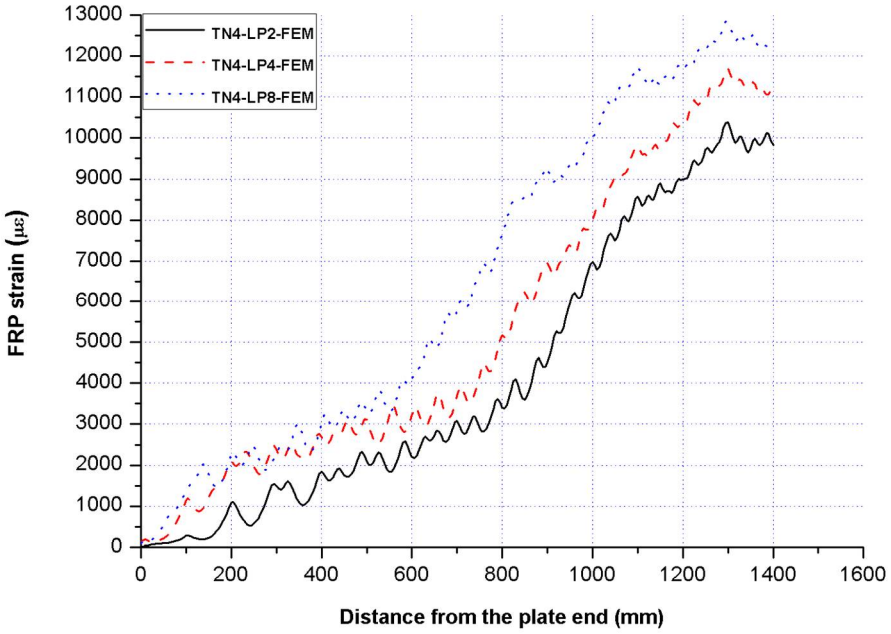

Figure 4.17 FRP strains at ultimate load for Series TN4 in Mazzotti and Savoia (2009)

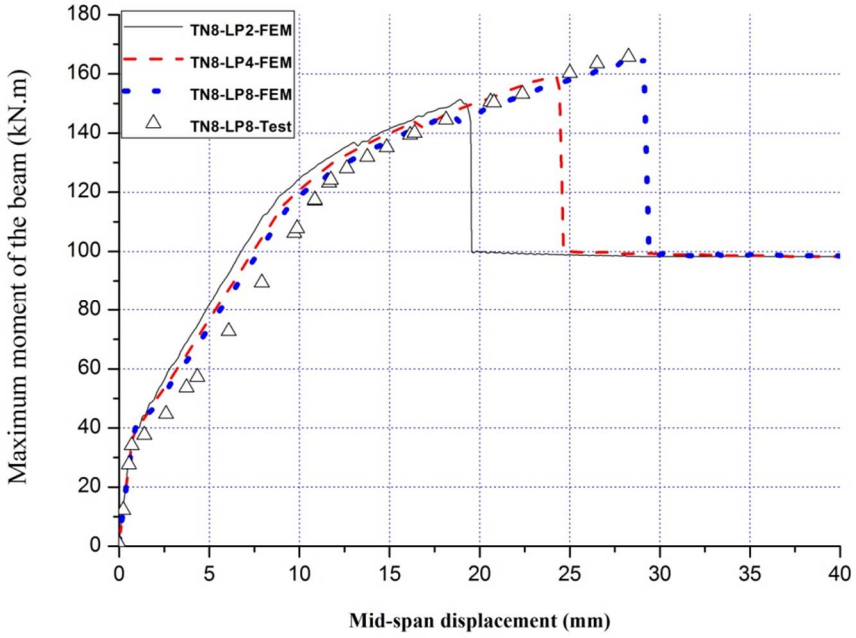

Figure 4.18 Moment-displacement curves for Series TN8 in Mazzotti and Savoia (2009)

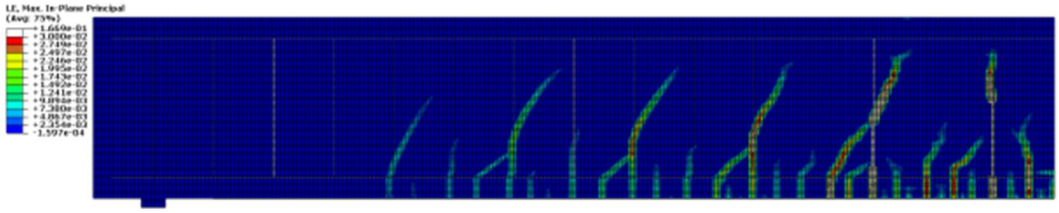

(a) TN8-LP2

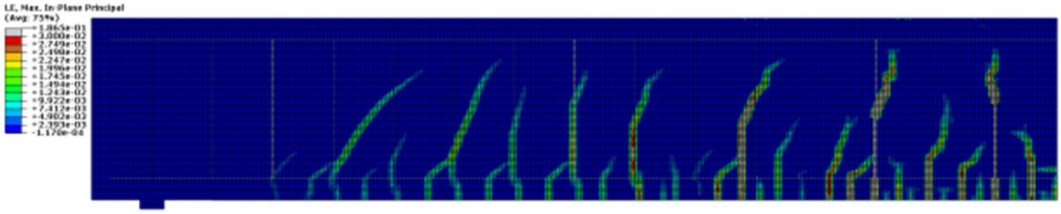

(b) TN8-LP4

(c) TN8-LP8

Figure 4.19 FE crack patterns at ultimate failure for Series TN8 in Mazzotti and Savoia (2009)

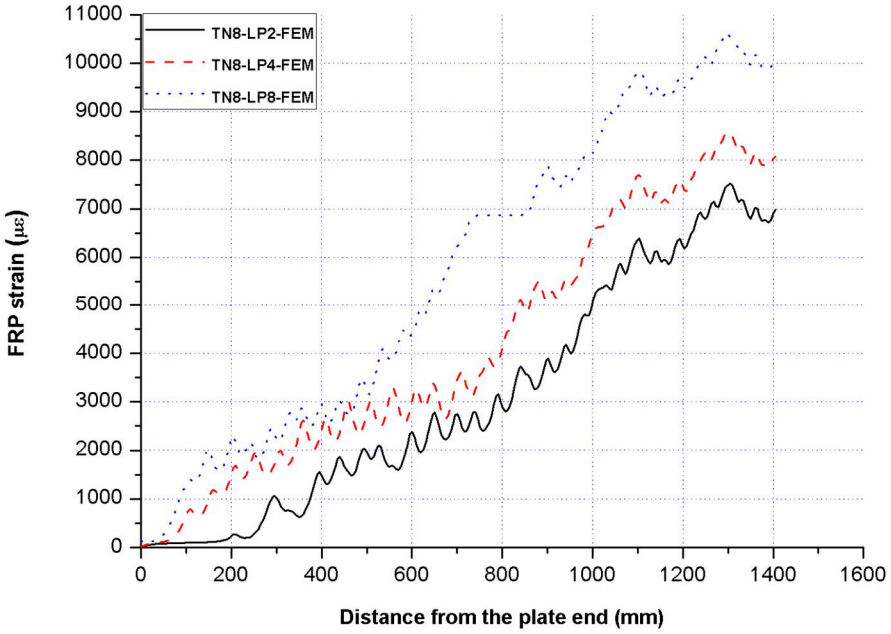

Figure 4.20 FRP strains at ultimate load for Series TN8 in Mazzotti and Savoia (2009)

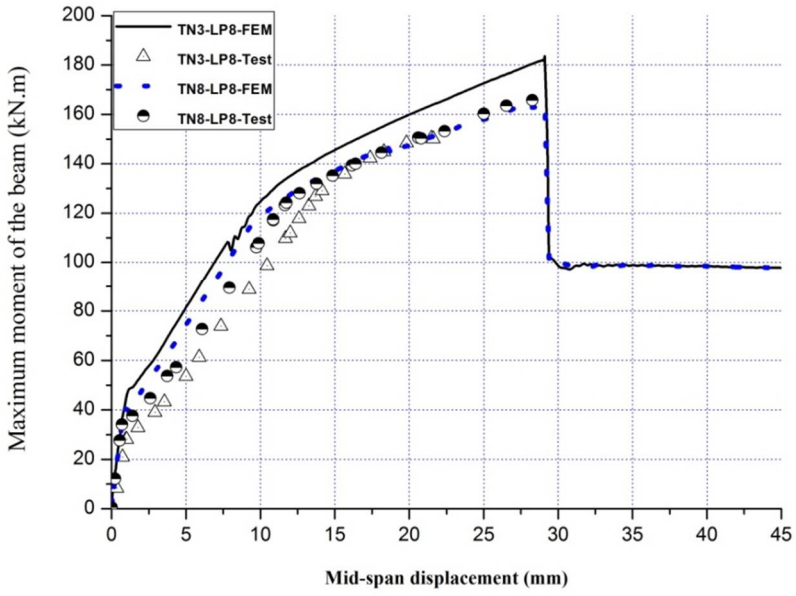

Figure 4.21Comparison of moment-displacement curves for Specimens TN3-LP8 and TN8-LP8 in Mazzotti and Savoia (2009)

CHAPTER 5

EVALUATION OF IC DEBONDING STRENGTH MODELS THAT CATER FOR DIFFERENT LOAD DISTRIBUTIONS

5.1 INTRODUCTION

Both the experimental observations presented in Chapter 3 and the extensive finite element results described in Chapter 4 have indicated that the effect of load distribution on IC debonding can be significant. Therefore, a robust design model against IC debonding should consider this effect. Three existing IC debonding strength models [i.e. the models of *fib* (2001), Chen et al. (2006), and Rosenboom and Rizkalla (2008)] have the potential to account for the effect of load distribution on IC debonding of FRP-plated RC beams although they were proposed and verified using on results of beams tested under one- or two-point loading. This chapter first presents an assessment of the ability of these three IC debonding models in accurately predicting the IC debonding strength under different loading distributions using limited test data, including the test data presented in Chapter 3, as well as the

numerical results presented in Chapter 4.

5.2 EXISTING IC DEBONDING STRENGTH MODELS

A brief summary of the three existing IC debonding strength models (e.g. *fib* 2001; Chen et al. 2006; Rosenboom and Rizkalla 2008) mentioned above is presented in this section before they are assessed using test and numerical results.

5.2.1 *fib*'s (2001) approach

The *fib* (2001) guideline includes three different approaches for predicting IC debonding of FRP-plated RC beams. Among them, the second approach can be applied to predict IC debonding failure for different load distributions. This approach is based on fracture mechanics and calibrated using results of tests under one- or two-point loading. It assumes that IC debonding of FRP-plated RC beams occurs when the stress difference in the FRP soffit plate between two adjacent cracks exceeds the failure criterion as expressed below:

$$\Delta\sigma_f \geq \Delta\sigma_{f,IC} \tag{5.1}$$

The procedure of this approach includes three main steps, which are given as follows.

Step 1: Determine the most unfavourable spacing of flexural cracks.

The crack spacing has an important influence on IC debonding and can be calculated

with the assumption that the shear stresses of both the steel-to-concrete and FRP-to-concrete interfaces are constant between two significant cracks. The average crack spacing, S_{rm}, can be expressed as follows:

$$S_{rm} = 2\frac{M_{cr}}{Z_m}\frac{1}{\left(\sum \tau_{fm} b_f + \sum \tau_{sm} d_s \pi\right)} \tag{5.2}$$

where M_{cr} is the bending moment causing initial cracking; Z_m is the mean lever arm of reinforcements; τ_{fm} and τ_{sm} are the mean bond stress of the external and the internal reinforcements respectively; b_f is the width of the FRP soffit plate; and d_s is the diameter of internal reinforcement. They can be determined by the following equations:

$$\tau_{sm} = 1.85 f_{ctm} \tag{5.3}$$

$$\tau_{fm} = 0.44 f_{ctm} \tag{5.4}$$

$$M_{cr} = \frac{1.64 f_{ctm} b h^2}{6} \tag{5.5}$$

$$Z_m = 0.85\frac{\left(\sum h E_f A_f + \sum d E_s A_s\right)}{\left(\sum E_f A_f + \sum E_s A_s\right)} \tag{5.6}$$

where f_{ctm} is the mean value of cylinder compressive strength of concrete; b is the width of the concrete beam; h is the height of the concrete beam; A_f and A_s are the total cross-sectional areas of the FRP soffit plate and the steel tension bars, respectively; and E_f and E_s are the elastic moduli of the FRP soffit plate and the steel tension bars, respectively.

Step 2: Determine the tensile stress of the FRP plate and the stress difference between two adjacent cracks

The tensile stress of the FRP plate can be determined using a section analysis taking into account strain compatibility and force equilibrium. The stress difference between two adjacent cracks along the beam, $\Delta\sigma_f$, is subsequently obtained for comparison with the maximum possible increase in the tensile stress of the FRP soffit plate, which is determined in Step 3.

Step 3: Determine the maximum possible increase in the tensile stress in the FRP soffit plate, $\Delta\sigma_{f,IC}$

A complex procedure to determine the maximum possible increase in the tensile stress in the FRP soffit plate is given in *fib* (2001), and can be briefly summarised as follows. The equation for determining $\Delta\sigma_{f,IC}$ is dependent on the minimum stress between the two cracks, σ_{min}.

- For cases with $\sigma_{min} \leq \left(c_3 E_f / S_{rm} - c_4 \left(S_{rm}/4t_f\right)\sqrt{f_{ck} f_{ctm}}\right)$ (MPa), in which c_3 and c_4 are constants and equal to 0.185 and 0.285, respectively,

$$\Delta\sigma_{f,IC} = \Delta\sigma_{f,IC}^{A} - \left(\Delta\sigma_{f,IC}^{B} - \Delta\sigma_{f,IC}^{A}\right)\sigma_{min}/\sigma_{f,IC}^{B} \tag{5.7}$$

where σ_{min} is the minimum stress between the two cracks; $\Delta\sigma_{f,IC}$ is the maximum possible increase in the tensile stress in the soffit plate; f_{ck} is the characteristic value of cylinder compressive strength of concrete; and $\Delta\sigma_{f,IC}^{A}$, $\Delta\sigma_{f,IC}^{B}$ and $\sigma_{f,IC}^{B}$ are given by the following equations, respectively.

$$\Delta\sigma_{f,IC}^{A} = c_1\sqrt{E_f\sqrt{f_{ck}f_{ctm}/t_f}} \tag{5.8}$$

$$\Delta\sigma_{f,IC}^{B} = \sqrt{\frac{c_1^2 E_f\sqrt{f_{ck}f_{ctm}}}{t_f} + \left(\sigma_{f,IC}^{B}\right)^2} - \sigma_{f,IC}^{B} \tag{5.9}$$

$$\sigma_{f,IC}^{B} = c_3 E_f/S_{rm} - c_4\left(S_{rm}/4t_f\right)\sqrt{f_{ck}f_{ctm}} \tag{5.10}$$

where c_1 and c_2 are constants and equal to 0.23 and 1.44, respectively.

- For cases with $\sigma_{min} > \left(c_3 E_f/S_{rm} - c_4\left(S_{rm}/4t_f\right)\sqrt{f_{ck}f_{ctm}}\right)$(MPa).

$$\Delta\sigma_{f,IC} = \sqrt{\frac{c_1^2 E_f\sqrt{f_{ck}f_{ctm}}}{t_f} + (\sigma_{min})^2} - \sigma_{min} \tag{5.11}$$

5.2.2 Chen et al.'s (2006) model

A series of cracks exist in an FRP-plated RC beam. As a result, occurrence and propagation of IC debonding depends on not only the tensile force in the FRP plate at the critical crack but also that at the adjacent crack (Figure 5.1). Based on this observation, an FRP-to-concrete bonded joint in which both ends of the FRP plate are subjected to tension (Figure 5.2) can be used to represent the IC debonding mechanism. Analytical solutions for the debonding process of the FRP plate in such bonded joints were given by Teng et al. (2006) and Chen et al. (2007).

A bilinear bond-slip relationship of FRP-to-concrete interface was used in Teng et al. (2006), and led to an implicit solution for the debonding of the FRP-to-concrete bonded joint. Chen et al. (2007) modified Teng et al.'s (2006) solution by adopting a linearly softening bond-slip relationship (i.e. without the ascending branch). This

modification by Chen et al. (2007) led to an explicit and simple solution for the ultimate load of P_1 (the larger tensile force acting on the FRP plate) without a significant loss of accuracy. The solution for the ultimate load of P_1 is explicitly given as follows

$$P_{1,u} = \begin{cases} b_p\sqrt{2G_f E_p t_p}\,(1-\beta^2)^{-1/2} & \text{if} \quad L \geq a_u \\ b_p\sqrt{2G_f E_p t_p}\,\sin(\lambda L)\left[1-\beta\cos(\lambda L)\right]^{-1} & \text{if} \quad L < a_u \end{cases} \tag{5.12}$$

where

$$\beta = \frac{P_2}{P_1} \tag{5.13a}$$

$$a_u = \frac{1}{\lambda}\arccos\beta \tag{5.13b}$$

$$\lambda^2 = \frac{\tau_f{}^2}{2G_f}\frac{1}{E_p t_p} = \frac{\tau_f}{\delta_f}\frac{1}{E_p t_p} \tag{5.13c}$$

in which β is the ratio between the smaller tensile force (i.e.at the adjacent crack of IC debonding in an FRP-plated RC beam) and the larger tensile force (at the critical crack of IC debonding in an FRP-plated RC beam); τ_f is the peak shear stress from the bond-slip model; δ_f is the slip when the interfacial shear stress reduces to zero and $G_f = \tau_f\delta_f/2$ is the fracture energy of the interface; and E_p and t_p are the elastic moduli and thickness of the FRP plate, respectively.

An IC debonding strength model has been proposed by Chen et al. (2006) based on the analytical solution for the ultimate load of P_1 given by Eq. 5.12. The IC debonding strength can be expressed in terms of the maximum stress in the plate at the critical crack by dividing the ultimate force by the plate cross-sectional area $b_p t_p$,

as follows:

$$\sigma_{IC} = \alpha\beta_\sigma\beta_w\beta_L\sqrt{\frac{E_p\sqrt{f_c'}}{t_p}} \tag{5.14}$$

in which f_c' is the cylinder compressive strength of concrete; β_σ is the coefficient reflecting the effect of the ratio of the plate stress at the adjacent crack to that at the critical crack (α_σ); β_w is the coefficient representing the effect of the ratio between plate width and concrete beam width; β_L is the coefficient for the effect of spacing between the critical crack and the adjacent crack. These coefficients are defined as follows:

$$\beta_\sigma = \begin{cases} \dfrac{1}{\sqrt{1-\alpha_\sigma^2}} & if \quad L \geq L_e \\ \dfrac{1}{1-\alpha_\sigma \cos\dfrac{\pi L}{2L_e}} & if \quad L < L_e \end{cases} \tag{5.15a}$$

$$\beta_w = \begin{cases} \dfrac{b_p + 2\delta}{b_p} & if \quad b_p + 2\delta < b_c \\ \dfrac{b_c}{b_p} & if \quad b_p + 2\delta \geq b_c \end{cases} \tag{5.15b}$$

$$\beta_L = \begin{cases} 1 & if \quad L \geq L_e \\ \sin\dfrac{\pi L}{2L_e} & if \quad L < L_e \end{cases} \tag{5.15c}$$

The effective bond length in Eq. 15 is given by

$$L_e = \frac{2}{\pi}\sqrt{\frac{E_p t_p}{\sqrt{f_c'}}}\arccos\alpha_\sigma \tag{5.15d}$$

The definition of the effective bond length in Eq. 5.15d reduces to that in Chen and Teng (2001) when the stress ratio α_σ is zero. In Chen at al. (2006), for ease of

assessment, the stress ratio α_σ was approximated by the ratio between bending moments, M_{IC} and M_{adj} at the critical crack and its adjacent crack respectively. However, this approximation may result in errors especially when the section at the critical crack experiences abrupt stress/strain changes in the component materials, such as yielding of steel bars, but the other section at the adjacent crack remains elastic. In order to exclude such errors, the present study resorts to section analysis to determine the stress states of the FRP plate at different locations. The width ratio coefficient given by Eq. 5.15b is believed to reflect better the width ratio effect than that in Chen and Teng (2001). Based on a test database collected from the literature, δ=10mmwas adopted by Chen et al. (2006). α in Eq. 5.3 needs to be reduced from a value of 0.427 in Chen and Teng's (2001) bond strength model to 0.528 for the model to provide best-fit predictions for beams under one- or two-point loading (Chen et al. 2006). The bond length, *L*, is the spacing between the critical crack and its adjacent crack in the direction of debonding propagation.

The ultimate moment of the FRP-plated RC beam can be obtained using an iteration process, whose flowchart is given in Figure 5.3. The beam is first assigned an initial value for its maximum moment, M_0, to calculate the initial moments of sections along the beam. The FRP strain of each section corresponding to the load level can be determined from the section analysis described in the next section. With the known FRP strain of each section, the force ratio, α_σ, is determined by the ratio of the FRP strain at the adjacent crack to the FRP strain at the critical crack. The critical crack is assumed to occur at any position and the adjacent crack to occur at a position in the direction of decreasing moment. The spacing between these two cracks is assumed to be fixed for all the beam sections. With the given force ratio, α_σ, the

debonding strain of FRP at a specific section can be calculated by Eq. 5.14. During the iteration process as shown in Figure 5.3, if the strain difference between the actual FRP strain determined in Step 2 and the debonding strain criterion in Step 4 is available after Step 4, the minimum strain difference along the beam can be found. If the minimum strain difference is smaller than 10.0 $\mu\varepsilon$, the iteration process ends, otherwise, the applied section moment is changed and Steps 2 to 5 are repeated.

5.2.3 Rosenboom and Rizkalla's (2008) model

An analytical model for predicting IC debonding was proposed by Rosenboom and Rizkalla (2008), which was based on the characterization of the interfacial shear stress. The procedure for this analytical model consists of the following nine steps:

Step1: Determine the moment resistance at the initiation of yielding of tension steel bars,M_y, and the corresponding strain of the FRP plate, ε_{fy};

Step2: Set an initial value for the FRP strain at IC debonding, ε_{ic}, which should be larger than ε_{fy};

Step3: Calculate the nominal moment resistance of the section at IC debonding, M_{db}, with the assumed debonding strain in Step2;

Step4: Determine the maximum interfacial shear stress induced by the applied load, τ_{wmax}, using, using Eq. 5. 16

$$\tau_{wmax} = E_f t_f \frac{\varepsilon_{ic} - \varepsilon_{fy}}{a - x_y} \tag{5.16}$$

where E_f is the elastic moduli of the bonded plate; t_f is the thickness of the bonded

plate; a is the distance from the support to the location where the maximum moment along the beam exists;x_y isthe distance from the support to the location of first yielding of internal tensile steel, and is given by

$$x_y = \begin{cases} a\frac{M_y}{M_{db}}, & \text{for } 3-\text{or } 4-\text{point bending} \\ -\frac{L^2}{8M_{db}}\left(-\frac{4M_{db}}{L}+\sqrt{\left(\frac{4M_{db}}{L}\right)^2-16\left(\frac{M_{db}}{L^2}\right)M_y}\right), & \text{for UDL} \end{cases} \quad (5.17)$$

in which UDL indicates uniformly distributed loading.

Step5: Determine the maximum interfacial shear stress induced by stress concentration, τ_{scmax}, by the following equation:

$$\tau_{scmax} = 3\left(1.1-\frac{M_y}{M_{db}}\right)\sqrt{f_c'} \quad (5.18)$$

Step 6: Calculate the total maximum interfacial shear stress τ_i by superposing τ_{wmax} and τ_{scmax};

Step 7: Adjust the IC debonding strain ε_{ic} until τ_i is equal to the critical value $\tau_{cmax} = 1.8\left(0.63\left(f_c'\right)^{0.5}\right)$;

Step 8: Calculate the maximum strain in the FRP plate from Eq. 5.19.

$$\varepsilon_{cmax} = \varepsilon_{ic} + 0.114\frac{\tau_{scmax}}{\sqrt{E_f t_f}} \le \varepsilon_u \quad (5.19)$$

Step9: If the maximum strain in the FRP plate,ε_{cmax}, is greater than ε_u, the member is deemed to fail by FRP rupture.

5.3 SECTION ANALYSIS

A sectional analysis is required to determine the FRP strain/stress in an FRP-plated RC beam based on a known section moment or to determine the section moment based on a known FRP strain. In an analysis for a cracked section of a reinforced concrete member, the contribution of concrete in resisting tension has been widely neglected (Owen 2006). However, unlike plain concrete, concrete with internal or external reinforcement could still carry some tension through the bond between the reinforcement and the concrete so that the reinforced concrete has a stiffer response than a bare bar. Nayal and Rasheed (2004) compared the results of a cracked section analysis with those from tests, and the comparison has indicated that neglecting the tensile resistance of concrete leads to a softer response than that from tests. This effect is referred to as the tension stiffening effect, and has been widely investigated for concrete members with internal steel bars. Different tensions stiffening models via revising the stress-strain constitutive models of either the steel tension bars or the surrounding concrete or both have been proposed to capture this effect for conventional steel reinforced concrete (e.g CEN 2004; ACI 2008).

Existence of both internal steel tension bars and an external FRP soffit plate in FRP-plated RC beams means that the tension stiffening effect is more complicated and more significant. Therefore consideration of the tensile resistance of concrete in section analysis is essential for accurately predicting the behaviour of FRP-plated RC beams. However a reliable tension stiffening model for FRP-plated RC beam is not yet available for use in section analysis. Development of a reliable tension stiffening model for FRP-plated RC beams is out of the scope of this thesis although such a

reliable tension stiffening model is essential for accurately predicting the FRP strain based a given section moment or for accurately predicting the section moment based a given FRP strain. In this thesis, the tension stiffening effect is considered by revising the tensile strain-stress curve of concrete. A constitutive model for concrete under tension, which is similar to that used in FE analysis, is adopted and simply calibrated by comparing the FRP strains from section analysis with those from FE modelling.

The constitutive model for concrete under tension is given in terms of stress-crack displacement response, and such a stress-crack displacement response is converted to one in terms of stress-strain response via an assumed 'characteristic length'. The assumed 'characteristic length' is the only variable to be calibrated by comparing the FRP strains from the section with those from FE analysis. It should be noted that only one value of the assumed characteristic length exists for all cases, and the value is fixed once it is calibrated. Comparison between the FRP strains from section analysis and those from FE modelling indicates that this simple approach would be reliable for the limited cases already investigated using FE modelling or cases with similar geometrical and mechanical characteristics, although its suitability for extrapolation to more general cases should be further verified.

Concrete under tension is assumed to behave linear-elastically prior to concrete cracking with its elastic moduli being taken to be the initial elastic moduli of concrete under compression[e.g. $E_c = 4730\sqrt{f_c'}$ in ACI 318(2008).)]. After the concrete strain under tension exceeds the cracking strain, the stress of concrete

decreases with increase in the concrete strain. It is described in terms of stess-crack displacement response as follows.

$$\frac{\sigma_t}{f_t} = \left[1 + \left(c_1 \frac{w_t}{w_{cr}}\right)^3\right] e^{\left(-c_2 \frac{w_t}{w_{cr}}\right)} - \frac{w_t}{w_{cr}}(1 + c_1^3) e^{(-c_2)} \tag{5.21}$$

$$w_{cr} = 5.14 \frac{G_F}{f_t} \tag{5.22}$$

In the above equations, w_t is the crack displacement; w_{cr} is the crack displacement at the complete release of concrete stress; G_F is the concrete fracture energy (the area covered by the strain-stress curve of concrete under uniaxial tension); $c_1$andc_2 are constants determined from tensile tests of concrete and can be set to equal to 3.0 and 6.93, respectively, for normal concrete. f_t and G_F can be estimated from the cylinder compressive strength based on the equations in CEB-FIP (1993), if no specific tests are provided for the determination of values of these two parameters.

$$f_t = 1.4 \left(\frac{f_c' - 8}{10}\right)^{(2/3)}, \qquad \text{MPa} \tag{5.23}$$

$$G_F = (0.0469 d_a^2 - 0.5 d_a + 26) \left(\frac{f_c'}{10}\right)^{0.7}, \qquad \text{Nm/m}^2 \tag{5.24}$$

where d_a represents the maximum aggregate size, which can be assumed to be 20 mm if no test data is available.

For use in the section analysis, the crack displacement needs to be converted to the concrete strain. In the FE modelling presented in Chapter 4, the crack opening

displacement is transformed to the concrete strain using the characteristic length of concrete elements, which is $\sqrt{2}e$, where e is the length of the concrete element. As there is no actual characteristic length in the section analysis, an assumed 'characteristic length' is used to convert the crack displacement to the crack strain. Obviously, different concepts are used for treating concrete cracks in FE modelling and section analysis and therefore different characteristic lengths should be used for these two modelling methods. The value of the characteristic length of the section analysis is determined by comparing the FRP strains with that from the FE analysis. It should be noted that once a reasonable 'characteristic length' is determined, it will be used for all the section analysis.

Figures 5.4a to 5.4c compare the FRP strain distributions of Specimen LP2BS210 from FE analysis in the parametric study of Chapter 4 with those from section analysis using different characteristic lengths. With an increase of the characteristic length of concrete in the section analysis, the FRP strain tends to increase at the same load level. The maximum FRP strain at debonding from the section analysis with the characteristic length of 7.0 mm (i.e. 0.5 times that used in FE analysis) is smaller than its FE counterpart by about 700 με, while the maximum FRP strain at debonding from the section analysis with the characteristic length of 14 mm (i.e. equal to that used in FE analysis)is smaller than its FE counterpart by about 150 $\mu\varepsilon$. With the characteristic length being 28 mm (i.e. 2.0 times that in FE analysis), a good match in the FRP strain distribution at different load levels is achieved between the section analysis and the FE analysis. Comparison of the FRP strain for other specimens, which is not presented herein, also indicates that 28 mm is the best candidate for the assumed character length of the section analysis. Therefore, a

characteristic length of 28 mm is used in the section analysis for cases presented in this thesis.

The constitutive models of the materials are similar to those used in the finite element analysis in Chapter 4.In particular, the steel reinforcement is modelled as an elastic-perfectly plastic material; the FRP plate is assumed to behave linear elastically prior to tensile rupture. Tension resisted by concrete is also considered by using a constitutive model of concrete similar to that used in the FE analysis presented in Chapter 4. All the corresponding material parameters are defined based on material test data if available; otherwise, typical data from the manufacturer are adopted.

The uniaxial compressive stress-strain equation for concrete proposed by Saenz (Eq. 5.20) is adopted:

$$\sigma = \frac{\alpha\varepsilon}{1 + \left[\left(\alpha\varepsilon_p/\sigma_p\right) - 2\right]\left(\varepsilon/\varepsilon_p\right) + \left(\varepsilon/\varepsilon_p\right)^2} \tag{5.20}$$

where σ_p is set to be equal to the cylinder compressive strength of concrete,$f_c^{'}$ [in some papers only the cube compressive strength, f_{cu},is reported, and in such cases it is assumed that $f_c^{'} = 0.8f_{cu}$ (Lu et al. 2007)];ε_p is the concrete axial compressive strain when the concrete reaches the ultimate compressive stress and is set to be equal to 0.002; α is the initial elastic moduliof concrete and can be approximated from the concrete compressive strength according national codes (e.g. $E_c = 4730\sqrt{f_c^{'}}$ in ACI 318(2008).

Further the plane section assumption together with strain compatibility is used in the section analysis to determine strain and stress distributions along the section. The concrete is divided into a sufficiently large number of horizontal layers (e.g. 1000 layers for beams of 450 mm in height)over the height, with each layer havingthe same strain. Generally the more layers it is divided, more accuracy is obtained. 1000 layers is sufficient for beam of 450 mm in height and affordable in the computation cost.

5.4 COMPARISONS BETWEEN STRENGTH MODELS' PREDECTIONS AND TEST RESULTS

The test data of IC debonding of FRP-plated RC beams under different load distributions used next come from three independent sources (i.e. Mazzotti and Savoia 2009; Pan et al. 2009; Chapter 3 of this thesis). Geometric and material properties of the beam specimens are summarised in Table 5.1. Ten specimens were included in the test database. Among the tests included in the database, three specimens tested under eight-point loading, which failed by IC debonding, were selected from Mazzotti and Savoia (2009), but the other specimens in their experimental programme were excluded because these test results may be unreliable, as discussed in Chapter 4. For example, the axial stiffness of the FRP soffit plate in TN3 is higher than that used in TN8. It is logical that the moments at the initiation of concrete cracking and tension steel yielding of Specimen TN3 are higher than the corresponding values of Specimen TN8. However; the test values of Specimen TN3-LP8 for these moments are much lower than the corresponding test values of Specimen TN8-LP8. Four specimens from Pan et al. (2009) were included in the

database. Those specimens, which did not fail by IC debonding, were excluded from the database. Three full-scale FRP-plated RC beams presented in Chapter 3 of this thesis (e.g. Specimens LP2SP1000, LP4SP1000 and LP8SP1000) were also included in this database.

The predictions of each model are compared with test results in Table 5.2 and Figures 5.5a to 5.5c. As shown in these figures, Chen et al.'s (2006) model appears to be the most conservative model with the average ratio of predicted load to test load being 0.89. Nevertheless, Chen et al.'s (2006) model has the lowest coefficient of variation (4.1%), and has the smallest difference between the maximum and the minimum predicted-to-test load ratios (11%). Its maximum predicted-to-test load ratio is 0.94, for Specimen TN1 from Mazzotti and Savoia (2009) while its minimum ratio is 0.84, for Specimen D3-P4-l2 from Pan et al. (2009). The *fib*'s (2001) model has an averaged predicted-to-test load ratio of 1.05 and coefficient of variation of 14.8%; the difference between the maximum and the minimum predicted-to-test load ratios is 40%, with the maximum ratio 1.26 for SpecimenD2-P2-l2 in Pan et al. (2009) and the minimum 0.86 for SpecimenLP4SP1000 from Chapter 4 of this thesis. Rosenboom and Rizkalla's (2008) model has an average predicted-to-test load ratio of 0.91; the difference between the maximum and the minimum predicted-to-test load ratios is 46%,with the maximum ratio 1.16 for Specimen LP4SP1000 and the minimum ratio 0.70 for D5-P8-l4 from Pan et al. (2009). This model has the highest degree of scatter, with its coefficient of variation 18.4%.

5.5 COMPARISONS BETWEEN STRENGTH MODELS' PREDICTIONS AND FE RESULTS

The comparisons presented in Section 5.4above indicate that all three IC debonding strength models can produce reasonable predictions of IC debonding strength for different load distributions. As the test data used in the comparisons of the preceding section are rather limited, a more in-depth assessment of these IC debonding strength models was also undertaken using results obtained from the parametric study presented in Chapter 4.

As demonstrated in Chapter 4, the parametric study investigated the effects of a few major factors affecting the IC debonding strength, including the concrete strength, yield stress and amount of steel tension bars, width and thickness of the FRP soffit plate, and depth-to-span ratio of the beam. For each factor, at least three values were examined in the parametric study to cover a wide range. Two loading distributions typical in practice were examined for each case. The detailed values for each factor and the corresponding loading condition were presented in detail in Chapter 4.

The predicted results from the three IC debonding strength models are compared with FE results in Tables 5.3 to 5.9, while the distributions of the predicted-to-test load ratios for beams under two-point loading or UDL are shown in Figures 5.5 to 5.8. As indicated in these figures, for beams under two-point loading, *fib's* (2001) model is the most conservative model, having an averaged predicted-to-test load ratio of 0.86 and a coefficient variation of 10.0%; while both Chen et al.'s (2006)

model and Rosenboom and Rizkalla's (2008) model have the same average predicted-to-test ratio of 0.94, with their coefficients of variation10.1% and 8.5% respectively. For FRP-plated beams under UDL, both *fib's* (2001) model and Rosenboom and Rizkalla's (2008) model have the same averaged predicted-to-test ratio of 0.95, with their coefficients of variation 9.5% and 11.1% respectively; while Chen et al.'s (2006) model has an averaged predicted-to-test load ratio of 1.09, with its coefficient of variation 12.1%; it is the least conservative model among the three models evaluated. The averaged predicted-to-test load ratios for beams under UDL are higher than those of beams under two-point loading by 0.09, 0.15, and 0.01 for *fib's* (2001), Chen et al.'s (2006) and Rosenboom and Rizkalla's (2008) models respectively. It indicates that both Chen et al.'s (2006) and *fib*'s (2001) models may have exaggerated the effect of load distribution on IC debonding. More detailed discussions on the accuracy of the three models are given below.

The FE analysis predicts that the effect of loading distribution on IC debonding becomes more significant with an increase in the concrete strength (Table 5.3). The differences between the IC debonding strengths for UDL and two-point loading are 7.1%, 11.1% and 12.5% for FRP-plated RC beams with the concrete strengths30 MPa, 40 MPa, and 50 MP, respectively. Both *fib*'s (2001) model and Chen et al.'s (2006) model produce predictions with the same trend as that of the FE results; namely, the effect of load distribution on IC debonding becomes more significant with an increase in concrete strength. However Rosenboom and Rizkalla's (2008) model predicts that an increase in concrete strength does not significantly affect the effect of load distribution on IC debonding strength.

The numerical results from FE analysis indicate that the effect of load distribution on IC debonding becomes less significant as the yield stress of steel tension bars increases(Table 5.4).The differences between the IC debonding strengths for UDL and two-point loading are 13.0%, 10.9%,7.1% and 6.2% for FRP-plated RC beams with the yield stresses of steel tension bars 250 MPa, 300MP, 400MPa, and 500MP, respectively. The corresponding differences predicted by the *fib*'s (2001) model are 27.0%, 25.2%, 20.6% and 12.6% while the differences predicted by Chen et al.'s (2006) model are 39.9%, 34.9%, 26.1% and 19.2%. However, Rosenboom and Rizkalla's (2008) model predicts an opposite trend with the corresponding differences 11.3%, 11.8%, 13.2% and 14.9%.

The FE analysis predicts that the effect of loading distribution on IC debonding becomes less significant with an increase in the volume ratio of steel tension bars (Table 5.5).The differences between the strength of IC debonding under UDL and two-point loading are 12.9%, 7.1% and 6.0% for FRP-plated RC beams with two 10mm-, two 16 mm-, and three 16mm-steel tension bars, respectively. Both *fib*'s (2001) model and Chen et al.'s (2006) model produce predictions with the same trend as that of the FE results; namely the effect of load distribution on IC debonding becomes less significant with an increase in the volume ratio of steel tension bars. However, Rosenboom and Rizkalla's (2008) model predicts that an increase in the volume ratio of steel tension bars leads to the effect of load distribution on IC debonding strength be less significant.

The FE predicts that that the thickness of the FRP plate has a marginal influence on the effect of loading distribution on IC debonding; while the effect of load

distribution on IC debonding strength seems to be more significant as the FRP plate width increases (Tables 5.6 and 5.7). The differences between the strength of IC debonding under UDL and that under two-point loading for the beam with the FRP soffit plate of 200 mm is 16.6%, and is much higher than 10.8% and 7.1% for the beams with the FRP plate widths of 100 mm and 150 mm, respectively. The corresponding differences predicted by Chen et al.'s (2006) model are 15.7%, 26.1% and 30.7%. However , both *fib*'s (2001) model and Rosenboom and Rizkalla's (2008) model predicts an opposite trend. The corresponding difference predicted by *fib*'s (2001) model are 40.5%, 20.6% and 27.4%; while the corresponding differences predicted by Rosenboom and Rizkalla's (2008) model are 18.1%, 13.2% and 11.0%.

The numerical results from FE analysis indicate that the effect of loading distribution on IC debonding tends to be more significant as the span-to-height ratio of FRP-plated RC beams increases. The differences between the strength of IC debonding under two-point loading and that under UDL are 7.1%, 11.2% and 28.3% for FRP-plated RC beams with the span-to-height ratio 8.89, 11.0 and 16.0, respectively. The corresponding differences predicted by the *fib*'s (2001) model are 20.6%, 22.3% and 19.4%. Chen et al.'s (2006) model captured such differences being 26.1%, 34.2% and 42.2% for FRP-plated RC beams with the span-to-height ratio 8.89, 11.0 and 16.0, respectively. However Rosenboom and Rizkalla's (2008) model predicts an opposite trend with the corresponding differences being 13.1%, 12.4% and 11.7%.

5.6 CONCLUSIONS

Both test results presented in Chapter 3 and FE analyses presented in Chapter 4 indicate that the effect of load distribution on IC debonding can be significant. This effect should be appropriately considered in IC debonding strength models for use in design. Although some of the existing IC debonding strength models have the potential to capture this effect, reliable test data are needed to evaluate these models. In this chapter, three existing IC debonding strength models having the capability to consider the effect of load distribution have been evaluated using limited existing test results and results from a parametric study conducted using a reliable FE approach presented in Chapter 4. The following conclusions can be drawn from comparisons and discussions presented in this chapter:

(1) Both *fib*'s (2001) model and Chen et al.'s (2006) model tend to exaggerate the effect of load distribution on IC debonding while Rosenboom and Rizkalla's (2008) model can capture the strength difference between two-point loading and UDL well.

(2) Rosenboom and Rizkalla's (2008) model may produce some questionable trends for some factors affecting the load distribution on IC debonding. For example, the effect of load distribution is predicted by FE analysis to become more significant with an increase in the span-to-height ratio, the FRP plate width, the concrete strength, and the steel yield stress, but Rosenboom and Rizkalla's (2008) model predicts opposite trends for these factors.

(3) All three existing IC debonding strength models cannot capture well the effect of load distribution on IC debonding, and a new IC debonding strength model, which can predict the effect of load distribution on IC debonding well, is needed.

5.7 REFERENCES

ACI 318 (2008). *Building code requirements for structural concrete and commentary*, ACI Committee, Detroit, USA.

CEB-FIP MC90 (1993). *CEB-FIP model code 1990*, Thomas Telford, London, 1993.

Chen, J.F. and Teng, J.G. (2001). "Anchorage strength models for FRP and steel plates bonded to concrete", *Journal of Structural Engineering-ASCE*, Vol. 127, No. 7, pp. 784-791.

Chen, J.F., Teng, J.G. and Yao, J. (2006). "Strength model for intermediate crack debonding in FRP-strengthened concrete members considering adjacent crack interaction", *Proceedings, Third International Conference on FRP Composites in Civil Engineering (CICE 2006)*, Miami, Florida, USA,, 67-70.

Chen, J.F., Yuan, H. and Teng, J.G. (2007). "Debonding failure along a softening FRP-to-concrete interface between two adjacent cracks in concrete members", *Engineering Structures*, Vol. 29, No. 2, pp. 259-270.

European Committee for Standardizations (CEN) (2004). *Design of concrete structures - Part 1: General rules and rules for buildings*, EN1992-1-1, Eurocode 2, Brussels.

fib (2001).*Externally bonded FRP reinforcement for RC structures*, International Federation for Structural Concrete, Lausanne, Switzerland.

Mazzotti, C. and Savoia, M. (2009). "Experimental Tests on Intermediate Crack Debonding Failure in FRP-Strengthened RC Beams", *Advances in Structural Engineering*, Vol. 12, No. 5, pp. 701-713.

Pan, J.L., Chung, T.C.F. and Leung, C.K.Y. (2009). "FRP debonding from concrete beams under various load uniformities", *Advances in Structural Engineering*, Vol. 12, No. 6, pp.807-819.

Nayal, R. and Rasheed, H.A. (2006). "Tension stiffening model for concrete beams reinforced with steel and FRP bars", *Journal of Materials in Civil Engineering*, Vol. 129, No. 6, pp. 717-724.

Rosenboom, O.A. (2006). *Behavior of FRP repair/strengthening systems for prestressed concrete*, PhD Thesis, North Carolina State University, USA.

Rosenboom, O., and Rizkalla, S. (2008). "Modeling of IC debonding of FRP strengthened concrete flexural members", *Journal of Composites for Construction*, ASCE, Vol. 12, No. 2, pp. 168–179.

Teng, J.G., Yuan, H. and Chen, J.F. (2006). "FRP-to-concrete interfaces between two adjacent cracks: Theoretical model for debonding failure", *International Journal of Solids and Structures*, Vol. 43, No. 18-19, pp. 5750-5778.

5.8 TABLES AND FIGURES

Table 5.1 Geometrical and material properties of specimens failing by IC debonding under different loading distributions

Sources		Mazzotti and Savoia (2009)			Pan et al. (2009)				Chapter 3 of this thesis		
Specimen name		TN1	TN4	TN8	D2-P2-l2	D3-P4-l2	D4-P8-l2	D5-P8-l4	LP2SP100	LP4SP100	LP8SP100
$f_c^{'}$		47.6#	48.0#	44.5#	59.0				48.2	48.5	48.5
Dimensions	L	3000	3000	3000	1800				4000		
	b_c	250	250	250	150				200		
	h_c/d	400/370	400/370	400/370	200/163				450/395		
Steel bars	f_{yt}	5Y14/550	5Y14/550	3Y14/550	2Y10/550				2Y16/431		
	f_{yc}	2Y12/550	2Y12/550	2Y12/550	2Y8/550				2Y16/431		
	Stirrups	Y10@90+Y10@200 (double legs)			Y12@80				Y8@100		
	f_{yv}	550			550				370		
	E_s	200			202				200		
FRP plate	$n \times t_f$	1 x 1.2	2 x 0.13	2 x 0.13	2 x 0.11			4 x 0.11	3 x 0.333		
	b_f	100	250	250	150				100		
	L_f	2800	2800	2800	1650				3800		
	f_f	3100	3900	3900	4200				4654		
	E_f	195	290	290	235				258		
Loading points	*LP1*	340			787.5	337.5	112.5	112.5	1000	500	250
	LP2	620			--	787.5	337.5	337.5	--	1500	750
	LP3	1000			--	--	562.5	562.5	--	--	1250
	LP4	1280			--	--	787.5	787.5	--	--	1750

#converted from cube compressive strength of concrete using $f_c^{'} = 0.8 f_{cu}$; $f_c^{'}$ =cylinder compressive strength of concrete, in MPa; L, b_c, $h_c$and d= clear span, width, height and effective depth of specimen, respectively, all in mm; f_{yt}, f_{yc}, and f_{yv}=yielding strength of tension bars, compression bars and stirrup respectively, all in MPa; E_s= Young's moduli of steel bars; $n \times t_f$= no. of plies and thickness of each ply of FRP sheets or plates; b_f, L_f, E_f= width, length and Young's moduli of FRP plate, and in mm, mm and GPa respectively;*LP1, LP2, LP3* and *LP4* are the positions of loading points from the left support, in mm.

Table 5.2 Comparisons between predictions of IC debonding models and test data for beams under different loading distributions

		Test		*fib 2001*		Chen et al.'s model		Rosenboom and Rizkalla's model	
Sources	Specimen name	M_u (kN.m)	ε_f^{IC} (με)	M_u (kN.m)	ε_f^{IC} (με)	M_u (kN.m)	ε_f^{IC} (με)	M_u (kN.m)	ε_f^{IC} (με)
Mazzotti and Savoia (2009)	TN1	214.6	6000	220.54	8090	201.95	5651	213.0	7265
	TN4	236.5	11000	232.08	11890	209.59	8413	225.4[#1]	11030
	TN8	166.7	13000	152.26	8366	143.45	6965	157.3	9255
Pan et al. (2009)	D2-P2-l2	26.3	NA	33.11	13360	24.62	7146	25.7	8074
	D3-P4-l2	29.7	NA	36.61	16050	24.93	7382	26.7	8774
	D4-P8-l2	31.0	NA	37.87	17060	26.71	8696	26.6	8699
	D5-P8-l4	40.4	NA	46.58	11740	34.31	7058	32.9	6582
Chapter 3 of this thesis	LP2SP1000	143.6	6675	128.44	3945	128.59	3961	129.5	4139
	LP4SP1000	151.1	6773	130.47	4174	131.87	4338	151.5	6593
	LP8SP1000	156.7	6839	143.84	5691	145.26	5843	153.9	6840

Note #1: FRP rupture failure; NA=not available in the original paper.

Table 5.3 Comparison between predictions of IC debonding models and FE predicted results for specimens with varied concrete strengths

	FEM		*fib 2001*		Chen et al.'s model		Rosenboom and Rizkalla's model	
Specimen name	M_u (kN.m)	ε_f^{IC} (με)	M_u (kN.m)	ε_f^{IC} (με)	M_u (kN.m)	ε_f^{IC} (με)	M_u (kN.m)	ε_f^{IC} (με)
LP2CS20	116.67	3920	89.96	2119	112.10	3291	113.3	3417
UDLCS20	124.31	4310	107.80	2941	139.12	5282	129.7	4633
LP2CS30	134.72	4900	108.00	2610	119.72	3515	120.9	3644
UDLCS30	144.31	5440	130.25	4289	150.94	5834	136.8	4842
LP2CS40	151.53	5890	121.21	3354	125.48	3689	126.7	3827
UDLCS40	168.30	6980	153.59	5795	159.43	6236	142.6	5043
LP2CS50	166.80	6830	131.97	3974	130.15	3830	131.5	3985
UDLCS50	187.73	8090	174.69	7165	166.09	6556	147.6	5234

Table 5.4 Comparison between predictions of IC debonding models and FE predicted results for specimens with varied yield stresses of tension steel bars

	FEM		*fib 2001*		Chen et al.'s model		Rosenboom and Rizkalla's model	
Specimen name	M_u (kN.m)	ε_f^{IC} (με)	M_u (kN.m)	ε_f^{IC} (με)	M_u (kN.m)	ε_f^{IC} (με)	M_u (kN.m)	ε_f^{IC} (με)
LP2BY250	87.27	3100	89.08	2632	95.27	3229	88.5	2727
UDLBY250	98.59	3780	113.12	4459	133.35	6061	98.5	3510
LP2BY300	98.4	3700	94.27	2606	103.15	3303	99.3	3038
UDLBY300	109.16	4010	118.07	4413	139.19	5981	111.0	3938
LP2BY400	134.72	4900	108.00	2610	119.72	3515	120.9	3644
UDLBY400	144.31	5440	130.25	4298	150.94	5834	136.8	4842
LP2BY500	155.40	5440	127.25	3052	136.49	3750	141.9	4208
UDLBY500	165.07	5960	143.41	4248	162.77	5702	163.1	5782

Table 5.5 Comparison between predictions of IC debonding models and FE predicted results for specimens with varied amount of tension steel bars

	FEM		*fib 2001*		Chen et al.'s model		Rosenboom and Rizkalla's model	
Specimen name	M_u (kN.m)	ε_f^{IC} (με)	M_u (kN.m)	ε_f^{IC} (με)	M_u (kN.m)	ε_f^{IC} (με)	M_u (kN.m)	ε_f^{IC} (με)
LP2BS210	85.16	3850	66.23	2117	85.83	3502	86.0	3545
UDLBS210	96.11	4450	84.21	3347	117.38	5840	94.4	4183
LP2BS216	134.72	4900	108.00	2610	119.72	3515	120.9	3644
UDLBS216	144.31	5440	130.25	4298	150.94	5834	136.8	4842
LP2BS316	156.13	4540	152.56	4026	148.70	3639	147.4	3594
UDLBS316	165.42	5140	170.19	5230	189.69	6678	170.5	5320

Table 5.6 Comparison between predictions of IC debonding models and FE predicted results for specimens with varied number of layers of FRP sheet

	FEM		*fib 2001*		Chen et al.'s model		Rosenboom and Rizkalla's model	
Specimen name	M_u (kN.m)	ε_f^{IC} (με)	M_u (kN.m)	ε_f^{IC} (με)	M_u (kN.m)	ε_f^{IC} (με)	M_u (kN.m)	ε_f^{IC} (με)
LP2FL2	113.12	5240	97.99	2924	106.86	3998	108.6	4259
UDLFL2	123.52	6050	118.31	5303	128.88	6516	122.3	5843
LP2FL3	134.72	4900	108.00	2610	119.72	3515	120.9	3644
UDLFL3	144.31	5440	130.25	4298	150.94	5834	136.8	4842
LP2FL4	139.43	3990	118.31	2491	131.6	3246	132.6	3334
UDLFL4	152.83	4590	139.20	3653	171.07	5421	151.2	4367

Table 5.7 Comparison between predictions of IC debonding models and FE predicted results for specimens with varied width of the FRP plate

	FEM		*Fib's* model		Chen et al.'s model		Rosenboom and Rizkalla's model	
Specimen name	M_u (kN.m)	ε_f^{IC} (με)	M_u (kN.m)	ε_f^{IC} (με)	M_u (kN.m)	ε_f^{IC} (με)	M_u (kN.m)	ε_f^{IC} (με)
LP2FW100	94.54	3290	75.61	2721	102.99	3538	101.6	3431
UDLFW100	104.78	4050	106.28	3910	119.23	5426	120.0	5575
LP2FW150	134.72	4900	108.00	2610	119.72	3515	120.9	3644
UDLFW150	144.31	5440	130.25	4298	150.94	5834	136.8	4842
LP2FW200	163.03	5190	120.79	2634	132.48	3293	137.8	3624
UDLFW200	190.02	6663	154.00	4468	173.18	5538	153.0	4468

Table 5.8 Comparison between predictions of IC debonding models and FE predicted results for specimens with varied span-to-heightratio of beams

	FEM		*fib's* model		Chen et al.'s model		Rosenboom and Rizkalla's model	
Specimen name	M_u (kN.m)	ε_f^{IC} (με)	M_u (kN.m)	ε_f^{IC} (με)	M_u (kN.m)	ε_f^{IC} (με)	M_u (kN.m)	ε_f^{IC} (με)
LP2DS09	134.72	4900	108.00	2610	119.72	3515	120.9	3644
UDLDS09	144.31	5440	130.25	4298	150.94	5834	136.8	4842
LP2DS11	98.17	4530	87.56	3279	91.57	3662	91.4	3684
UDLDS11	110.19	5610	107.11	5125	122.89	6634	102.7	4766
LP2DS16	70.77	4590	69.23	4545	64.92	3970	63.0	3753
UDLDS16	90.79	7610	82.69	6360	92.3	7700	70.4	4744

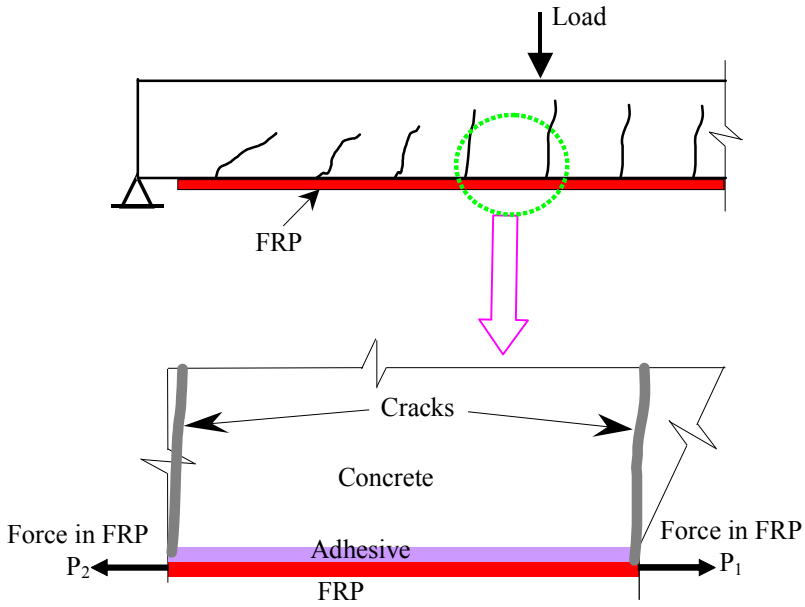

Figure 5.1 Intermediate crack debonding in FRP-plated RC beams[from Teng et al. (2006)]

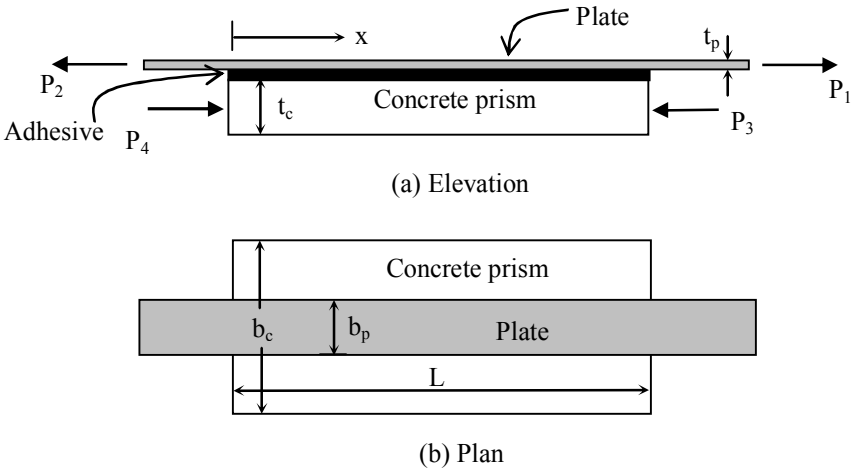

Figure 5.2 FRP-to-concrete bonded joint model between two adjacent cracks [from Teng et al. (2006)]

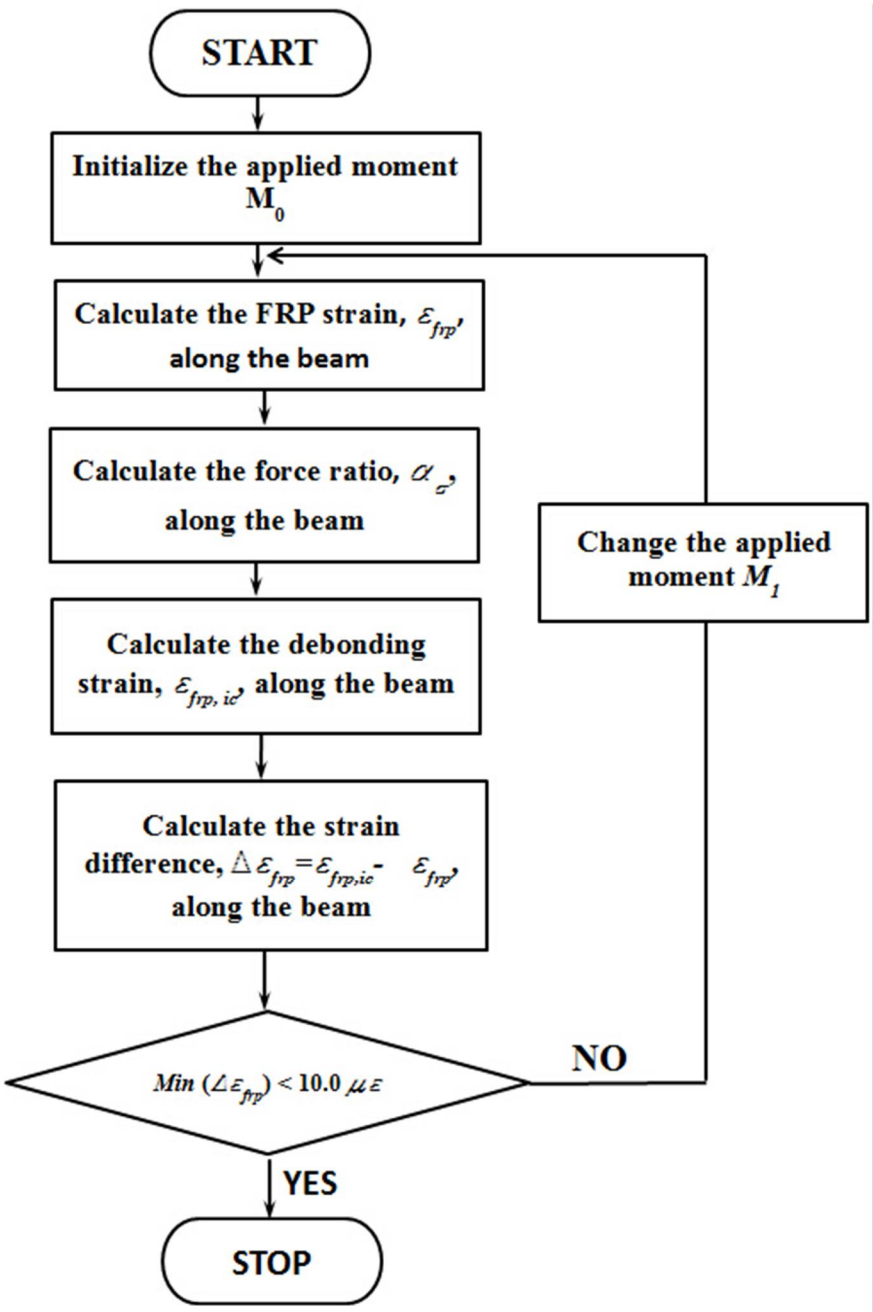

Figure 5.3 Flowchart for the prediction of IC debonding strength

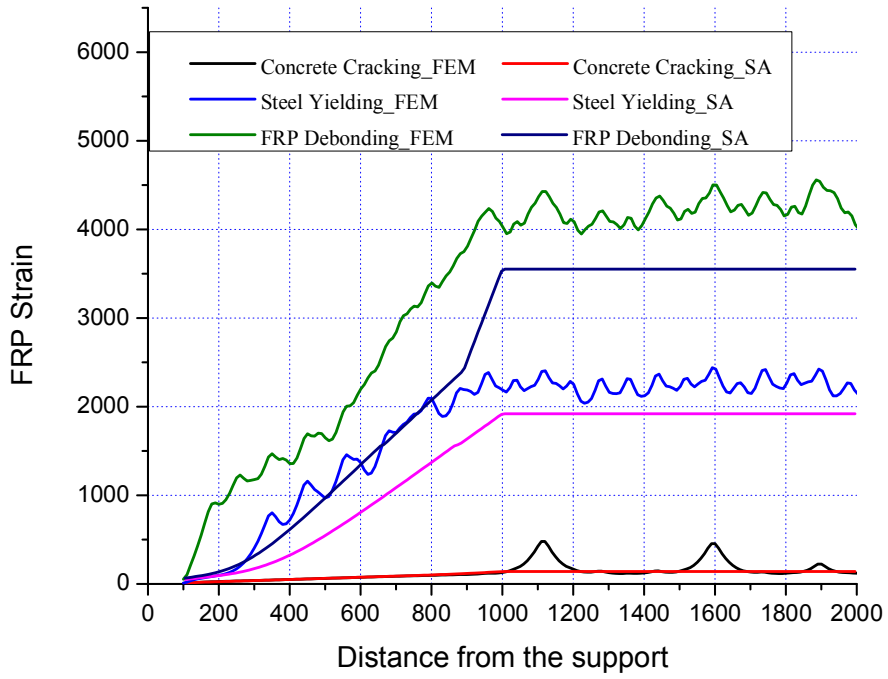

(a) with the characteristic length being 0.5 times that in FEM

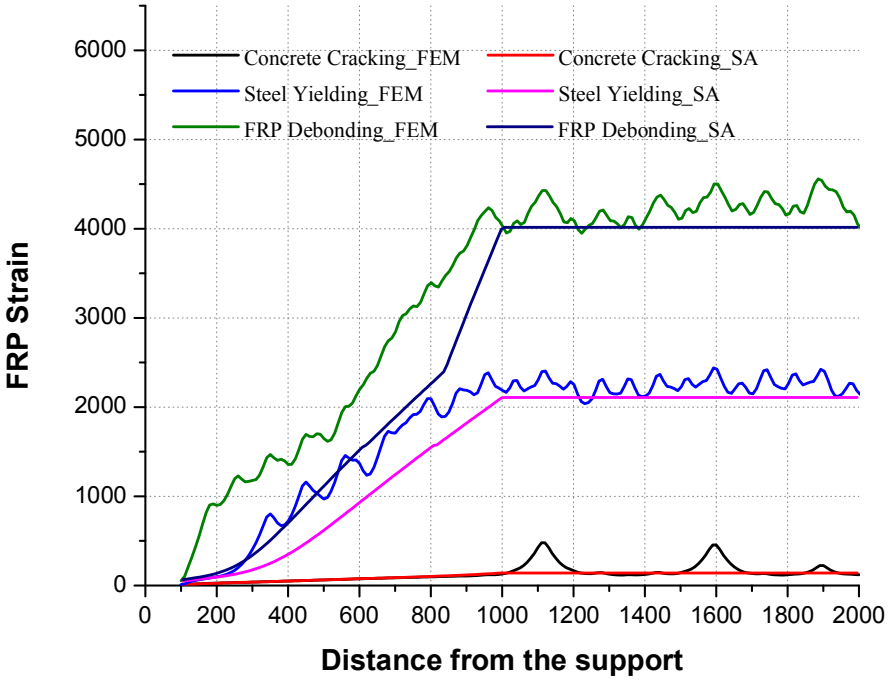

(b) with the characteristic length being equal to that in FEM

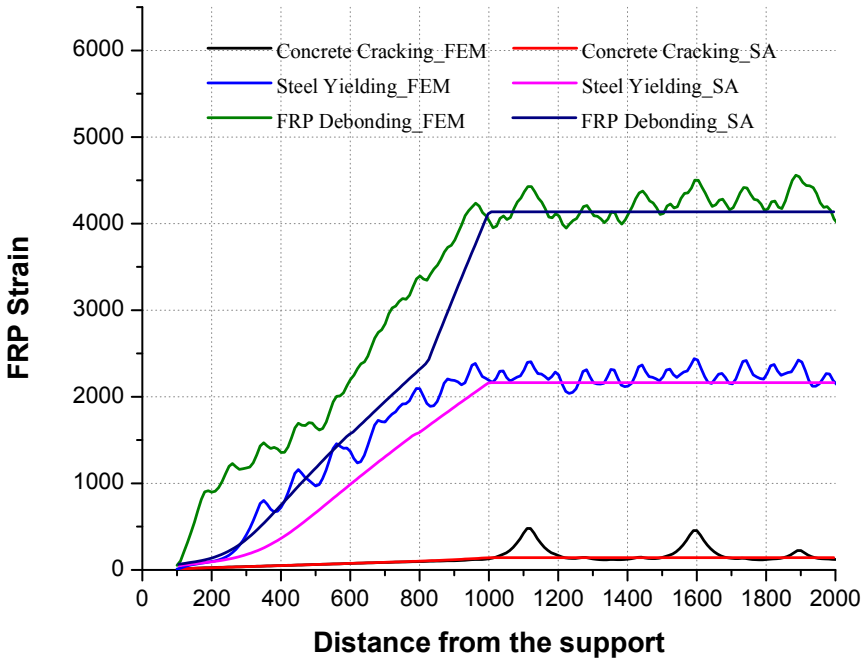

(c)with the characteristic length being 2 times that in FEM

Figure 5.4 Section analysis predicted versus FE predicted FRP strain distributions

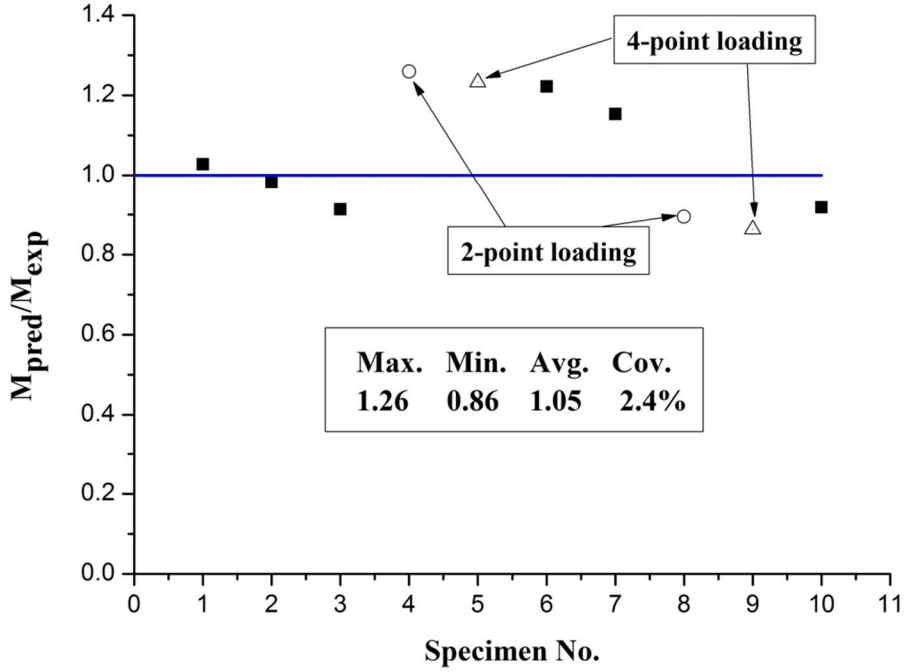

(a) *fib* (2001) model

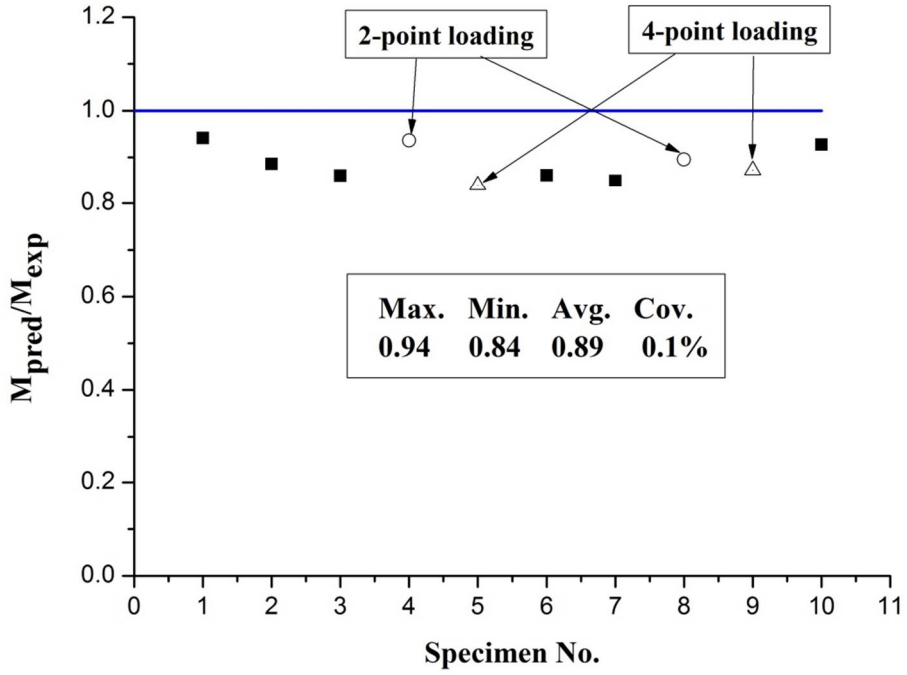

(b) Chen et al. (2006) model

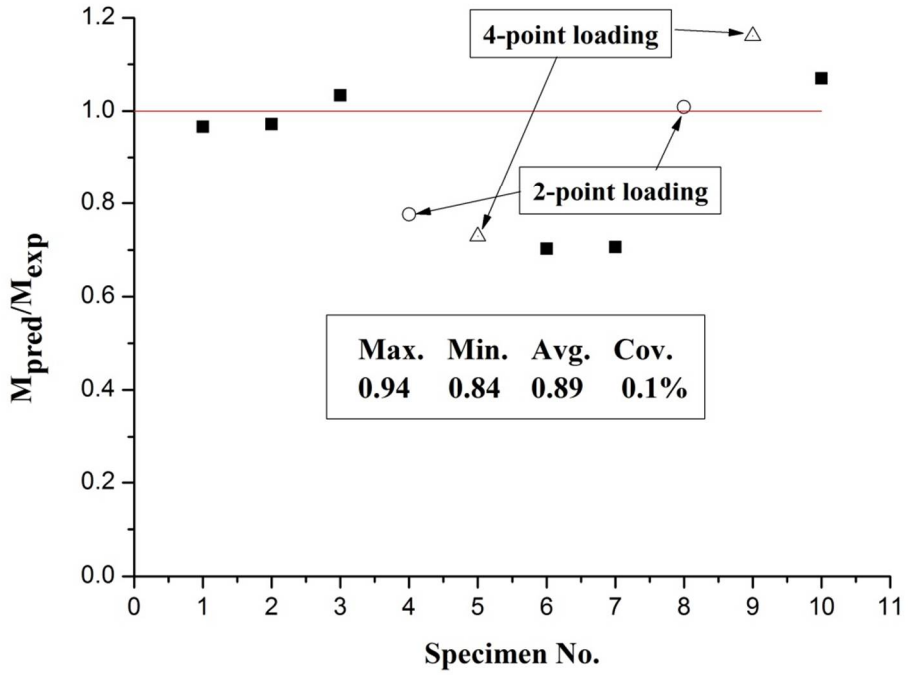

(c) Rosenboom and Rizkalla (2008) model

Figure 5.5 IC debonding strength model predicted versus test debonding strength

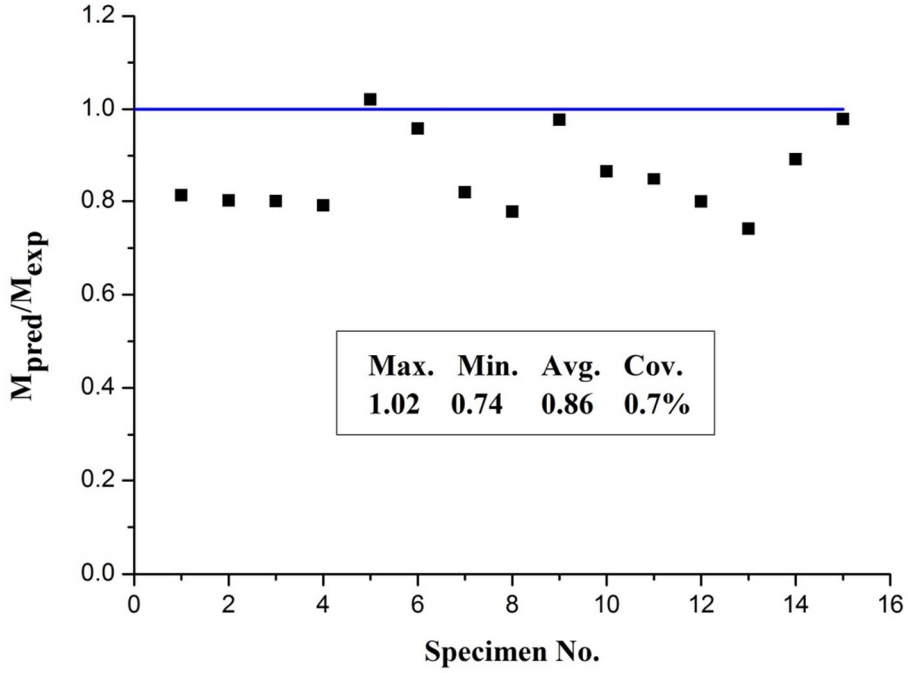

(a) two-point loading

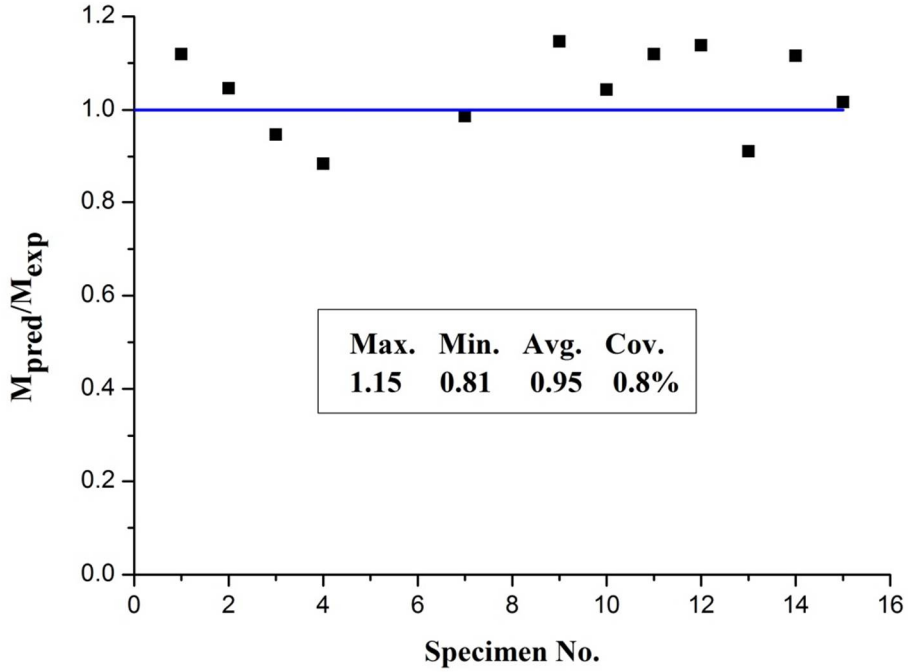

(b) uniformly distributed loading

Figure 5.6 Predictions from *fib* (2001) model

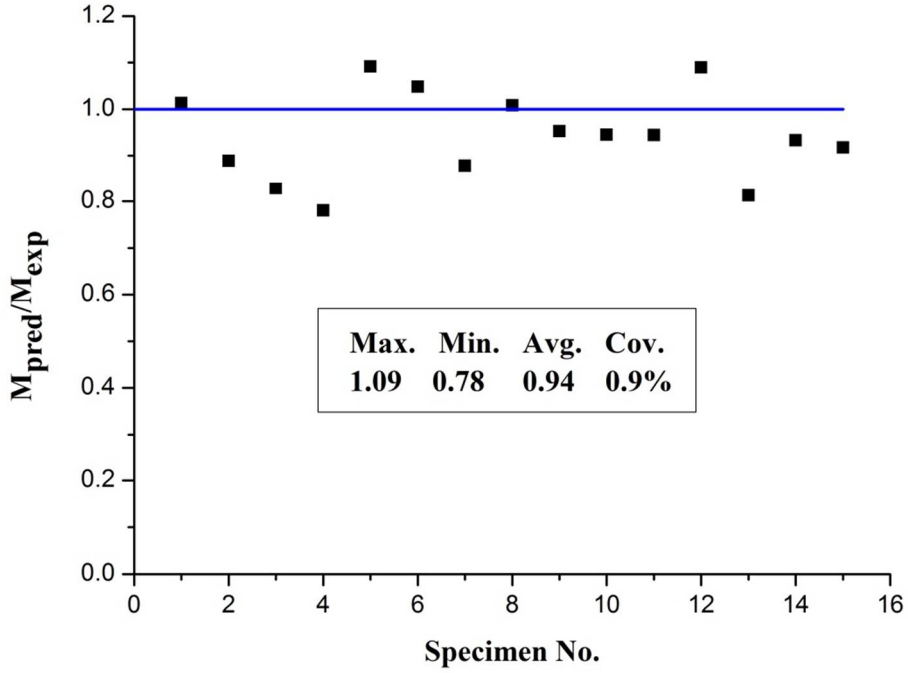

(a) two-point loading

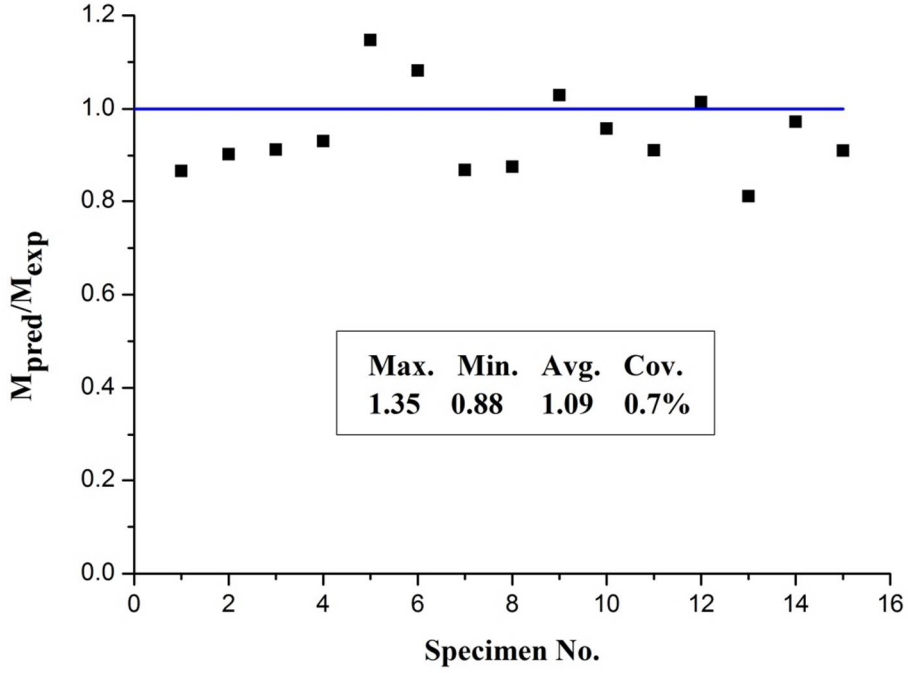

(b) uniformly distributed loading

Figure 5.7 Predictions from Chen et al. (2006) model

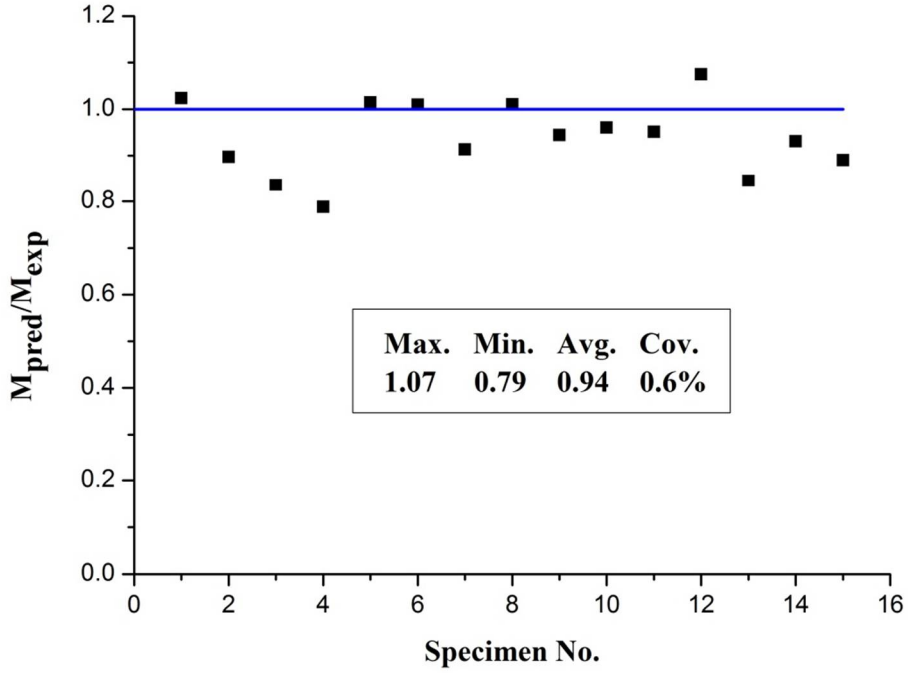

(a) two-point loading

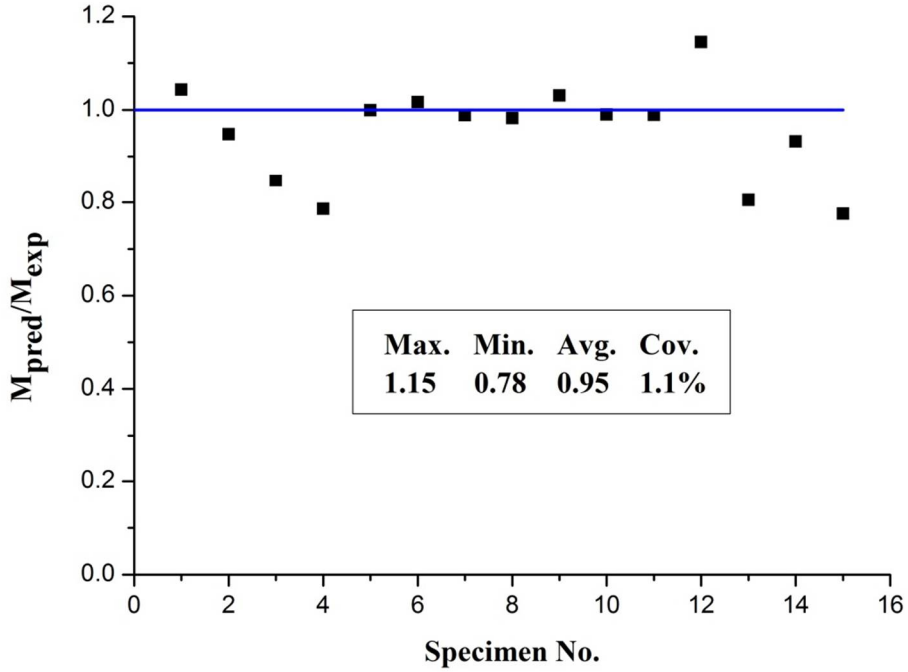

(b) uniformly distributed loading

Figure 5.8 Predictions from Rosenboom and Rizkalla (2008) model

CHAPTER 6

EFFECT OF FRP U-JACKETS ON IC DEBONDING FAILURE

6.1 INTRODUCTION

FRP-plated RC beams often fail by IC debonding, which limits the strengthening efficiency and utilization of the expensive FRP material. When IC debonding occurs, the maximum strain in the FRP plate is often below 50% of the FRP rupture strain (Kalfat et al. 2013). The use of externally wrapped FRP U-jackets with fibres perpendicular to the beam axis is an attractive choice of anchorage measures for the mitigation of debonding failures due to their ease of installation and excellent corrosion resistance. Nevertheless, only a very small number of studies (Matthys 2000; Brena et al. 2003; Leung 2006; Kotynia et al. 2008; Rosenboom and Rizkalla 2008) have been conducted on the effect of FRP U-jackets on IC debonding. Moreover, the findings from these limited studies are somewhat contradictory. The results of one beam test reported in Brena et al. (2003) indicate that the IC debonding strength can be significantly increased by the installation of FRP U-jackets. However, others found that FRP U-jackets have only a marginal beneficial effect on improving the IC debonding strength, especially when the U-jackets were installed only at plate

ends. Leung (2006) found that the locations of U-jackets played a significant role in enhancing the IC debonding strength. A comprehensive review of the effect of vertical FRP U-jackets on IC debonding is given in Section 6.2.

Following the review on the effect of FRP U-jacket on IC debonding is a experimental programme consisting of eight full-scale RC beam tests in two series (Series I and Series II). These tests were conducted with two main objectives: (1) to clarify the effect of vertical FRP U-jackets on IC debonding strength; and (2) to identify a proper layout of FRP U-jackets to postpone/suppress IC debonding failure. Besides vertical FRP U-jackets, other forms of FRP U-jackets were also examined in the tests.

6.2 EXISTING TESTS

Only a limited number of tests have been conducted on FRP-plated RC beams to investigate the effect of FRP U-jackets on IC debonding. These tests have all been concerned with vertical U-jackets with fibres oriented also in the vertical direction (i.e. perpendicular to the beam axis) and have led to somewhat contradictory conclusions. Therefore, a comprehensive review into these studies is given in this section to clarify the sources of the contradictory conclusions. Ten FRP-plated RC beams installed with vertical FRP U-jackets for mitigating IC debonding were collected from four independent sources. Their control specimens, which were strengthened with an FRP soffit plate only, were included for comparison to identify the effect of U-jackets on IC debonding failure. All the test information is listed in Table6.1.

The increase in the ultimate load of specimens as a result of the installation of FRP U-jackets ranges from 6.0% to18% (Table 6.1). In Breana et al. (2003), four beams were provided with 8 or 12 FRP U-jackets, which were uniformly distributed along the beam. Three of these four beams failed by the rupture of the FRP plate while the other one still failed by IC debonding. In Specimen C3 in Brena et al. (2003), an increase in the ultimate load of about 18% was achieved due to the installation of 12vertical FRP U-jackets, which were distributed along the beam, although the other three beams did not show a significant increase in the ultimate load as a result of the FRP U-jackets. As a result, Brena et al. (2003) concluded that IC debonding could be delayed or in some cases suppressed by bonding vertical FRP U-jackets along the shear span. Similar statements can also be found in Leung (2006). However, the strains in the FRP plates of the four beams tested by Breana et al. (2003) had not been significantly increased and were far below the rupture strain of the FRP soffit plate.

Other researchers found that there was only a marginal, beneficial effect of FRP U-jackets on IC debonding strength, especially for cases with FRP U-jackets installed only at the plate ends (Matthys 2000; Rosenboom and Rizkalla 2008; Kotynia et al. 2008). Kotynia et al. (2008) conducted two series of tests on full-scale beams to investigate the effectiveness of vertical FRP U-jackets in mitigating IC debonding. Increases of only 6%-9% in the ultimate load were achieved by using FRP U-jackets, even when continuous U-jackets were used. Rosenboom and Rizkalla (2008) also concluded that vertical FRPU-jackets placed throughout the girder length could increase the ultimate load and the tensile strain of the FRP soffit plate at failure

by as much as 9% and 20%, respectively. In Matthys (2000), only one of the specimens (Specimen BF6) was installed with one FRP U-jacket at each end of the FRP soffit plate, and only a 1% decrease in the ultimate load was observed compared to the control specimen.

As shown in the above review, the findings of existing studies are somewhat contradictory. In some cases, the failure mode of the test specimen did shift from IC debonding to the rupture of the FRP soffit plate, but often without a significant increase in the ultimate load. No clear explanation of this phenomenon has been given. Therefore this chapter presents an experimental study that included specimens with vertical FRP U-jackets to clarify their effect on IC debonding as well as other specimens with FRP U-jackets of other forms (e.g. inclined FRP U-jackets and strips parallel to the beam axis) to identify a more effective FRP U-jacket layout for postponing or suppressing IC debonding.

6.3 EXPERIMENTAL PROJECT

6.3.1 Specimen design

The experimental project consisted of eight full-scale FRP-plated RC beams in two series (four specimens in each series). In Series I, four rectangular simply-supported RC beams were tested primarily to investigate the effect of vertical FRP U-jackets on IC debonding. All the specimens had the same dimensions: 3900 mm in length (with a clear span of 3600 mm), 200 mm in width and 450 mm in height. The beams were under-reinforced with the same high yield steel bars: three 16 mm tension bars and

two 16 mm compression bars. Eight-mm stirrups at 150 mm centres were also provided to avoid premature shear failure of the RC beams. Some small concrete cover blocks of 42 mm in height were used at the bottom of the beam mould to position the steel cages. Detailed information on beam dimensions and reinforcements can be found in Figure 6.1. The FRP soffit plates of all four RC beams in Series I were 2800 mm in length, 0.674 mm in nominal thickness (two layers of 0.337 mm in nominal thickness), and 145.0 mm in width, and were formed in a wet layup process.

As the experimental project was to investigate the effect of FRP U-jackets on IC debonding, the specimens were designed to avoid the occurrence of concrete cover separation. FRP U-jackets at the ends of the FRP soffit plate have been found by previous research to have little effect on IC debonding other than to suppress or postpone concrete cover separation (Smith and Teng 2003). In all specimens of Series I except the control specimen, a vertical CFRP U-jacket of 150 mm in width extending to the top of beam was installed at each end of the FRP soffit plate to avoid unexpected concrete cover separation failure. This U-jacket near the end of the FRP soffit plate was denoted by U-jacket 1 for ease of description in the reminder of this chapter. In addition, for ease of instrumentation and observation, it was desirable to limit the failure of specimen to one of the two shear spans (or sides); for this reason, it was decided to apply a strong anchorage measure in the non-test shear span. Strain gauges were only used in the test shear span, where failure was expected to occur. In beams with vertical FRP U-jackets (B2S1 and B3S1), three steel jackets equally spaced along the shear span were installed in the non-test shear span (they are

equivalent to strong FRP U-jackets) to avoid failure in the non-test shear span. In Beam B4S1, in which a parallel CFRP side strip (0.674 mm in nominal thickness, 75.0 mm in width and 450.0 mm in length) was bonded on each side surface of the beam in the test shear span, a 'stronger' CFRP strip of 0.674 mm in nominal thickness, 100.0 mm in width and 600.0 mm in length was installed in the non-test shear span to attempt to ensure that failure would occur in the test shear span.

The control beam in Series I was strengthened with an FRP soffit plate and a vertical FRP U-jacket at the end of the soffit plate. The other three specimens differed from each other in the anchorage measure (vertical FRP U-jackets or parallel FRP side strips). Specimens B2S1 and B3S1were provided with vertical FRP U-jackets in the test shear span. In Specimen B2S1, two vertical FRP U-jackets, denoted by U-jacket 2 for the U-jacket closer to the U-jacket at the end of the FRP soffit plate and by U-jacket 3 for the U-jacket closer to the mid-span, were equally spaced in the test shear span with a clear spacing of 262.5 mm. The height of these two vertical FRP U-jackets from the beam bottom was 150.0mm having their length longer than their effective bond length. In Specimen B3S1, except U-jacket 1 at the end of the soffit plate, one FRP U-jacket of 300.0 mm in width and 150.0 mm in height from the beam bottom denoted by U-jacket 2 was installed near the load point of the test shear span. In Specimen B4S1, an FRP side strip of 0.674 mm in nominal thickness, 80.0 mm in width and 480.0 mm in length denoted by side strip 2was installed on each side surface of the beam in the test shear span as the anchorage measure. The side FRP strip was bonded with fibres parallel to the beam axis with the starting point directly under the loading point. Details of the anchorage measures of these three

beams are given in Figures 6.2a-6.2c.

Series II, which was designed to investigate the effect of inclined FRP U-jackets on IC debonding, also consisted of four full-scale RC beams including a control specimen. Series II was designed after testing of specimens of Series I, some modifications of beam dimensions and details were therefore made based on the test observations in Series I. The vertical FRP U-jackets at the ends of the FRP soffit plate were not used any more. The entire FRP plate was monitored using a large number of strain gauges, as failure of some specimens in Series I occurred in the non-test shear span.

All four beams in Series II were identical except the experimental variable (i.e. the inclined FRP U-jackets used). The beams all had a cross-section of $200\ \text{mm} \times 450\ \text{mm}$ and a clear span of 3600 mm. Two 16mm deformed steel bars were used as both the compression and the tension reinforcements with a clear cover of 40 mm. To avoid the occurrence of undesirable shear failure, 8 mm steel stirrups at 100 mm centres with the exception of a 150 mm spacing near the loading points were used in the shear spans of the beam (Figure 6.1b). The FRP soffit plates of all four RC beams in Series II had the same dimensions: 3400 mm in length, 0.674 mm in nominal thickness, and 145.0 mm in width; they were all formed via the wet layup process.

The control specimen (B1S2) was strengthened with an FRP soffit plate only. In Specimen B2S2, two different inclined GFRP U-jackets at 30 and 45 degrees to the beam axis but with the same thickness and amount of FRP (i.e. the amount of FRP=the length x width x thickness of FRP) were installed near the two loading

points respectively. Two L-shaped jackets were bonded to the two beam side surfaces respectively and then overlapped at the beam soffit to form an inclined GFRP U-jacket. The inclined U-jackets were 0.716 mm in nominal thickness, 300 mm in height from the beam bottom, and 318 mm or 225 mm in width for the 30- or 45-degreeinclined GFRP U-jacket. The height of the inclined GFRP U-jackets was chosen to be 300.0 mm to avoid their debonding induced by major cracks. In Specimen B3S2, two 45-degree inclined FRP U-jackets with different nominal thicknesses were installed near the two ends of the FRP soffit plate, respectively. These two inclined GFRP jackets had different nominal thicknesses (i.e. different numbers of layers), being 0.716 mm in the test shear span and 1.074 mm in the non-test side respectively; they were otherwise the same (i.e. 318 mm in width and 300 mm in height). Specimen B4S2 was the same as Specimen B3S2, except that the nominal thicknesses of the inclined GFRP jackets were 0.358 mm and 0.716 mm for the test and the non-test shear spans respectively. The detailed layouts of FRP U-jackets in the Series II specimens are given in Figures 6.2d and 6.2e.

6.3.2 Specimen preparation

The specimens of each series were cast with the same batch of commercially supplied concrete. Before the bonding of FRP, all beams had been cured for about four weeks in open air. During the first seven days of curing, the test beams were sprayed with clean water and then covered with plastic film. All the cylinder specimens for determining the concrete strength were cured under the same condition.

The concrete surface was prepared for bonding both the FRP soffit plate and the FRP U-jackets/strips. Removal of cement laitance, loose and friable materials from the concrete surface was achieved by a chisel gun, which was driven by high-pressure air of about 0.7 MPa. The beam corners to be covered by FRP U-jackets were rounded to a radius of 25.0 mm using a grinder. The dust on the ground surfaces and corners was blown away by high-pressure air of about 0.7 MPa before applying the epoxy adhesive. During the process of bonding FRP, a thin layer of well-mixed epoxy primer formed from two components was first applied to assure a good bond between FRP and concrete. Within one hour after the application of epoxy primer, the FRP material was formed by impregnating fibre sheets with epoxy and bonded to the desired parts of the concrete surface. The FRP plates/jackets/strips were left for curing for at least seven days before the test.

6.3.3 Material properties

The experimental project required a large amount of concrete, which was difficult to produce using the small-capacity mixer in the laboratory. Therefore, commercially supplied ready-mixed concrete was used to ensure consistent concrete properties for all specimens in the series. The cylinder compressive strength of concrete was determined on the day of testing each beam according to British standard (BS EN 12390-32009); it was averaged from the results of three cylinders of 150 mm in diameter by 300 mm in height. These test data are given in Table 6.3.

Three steel bars were tested to obtain the mechanical properties of the bars in accordance with British Standard (BS EN ISO 6892-12009), and the obtained tensile

properties are listed in Table 6.2. The mechanical properties of the FRP plates were determined from six coupon tests in accordance with ASTM D3039/D3039M-08 (2008) and ASTM D7565/D7565M-10 (2010), and listed in Table 6.2.

6.3.4 Test procedure and instrumentation

Five Linear Variable Differential Transformers (LVDTs) were used to measure deflections at different locations: two at the loading points respectively, two at the two supports respectively, and one at the mid-span of the beam (Figure 6.3). The true mid-span deflection displacement of the beam was determined by subtracting the average displacement of the two supports from the mid-span vertical displacement from the LVDT.

The load was applied using a single hydraulic jack and equally distributed through a stiff steel beam to the two loading points. A load cell was installed at each loading point to precisely measure the load exerted. The load was applied with force control at steps of about 5.0 kN in total (i.e. 2.5 kN for each loading point) before concrete cracking and at steps of 10.0 kN afterwards; after the yielding of steel tension bars, the loading process was changed to displacement control at steps of 0.5 mm for the mid-span displacement.

Many strain gauges were installed at important positions in the beam. One strain gauge of 80 mm in gauge length was installed on the compression face at mid-span of the beam to monitor the maximum compressive concrete strain in the beam. One strain gauge of 5 mm in gauge length was installed at the mid-span of each steel

tension bar (Figure 6.3). A large number of strain gauges of 20 mm in gauge length were installed on the FRP soffit plate (over half the plate in the test shear span in Series I and over the whole FRP plate in Series II) to obtain the strain distributions during the loading process. The region of the FRP soffit plate near its end (Series I only) and near the loading points (both Series I and II) were provided with more closely-spaced strain gauges. Figure 6.4(a) and (b) give positions of strain gauges on the FRP soffit plate for specimens of Series I and Series II, respectively. In some of the beams, some strain gauges on the FRP soffit plate had to be omitted due to the presence of FRP U-jackets. The behaviour of U-jackets or parallel side strips were also monitored using strain gauges at the height of tension steel bars for U-jackets or at the ends and centre of the side strips. Test data including the applied loads, vertical displacements and strains were all collected using a data logger when the readings had stabilized after a load step (i.e. about one minute after each loading step).

6.4 TEST RESULTS OF SERIES I

6.4.1 Failure modes and load-deflection responses

The load-deflection curves of specimens in Series I are given in Figure 6.5, and details of the applied load, deflection and plate strain are summarized in Table 6.3. The load or ultimate load refer to the load or ultimate load at each loading jack; and the total load refer to the load summing the loads from both loading jacks of specimens in the reminder of this chapter for ease of description. The control specimen, with an FRP soffit plate only, failed by IC debonding with the ultimate load (see Figure 6.6 for failure modes of specimens in Series I) and the

corresponding mid-span deflection being 137.7 kN and 25.5 mm respectively. The provision of FRP U-jackets in both Specimens B2S1 andB3S1led to very similar increases in the ultimate load (about 11%) and the ultimate deflection (about 22%) over those of the control specimen (i.e. SpecimenB1S1). However Specimen B2S1 failed by IC debonding, while Specimen B3S1 failed by the rupture of the FRP plate, which occurred near the steel jackets in the non-test shear span instead of the test shear span where FRP U-jackets were installed. However, the FRP plate strains at mid-span of both Specimens B2S1 and B3S1 were about 7000 $\mu\varepsilon$, which was far below the rupture strain of the FRP material. The rupture of the FRP soffit plate is believed to have been caused, at least partially, by plate bending as a result of the strong constraint imposed by the strong steel jackets. Specimen B4S1 failed by IC debonding, which was initiated at the end of the parallel FRP strip closer to the mid-span. With the ultimate load and the ultimate deflection at mid-span 152.4 kN and 28.90 mm, Specimen B4S1 also achieved increases of about 11% in the ultimate load and about 22% in the ultimate mid-span deflection over those of the control specimen.

There are some minor differences between the load-deflection curves of different Series I specimens due to the use of different FRP U-jackets or parallel FRP strips (Figure 6.5). Before the cracking of concrete, the load-deflection responses of different test specimens coincide. This is because the FRP U-jackets or the FRP side strips did not make a significant contribution to the initial stiffness of the beam. After concrete cracking, Specimen B4S1 showed a stiffer response than the other three beams as the parallel FRP strips with fibres oriented in the horizontal direction were

able to make a greater contribution to beam stiffness. These side strips were effective in restraining the development of flexural cracks near the mid-span. During this stage, however, the two specimens with vertical U-jackets (i.e. B2S1 and B3S1) still showed the same load-displacement behaviour as that of the control specimen. This is because the vertical FRP U-jackets were not yet mobilized during this stage, as the flexural cracks developed during this stage were mostly parallel to the fibre direction of the vertical FRP U-jackets. When the steel tension bars were about to yield, many of the flexural cracks developed into inclined cracks and some of them intersected the vertical U-jackets. As a result, the cracks intersecting the U-jackets were restrained by the latter so that the load-displacement curves of Specimens B2S1 and B3S1 began to deviate from that of the control specimen. The yield load of Specimen B4S1 is higher than those of the other three specimens by about 10.0 kN as the FRP parallel side strips were mobilized before the yielding of steel.

The ductility of beams was also enhanced by the FRP U-jackets or parallel FRP side strips. In order to quantify the ductility of beams, a popular index is adopted herein. This ductility index, equal to the mid-span deflection at failure divided by the mid-span deflection at the yielding of steel tension bars, is given by

$$\mu_{\Delta} = \frac{\Delta_u}{\Delta_y} \tag{6.1}$$

in which Δ_u is the mid-span deflection at failure; and Δ_y is the mid-span deflection at the yielding of steel tension bars. As shown in Table 6.5, the values of this ductility index for Specimens B2S1, B3S1 and B4S1 are 2.09, 2.09 and 1.79, representing

increases of 15.8%, 15.8% and 1.6% over that of the control specimen respectively.

6.4.3 Cracking behaviour

The cracking behaviour of a beam is closely related to the debonding or rupture behaviour of the FRP soffit plate. Therefore, the cracking information, such as positions and widths of major cracks, was carefully recorded during the tests. The ultimate cracking patterns of the test shear span of all four specimens in Series I, including the positions of major cracks, are given in Figure 6.7. The positions of cracks were measured from the nearest support. There are 13, 15, 14, and 12 major cracks in the test half-span of Specimens B1S1, B2S1, B3S1 and B4S1 respectively. Minor differences are seen between the crack pattern of the control specimen and those of specimens with vertical FRP U-jackets; compared to the other three specimens, the cracks covered by the parallel side strips in Specimen B4S1 are spaced more sparsely while the cracks near the inner end of the parallel strips are spaced more densely. These results indicate that the vertical FRP U-jackets had a marginal effect on the crack pattern while the parallel FRP side strips changed the crack pattern significantly.

The major crack near the loading point in the test shear span played a critical role in the failure of all the beams. In Specimens B1S1, B2S1 and B4S1, the major crack near the loading point induced the initiation of IC debonding. Although Specimen B3S1 failed by the rupture of the FRP soffit plate, which occurred between the strong steel jackets, the major crack near the loading point achieved a similar width (about 0.50 mm) to those of Specimens B1S1 and B2S1 when the beam failed. Vertical FRP

U-jackets were ineffective in restraining the widening of the critical crack that initiated IC debonding but could slightly improve the ultimate load by offering resistance to the interfacial peeling (normal) stresses between the concrete and the FRP soffit plate. The parallel FRP side strips increased the spacing of cracks covered by them, but their abrupt termination near the loading point exacerbated the opening-up of the major crack near the loading point. As a result, in addition to the major crack near the loading point, some secondary cracks also existed near the major crack in SpecimenB4S1, which may have had a detrimental effect on IC debonding.

6.4.4 Strain distributions over the FRP soffit plate

Detailed strain distributions over the FRP soffit plate at representative load levels are given in Figure 6.8 to gain a better understanding of the debonding mechanism. In general, the strains in the FRP soffit plate are proportional to the moments. Local fluctuations in the FRP soffit plate strain are seen and these occur near the toes of major cracks. In all the specimens, the maximum measured strain in the FRP plate was recorded by the strain gauge near the toe of the critical crack under one of the loading points. The maximum strains in the FRP soffit plate at different load levels given in Table 6.3indicate that slight increases were achieved by the vertical FRP U-jackets and side strips. At the failure, the maximum measured strain in the FRP soffit plate (i.e. the debonding/failure strain) was 7500 $\mu\varepsilon$ in the control specimen (Specimen B1S1) but increased to 8153 $\mu\varepsilon$ and 8038 $\mu\varepsilon$ in Specimens B2S1 and B3S1 respectively. All the debonding/failure strains are only approximately 50% of the FRP rupture strain. Despite the fact that the ultimate load of Specimen B4S1 is

14.7 kN higher than that of the control specimen, the failure strain of the former is slightly lower than that of the latter. This is because the parallel side FRP strips shared the tensile force with the FRP soffit plate.

6.4.4 Strains in U-jackets and parallel side strips

Figure 6.9 presents results from strain gauges installed on FRP U-jackets and FRP parallel side strips. For beams with vertical FRPU-jackets (i.e. B2S1, B3S1), the strains on the U-jackets at steel yielding and ultimate failure are given in Figures 6.9a and 6.9b while those at the initiation of concrete cracking are not presented herein due to their small values (less than 100 $\mu\varepsilon$). Strains in the vertical FRP U-jackets increased with the applied load. Strains in the U-jackets at the plate end (i.e. U-jacket 1) were generally much higher than that in U-jacket 2 and U-jacket 3. The maximum strains recorded in U-jacket 1 were around 2000 $\mu\varepsilon$, occurring at about 100 mm from the beam bottom, where a flexural-shear crack intersected. This observation indicates the U-jackets have the ability to constrain the development of these cracks and to possibly eliminate concrete cover separation failure. The maximum strain of U-jacket 3 of Specimen B2S1 and U-jacket 2 of Specimen B3S1 at failure was about 1400 με, which is lower than that of U-jacket 1. The relatively low strains in the mid-span U-jackets show that these vertical U-jackets are not so ineffective in suppressing IC debonding. In addition, Specimen B3S1 failed by the rupture of the FRP soffit plate, with the maximum strain in the FRP soffit about 8038 $\mu\varepsilon$, which is much lower than the rupture strain of the CFRP plate. It is believed that this rupture resulted from bending induced by the constraint by the strong steel jacket near the loading point.

The strain distributions over the parallel FRP side strips in Specimen B4S1 are given in Figure 6.9(c). The parallel FRP side strips carried the tensile force together with steel tension bars, and bridged flexural-shear cracks covered by them. These side strips were under tension and led to the opening-up of cracks at the inner strip end (closer to the mid-span), thus inducing IC debonding, as a large interfacial shear stress gradient occurred near the ends of the FRP side strips. The maximum strains of the FRP side strips occurred near the mid-length of these side strips. After the occurrence of a major crack at the end of the FRP side strips (near the loading point), part of the FRP side strips near this major crack debonded.

6.5 TEST RESULTS OF SERIES II

6.5.1 Failure modes and load-deflection responses

The four specimens in Series II were conducted to investigate the effect of inclined FRP U-jackets on IC debonding in FRP-plated RC beams. In addition to the bonded FRP soffit plate, all the beams except the control specimen (Specimen B1S2) were provided with inclined FRP U-jackets as an anchorage measure against IC debonding. The key results of the tests, including the applied load, mid-span deflection and maximum strain of the FRP soffit plate at key stages are listed in Table 6.4. As expected, the control specimen failed by IC debonding, with the ultimate load and the ultimate mid-span deflection being 121.2kN and 34.42 mm respectively. The other three beams in Series II failed by the rupture of the FRP soffit plate; that is, IC debonding was successfully suppressed by the inclined FRP U-jackets (Figure 6.11). Both Specimens B3S2 and B4S2 were also close to concrete crushing at the rupture

of the FRP soffit plate as the concrete strains on the compression face at mid-span were about 3000 $\mu\varepsilon$, which is close to crushing strain of concrete.

Compared with the control specimen (Specimen B1S2), the ultimate load of Specimen B2S2 is slightly higher by 3.7% while the deflection at mid-span at failure is significantly lower by 23.5%. Specimens B3S2 and B4S2 achieved a significant increase of about 42.9% in the deflection at mid-span at failure although their ultimate loads increased by only about 8.1%. Similar performance of Specimens B3S2 and B4S2 indicated that U-jacket in Specimen B3S2 (0.358 mm in the nominal thickness, 318 mm in width and 424 mm in length), although the amount of the U-jacket is less than that in Specimen B4S2 (0.716 in the nominal thickness, 318 mm in width and 424 mm in length), was strong enough to suppress IC debonding. The ductility indices of Specimens B2S2, B3S2, and B4S2 are 1.92, 2.90 and 3.02, recording changes of -9.5%, 36.6% and 42.2% respectively compared to a value of 2.12 for the control specimen (Table 6.4). That is, the ductility of Specimen B2S2 is significantly lower than that of the control specimen. These comparisons indicate that to achieve a significant increase in both the ultimate load and the ductility, the inclined FRP U-jackets need to be installed in a low moment region (i.e. near the supports of a simple-supported beam).

The load-deflection curves of specimens at mid-span in Series II are given in Figure 6.10. They are divided into three distinct parts by the initiation of concrete cracking, the yielding of steel tension bars, and debonding failure. Before concrete cracking, the different load-deflection curves coincide. Specimen B2S2 had a stiffer response after concrete cracking as the inclined FRP U-jackets near the loading points began

to restrain the development of flexural cracks near the loading points. The other two specimens (Specimens B3S2 and B4S2) installed with inclined FRP U-jackets showed similar behaviour. Before the load, as each loading jack reached about 110 kN, the load-deflection curves of these two specimens coincide with that of the control specimen, which indicates that no significant contribution to beam stiffness was made by the inclined FRP U-jackets. In addition, slight drops of about 5 kN in the applied load are seen at loads of 118.11 kN for Specimen B3S2 and 115.6kN and 119.2 kN for Specimen B4S2. Such slight drops were induced by the thorough debonding of the bonded FRP plate throughout the critical shear span of the beam; however, the beams were able to carry further loads until the rupture of the FRP soffit plate because the FRP soffit plate could transfer its tensile force to the inclined GFRP U-jackets.

6.5.2 Cracking behaviour

The ultimate crack patterns of all four specimens in Series II are given in Figure 6.12. The positions of all major cracks given in Figure 6.12 are measured from the left support. In the control specimen, 33 major cracks were present, and the FRP soffit plate debonding initiated at the toe of the crack at 1224 mm from the left support. The spacing between the critical crack at 1224 mm from the left support and its adjacent crack in the shear span is 105 mm. In Specimen B2S2, cracks covered by the inclined FRP U-jackets were well restrained by them, which led to tension in the inclined FRP U-jackets and increased the stiffness of the beam. However, the cracks near the support were wider in Specimen B2S2 than in Specimen B1S2. Both Specimen B3S2 and Specimen B4S2 had a crack pattern at failure, which is similar

to that of the control specimen; they had 32 and 31 major cracks respectively at failure.

6.5.3 Strain distributions over the FRP soffit plate

Figure 6.13 gives the strain distributions over the FRP soffit plate at representative load levels. At failure, the maximum measured strain in the FRP soffit plate was 5610 $\mu\varepsilon$ in the control specimen (B1S2), but increased to 9323 $\mu\varepsilon$, 10612 $\mu\varepsilon$ and 11127 $\mu\varepsilon$ for Specimens B2S2, B2S3, and B4S2 respectively. In general, the FRP strain distribution is proportional to the moment distribution except for slight fluctuations due to presence of major cracks. However, in Specimen B2S2, the strain gradient in the FRP soffit plate near a loading point is much higher than the moment gradient of the same region due to the load transfer between the inclined U-jacket and the FRP soffit plate. After the thorough debonding of the FRP soffit plate between the two inclined FRP U-jackets, the strains in the FRP soffit plate in both Specimens B3S2 and B4S2 became uniform, with the FRP soffit plate supported at the two ends by the inclined FRP U-jackets.

6.5.4 Effects of U-jackets

The U-jacket strain values shown in Figure 6.14 were averaged from the readings of three strain gauges installed near the bottom of the U-jacket (Figure 6.14). Before concrete cracking, the strains in the U-jackets in Specimen B2S2 were small (less than 100 $\mu\varepsilon$). During this stage, no significant force transfer between the U-jackets and the FRP soffit plate existed, so the strain distribution over the FRP soffit plate

was proportional to the moment distribution. After concrete cracking near the loading points, the strains in the U-jackets of SpecimenB2S2 increased abruptly due to occurrence of major cracks. Afterwards, significant force transfer from the inclined U-jackets to the FRP soffit plate developed, which resulted in an abrupt variation of strains in the FRP soffit plate nearby. In Specimens B3S2 and B4S2, before the load reached 40 kN, the U-jacket strains were close to zero and increased gradually when cracking occurred near the U-jacket. An abrupt increase in the U-jacket strain was observed in both beams when the FRP soffit plate debonded thoroughly but was subsequently supported by the bonded U-jackets.

The strains in the inclined U-jackets indicate that inclined U-jackets in the mid-span region (e.g. those used in Specimen B2S2) and a low-moment region (e.g. those used in SpecimensB3S2 and B4S2) both have a significant effect on IC debonding in FRP-plated RC beams. Inclined U-jackets in the mid-span region can be highly mobilized by the widening of major cracks in the region, and the forces in the highly tensioned U-jackets are then transferred to the FRP soffit plate. For inclined U-jackets installed in a low-moment region (e.g. near the supports of a simply-supported beam), the U-jackets are much less mobilized by cracks in the region, so a significant force transfer from the inclined U-jackets to the FRP soffit plate does not exist. On the contrary, the tensile force in the FRP soffit plate can be transferred to the inclined U-jackets, which allows the beam to carry further loading after the thorough debonding of the FRP soffit plate. Therefore, inclined FRP U-jackets in the low moment regions (i.e. near the plate ends) are more effective in mitigating IC debonding failures.

6.6 CONCLUSIONS

Eight tests in two series on full-scale FRP-plated RC beams installed with vertical FRP U-jackets, parallel FRP side strips, or inclined FRP U-jackets for the mitigation of IC debonding have been reported and interpreted in this chapter. In Series I, four specimens were tested to investigate the effect of vertical FRP U-jackets on IC debonding, while the four tests of Series II were conducted to investigate the effect of inclined FRP U-jackets on IC debonding. Detailed results including failure modes, crack patterns, deflections and strains were presented and discussed with an emphasis on clarifying the mechanism of IC debonding in FRP-plated beams with U-jacket anchorage. The main experimental observations and conclusions are summarised below.

(1) The effect of vertical FRP U-jackets on IC debonding is marginal. About a 10% increase in the ultimate load was observed in the two specimens installed with vertical U-jacket anchorage compared with that of the control beam bonded with an FRP soffit plate only. The tensile force in the FRP soffit plate cannot be effectively transferred to the vertical FRP U-jackets.

(2) The effect of parallel FRP side strips on IC debonding is also marginal, and the associated ultimate load increase as a result of these strips was found to be also around 10% for the specimen tested in the present study. The abrupt termination of the parallel side strips under the loading point exacerbates the development of cracks there, which leads to IC debonding initiating at these cracks.

(3) Strong vertical FRP U-jackets may result in premature rupture of the FRP soffit plate as these strong vertical FRP U-jackets can cause undesirable bending in the soffit plate. This bending phenomenon explains the fact that some specimens in both the present study and the existing literature (e.g. specimens B2, B4 and C3 in Brena et al. (2003)) failed by the rupture of the FRP soffit plate at a maximum strain in the FRP soffit plate far below its rupture strain.

(4) Results of tests on specimens with 45^{o} inclined FRP U-jackets indicated that inclined U-jackets near the mid-span (e.g. Specimen B2S2) and in a low moment region (e.g. Specimens B3S2 and B4S2) have different effects on IC debonding. Inclined U-jackets near the mid-span can be highly tensioned by the widening of major cracks, and the resulting tensile forces in the inclined U-jackets need to be transferred to the FRP soffit plate, which may result in the premature rupture of the FRP soffit plate with only a slight increase in the ultimate load of the beam. Inclined FRP U-jackets in low moment regions can significantly increase both the ultimate load and the ductility of FRP-plated RC beam as they can carry forces transferred from the FRP soffit plate. In particular, such included FRP U-jackets can even carry the tensile force from the FRP soffit plate when the soffit plate has otherwise completely debonded from the concrete substrate. As a result of this force transfer, the FRP-plated RC beam is able to carry additional loading after the thorough debonding of the FRP soffit plate until the included FRP U-jackets fail by debonding or rupture. Therefore, inclined FRP U-jackets in low-moment regions (e.g. near

the supports of a simply-supported beam) are an attractive measure for the mitigation of IC debonding in FRP-plated RC beams.

6.7 REFERENCES

ASTM D3039/D3039M-08 (2008). *Standard test method for tensile properties of polymer matrix composite materials*, ASTM International, West Conshohocken, Philadelphia (PA).

ASTM D7565/D7565M-10 (2010). *Standard test method for determining tensile properties of fiber reinforced polymer matrix composites used for strengthening of civil structures*, ASTM International, West Conshohocken, Philadelphia (PA).

Brena, S.F., Bramblett, R.M., Wood, S.L. and Kreger, M.E. (2003). "Increasing flexural capacity of reinforced concrete beams using carbon fiber-reinforced polymer composites", *ACI Structural Journal*, Vol. 100, No. 1, pp.36-46.

BS EN 12390-3 (2009). *Testing hardened concrete Part 3: Compressive strength of test specimens*, British Standard Institution, London, UK.

BS EN ISO 6892-1 (2009). *Metallic materials-Tensile testing Pat 1: Method of test atambient temperature*, British Standard Institution, London, UK.

Kalfat, R., Al-Mahaidi, R. and Smith, S.T. (2013). "Anchorage devices used to improve the performance of reinforced concrete beams retrofitted with FRP composites: state-of-the-art review", *Journal of Composites for Construction*, ASCE,Vol. 17, No. 1, pp.14-33.

Kotynia, R., Baky, H.A., Neale, K.W. and Ebead, U.A. (2008). "Flexural strengthening of RC beams with externally bonded CFRP systems: Test results

and 3D nonlinear FE analysis", *Journal of Composites for Construction*, ASCE, Vol. 12, No. 2, pp. 190-201.

Leung, C.K.Y. (2006). "FRP debonding from a concrete substrate: Some recent findings against conventional belief", *Cement & Concrete Composites,* Vol. 28**,**No. 8, pp.742-748.

Matthys, S. (2001). "Structural behavior and design of concrete members strengthened with externally bonded FRP reinforcement", Doctoral thesis, University of Ghent, Belgium.

Rosenboom, O. and Rizkalla, S. (2008). "Experimental study of intermediate crack debonding in fiber-reinforced polymer strengthened beams", *ACI Structural Journal*, Vol. 105, No. 1, pp.41-50.

Smith, S.T. and Teng, J.G.(2003). "Shear-bending interaction in debonding failures of FRP-plated RC beams", *Advances in Structural Engineering,* Vol. 6**,** No.3, pp.183-199.

6.8 TABLES AND FIGURES

Table 6.1 Geometrical and material properties of beam specimens with FRP U-jackets for mitigating IC debonding (to be continued)

Source		Brena et al. 2003						Matthys 2000	
Specimen		A3(C)[#1]	B2	B4	B5	C2(C)	C3	BF2	BF6
Concrete cylinder compressive strength f_c', MPa		35.1	37.2	34.3	34.3	35.1	35.1	36.5	35.9
Beam dimensions	Clear span L, mm	2690				3000		3800	
	Width b_c, mm	203				203		200	
	Heighth_c/effective depth d, mm	356/318				406/368		450/405[#3]	
Steel reinforcement	Tension bars (deformed)/yield strength f_{yt}, MPa	2T16/440				2T16/440		4T16/590	
	Compression bars (deformed)/yield strength f_{yt}, MPa	2T10/440				2T10/440		2T/16/590	
	Stirrups	Y7@102				Y7@102		NG	
	Yield strength of stirrups f_{yv}, MPa	596				596			
	Elastic modulus of all steel bars E_s, GPa	200				200			
FRP soffit plate	Type	Wet lay-up	Wet lay-up	Wet lay-up	Wet lay-up	Wet lay-up		Pultruded	
	Nominal (fibre) thickness$n \times t_f$, mm	$\mathbf{2 \times 0.165}$	$\mathbf{2 \times 0.168}$	$\mathbf{2 \times 0.168}$	$\mathbf{2 \times 0.168}$	$\mathbf{2 \times 1.04}$		$\mathbf{1 \times 1.2}$	
	Strip width b_f, mm	50	50	50	50	50		100	
	Strip length L_f, mm	2084	2338	2338	1780	2774		3700	
	Tensile strength f_f, MPa	3790	3400	3400	3400	760		3200	
	Elastic modulus E_f, GPa	230	230	230	230	62		159	
FRP U-jackets[#4]	Type	/	Wet lay-up	Wet lay-up	Wet lay-up	/	Wet lay-up	Wet lay-up	
	Nominal (fibre) thickness$n \times t_f$, mm		N	N	N		N	$\mathbf{1 \times 0.111}$	
	Strip width $\boldsymbol{b_f}$, mm		50	50	50		50	300	
	Strip number		6[#5]	4	4		6	1	
	Start point		distributed	distributed	distributed		distributed	100	
	End point							430	
	Tensile strength f_f, MPa		3400	3400	3400		760	3500	
	Elastic modulus E_f, GPa		230	230	230		62	233	
Test results	Failure mode	IC	FR	FR	IC	IC	FR	IC	IC
	Ultimate strength (kN)	69.2	71.0	66.3	65.0	63.0	74.5	185.0	183.0
	Increase ratio	/	2%	- 4%	-6%	/	18%	/	-1%

Table 6.1 Geometrical and material properties of beam specimens with FRP U-jackets for mitigating IC debonding (continued)

Source		Rosenboom and Rizkalla 2008		Kotynia et al. 2008					
Specimen		EB1SB	EB1S	B-08S	B-08Sm	B-08Sk	B-08M	B-08Mm	B-08Mk
Cylinder compressive strength of concrete, f_c', MPa		37.3	61.3	32.3	33.5	33.8	32.3	38.2	32.0
Beam dimensions	Clear span L, mm	8928		4200			4200		
	Width b_c, mm	127		150			150		
	Heighth_c/effective depth d, mm	432/274		300/270			300/270		
Steel reinforcement	Tension bars (deformed)/yield strength f_{yt}, MPa	10T11/702.6		3T12/524			3T12/524		
	Compression bars (deformed)/yield strength f_{yt}, MPa	N		2T12/524			2T12/524		
	Stirrups			Y6@100+ Y6@200			Y6@100+ Y6@200		
	Yield strength of stirrups f_{yv}, MPa			437			437		
	Elastic modulus of all steel bars E_s, GPa			207			207		
FRP soffit plate	Type	Wet lay-up		Wet lay-up			Wet lay-up		
	Nominal (fibre) thickness$n \times t_f$, mm	$\mathbf{1 \times 1.19}$		$\mathbf{1 \times 1.20}$			$\mathbf{1 \times 1.40}$		
	Strip width b_f, mm	102		50			120		
	Strip length L_f, mm	8230		4050			4050		
	Tensile strength f_f, MPa	2800		2915			2743		
	Elastic modulus E_f, GPa	165		172			220		
FRP U-jackets	Type	/	Wet lay-up	/	Wet lay-up	Pultruded	/	Wet lay-up	Pultruded
	Nominal (fibre) thickness$n \times t_f$, mm		/		$\mathbf{1 \times 0.13}$	$\mathbf{1 \times 1.4}$		$\mathbf{1 \times 0.13}$	$\mathbf{1 \times 1.4}$
	Strip width $\boldsymbol{b_f}$, mm		/		1000	40		1000	40
	Strip number		5		1	6		1	6
	Start point		distributed		1100	1000		1100	1000
	End point				2100	2100		2100	2100
	Tensile strength f_f, MPa		N		3500	2295		3500	2295
	Elastic modulus E_f, GPa		N		230	132		230	132
Test results	Failure mode	IC	IC	IC	IC	IC	IC	IC	IC
	Ultimate strength (kN)	81.0	88.1	48	51	51	70	76	75
	Increase ratio	-	9%	/	6%	6%	/	9%	7%

Table 6.2 Material properties of steel and FRP

	Material	Yield stress, f_y (MPa)	Ultimate stress, f_u (MPa)	Elastic modulus, E (GPa)
Series I	8 mm bars	367	488	208
	16 mm bars	531	620	214
	FRP	/	3263	251
Series II	8 mm bars	368	526	202
	16 mm bars	525	648	206
	CFRP	/	3263	251
	GFRP	/	2316	78

Table 6.3 Summary of test results of Series I

Specimen		**B1S1**	**B2S1**	**B3S1**	**B4S1**
Cylinder concrete strength (MPa)		49.0	51.1	51.1	52.7
Initiation of concrete cracking	Load at each loading jack (kN)	31.0	30.3	31.1	30.1
	Mid-span displacement (mm)	1.60	1.48	1.52	1.26
	Maximum strain in soffit plate (με)	444	476	689	349
Initiation of yielding of steel tension bars	Load at each loading jack (kN)	111.4	124.4	121.5	132.0
	Mid-span displacement (mm)	13.98	15.00	15.82	16.40
	Maximum strain in soffit plate (με)	3227	3458	3641	3665
Beam failure	Load at each loading jack (kN)	137.7	151.3	152.9	152.4
	Mid-span displacement (mm)	25.47	31.30	30.88	28.90
	Maximum strain in soffit plate (με)	7401	8153	8038	7434
Ductility index		1.75	2.09	2.09	1.79
Failure mode		IC	IC	FR	IC

Note: IC = IC debonding; FR = FRP rupture

Table 6.4 Summary of test results of Series II

Specimen		B1S2	B2S2	B3S2	B4S2
Cylinder concrete strength (MPa)		25.9	27.1	27.8	28.3
Initiation of concrete cracking	Load at each loading jack (kN)	18.7	21.1	23.3	21.2
	Mid-span displacement (mm)	1.41	1.81	1.68	1.37
	Maximum strain in soffit plate (με)	239	337	290	330
Initiation of yielding of steel tension bars	Load at each loading jack (kN)	92.4	92.4	92.8	93.0
	Mid-span displacement (mm)	16.20	13.70	16.23	16.92
	Maximum strain in soffit plate (με)	2497	4239	3545	4555
Beam failure	Load at each loading jack (kN)	121.2	125.7	131.0	130.5
	Mid-span displacement (mm)	34.42	26.34	47.12	49.02
	Maximum strain in soffit plate (με)	5610	9323	10612	11127
Ductility index		2.12	1.92	2.90	3.02
Failure mode		IC	FR	FR	FR

Note: IC = IC debonding; FR = FRP rupture

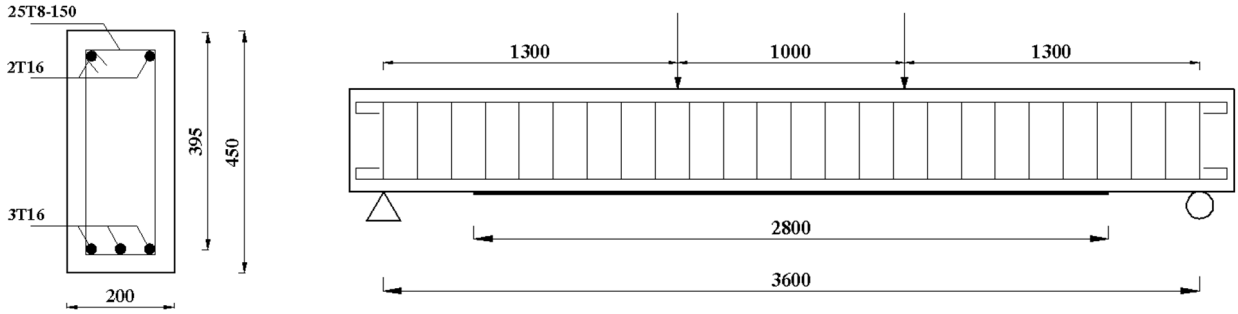

(a) B1S1

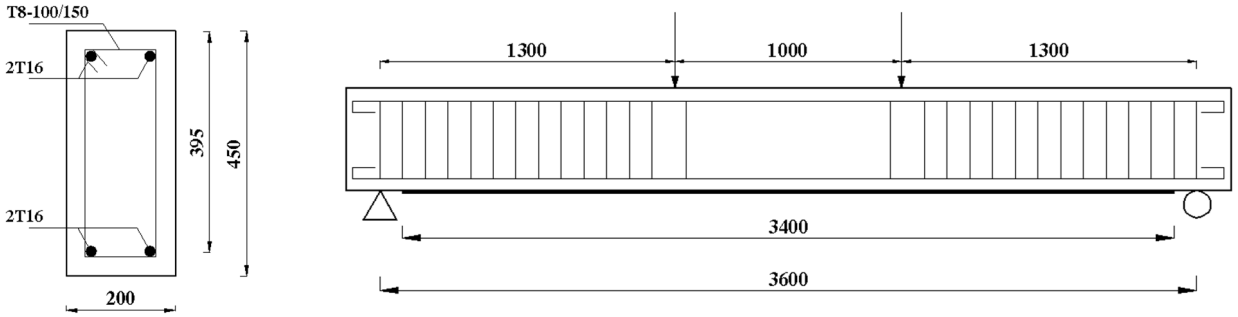

(b) B1S2

Figure 6.1 Geometries of control beams (all dimensions in mm)

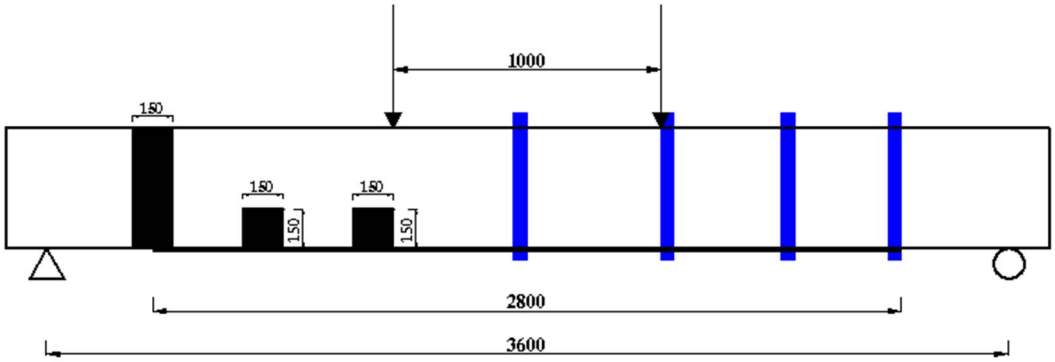

(a) B2S1

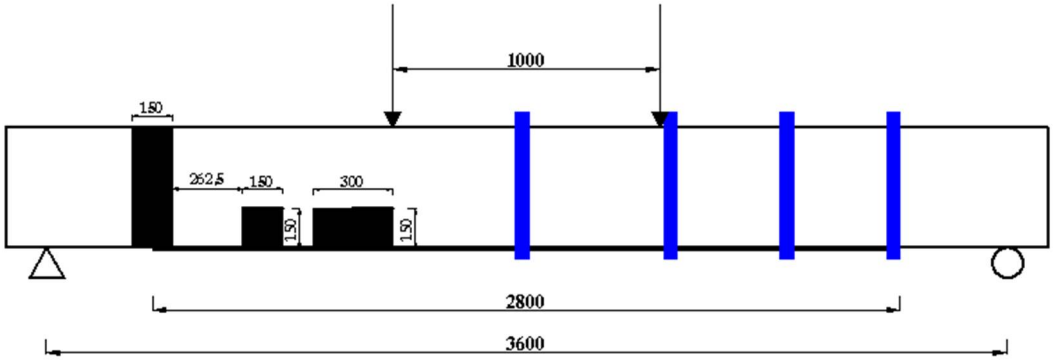

(b) B3S1

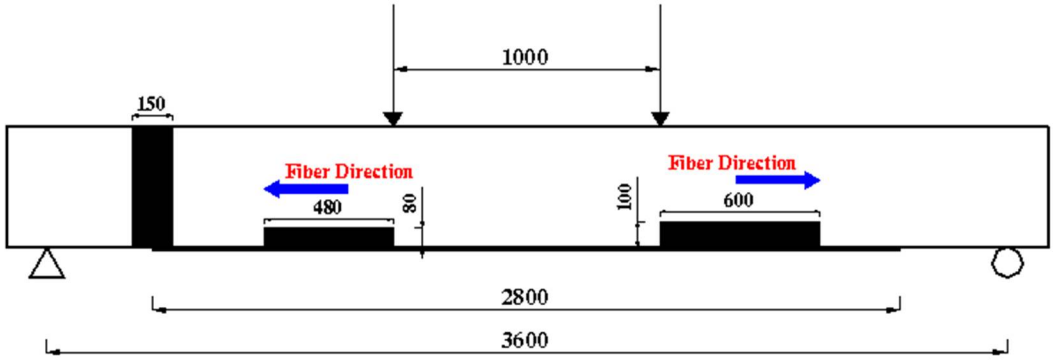

(c) B4S1

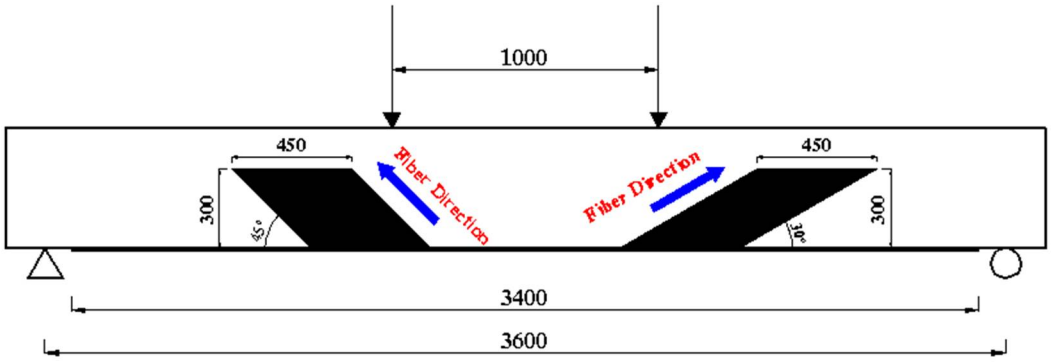

(d) B2S2

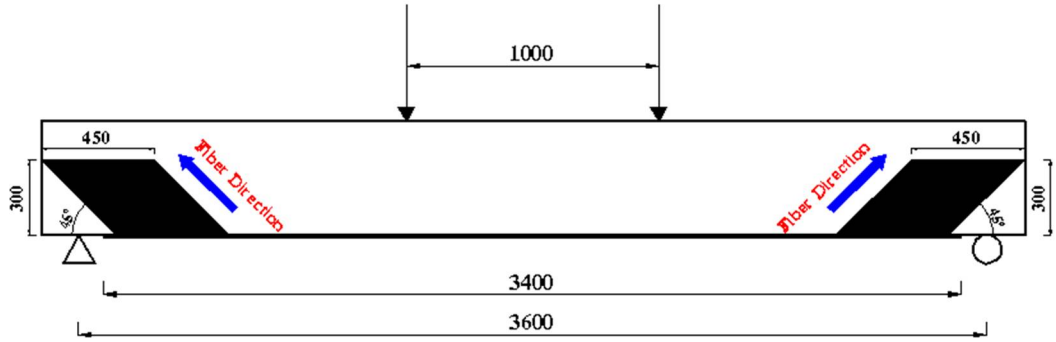

(e) B3S2 and B4S2

Figure 6.2 FRP U-jacket layouts (all dimensions in mm)

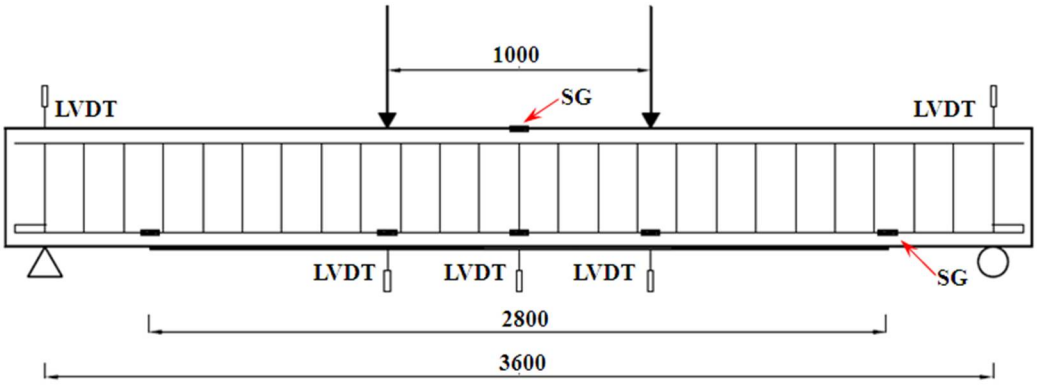

Figure 6.3 Positions of LVDTs and strain gauges on steel tension bars

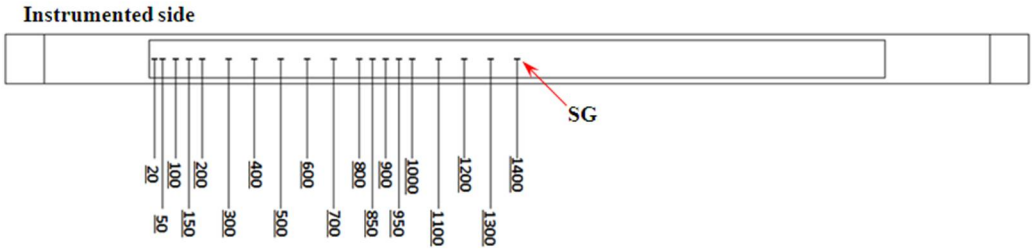

(a) Series-I

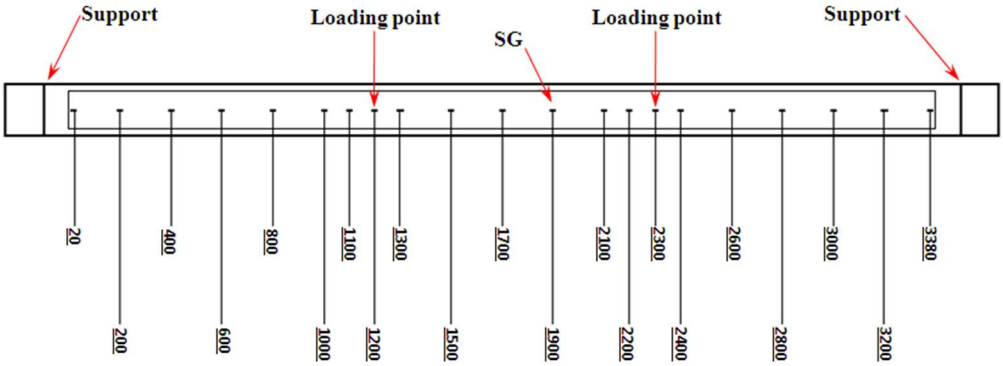

(b) Series-II

Figure 6.4 Positions of strain gauges on the soffit plate of control specimens

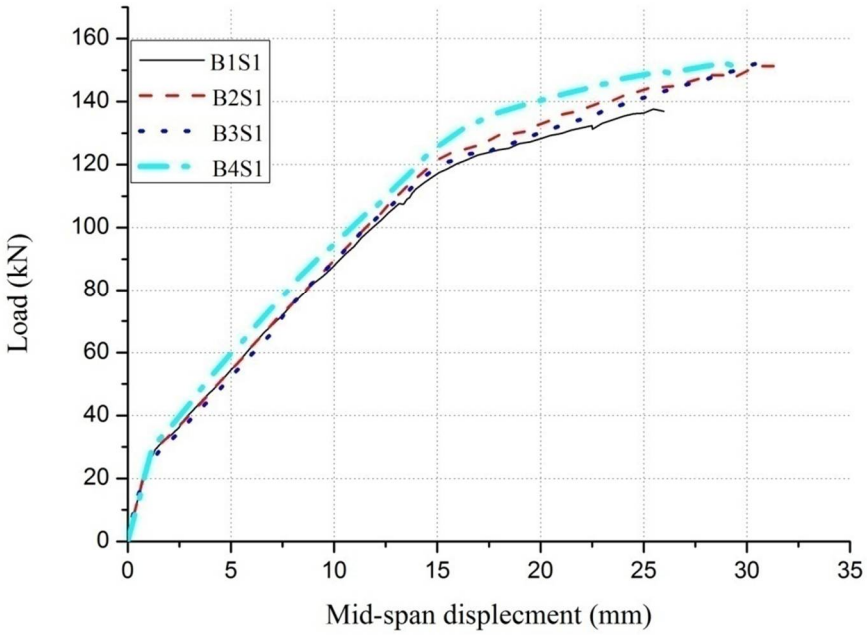

Figure 6.5 Load-deflection curves of specimens in Series I

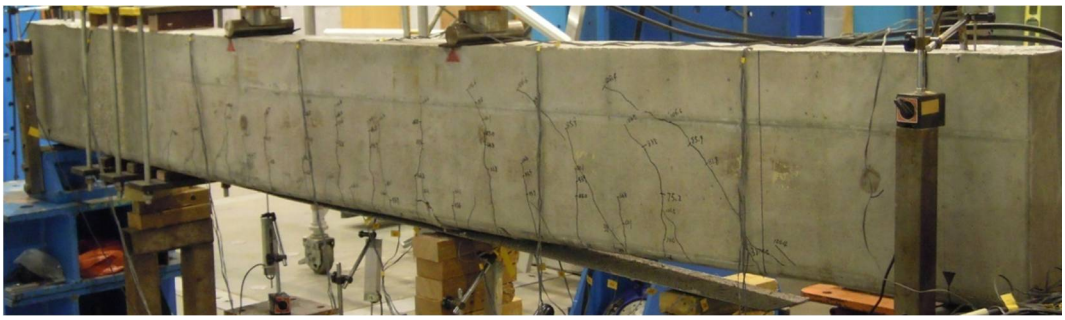

(a) Specimen B1S1

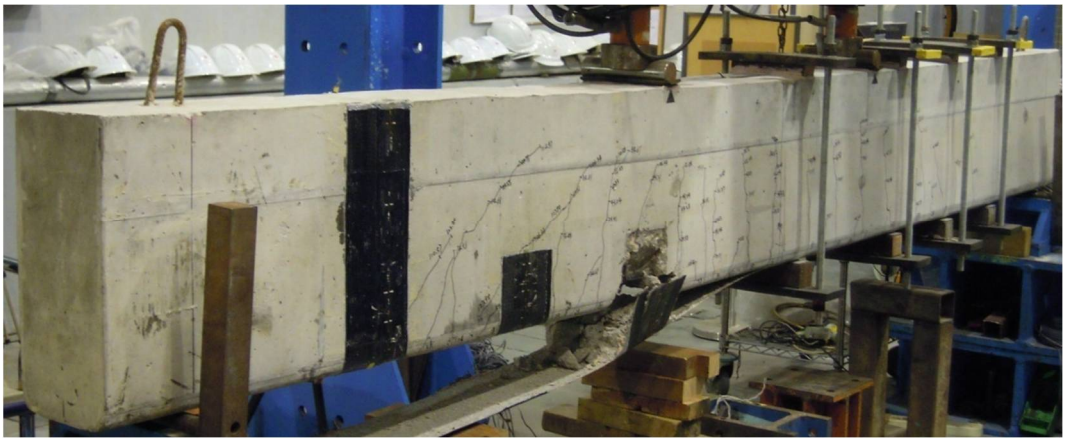

(b) Specimen B2S1

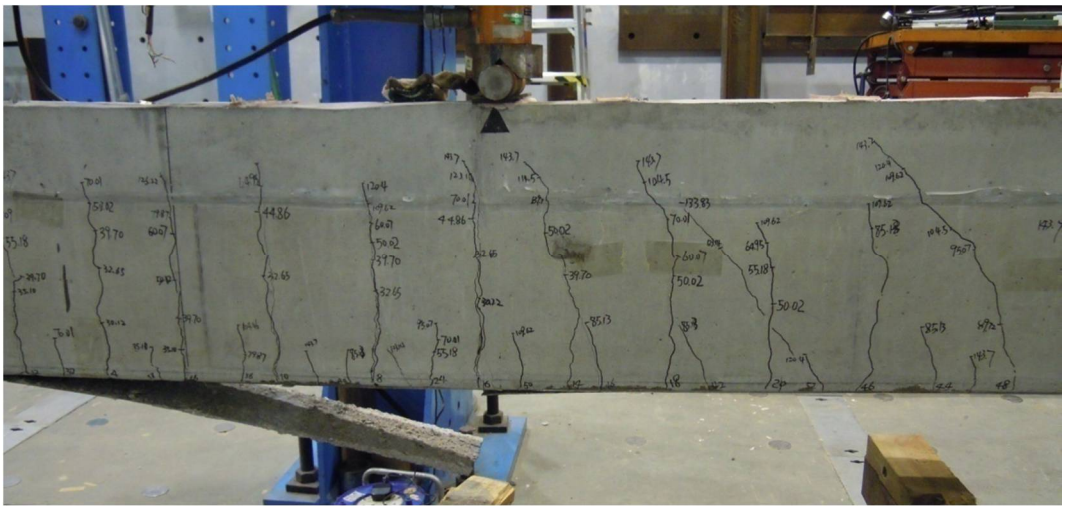

(c) Specimen B3S1

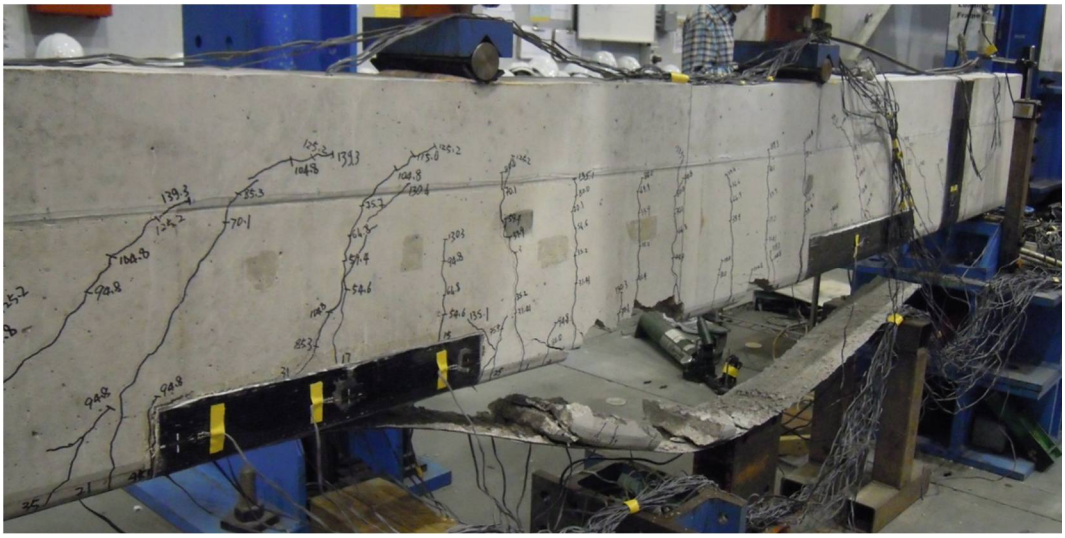

(d) Specimen B4S1

Figure 6.6 Failure modes of specimens in Series I

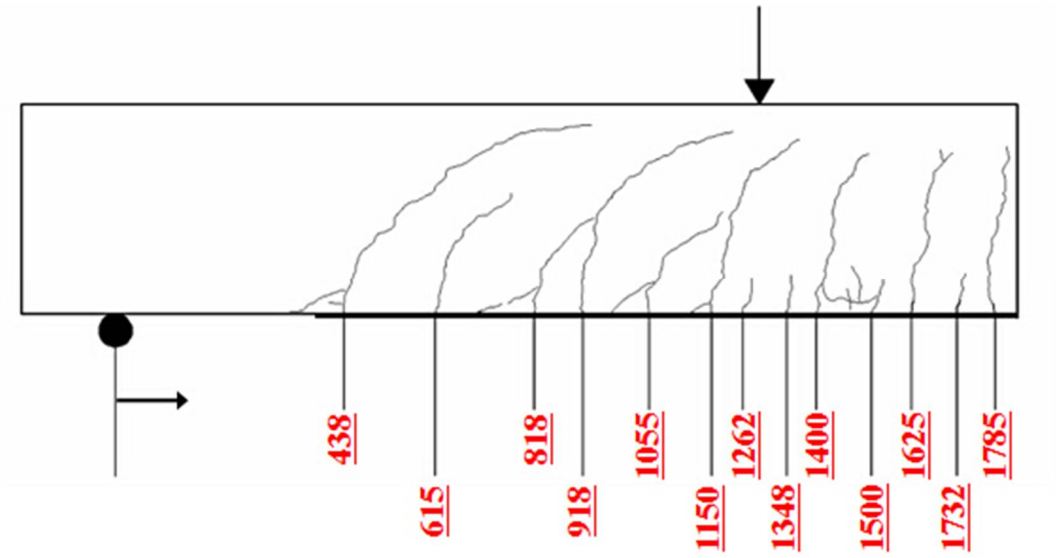
438
615
818
918
1055
1150
1262
1348
1400
1500
1625
1732
1785

(a) B1S1

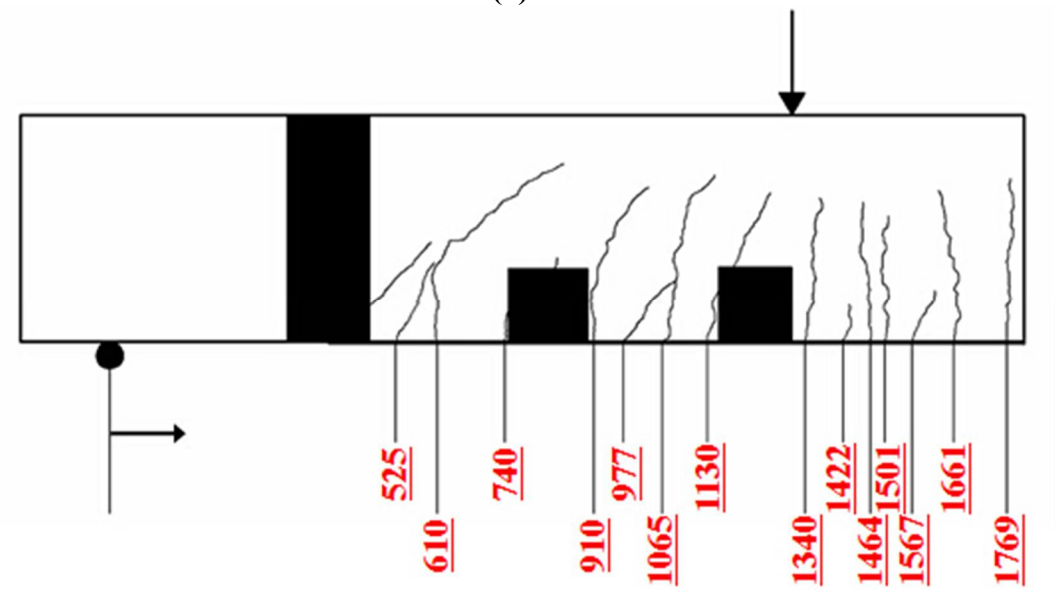
525
610
740
910
977
1065
1130
1340
1422
1464
1501
1567
1661
1769

(b) B2S1

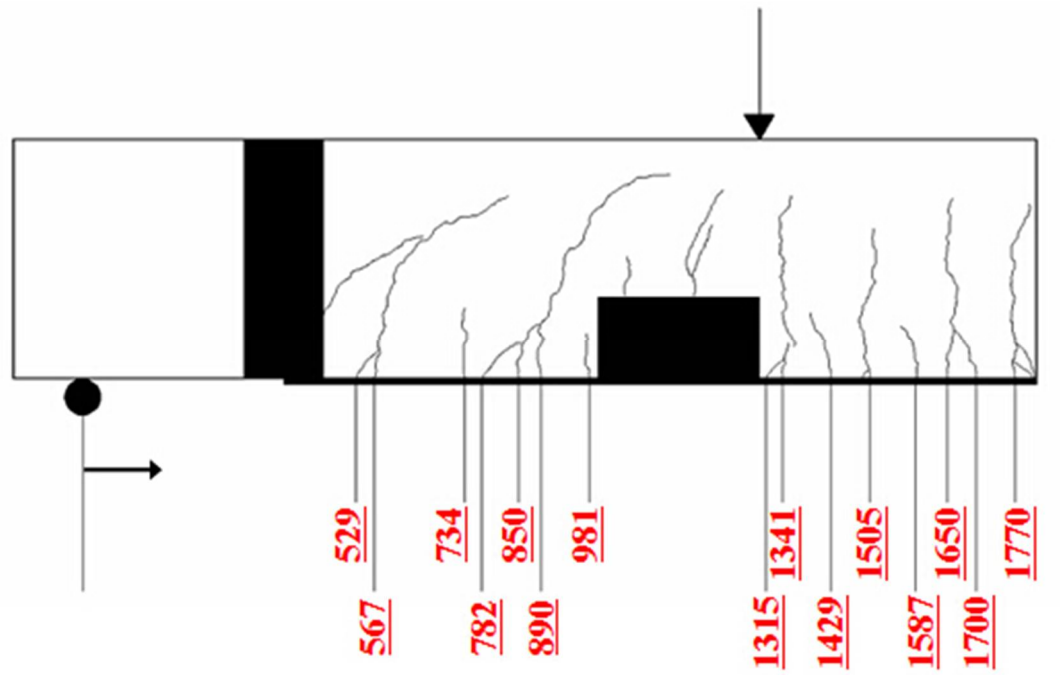

(c) B3S1

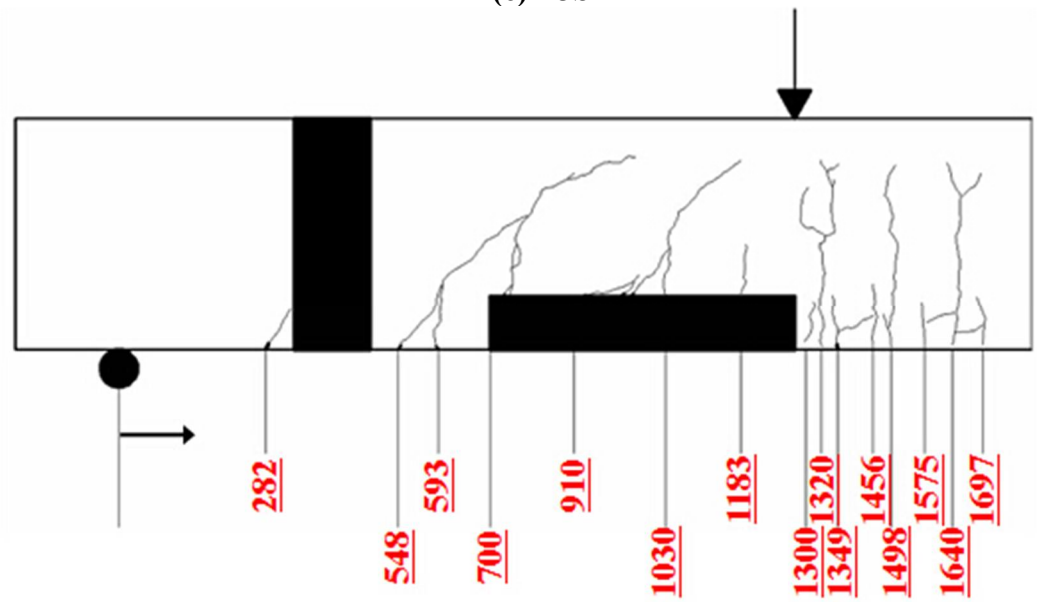

(d) B4S1

Figure 6.7 Crack patterns at failure of specimens in Series I

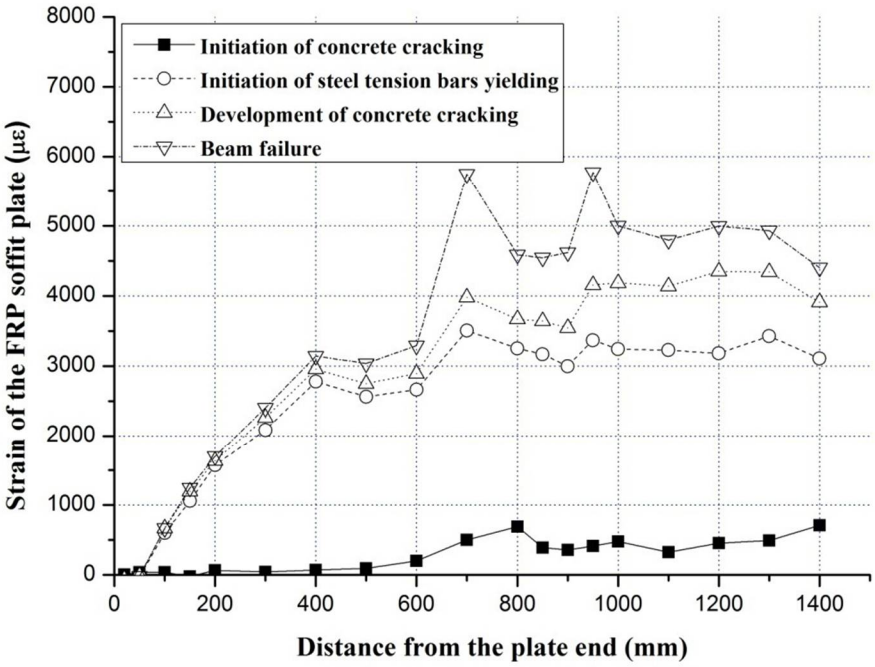

(a) Specimen B1S1

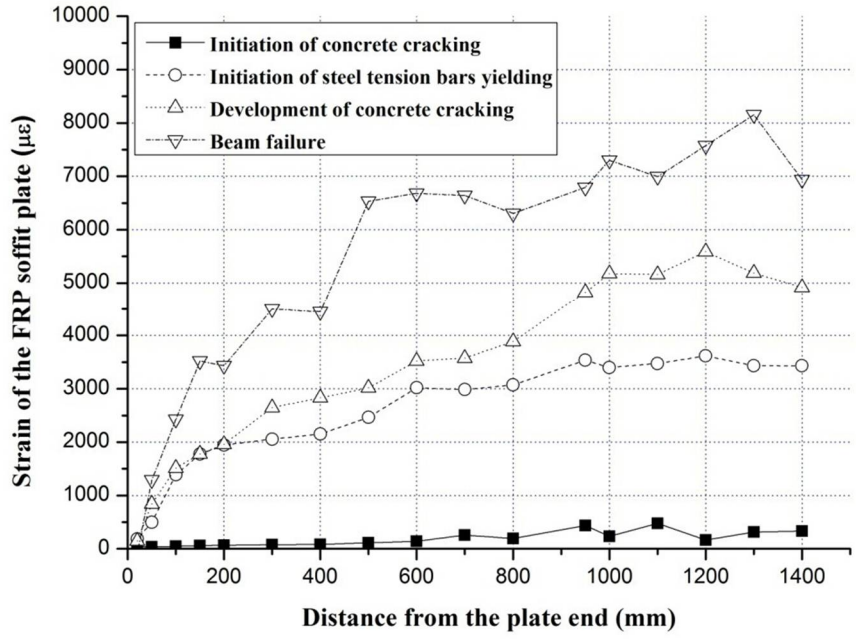

(b) Specimen B2S1

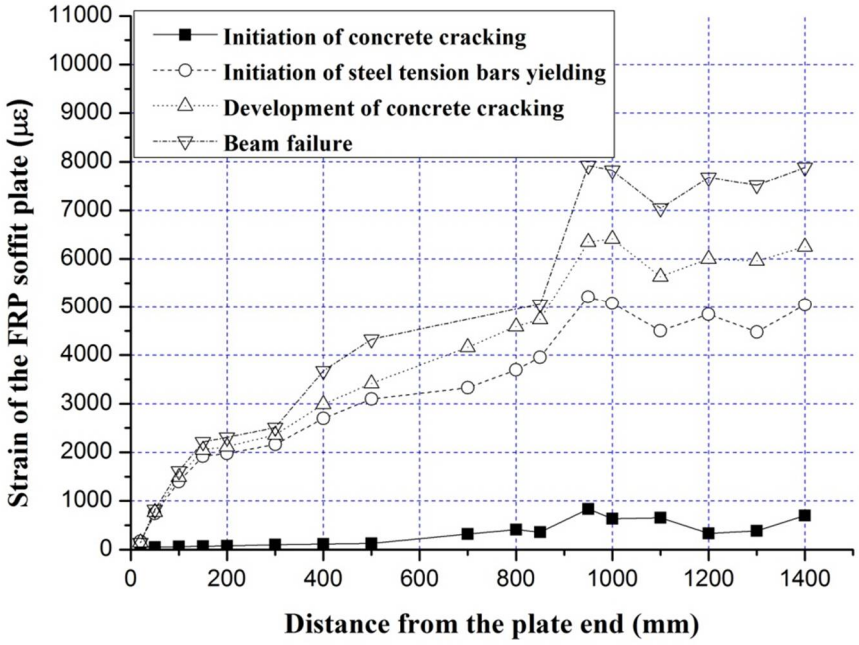

(c) Specimen B3S1

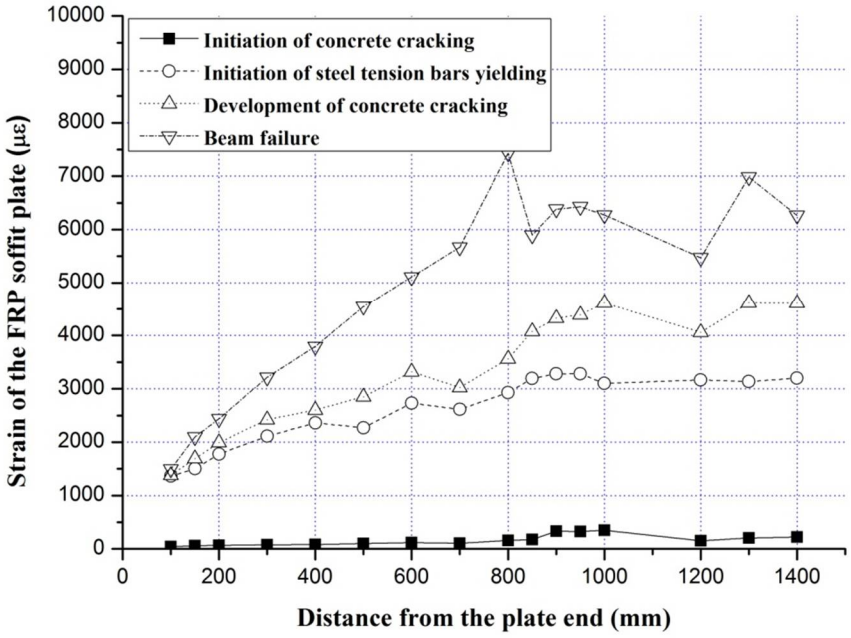

(d) Specimen B4S1

Figure 6.8 Strain distributions over the FRP soffit plate of specimens in Series I

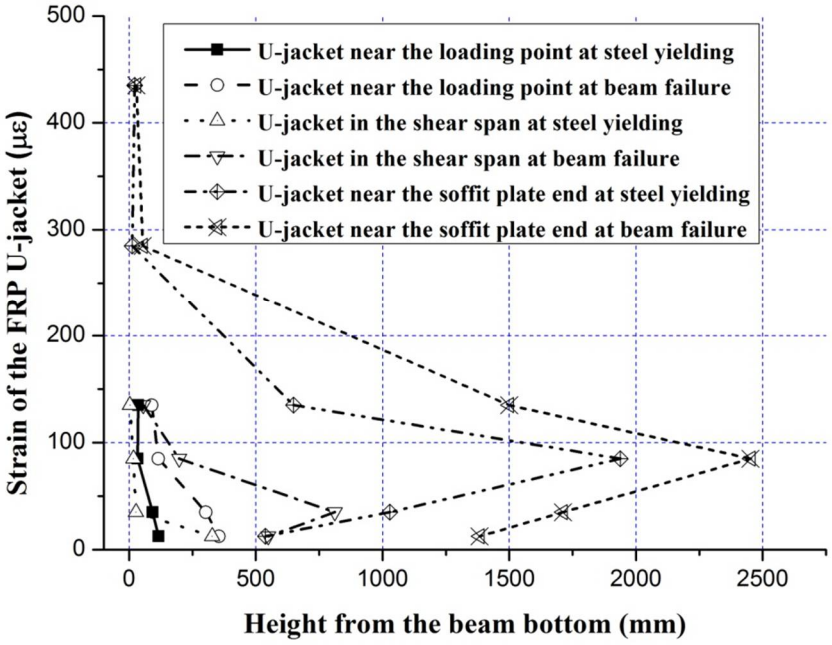
U-jacket near the loading point at steel yielding
U-jacket near the loading point at beam failure
U-jacket in the shear span at steel yielding
U-jacket in the shear span at beam failure
U-jacket near the soffit plate end at steel yielding
U-jacket near the soffit plate end at beam failure
Strain of the FRP U-jacket (με)
Height from the beam bottom (mm)
0
100
200
300
400
500
0
500
1000
1500
2000
2500

(a) B2S1

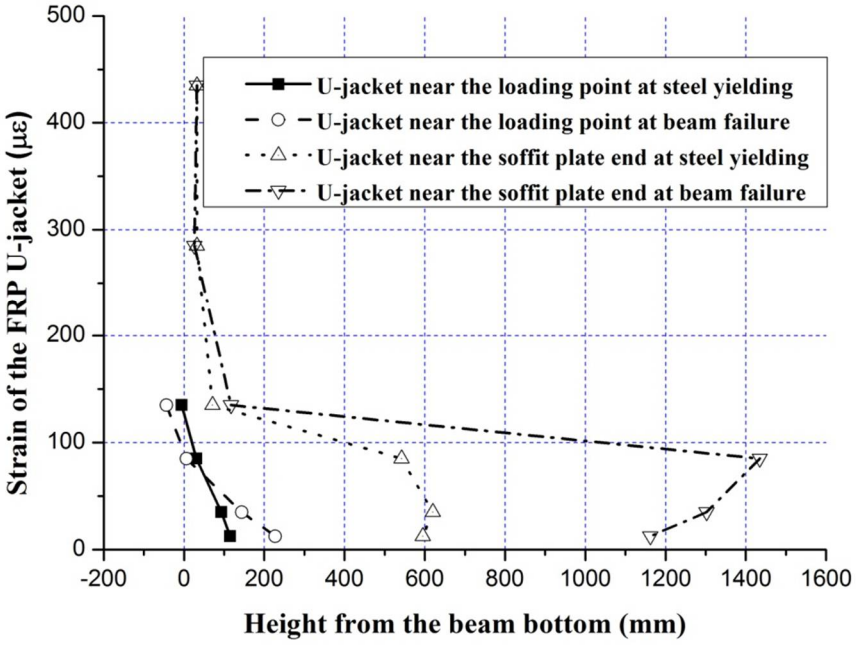
U-jacket near the loading point at steel yielding
U-jacket near the loading point at beam failure
U-jacket near the soffit plate end at steel yielding
U-jacket near the soffit plate end at beam failure
Strain of the FRP U-jacket (με)
Height from the beam bottom (mm)
0
100
200
300
400
500
-200
0
200
400
600
800
1000
1200
1400
1600

(b) B3S1

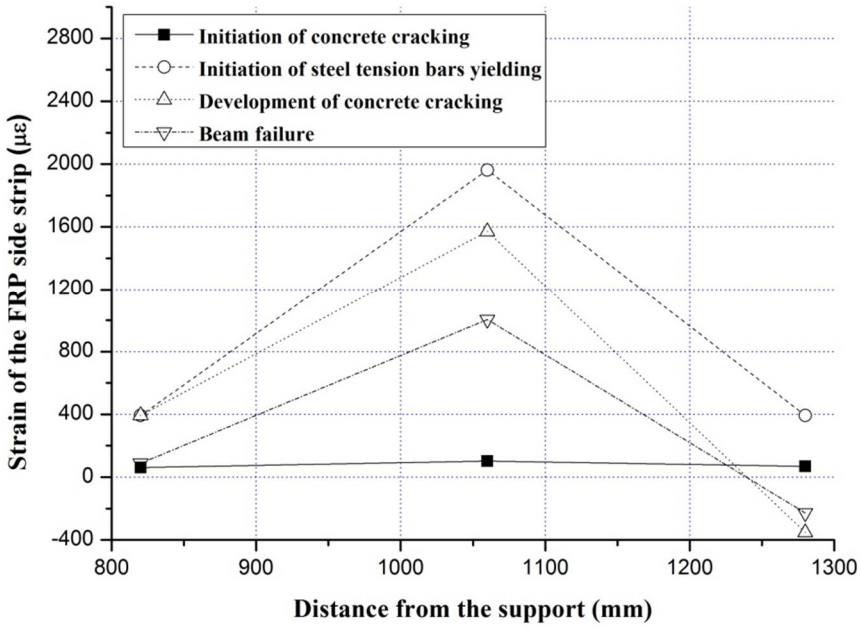

(c) B4S1

Figure 6.9 Strain distributions over the U-jacket or side strip of specimens in Series I

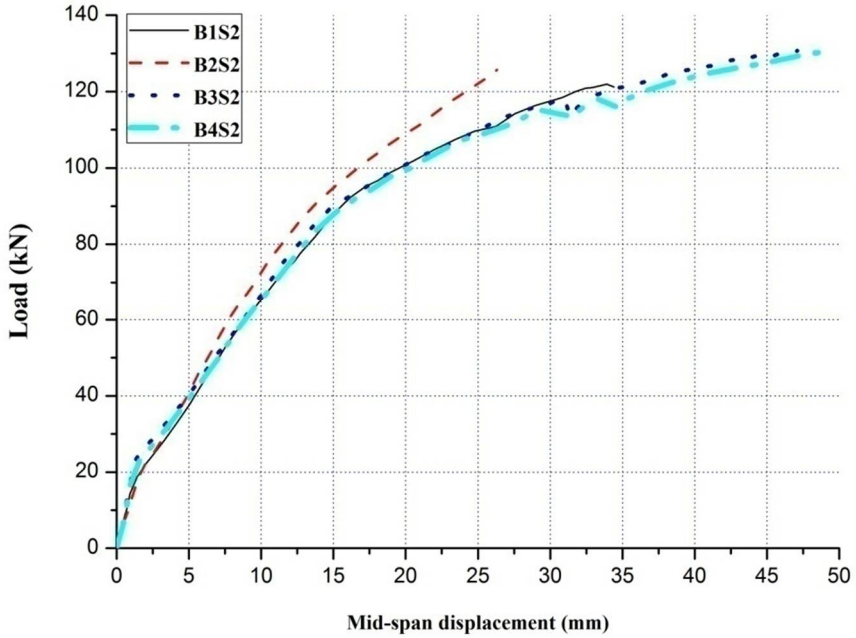

Figure 6.10 Load-deflection curves of specimens in Series II

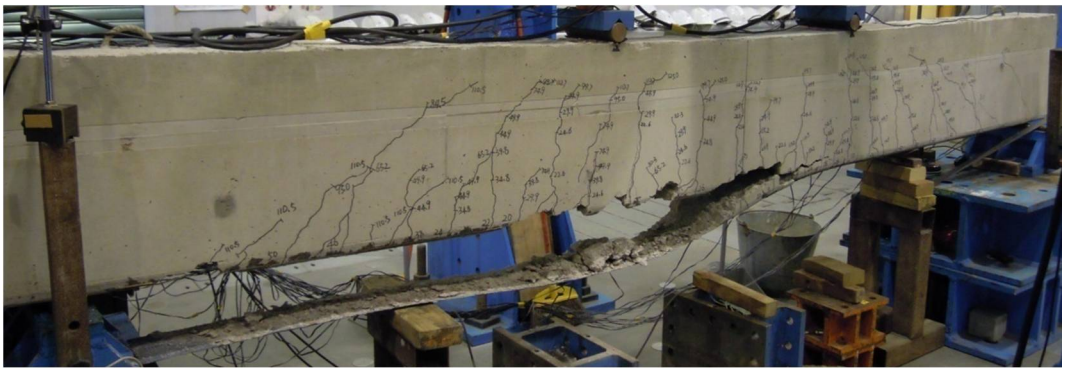

(a) Specimen B1S2

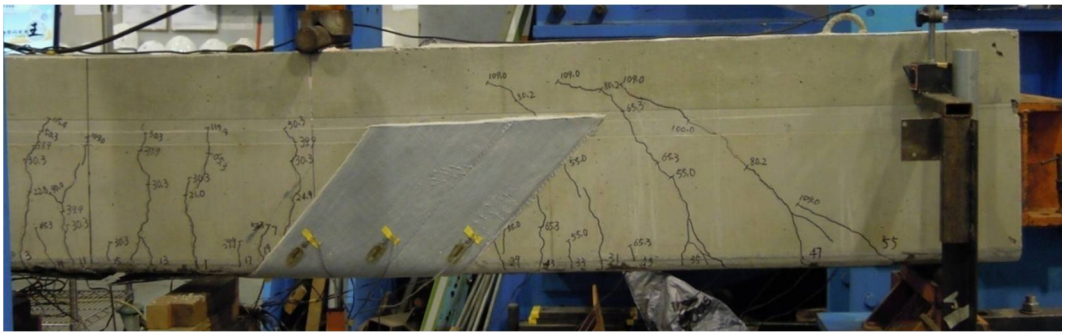

(b) Specimen B2S2

(c) Specimen B3S2

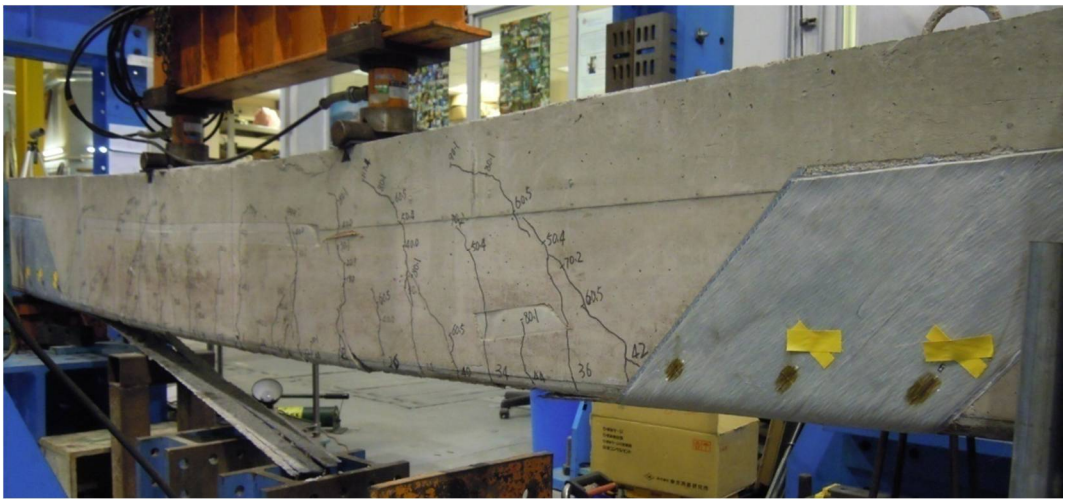

(d) Specimen B4S2

Figure 6.11 Failure modes of specimens in Series II

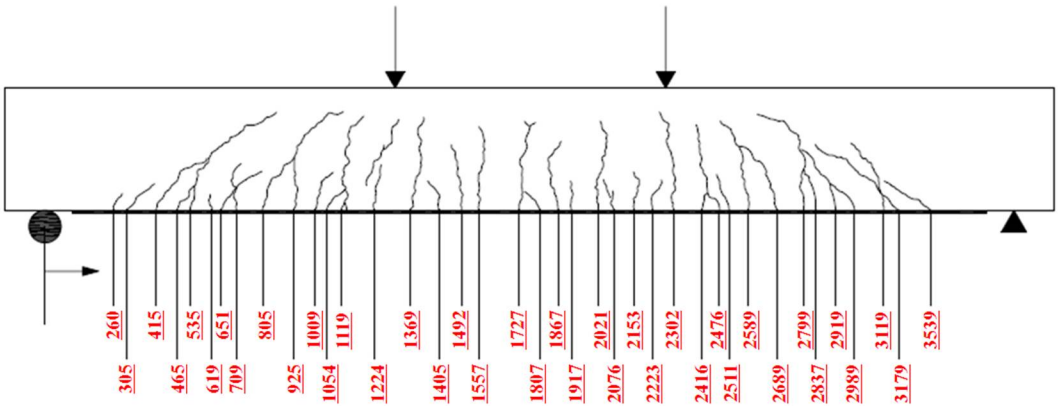

(a) Specimen B1S2

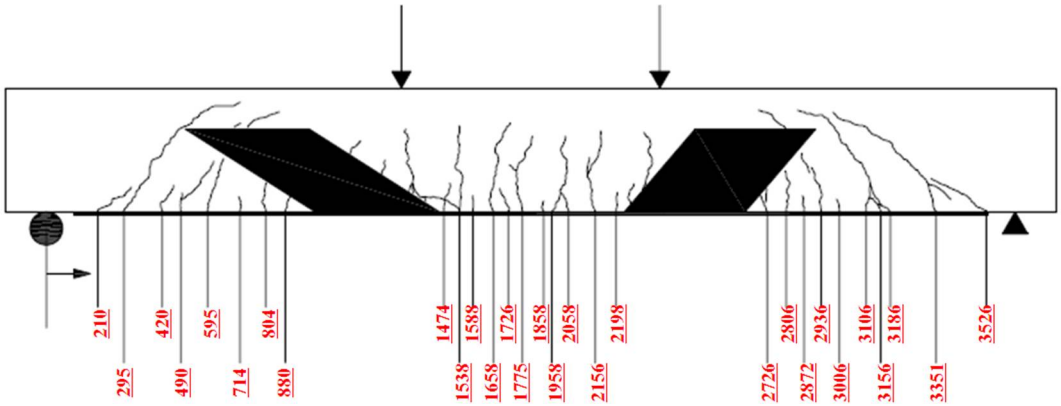

(b) Specimen B2S2

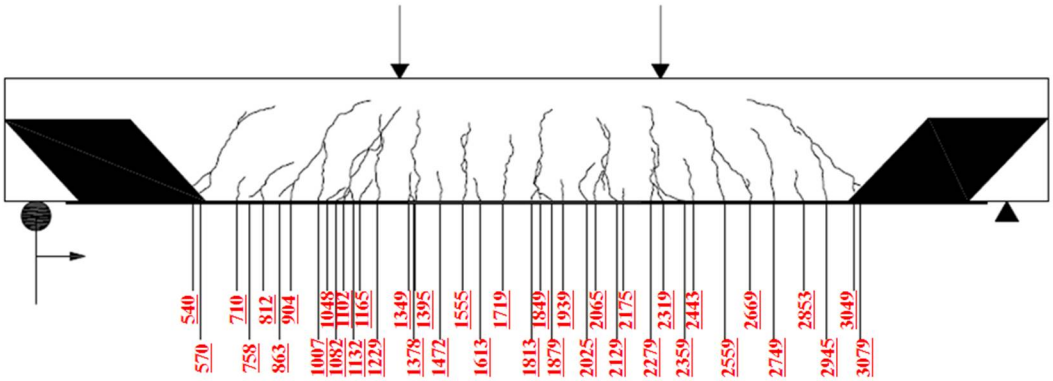

(c) Specimen B3S2

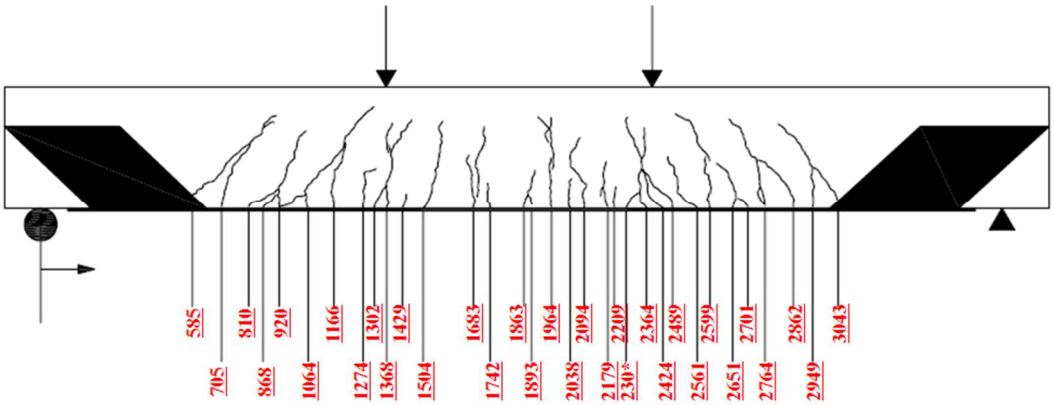

(d) Specimen B4S2

Figure 6.12 Crack patterns at failure of specimens in Series II

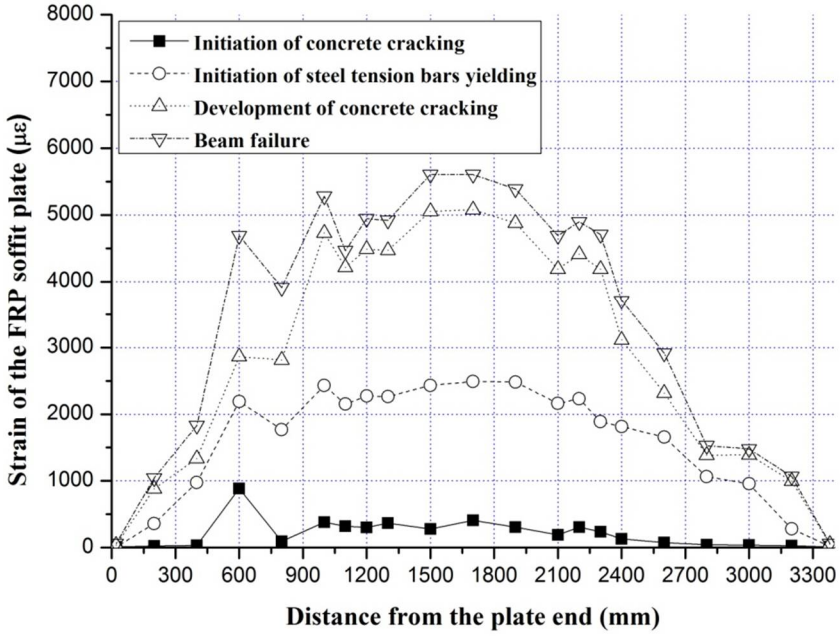

(a) B1S2

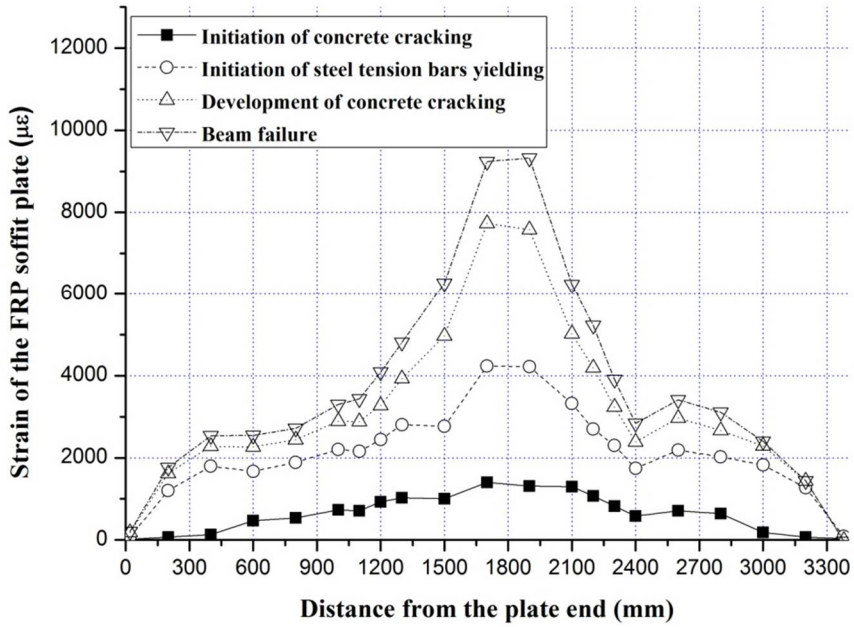
Initiation of concrete cracking
Initiation of steel tension bars yielding
Development of concrete cracking
Beam failure
Strain of the FRP soffit plate (με)
Distance from the plate end (mm)
0
2000
4000
6000
8000
10000
12000
0
300
600
900
1200
1500
1800
2100
2400
2700
3000
3300

(b) B2S2

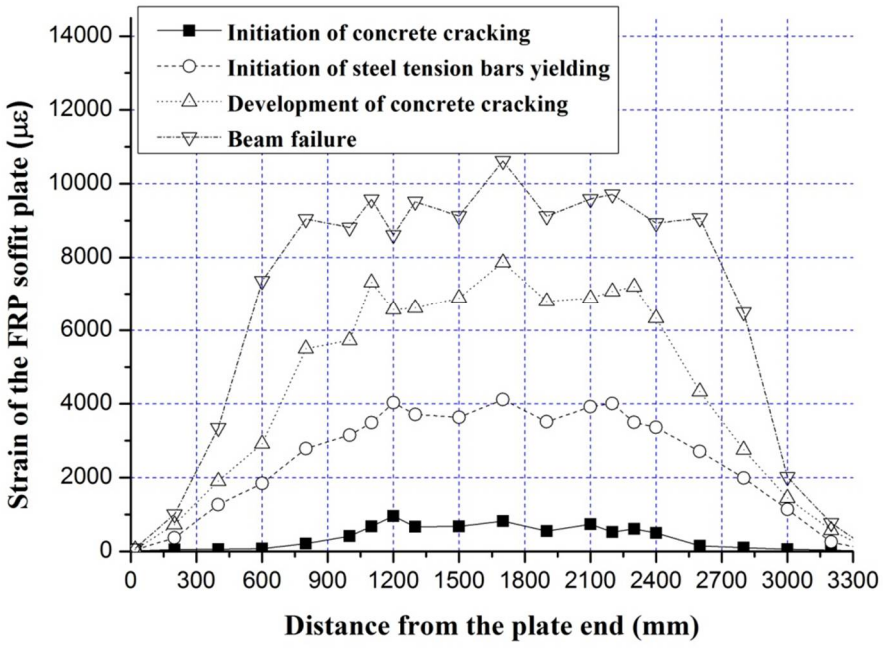
Initiation of concrete cracking
Initiation of steel tension bars yielding
Development of concrete cracking
Beam failure
Strain of the FRP soffit plate (με)
Distance from the plate end (mm)
0
2000
4000
6000
8000
10000
12000
14000
0
300
600
900
1200
1500
1800
2100
2400
2700
3000
3300

(c) B3S2

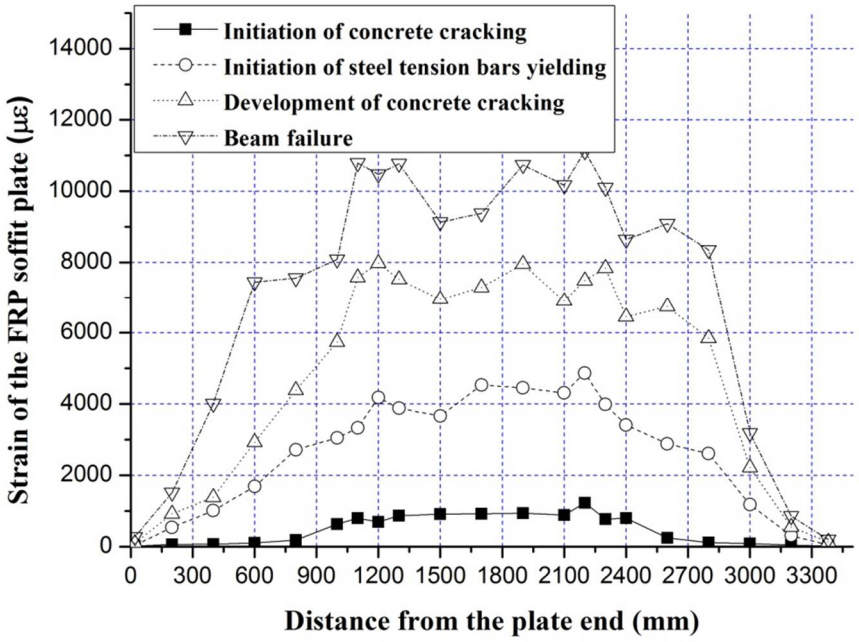

(d) B4S2

Figure 6.13 Strain distributions over the FRP soffit plate of specimens in Series II

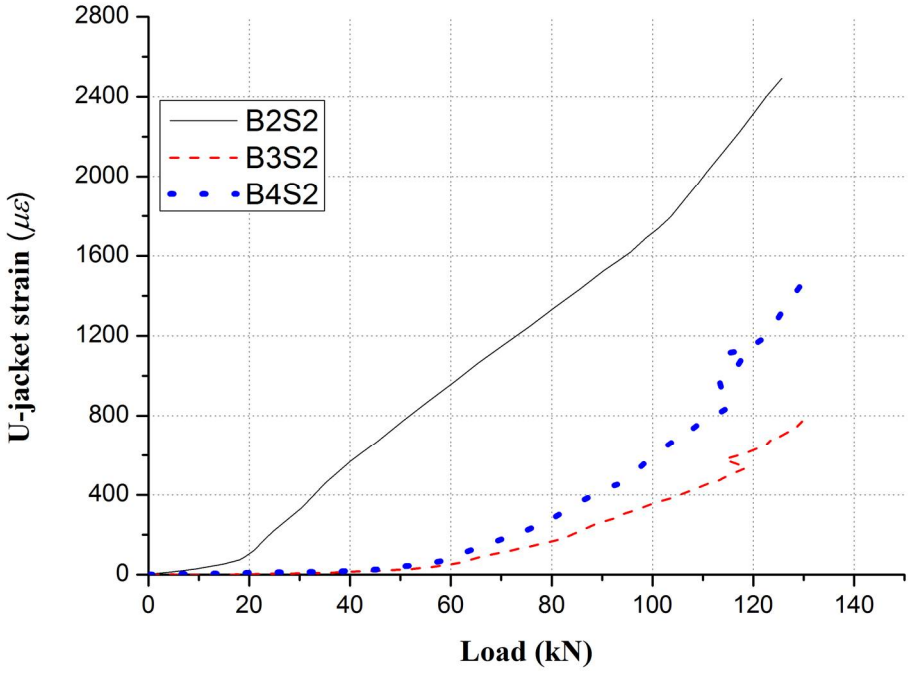

Figure 6.14 Strain distribution over U-jackets of specimens in Series II

CHAPTER 7

MITIGATION OF CONCRETE COVER SEPARATION USING FRP U-JACKETS

7.1 INTRODUCTION

As mentioned in Chapter 2, concrete cover separation failure is more brittle than IC debonding, and should be prevented from becoming the governing failure mode of an FRP-plated RC beam. Different plate-end anchorage measures have been used as an attempt to suppress concrete cover separation. Although other methods of end anchorage are possible (e.g. fibre anchors, see Lam and Teng 2001; Zhang et al. 2012), the use of bonded FRP U-jackets is more attractive than other options are in terms of ease of application: the same strengthening material is used and the installation procedure is simple. A number of studies have explored the effectiveness of FRP U-jackets in mitigating or suppressing concrete cover separation in FRP-plated RC beams (Ritchie et al. 1991; Smith and Teng 2003; Piamanmas and Porpongsaroj 2004; Ceroni 2010; Kalfat et al. 2013). Almost all these studies were conducted with the mitigation of concrete cover separation using FRP U-jackets as a secondary issue. To the best of the author's knowledge, no systematic study has

previously been carried out focusing on the optimal design/layout of these U-jackets as revealed by the literature review given in Chapter 2.

The ACI guidance document (ACI 440.2R 2008) includes a provision for the design of FRP U-jacket anchorage for preventing concrete cover separation based on the requirement that the transverse force resisted by the U-jackets is equal to the force from the bonded FRP soffit plate at failure. This rule was based on the test results of three beam specimens (Reed et al. 2005). An equation of similar form but with different coefficients from that in the ACI guidance document is adopted in UK's Concrete Society (2012) document to determine the required area of vertical FRP U-jackets. The Chinese national standard (GB50608 2010) specifies the use of FRP U-jackets as plate-end anchorage via a prescriptive detailing requirement, but no design calculations are required. These provisions for the design of FRP U-jacket anchorage for suppressing concrete cover separation are preliminary, and lack a solid research basis.

Against the above background, the author conducted a systematic study on the use of FRP U-jackets of different forms for mitigating concrete cover separation failure in FRP-plated RC beams. The experimental results are reported and interpreted in this chapter.

7.2 EXPERIMENTAL PROGRAMME

7.2.1 Specimen design

The experimental programme consisted of ten full-scale T-shaped RC beams in two series. They all had the same geometry (Figure 7.1): a clear span of 3250 mm, an overall depth of 450 mm, a web thickness of 220 mm, a flange width of 600 mm, and a flange thickness of 120 mm. Each beam contained four 16 mm steel tension bars and four 12 mm steel compression bars. They were heavily reinforced in shear to avoid shear failure, with 10 mm steel stirrups at a centre-to-centre spacing of 100 mm throughout the beam length except the three stirrups near the mid-span, which had a spacing of 125 mm. All the specimens were tested as simply-supported beams in four-point bending, with the two loads at 1250 mm apart. The dimensions were designed carefully to ensure that the control specimen only with an FRP soffit plate would fail by concrete cover separation using strength models by Zhang (2011) as well as IC debonding strength models by Lu et al. (2007). In addition, a trial test, which is not given herein, was carried out prior the present experimental programme to ensure concrete cover separation became the failure mode of the control specimen. Furthermore, a large difference between the strengths controlled by concrete cover separation and another failure mode, normally intermediate crack debonding (i.e. IC debonding), was intended in the design of test specimens to investigate the effect of different FRP U-jacket layouts on the mitigation of concrete cover separation,

Of the 10 specimens, two (one for each series of tests) served as the control beams, which had only a soffit FRP plate but did not have U-jackets at the plate ends. The rest were bonded with vertical or inclined FRP U-jackets as anchorage measures in the plate-end regions. The inclined FRP U-jackets were formed from two L-shaped jackets, which were bonded onto the two beam sides and overlapped at the beam

soffit. All the FRP plates/jackets were formed using the wet-layup method.

Series I, consisting of eight beams (including one control beam), was tested to investigate the effect of different forms of FRP U-jackets on the mitigation of concrete cover separation failure. Both the FRP soffit plate and the FRP U-jackets were formed from plies of the same carbon FRP (CFRP), with a ply nominal thickness of 0.333 mm. The FRP soffit plates for all beams in Series I had the same nominal dimensions: 165 mm wide, 1.332 mm thick (i.e. four plies x 0.333 mm), and 2450 mm long. For ease of monitoring the behaviour of beams during the test, only the test side of each specimen was instrumented with strain gauges on the FRP plate. On the other (non-test) side of the soffit plate, stronger FRP U-jackets and/or a steel jacket was used to avoid cover separation failure there. A steel jacket consisted of two bolts of 20 mm in diameter linking a steel plate (830mm x 100mm x 30 mm) on the beam soffit and another one of the same dimensions on the beam top face.

Series II, consisting of only two beams (including a control beam), was tested to gain better insight into the more effective form of FRP U-jackets identified through Series I. These two beams had the same geometry and materials as the specimens in Series I except for a shorter FRP soffit plate: the FRP soffit plate was terminated at 600 mm from the support for the plate end to be subjected to a different combination of shear force and moment than that of Series I. The control specimen was strengthened with only an FRP soffit plate while the other specimen was additionally provided with a 90mm wide inclined one-ply FRP U-jacket for plate-end anchorage. This form of U-jacketing was found to be the most effective from the tests of Series I.

Each specimen was assigned a name that consists of three letter-number sets except for the control specimen, which was named specimen CB for Series I. For the test specimens in Series I (excluding the control specimen), the name starts with the letter 'V' or 'I' to denote either vertical or inclined FRP U-jackets, followed by a number representing the number of FRP U-jackets used; the second set consists of the letter 'L' followed by the number of FRP layers (i.e. plies) used; and the third set consists of the letter 'W' followed by the width of the FRP U-jacket(s). For example, Specimen I1L1W90 is a specimen in Series I, with a 90mm wide one-ply FRP U-jacket inclined at 45^{o} at the plate-end in the test side. The control specimen and the other specimen in Series II are named CBb and I1L1W120b respectively, in which the additional letter 'b' is used to differentiate them from their counterparts in Series I. Further details of the test specimens are given in Figure 7.2.

7.2.2 Specimen preparation

All ten beams were cast with the same batch of commercial concrete following standard practice and cured in the same condition to ensure consistent properties for all specimens. These specimens were first cured for one week by covering them with a plastic film and spraying water frequently to ensure a good hydration reaction of silicates. After that, these specimens were left under normal indoor condition for curing for about three weeks. After curing for about 28days, the concrete surface for bonding of FRP was roughed using a hand-operated jet gun, which was driven by high-pressure air of about 0.7 MPa. The roughed surface was then left to dry for one day. Before applying the primer, dust on the concrete surface was cleaned using

high-pressure air. Unidirectional carbon fibre sheets were then applied layer by layer using a standard wet-layup process. The bonded FRP sheets were then left for curing for at least seven days before the beam tests.

7.2.3 Material properties

The mechanical properties of the concrete, steel and FRP were measured following either relevant British or ASTM standards. Concrete cylinder specimens were prepared from the same batch of commercial concrete as the beam specimens, and cured under the same condition. Compression tests on concrete cylinders were conducted following a British Standard (BS EN 12390-3 2009) on the day of testing the corresponding beam or an adjacent day. The average compressive strength of three 150mm x 300mm cylinder specimens was taken as the concrete compressive strength.

Three types of steel bars were used in the test beams: 10mm smooth bars for shear reinforcement, and 12 mm and 16 mm deformed steel bars for compression and tension reinforcements respectively. The average yield stress, ultimate stress and elastic modulus from tests on three tensile steel coupons for each type of steel bars(BS EN ISO 6892-1 2009) are listed in Table 7.1, together with the tensile strength and elastic modulus of the FRP material, which were obtained from flat FRP coupon tests following the ASTM standards (ASTM D3039/D3039M-08 2008 and ASTM D7565/D7565M-10 2010).Unfortunately, the steel elastic modulus is believed to have been overestimated as slips between the steel bar and the extensometer may

have existed and have led to underestimation of strains. An elastic modulus of 200 GPa is suggested to be used in numerical simulations or sectional analysis.

7.2.4 Test set-up and instrumentation

Loading was applied through two hydraulic jacks connected to a single manually-operated pump. This arrangement was mainly aimed at ensuring equal loading for the two jacks. Load cell measurements showed that the jack loads were indeed very close, with the difference being usually less than 3%and occasionally up to 5%. Five LVDTs were used to measure deflections: two at the two supports respectively, two at the two loading points respectively, and one at the mid-span (Figure 7.3). Three strain gauges of 50 mm in gauge length were attached to the compression face of the mid-span of the T-beam to measure the maximum concrete strain at the compression face in the beam. They were placed at distances of 50mm, 300mm and 550mm respectively from one flange side. Two 5-mm strain gauges were installed onto the two middle tension steel bars at the mid-span to measure the maximum strains of tension steel bars. Cracking information (crack locations and widths) was carefully recorded during the whole loading process.

Strains of both the FRP soffit plate and the FRP U-jackets were monitored using a large number of strain gauges. Figure7.4 gives strain gauge positions on the FRP soffit plate. A large number of strain gauges with a spacing of 25 mm or 50 mmwere employed in regions near the plate end or under one of the loading points as greater strain gradients were expected there. For the rest of the FRP soffit plate, the strain

gauge spacing was 100 mm, which was believed to be shorter than the typical spacing between two adjacent major cracks. A large number of strain gauges were also installed on the FRP U-jackets to examine the behaviour of FRP U-jackets in the mitigation of concrete cover separation. Both sides of the U-jackets were monitored with strain gauges as shown in Figure 7.5; the positions were chosen based on the position of steel tension bars, the effective bond length of the bonded FRP U-jackets, etc. In addition, a strain gauge was also bonded at the middle of bottom surface of an FRP U-jacket.

7.3 TEST RESULTS AND DISCUSSIONS

7.3.1 General

A summary of the key experimental results of all specimens is given in Table 7.2. These key results include the load, deflection at mid-span, maximum strain in the FRP soffit plate, maximum FRP U-jacket strain, concrete strain (measured at the compression surface of the beam) at mid-span at the initiation of cracking, first yielding of steel, and debonding failure. The load-deflection curves of all test specimens are shown in Figure7.6.

The two control beams in Series-I and II, namely Specimens CB and CBb, failed with ultimate loads of 277.3 kN and 239.9 kN respectively by the failure mode of concrete cover separation. The process of cover separation failure is as follows: a major flexural-shear crack first appeared at the plate end, which then turned

horizontal at the bottom of the tension steel bars and propagated towards the mid-span of the beam. The failure process of these two control specimens is presented in detail in the next section to reveal the mechanism of concrete cover separation failure. This mechanism provides a solid basis for understanding the effect of FRP U-jackets on concrete cover separation.

7.3.2 Mechanism of concrete cover separation

As expected, the two control beams, Specimens CB and CBb, of Series-I and Series-II respectively failed by concrete cover separation with their ultimate loads277.3kN and 239.9kN, respectively (Figures 7.7 and 7.8). This debonding failure mode limits the utilization of the expensive CFRP material; the maximum FRP strains of the FRP soffit plate at failure were only 2458 $\mu\varepsilon$ and 2355 $\mu\varepsilon$ for the specimens CB and CBb, respectively.

An enlarged view of the failed side of Specimen CB is given in Figure7.9. The failure processes of Specimens CB and CBb were similar, and the process of concrete cover separation failure in Specimen CB is given in detail as follows. Before the occurrence of concrete cracking, all components of the beam worked together and the strain measurements supported the plane section assumption. The strains of the FRP soffit plate increased proportionally with the applied load. When the load increased to 155.6 kN, a major flexural-shear crack occurred, and then gradually became more significant with its width reaching 0.28 mm at the load of 170.0 kN. After the formation of the major crack near the FRP plate end, the strains

in most parts of the FRP soffit plate still increased with the applied load; however, the strains near the FRP plate end decreased as the load increased (Figure7.10). As a result, the strain gradient near the FRP plate end became much larger, and the interfacial shear stress between the FRP plate and the concrete also increased. At the same time, the steel-to-concrete interface near the FRP plate end is expected to have experienced significant slips, which resulted in the wedge effect (Zhang and Teng 2014),exacerbating the tendency for the concrete cover to separate from the steel tension bars. With further increases in the applied load, the interfacial shear stress near the FRP plate end together with the wedge effect induced by the slips at the steel-to-concrete interface resulted in the occurrence of a horizontal crack, which started near the FRP plate end and developed toward mid-span along the level of steel tension bars. The horizontal crack developed to 0.04 mm in width and 50.0 mm in length at the load of about 185.2 kN, and became obvious with its width and length of 0.30 mm and about 90.0 mm, respectively, when the load increased to about 240.0 kN. Part of the concrete cover finally separated from the beam at the ultimate load of 277.3 kN, signifying the failure of the specimen.

Based on the experimental observation above, the process of concrete cover separation failure is illustrated in Figure 7.11. The process can be summarised into the following steps: (1) formation of the major flexural-shear crack near the FRP soffit plate end; (2) formation of a horizontal crack near the FRP soffit plate end at the level of steel tension bars; (3) propagation of the horizontal crack toward mid-span along the steel tension bars; (4) final failure when the horizontal crack has sufficiently developed. In the concrete cover separation failure, the interface between

the steel tension bars and the concrete is the weakest part, and the horizontal crack here induces the final failure. The appearance and widening of the horizontal crack along the interface between steel tension bars and concrete is mainly due to the wedge effect induced by slips between steel tension bars and concrete as revealed by Zhang and Teng (2014) and the high FRP-to-concrete interfacial shear stress.

It is therefore expected that bonding of FRP U-jackets near the plate end can counter-balance the effect of the high FRP-concrete interfacial shear stress and the wedge effect, and hence restrain the development of the horizontal crack at the level of steel tension reinforcement. In particular, if an inclined FRP U-jacket is provided at a plate end, the tensile force in the FRP soffit plate can be directly transferred to the U-jacket, and as a result, the interfacial stresses near the plate end can be greatly reduced.

7.3.3 Mitigation effects of vertical FRP U-jackets

Vertical FRP U-jackets of different layouts were employed in four beam specimens: V1L1W60, V2L1W60, V1L1W90 and V1L1W120. In Specimens V1L1W60, V1L1W90 and V1L1W120, only one vertical FRP U-jacket of 60 mm, 90 mm and 120 mm in width respectively was installed at the end of the FRP soffit plate on the test side. In Specimen V2L1W60, two vertical FRP U-jackets of 60 mm in width were installed; the centre-to-centre spacing between these two vertical FRP U-jackets was 250 mm, which is greater than the crack spacing near the plate end found in the test on the control specimen.

As shown in Figure 7.12, the ultimate load increases with the width of the vertical FRP U-jacket(s). Compared to the control specimen, increases of 6.5%, 10.5% and 14.8% in the ultimate load were observed in Specimens V1L1W60, V1L1W90 and V1L1W120, respectively. Specimens V1L1W60 and V1L1W90 still failed by concrete cover separation, but cover separation started at the inner side of the U-jacket close to the mid-span, instead of starting at the soffit plate end due to the presence of a vertical FRP U-jacket. However, concrete cover separation was suppressed in Specimen V1L1W120 by the vertical U-jacket of 120 mm in width. These observations mean that if the vertical FRP U-jacket is not wide enough, the appearance and subsequent opening-up of the major flexural-shear crack near the plate end induces a decrease of strains near the FRP soffit plate, and shifts the 'effective' end of the FRP soffit plate to the inner side of the U-jacket. As a result, when the vertical FRP U-jacket is not wide enough, cover separation starts from the inner side of the U-jacket. A wide vertical FRP U-jacket is more effective in mitigating/suppressing cover separation failure.

As expected, the difference in the ultimate load between Specimen V1L1W60 (with one vertical FRP U-jacket) and Specimen V2L1W60 (with 2 vertical FRP U-jackets), being 2.0kN, is small. This small difference is within the expected range of experimental errors, so their ultimate loads are practically the same. However, Specimen V2L1W60 showed a much more ductile response than Specimen V1L1W60 (Figure 7.12). This is mainly because the additional vertical U-jacket in Specimen V2L1W60 outside the first concrete tooth region provided restraint to cover separation of the second concrete tooth, thereby leading to a more gradual

process of cover separation failure. This comparison indicates that the provision of a second vertical FRP U-jacket outside the first concrete tooth can significantly improve the ductility of the beam although it has little effect on the ultimate load.

Figure 7.13 gives the strain distributions over the FRP soffit plate in Specimen V1L1W60at different loads levels. The strains in the FRP soffit plate in the high-moment region (i.e. at a distance of more than 400 mm from the plate end) increase with the load; some fluctuations are also seen near major cracks. The strain distributions near the FRP plate end are much more complicated due to the development of the shear-flexure crack and the horizontal crack at the level of steel tension bars. Before the appearance of the flexural-shear crack near the plate end, the strains near the plate end increased with the load; however, they decreased after the appearance of a major flexural-shear crack near the plate end at the load of about 150 kN; the strain gradient and the FRP-to-concrete interfacial shear stresses in the region also increased rapidly. Furthermore, the strains near the FRP plate end (within a distance of50 mm from the plate end) became negative, which indicates that this part of the FRP plate was in compression, due to development of both the flexural-shear crack and the horizontal crack near the FRP plate end. The strain profiles of the FRP soffit plate in Specimens V1L1W90, V1L1W120 and V2L1W60 are similar but with maximum FRP strains respectively 3472 $\mu\varepsilon$, 4180 $\mu\varepsilon$, and 4061 $\mu\varepsilon$ at failure.

The strain distributions down the height of the FRP U-jacket in Specimen V1L1W60are given in Figure 7.14a for different load levels, which have a close

relationship with the crack pattern near the FRP U-jackets (Figure 7.14b). An abrupt increase in strain at the height of 100 mm from the bottom side at the load level of 162 kN can be seen in the figure, which is the result of the appearance of a flexural-shear crack at the plate end that was close to the FRP U-jacket strain gauge at the height of 100 mm from the beam bottom. Another flexural-shear crack intersected the FRP U-jacket at a higher position at a load of 250 kN, causing an abrupt increase in the strain gauge reading at the height of 230mm. The horizontal crack at the height of steel tension bars occurred when the load increased to about 293 kN. As a result, a significant increase was observed in the FRP U-jacket strain at the height of 35 mm at load 290 kN (Figure 7.14a).

Figure 7.15 gives the strain distributions down the height of the vertical FRP U-jacket in Specimens V1L1W60, V1L1W90, V1L1W120 and V2L1W60 at failure. For ease of comparison, only the strain distribution in the vertical FRP U-jacket at the plate end in Specimen V2L1W60 is included in the figure. The strains of the FRP U-jackets in all four beams at the height of steel tension bars are larger than 2000$\mu\varepsilon$, which indicates the presence of a horizontal crack at the height of steel tension bars. Furthermore, the differences in strain at the tension steel level of U-jackets among the four beams are small, which indicates that a wider FRP U-jacket provided a larger force to restrain the widening of the horizontal crack; that is, a wider U-jacket was more effective. The positions of peak strain of the four specimens are different as a result of the different positions of the intersecting flexural-shear cracks.

7.3.4 Mitigation effects of inclined FRP U-jackets

Three beams, I1L1W90, I1L1W120 and I1L2W120, in Series-I were installed with a 45^{o}-inclined FRP U-jacket at the FRP plate end to mitigate concrete cover separation. The layouts of the inclined FRP U-jackets in these three beams are different as indicated by the specimen names: Specimens I1L1W90, I1L1W120 and I1L2W120 had a one-ply 90 mm wide, one-ply 120 mm wide, and two-ply 120 mm wide inclined FRP U-jacket respectively.

In these three beams with an inclined FRP U-jacket, concrete cover separation was successfully suppressed; they all failed by IC debonding following the debonding of the inclined FRP U-jacket (Figure 7.16). Before failure, the FRP soffit plate had already debonded completely from the concrete substrate and was held in place by the inclined FRP U-jacket; however, the beam could still sustain further loading until the inclined FRP U-jacket also debonded. The amount of additional load a beam was able to carry after the complete debonding of the FRP soffit plate depended on the width of the inclined FRP U-jacket. A wider inclined FRP U-jacket was able to carry a larger additional load. Specimens I1L1W90, I1L1W120 and I1L2W120 carried additional loads of 11.7 kN, 25.8 kN and 6.9 kN respectively after the complete debonding of the FRP soffit plate.

With an inclined FRP U-jacket at the FRP soffit plate end, both the ultimate load and ductility of the beam were increased significantly for all three beams (Figure 7.17). Specimens I1L1W90, I1L1W120 and I1L2W120 achieved increases in the ultimate load of 35.4 kN, 81.3 kN and 79.6 kN, and increases in mid-span deflection of 6.2 mm, 12.1 mm and 9.3 mm, respectively. The ultimate load increase is seen to be

related to the width of the inclined FRP U-jacket near the plate end. A comparison of the results of Specimens I1L1W120 and I1L2W120 indicates that a thicker U-jacket is not beneficial; indeed, a thicker jacket may have a small detrimental effect.

The utilization of the FRP soffit plate was improved significantly in all three beams. The maximum strain in the FRP soffit plate at beam failure increased from 2458 $\mu\varepsilon$ in the control specimen CB to 4292 $\mu\varepsilon$, 5504 $\mu\varepsilon$ and 5592 $\mu\varepsilon$ in Specimens I1L1W90, I1L1W120 and I1L2W120, respectively. The strain distributions in the FRP soffit plate of Specimen I1L1W120 at different load levels are given in Figure 7.18, which indicates that as the load increases, the strains in the FRP tension plate also increase before the appearance of a significant crack near the plate end; however, the strains near the plate end decrease after the appearance of a significant crack near the plate end despite increases in the load. Between the loads of 321 kN and 337 kN, the strains in the FRP plate in the region of 200 mm to 500 mm from the FRP plate end are seen to increase rapidly due to the complete debonding of the FRP soffit plate from the concrete substrate. The strain gauges near the end of the soffit plate had large negative values, when the soffit plate completely debonded from concrete substrate. It should be noted here that the strain gauges were attached on the part of the U-jacket wrapped outside the soffit plate and were parallel to the direction of fibres of the soffit plate to monitor the axial strains in the soffit plate. When no slips between the FRP U-jacket and the FRP soffit plate occurred, the readings of the strain gauges reflected the strains in the FRP soffit plate closely. However, when slips occurred between the soffit plate and the U-jacket, which resulted from the sudden debonding of the soffit plate, the readings of these strain gauges could no longer

closely represent the axial strains of the soffit plate.

Figure 7.19 gives the strain distributions down the height of the inclined FRP U-jacket in Specimen I1L1W120 to show the behaviour of the FRP U-jacket. Before the complete debonding of the FRP soffit plate, the maximum strain in the U-jacket occurred near the steel tension bar level due to the presence of a significant flexural-shear crack near the plate end; this strain distribution is similar to that of the corresponding vertical FRP U-jacket in Specimen V1L1W120. However, after the complete debonding of the FRP soffit plate, the maximum strain in the inclined FRP U-jacket moved to the bottom part of the FRP U-jacket because a large force in the soffit plate was transferred to the inclined FRP U-jacket. At failure, the maximum strain in the FRP U-jacket exceeded 10000 $\mu\varepsilon$. Such a high strain in the inclined FRP U-jacket indicates strong interaction between the inclined FRP U-jacket and the FRP soffit plate.

Figure 7.20 gives the strain distributions down the height of the inclined FRP U-jacket in Specimens I1L1W90, I1L1W120 and I1L2W120 at failure. Unlike specimens with a vertical FRP U-jacket, the maximum strain in the inclined FRP U-jacket occurred in the bottom part of the FRP U-jacket in all three beams as a result of the combined action of force transfer from the FRP soffit plate and the presence of large cracks near the FRP soffit plate end. In Specimens I1L1W90 and I1L1W120, the maximum strains in the inclined FRP U-jacket are larger than 10000$\mu\varepsilon$. In these two specimens, the difference in strain between the two FRP U-jackets near the height of steel tension bars is small, which indicates that the force

provided by the inclined FRP U-jacket is roughly proportional to the width of the inclined FRP U-jacket. By contrast, the maximum strain in the FRP U-jacket in Specimen I1L2W120 at failure is about 3000$\mu\varepsilon$, which is much smaller than those of Specimens I1L1W90 and I1L1W120 are; this is because a thicker inclined FRP U-jacket was used in the former, resulting in a smaller debonding strain (Chen and Teng2001).

Significant interaction between the FRP soffit plate and the inclined FRP U-jacket existed in these tests; in particular, the tensile force in the FRP soffit plate was transferred to the inclined FRP U-jacket after the complete debonding of the former. Therefore, an inclined FRP U-jacket cannot only restrain the widening/propagation of the horizontal crack but also help carry the tensile force from the FRP soffit plate into the beam through the beam sides. As a result, concrete cover separation can be suppressed by bonding an inclined FRP U-jacket. It is clear from the experimental results that an inclined FRP U-jacket is much more effective than a corresponding vertical FRP U-jacket (Figure 7.21).

7.3.5 Tests of Series-II

In Series-II, two specimens with a shorter FRP soffit plate, in which the distance from the support to the critical plate end was 600 mm, were tested to investigate further the effect of FRP U-jacket on cover separation for a plate end under a different moment-shear combination, which has a significant effect on cover separation failure (Smith and Teng 2003).Only the best U-jacket layout identified

through the tests of Series I, used in Specimen I1L1W120,was used in Series II to mitigate concrete cover separation. One of them, Specimen CBb, was the control specimen, without any FRP anchorage on the test side; the other one, Specimen I1L1W120b, was installed with a one-ply inclined FRP U-jacket of 120 mm in width (i.e. same as that in Specimen I1L1W120). At the load of about 300 kN, the inclined U-jacket experienced local debonding at its upper part due to the appearance of flexural-shear cracks intersected with U-jackets, and did not have enough bond strength to carry the soffit plate, when the soffit plate debonded from concrete substrate. Specimen I1L1W120b failed by IC debonding followed by debonding of U-jacket and concrete cover separation (Figure 7.22).Compared with the control specimen, Specimen I1L1W120b achieved a 29.5% increase in ultimate load and a 73.0% increase in the mid-span deflection at failure.

Due to the shorter FRP soffit plate used (i.e. having a higher moment-shear force ratio at the plate end), Specimen CBb failed by IC debonding followed by debonding of U-jacket and concrete cover separation with the ultimate load and mid-span deflection at failure 239.9 kN and 11.4 mm respectively, which are 15.6% and 16.5% lower than those of specimen CB in Series-I. The ultimate load and mid-span deflection at failure of Specimen I1L1W120bwere 310.7 kN and 17.0 mm, which were 15.4% and 38.3% lower than these of Specimen I1L1W120.Ideally, Specimen I1L1W120b should have very similar ultimate loads and displacements at failure as Specimen I1L1W120. This is because a strong FRP U-jacket was employed in both beams to mitigate concrete cover separation failure so that they were expected to fail by IC debonding, which is only marginally affected by the length of the FRP soffit

plate. However, the inclined FRP U-jacket in Specimen I1L1W120b suffered local debonding due to the appearance of more significant flexural-shear cracks in the higher moment region near the FRP soffit plate end. As a result, the inclined FRP U-jacket in Specimen I1L1W120b did not provide a large enough bonding force to carry the soffit plate after the complete debonding of the FRP soffit plate.

7.4 CONCLUSIONS

This chapter has presented an experimental study on the effect of FRP U-jackets on concrete cover separation failure in FRP-plated RC beams. The layout of the FRP U-jacket was the only variable in the first series of tests (Series I). Series II, consisting of only two beams (including a control beam), was tested to gain better insight into the more effective form of FRP U-jackets identified through Series I.

Both vertical and inclined FRP U-jackets were examined in the experimental study. A vertical U-jacket could be easily formed in a wet layup process from a single fibre sheet; an inclined FRP U-jacket was formed from two L-shaped jackets, which overlapped at the beam soffit. The results of the Series I tests demonstrated that the one-ply, 90 mm wide inclined FRP U-jacket in Specimen V1L1W120 performed the best among the U-jacket layouts examined in these tests. The performance of this FRP U-jacket layout was also further examined in Series II, where a beam with a shorter FRP soffit plate (i.e. a higher moment-shear force ratio at the plate end), was tested. The following observations and conclusions can be drawn from the present study.

(1) Two major reasons, high shear stresses at the FRP-to-concrete interface and significant radial stresses induced by slips at the steel-to-concrete interface, are responsible for the appearance and propagation of the critical horizontal crack at the level of steel tension bars toward the mid-span, causing the eventual occurrence of concrete cover separation in FRP-plated RC beams. To mitigate cover separation failure, the shear stresses at the FRP-to-concrete interface and the widening of the critical horizontal crack need to be minimized.

(2) Vertical FRP U-jackets have a beneficial effect in postponing or suppressing concrete cover separation. With an increase in the width of a vertical FRP U-jacket, both the ultimate load and the ductility of the beam increase. In beams installed with a narrow FRP U-jacket, the beam may fail by concrete cover separation away from the U-jacket within the strengthened region (i.e. starting at the inner side of the FRP U-jacket). Therefore, a sufficiently wide FRP U-jacket is needed to suppress cover separation failure successfully, and this width needs to be significantly larger than the crack spacing between the initiation crack and the critical crack within the strengthened region.

(3) Significant interaction between the FRP soffit plate and the inclined FRP U-jacket exists in an FRP-plated RC beam with inclined U-jacket anchorage at the plate end, as has been observed in the present tests. The main interaction involves the transfer of the tensile force in the FRP soffit plate to the sides of the beam via the inclined FRP U-jacket. As a result of this

interaction, the interfacial shear stresses at the FRP-to-concrete interface are greatly reduced, thus postponing/suppressing the concrete cover separation failure. All the test beams in Series I with an inclined FRP U-jacket failed by IC debonding, instead of concrete cover separation, which was observed in the control specimen. With an increase in the width of FRP U-jacket, both the ultimate load and the ductility of the beam increase. However, the intersection of flexural-shear cracks with the U-jacket in its upper part may result in debonding of the FRP U-jacket.

(4) FRP-plated RC beams with an inclined FRP U-jacket at the soffit plate end can further carry loads after the complete debonding of the FRP soffit plate, until eventual failure of the beam when debonding of the FRP U-jacket occurs. The magnitude of this additional load depends on the width of the inclined FRP U-jacket. Generally, a wider inclined FRP U-jacket leads to a greater additional load to be carried.

(5) Among the U-jacket layouts examined in the tests of Series I, a one-ply, 120 mm wide inclined FRP U-jacket at the plate end (i.e. Specimen I1L1W120) achieved the best performance. This layout was further examined in a specimen in Series-II with a shorter FRP soffit plate (i.e. Specimen I1L1W120b) to evaluate the effect of the layout in mitigating concrete cover separation for a higher moment-shear force ratio at the plate end. The inclined FRP U-jacket of this layout was found to perform well for the higher moment-shear force ratio but not as well as in I1L1W120; the included FRP

U-jacket in Specimen I1L1W120b suffered local debonding due to the higher moment at the plate end, making it less effective.

7.5 REFERENCES

ACI 440.2R (2008). *Guide for the design and construction of externally bonded FRP systems for strengthening concrete structures*, ACI Committee 440, American Concrete Institute, Farmington Hills, MI, USA.

ASTM D3039/D3039M-08 (2008). *Standard test method for tensile properties of polymer matrix composite materials*, ASTM International, West Conshohocken, Philadelphia, PA.

ASTM D7565/D7565M-10 (2010). *Standard test method for determining tensile properties of fiber reinforced polymer matrix composites used for strengthening of civil structures*, ASTM International, West Conshohocken, Philadelphia, PA.

Ceroni, F. (2010). "Experimental performances of RC beams strengthened with FRP materials", *Construction and Building Materials*, Vol. 24, pp.1547-1559.

GB-50608 (2010). *Technical code for infrastructure application of FRP composites*, China Planning Press, Beijing.

Kalfat, R., Al-Mahaidi, R. and Smith, S. T. (2013). "Anchorage devices used to improve the performance of reinforced concrete beams retrofitted with a FRP composite: State-of-the-art review", *Journal of Composites for Construction,* ASCE, Vol. 17, No. 1, pp. 14-33.

Lam, L. and Teng, J.G. (2001). "Strength of RC cantilever slabs bonded with GRFP strips", *Journal of Composites for Construction,* ASCE, 5, 221-227.

Lu, X.Z., Teng, J.G., Ye, L.P. and Jiang, J.J. (2007). "Intermediate crack debonding in FRP-strengthened RC beams: FE analysis and strength model", *Journal of Composites for Construction*, ASCE, Vol. 11, pp. 161-174.

Piamanmas, A. and Pornpongsaroj, P. (2004). "Peeling behaviour of reinforced concrete beams strengthened with CFRP plates under various end restraint conditions", *Magazine of Concrete Research*, Vol. 56, No. 2, pp. 73-81.

Reed, C. E., Peterman, R. J. and Rasheed, H. A. (2005). *Evaluating FRP repair method for cracked prestressed concrete bridge members subjected to repeated loadings (Phase 1)*, KTRAN Report No. KTRAN: KSU-01-2, Kansas Department of Transportation, Topeka, KS, 106 pp.

Ritchie, P.A., Thomas, D.A., Lu, L.W. and Connelly, G.M. (1991). "External reinforcement of concrete beams using fiber reinforcement plastic", *ACI Structural Journal*, Vol. 88, No. 4, pp. 490-500.

Smith, S.T. and Teng, J.G. (2003). "Shear-bending interaction in debonding failures of FRP-plated RC beams", *Advances in Structural Engineering*, Vol. 6, No. 3, pp. 183-199.

Teng, J.G. and Chen, J.F. (2008). "Mechanics of debonding in FRP-plated RC beams", *Proceedings, International Conference on Structures and Granular Solids: From Scientific Principles to Engineering Applications*, University of Edinburgh, Edinburgh, Scotland, UK, pp. 313-325.

Zhang, H.W., Smith, S.T. and Kim, S.J. (2012). "Optimisation of carbon and glass FRP anchor design", *Construction and Building Materials*, Vol. 32, pp. 1-12.

Zhang, S.S. (2011). *Behaviour and Modelling of RC Beams Strengthened in Flexure with Near-surface Mounted FRP*, PhD Thesis, The Hong Kong Polytechnic University, Hong Kong, China.

Zhang, S.S. and Teng, J.G. (2014). "Finite element analysis of end cover separation in RC beams strengthened in flexure with FRP", *Engineering Structures*, Vol. 75, pp. 550-560.

7.6 TABLES AND FIGURES

Table 7.1 Material properties of steel and FRP

Material	Yield stress, f_y (MPa)	Ultimate stress, f_u (MPa)	Elastic modulus, E (GPa)
10 mm steel bars	312	426	244
12 mm steel bars	404	537	211
16 mm steel bars	419	572	223
FRP	/	4654	258

Table 7.2 Summary of test results

Specimen		CB	V1L1W60	V2L1W60	V1L1W90	V1L1W120	I1L1W90	I1L1W120	I1L2W120	CBb	I1L1W120b
Cylinder compressive strength of concrete (MPa)		46.6	50.4	50.4	50.4	54.9	54.9	54.2	54.9	55.2	55.2
Initiation of concrete cracking	Load at each jack (kN)	55.7	55.5	55.1	56.1	55.2	57.0	56.7	55.0	55.4	60.2
	Displacement at mid-span (mm)	0.89	0.84	0.85	0.87	0.90	0.86	0.79	0.83	0.81	0.92
	Max. strain of the soffit plate ($\mu\varepsilon$)	218	242	295	238	217	274	180	193	236	276
	U-jacket strain at height of steel tension bar ($\mu\varepsilon$)	-	-6	-7	-9	-6	28	23	30	-	38
	Concrete strain at mid-span ($\mu\varepsilon$)	-104	-110	-105	-109	-102	-101	-96	-103	-96	-116
Initiation of yielding of steel tension bars	Load at each jack (kN)	-	283.2	281.6	281.9	284.0	275.4	283.5	285.0	-	280.2
	Displacement at mid-span (mm)	-	11.74	11.43	11.63	11.38	10.73	10.95	10.40	-	11.13
	Max. strain of the soffit plate ($\mu\varepsilon$)	-	2548	2850	2885	2755	2722	2444	2646	-	2973
	U-jacket strain at	-	1959	2877	2208	1847	3321	2243	1567	-	2927

	height of tension steel bar ($\mu\varepsilon$)										
	Concrete strain at mid-span ($\mu\varepsilon$)	-	-824	-758	-789	-784	-759	-696	-816	-	-802
Beam failure	Load at each jack(kN)	277.3	295.4	293.4	306.4	318.3	312.7	358.6	356.9	239.9	310.7
	Displacement at mid-span (mm)	11.44	13.67	12.95	14.98	15.85	17.59	23.50	20.71	9.82	16.99
	Max. strain of the soffit plate ($\mu\varepsilon$)	2485	3258	3472	4180	4061	4292	5504	5592	2355	4849
	U-jacket strain at height of steel tension bar ($\mu\varepsilon$)	-	2247	3039	2829	2130	7171	6290	2489	-	5643
	Concrete strain at mid-span ($\mu\varepsilon$)	-778	-979	-883	-966	-1034	-1045	-1076	-1293	-646	-1080
Failure mode		CS	CS	CS	CS	IC	IC	IC	IC	CS	CS

*IC = IC debonding; CS=concrete cover separation.

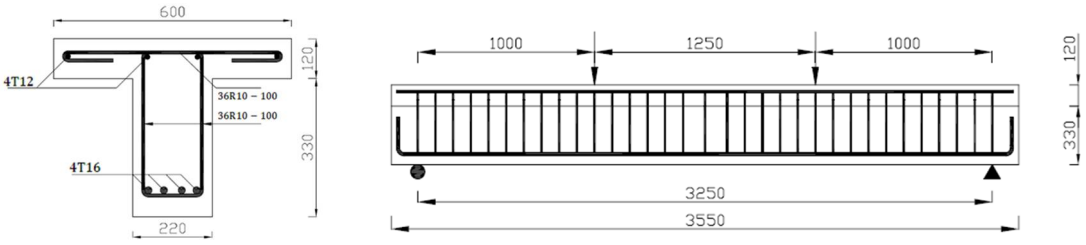

Figure 7.1 Dimensions of specimens

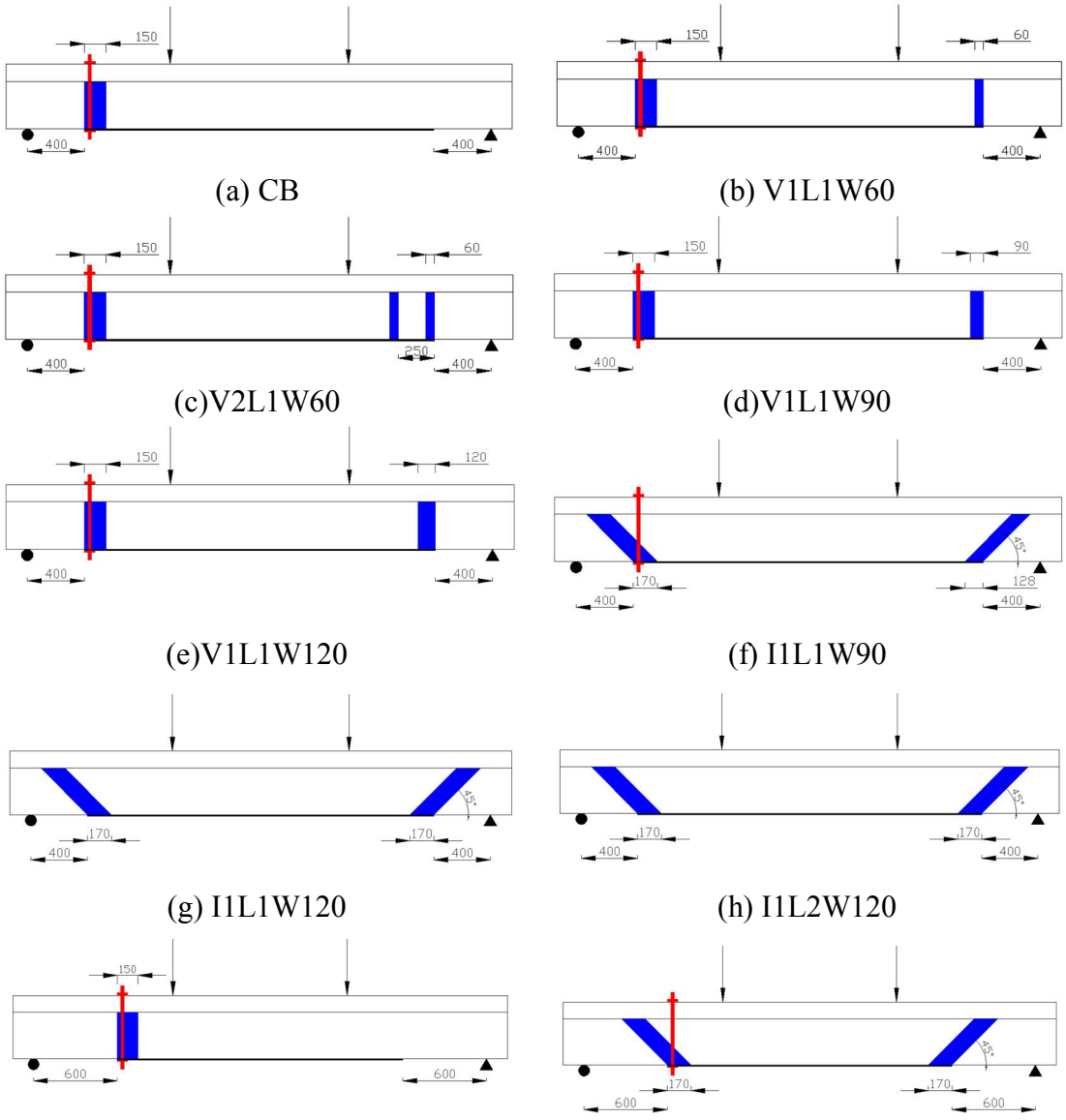

Figure 7.2 Layout of FRP U-jackets in specimens

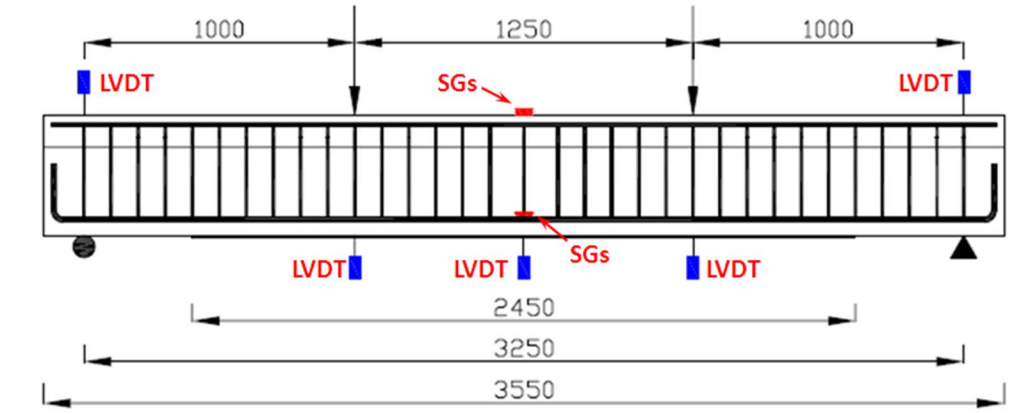

Figure 7.3 Positions of LVDTs and strain gauges on steel bars and concrete

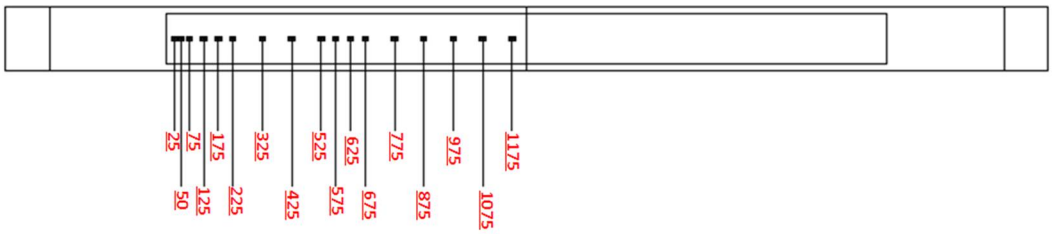

(a) Series-I

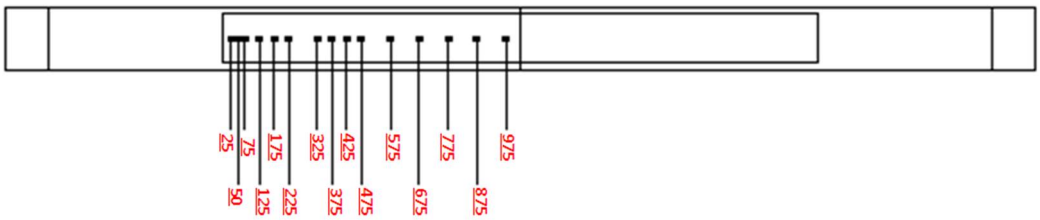

(b) Series-II

Figure 7.4 Positions of strain gauges on FRP soffit plate

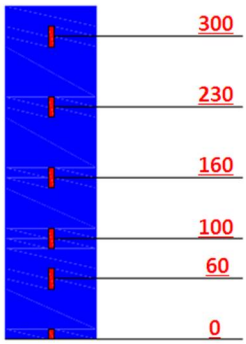

Figure 7.5 Positions of strain gauges on FRP U-jackets

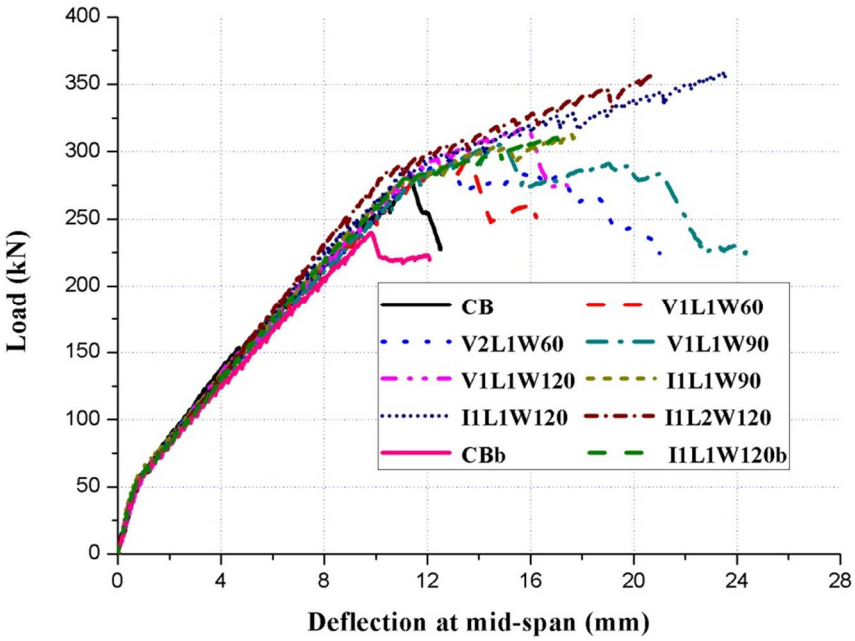

Figure 7.6 Load-deflection curves of all specimens

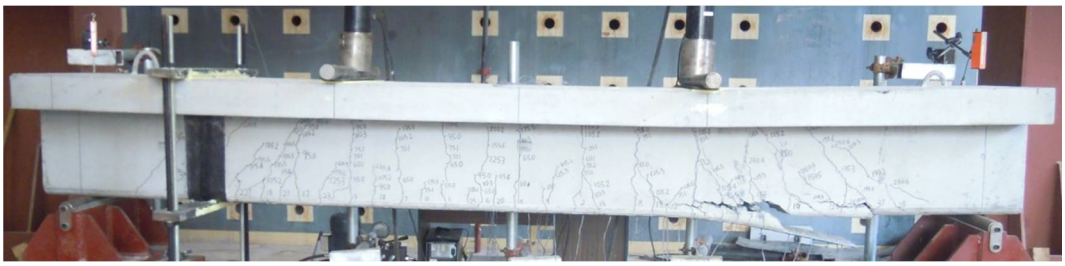

(a) CB

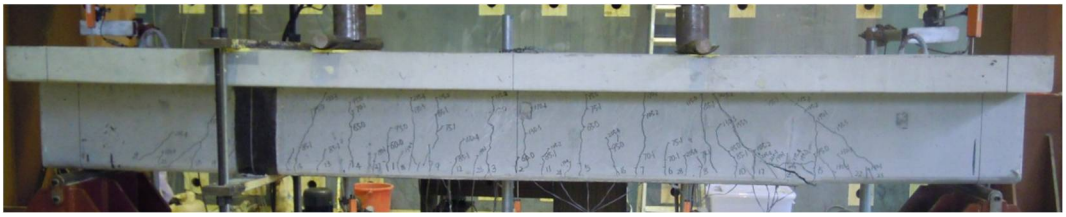

(b) CBb

Figure 7.7 Failure modes of control specimens

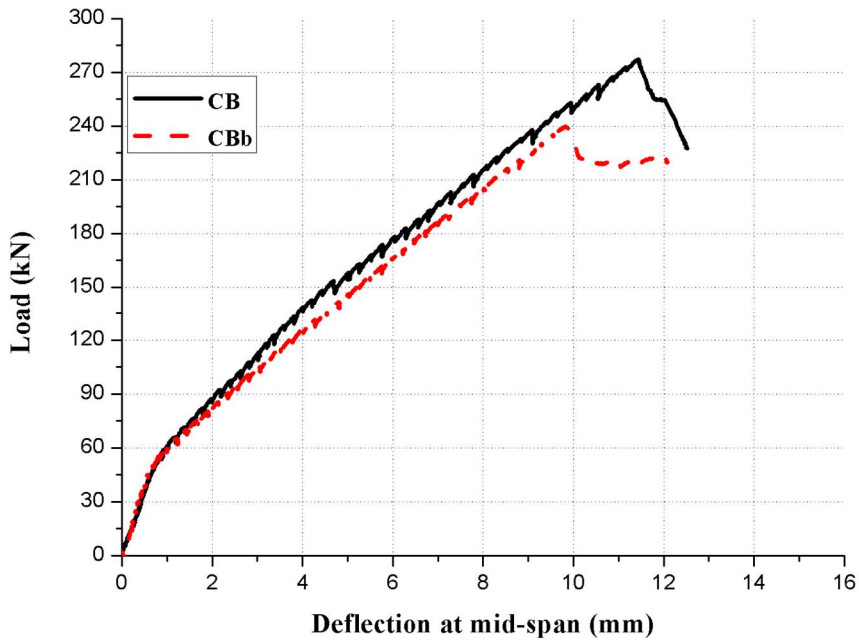

Figure 7.8 Load-deflection curves of control specimens

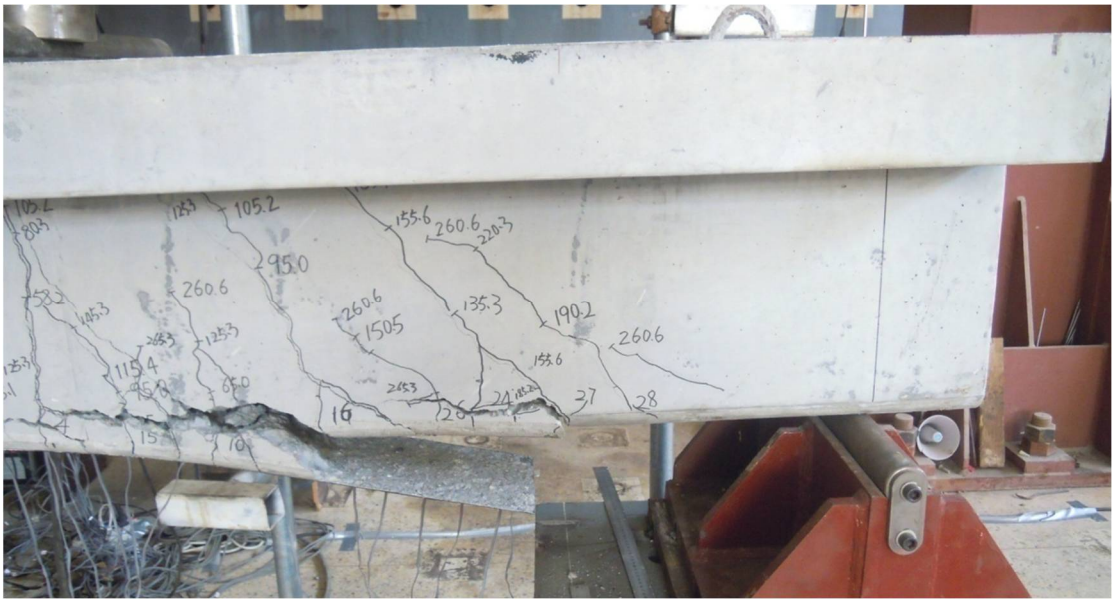

Figure 7.9 Details of the failure end

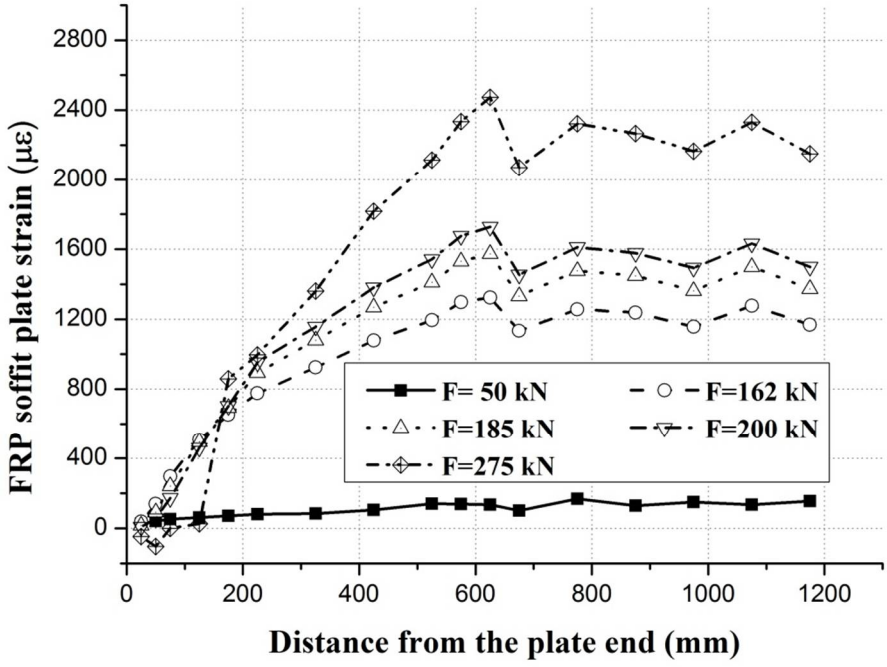

Figure 7.10 Strain distributions over FRP soffit plate of specimen CB at different load levels

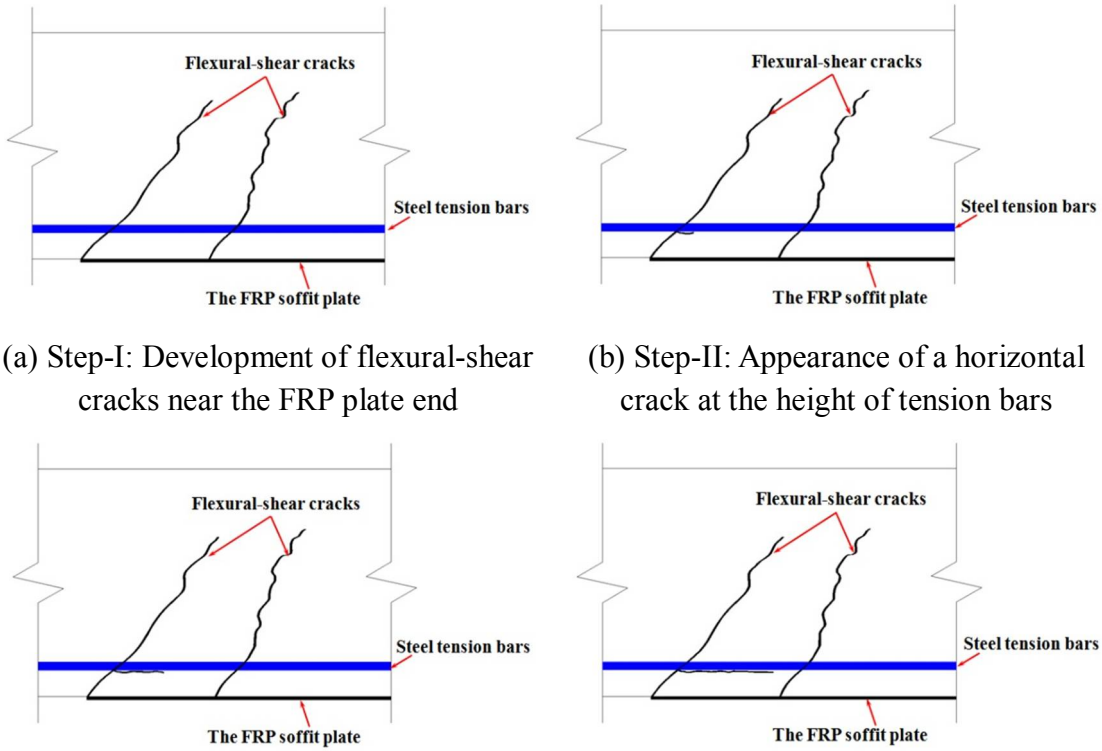

(a) Step-I: Development of flexural-shear cracks near the FRP plate end

(b) Step-II: Appearance of a horizontal crack at the height of tension bars

(c) Step-III: Propagation of the horizontal crack

(d) Step-IV: Ultimate failure by concrete cover separation

Figure 7.11 Simplified process of concrete cover separation

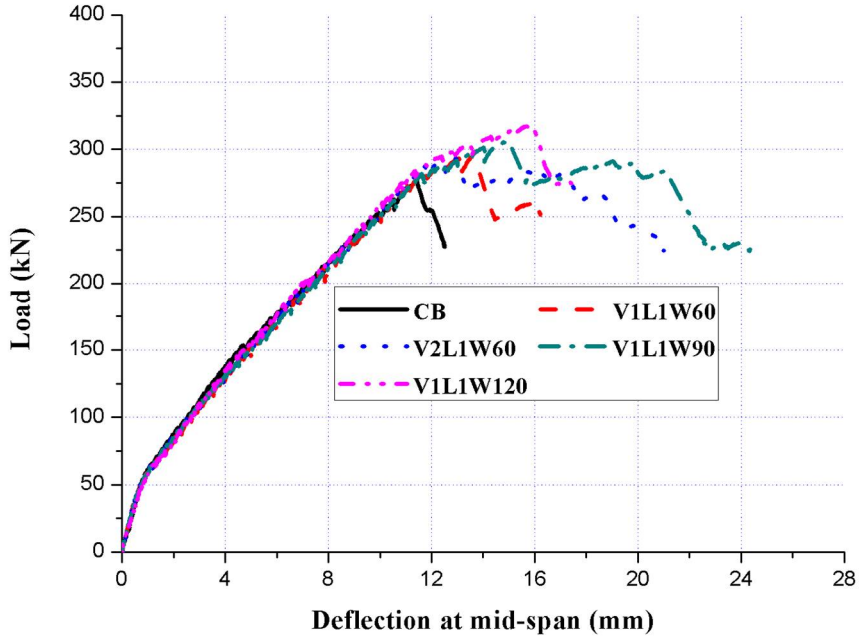

Figure 7.12 Load-deflection curves of beams with different vertical U-jackets

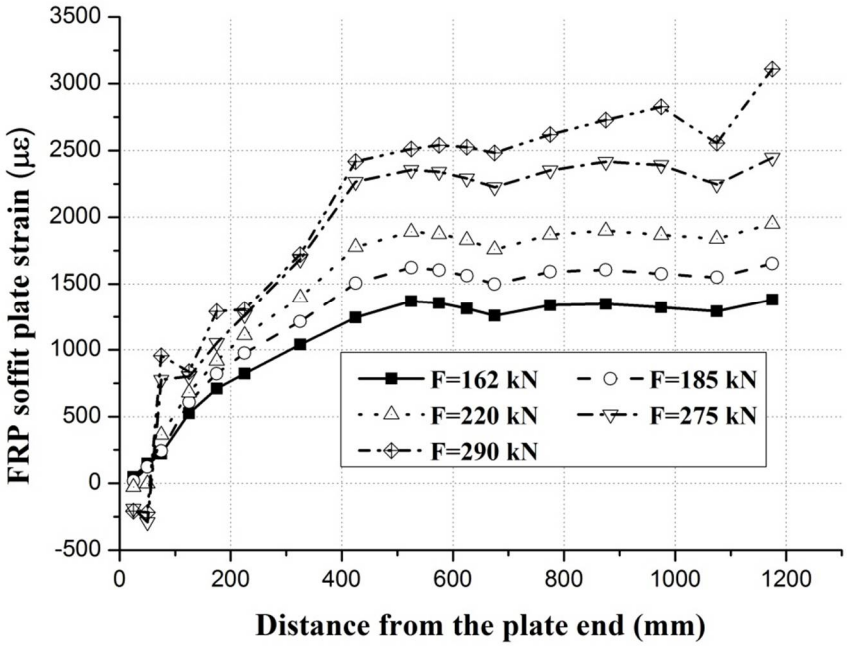

Figure 7.13 Strain distributions over the FRP soffit plate of Specimen VIL1W60 at selected load levels

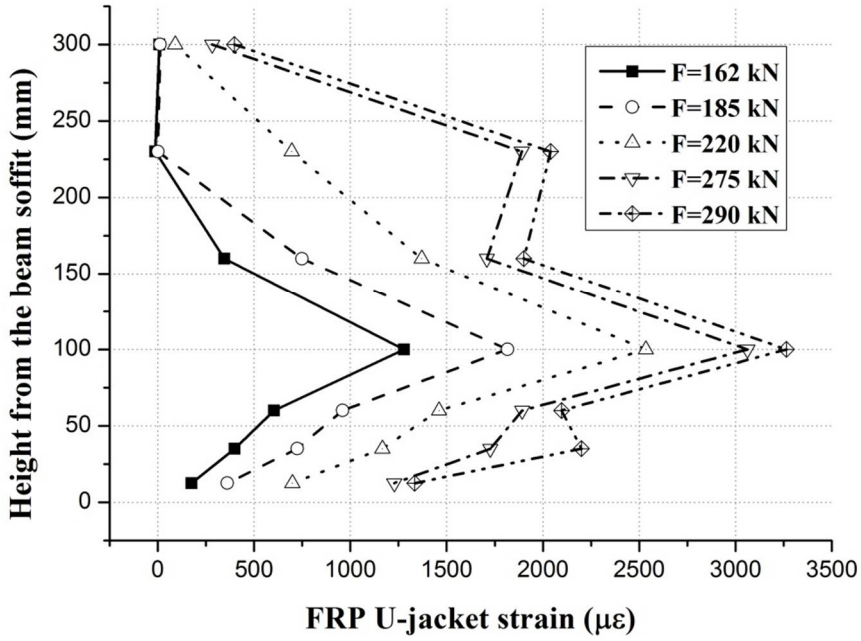

Figure 7.14a Strain distributions over the FRP U-jacket of Specimen V1L1W60 at selected load levels

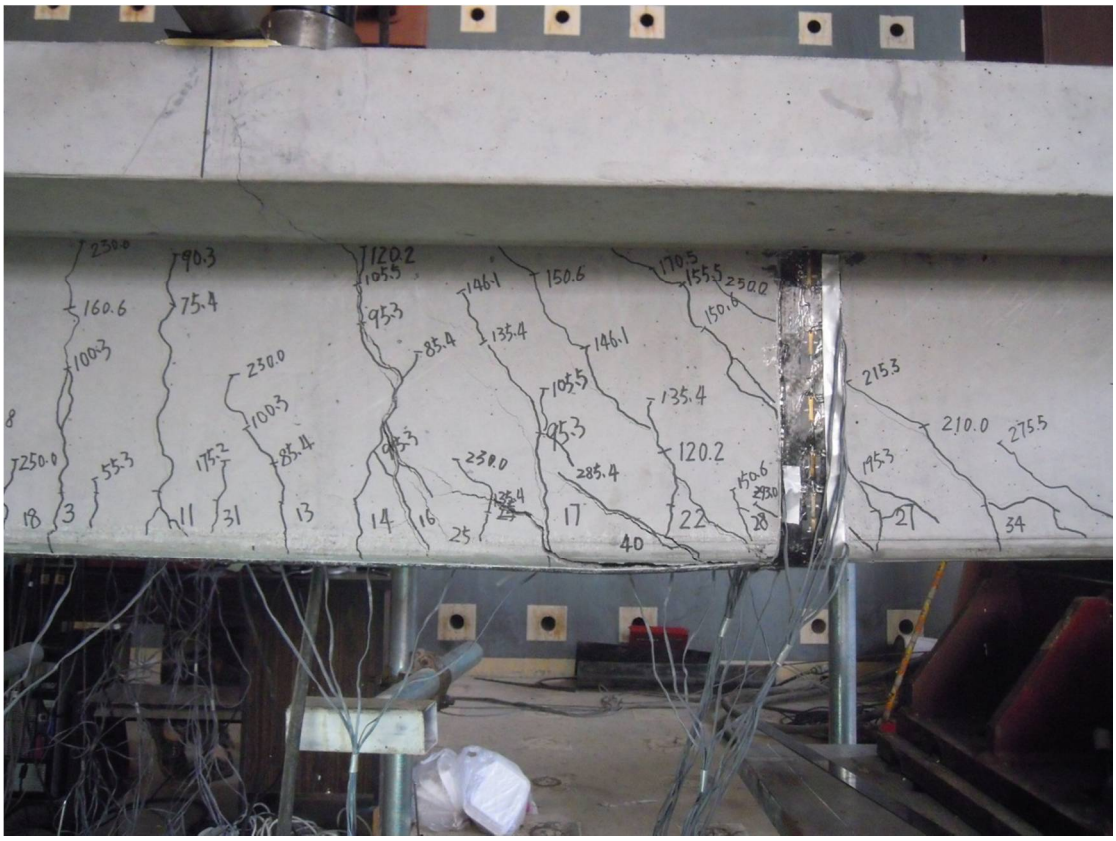

Figure 7.14b Crack pattern of Specimen V1L1W60

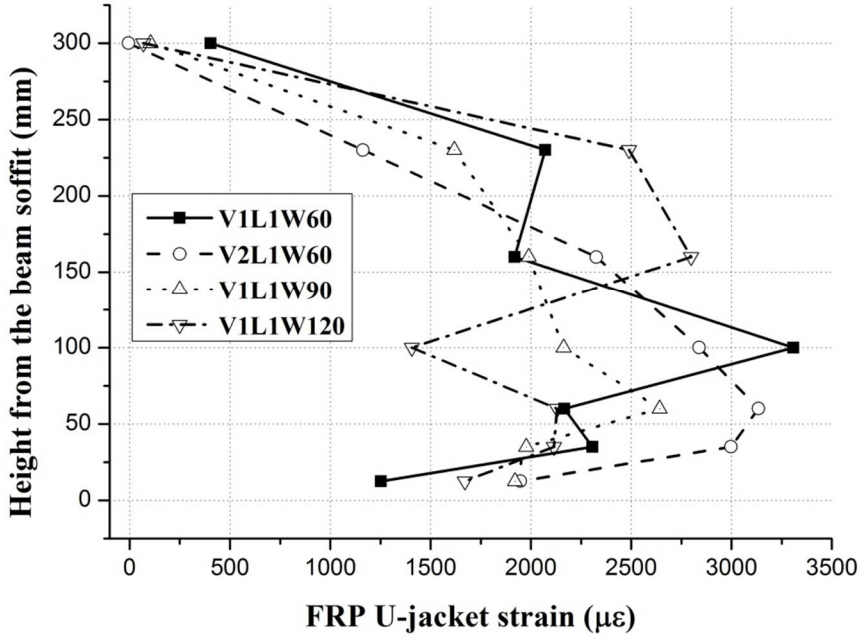

Figure 7.15 Strain distributions over the vertical FRP U-jacket at failure

(a) I1L1W90

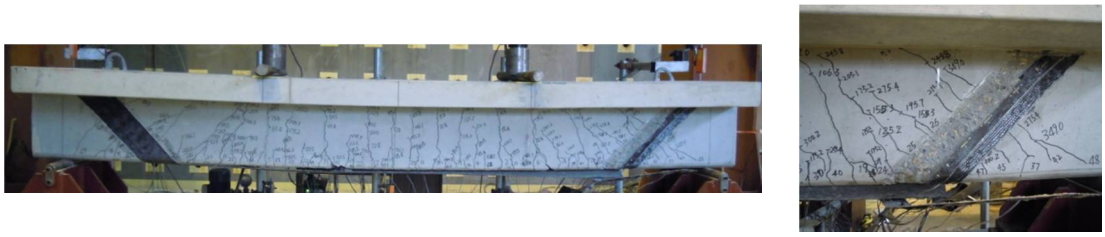

(b) I1L1W120

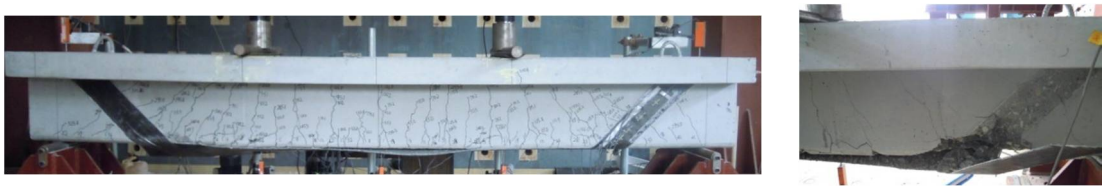

(c) I1L2W120

Figure 7.16 Failure modes of specimens with inclined FRP U-jackets in Series-I

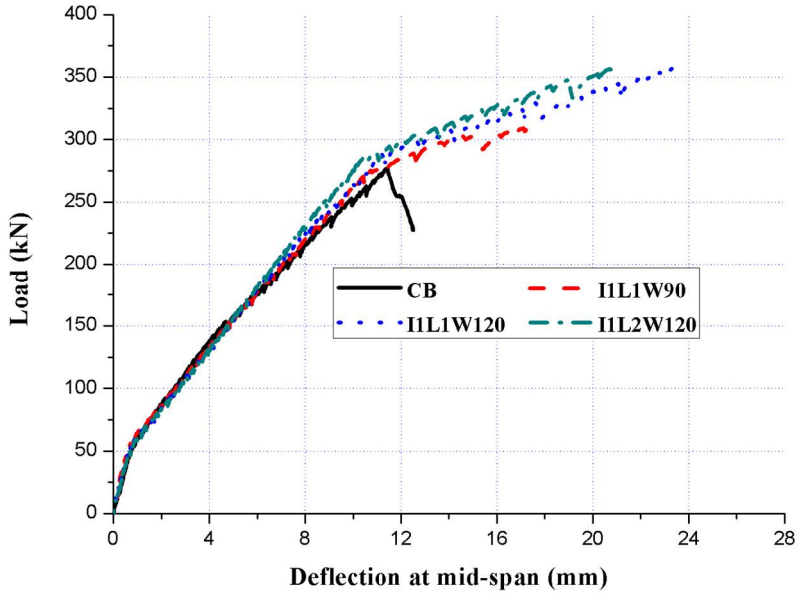

Figure 7.17 Load-deflection curves of beams with different inclined U-jackets

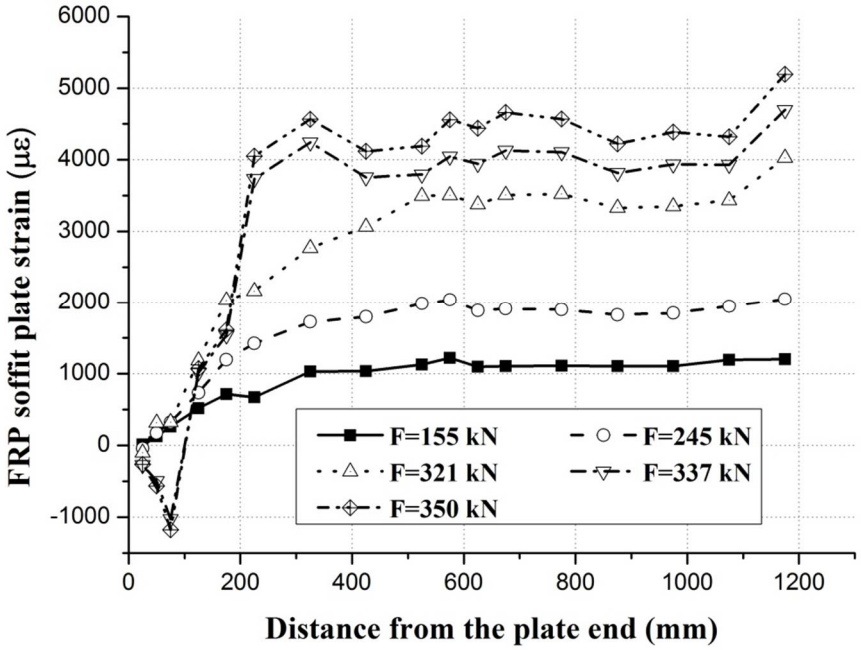

Figure 7.18 Strain distributions over the FRP soffit plate of Specimen I1L1W120 at selected load levels

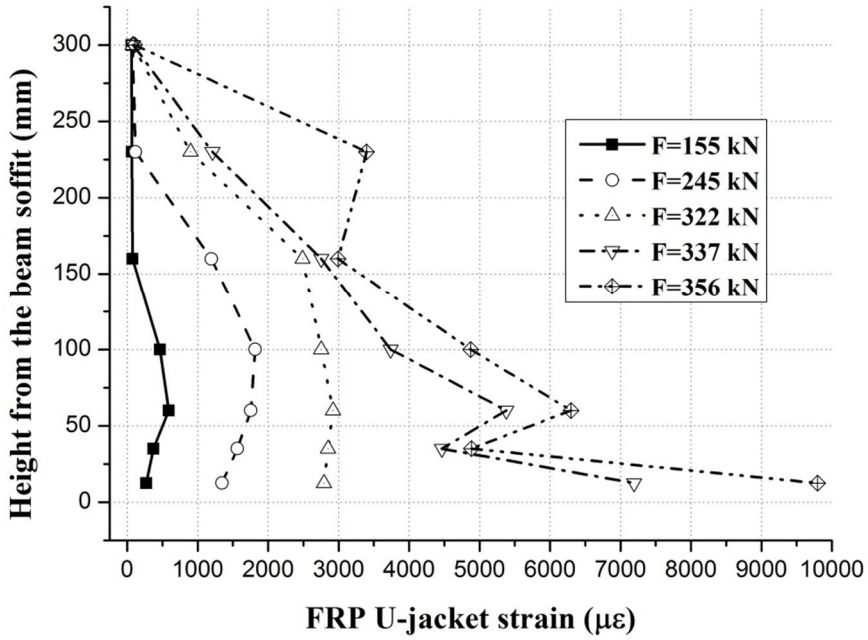

Figure 7.19 Strain distributions over the FRP U-jacket of Specimen I1L1W120 at selected load levels

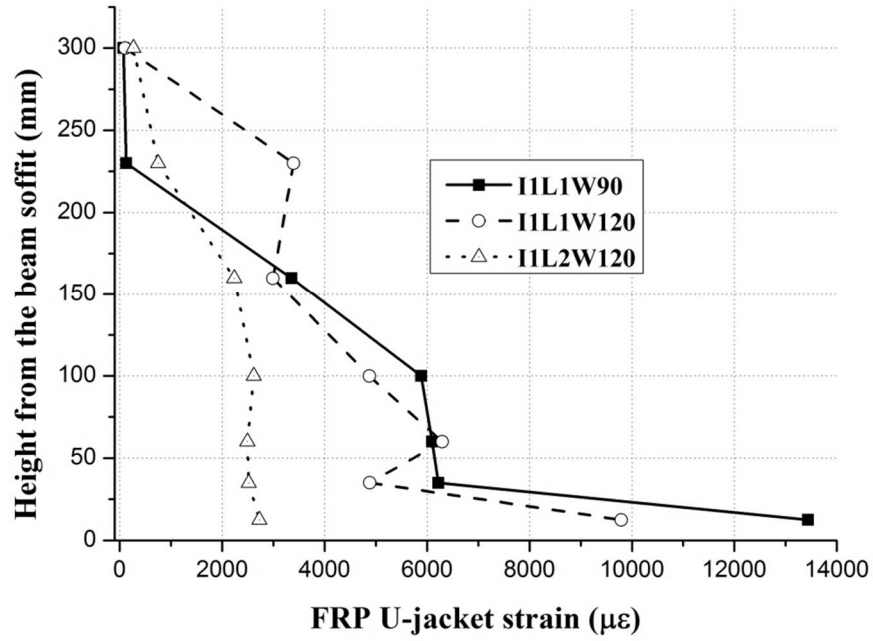

Figure 7.20 Strain distributions over the inclined FRP U-jacket at failure

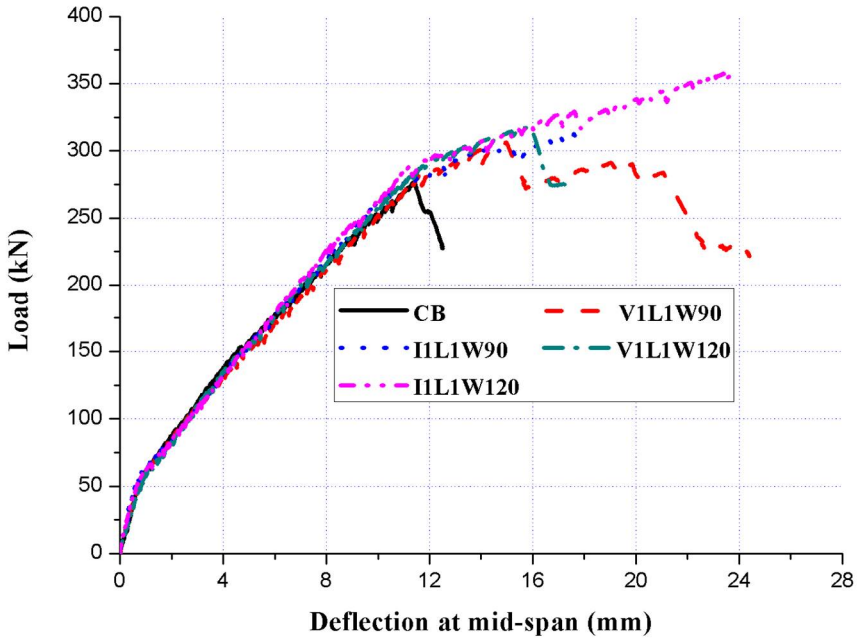

Figure 7.21 Load-deflection curves of beams with vertical and inclined U-jackets of the same width

Figure 7.22 Failure mode of Specimen I1L1W120b

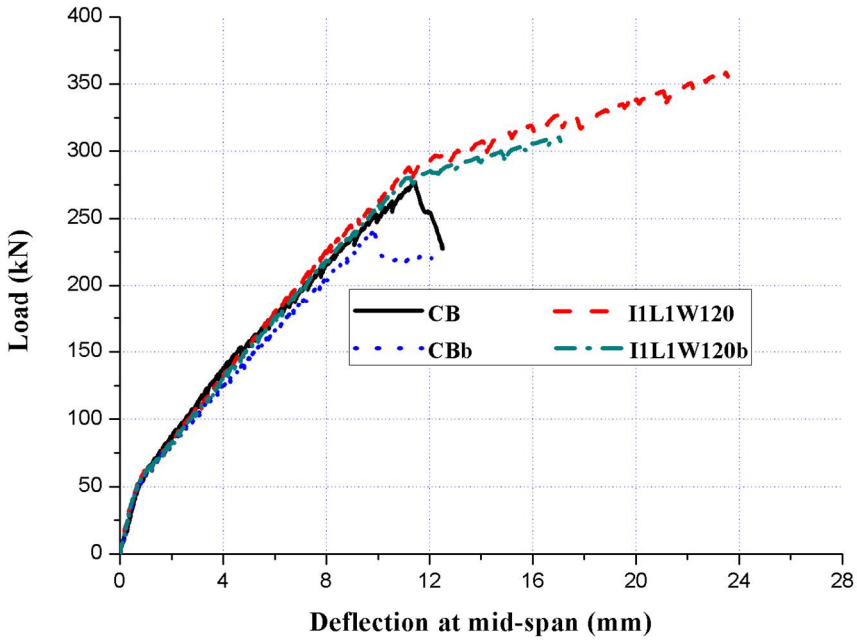

Figure 7.23 Load-deflection curves of selected beams of Series I and Series II

CHAPTER 8

DESIGN OF FRP U-JACKETS TO MITIGATE CONCRETE COVER SEPARATION FAILURE

8.1 INTRODUCTION

Chapter 7 has presented the first systematic experimental study on the use of FRP U-jackets to mitigate concrete cover separation failure, where the effect of FRP U-jackets of different forms was investigated. These test results have shown that both vertical and inclined FRP U-jackets can be effective in mitigating concrete cover separation. Use of vertical FRP U-jackets as end anchorage to suppress concrete cover separation has been commonly recommended by many design guidelines (e.g. ACI-440.2R 2008; Concrete Society 2012; CNR-DT-200/2004 2004 and GB-50608 2010). However, these design provisions have been established without a rigorous basis, and have not been evaluated using sufficient test data. In addition, test results in Chapter 7 indicated that inclined FRP U-jackets were superior to vertical FRP U-jackets in suppressing concrete cover separation, and an approach to the design of such U-jackets has yet to be established. This chapter is concerned with the development of a new design approach for FRP U-jackets provided for the

suppression of cover separation failures, following an evaluation of existing guideline provisions for the design of vertical FRP U-jackets using tests from the published literature together with tests presented in Chapter 7.

The new design approach presented in this chapter is based on the so-called 'concrete tooth' concept (Raoof and Zhang 1997;Raoof and Hassanen 2000; Gao et al. 2005). More specifically, the concrete tooth, referring to the concrete cover between the major crack at the plate end and the adjacent major crack within the strengthened region, is analysed as a cantilever beam. This cantilever beam is subjected to interfacial shear stresses at its free end from the FRP soffit plate and radial stresses induced by the wedge effect of the steel tension bars (Zhang and Teng 2014). Other significant factors include the thickness of concrete cover and the section weakening by the presence of steel tension bars. A detailed description of these factors is discussed in the following section.

The predictions of the existing provisions and the new design approach are compared with results of tests from the published literature and given in Chapter 7. The comparison indicates that the new design approach is superior to the existing methods in widely used guidelines such as the ACI (ACI-440.2R 2008) and the Concrete Society (2012) design guidelines.

8.2 CONCRETE COVER SEPARATION FAILURE

As the basis for the development of a design approach for FRP U-jackets to mitigate

concrete cover separation failure, the failure process, as observed in the control specimens presented in Chapter 7 (or that documented in the published literature),is examined again herein. In general, the failure process can be divided into four stages as inFigure8.1: (1) formation of a flexural-shear crack near the FRP soffit plate end (i.e. the initiation crack); (2) formation of a horizontal crack near the FRP soffit plate end at the level of steel tension bars; (3) propagation of the horizontal crack towards the mid-span at the level of steel tension bars; (4) occurrence of beam failure when the horizontal crack has sufficiently developed.

A significant flexural/flexural-shear crack occurs near the plate end once the moment of the section near the plate end exceeds the cracking moment. This significant flexural/flexural-shear crack plays an important role in a concrete cover separation failure, and is referred to as 'the initiation crack' hereafter. The initiation crack at the FRP plate end and the adjacent major crack within the strengthened region (referred as 'the critical crack' hereafter) isolate a beam segment, whose concrete cover forms the 'concrete tooth' in the proposed design approach. As the applied load further increases, the interfacial shear stresses at the interface between the FRP soffit plate and the concrete also increases, and both the initiation crack and the critical crack widen. At this stage, a horizontal crack at the level of steel tension bars occurs. The horizontal crack occurs at the level of steel tension bars rather than other locations for two reasons: (1) the horizontal section at the level of steel tension bars is weaker than those at other heights of the section due to the presence of steel tension bars; and (2) the wedge effect (Zhang and Teng 2014) as a result of slips between the deformed steel tension bars and concrete gives rise to significant radial stresses on

the concrete from the steel tension bars. These two factors together drive the propagation of the horizontal crack. Eventually, the concrete cover between the initiation crack and the critical crack (i.e. the concrete tooth)is completely detached from the RC beam, signifying the failure of the beam. The above discussion indicates that the concrete tooth can be analysed as a cantilever to predict concrete cover separation failure. In order to suppress/mitigate concrete cover separation, it is essential to constrain the development of the horizontal crack at the level of steel tension bars by counterbalancing the detrimental forces resulting from the shear stresses at the FRP-to-concrete interface near the end of the soffit plate and radial stresses as a result of slips between concrete and steel tension bars.

8.3 DATA OF TESTS WITH VERTICAL U-JACKETS

A total of eight pairs of beams were collected from the existing literature (Ceroni and Pecce 2010; Demakos and Koutsoukos 2003; Pimanmas and Pornpongsaroj 2004; Pham and Al-Mahaidi 2006; Smith and Teng 2003) and the tests presented in Chapter 7 to investigate the effect of vertical FRP U-jackets at the end of the soffit plate on concrete cover separation failure. All the specimens are small-scale beams with a width ranging from 100 mm to 151 mm and a height ranging from 150 mm to 260 mm. Key parameters of the collected beams are summarised in Table 8.1.Each of these pairs includes a control beam strengthened with an FRP soffit plate without plate-end U-jacket anchorage and another FRP-plated beam with a vertical FRP U-jacket as plate end anchorage. The two specimens of a pair are otherwise the same, and the control beam failed by concrete cover separation.

All the collected test data are used herein to evaluate the existing provisions in guidelines for suppressing/mitigating concrete cover separation. Concrete cover separation was successfully suppressed by vertical FRP U-jackets used in all the specimens with vertical FRP U-jackets except Specimen 5B in Smith and Teng (2003), which still failed by concrete cover separation. As a result, the amounts of these vertical FRP U-jackets in specimens other than Specimen 5B can be viewed as upper limits of the U-jacket required to suppress concrete cover separation successfully, while the amount of the vertical FRP U-jacket in Specimen 5B in Smith and Teng (2003) can be viewed as a lower limit of the U-jacket, which cannot satisfy the requirement of U-jacket to suppress concrete cover separation. In tests presented in Chapter 7, four specimens used vertical FRP U-jackets to mitigate/suppress concrete cover separation. Concrete cover separation was successfully suppressed in Specimen V1L1W120 with the largest amount of vertical FRP U-jacket among these four specimens; while the other three specimens still failed by concrete cover separation. Specimen V1L1W120 is also used to evaluate the provisions of guidelines to suppress concrete cover separation using vertical FRP U-jackets.

8.4 EXISTING PROVISIONS FOR DESIGN OF VERTICAL FRP U-JACKET

Use of vertical FRP U-jackets as end anchorage to suppress concrete cover separation has been commonly recommended by many design guidelines (ACI-440.2R 2008; Concrete Society 2012; CNR-DT-200/20042004 and GB-50608 2010).The ACI guideline (ACI 440.2R 2008) includes a provision for the design of

FRP U-jacket anchorage for preventing concrete cover separation based on the requirement that the force resisted by the U-jacket(s) is equal to the force from the longitudinal FRP reinforcement at failure. This rule was based on the test results of only three beam specimens (Reed et al. 2005). In the Concrete Society (2012) guideline, an equation, which is similar in form to but different in coefficients from that in the ACI guideline, is adopted to determine the area of the cross section of vertical FRP U-jacket(s). The Chinese national standard (GB-50608 2010) specifies the use of FRP U-jackets as plate-end anchorage that meets a prescriptive detailing requirement to avoid the occurrence of concrete cover separation. These design provisions have been established without a rigorous basis and have not been evaluated using sufficient test data. In this section, the provisions in these guidelines are reviewed and an evaluation of their accuracy using the results of existing tests from the published literature and those presented in Chapter 7 is presented.

8.4.1 ACI guideline

ACI-440.2R (2008) suggests the use of vertical FRP U-jackets as end anchorage to reduce the risk of occurrence of concrete cover separation. If vertical U-jackets are used, the area of the cross section of vertical FRP U-jackets is determined by simply equating the total force resisted by the FRP U-jackets at debonding to the force of the FRP tension plate at rupture, which is based only on very limited test results of three specimens (Reed et al. (2005). The equation for determining the total area of cross section of vertical FRP U-jackets is as follows:

$$A_{uf} = \frac{A_{tf} f_{tf}}{E_{uf} \kappa_{uf} \varepsilon_{uf}} \quad (8.1)$$

in which A_{uf} and A_{tf} are the cross-sectional areas of the FRP U-jacket(s) and the FRP tension plate, respectively; E_{uf} is the elastic modulus of the FRP U-jacket(s); ε_{uf} and f_{tf} are the rupture strain of the FRP U-jacket(s) and the rupture stress of the FRP tension plate; κ_{uf} is the bond-reduction coefficient, which can be determined using Eq. 8.2.

$$\kappa_{uf} = \frac{k_1 k_2 L_e}{11900 \varepsilon_{uf}} \quad (8.2)$$

The active (i.e. effective) bond length L_e is given by Eq. 8.3:

$$L_e = \frac{23300}{\left(n_{uf} t_{uf} E_{uf}\right)^{0.58}} \quad (8.3)$$

where n_{uf} and t_{uf} are the number of layers and the thickness of each layer of the FRP U-jacket(s), respectively.

The modification factors k_1 and k_2 in Eq.8.2 are related to the concrete strength and the type of FRP U-jacket used, and is given by:

$$k_1 = \left(\frac{f_c}{27}\right)^{2/3} \quad (8.4)$$

$$k_2 = \frac{d_{uf} - L_e}{d_{uf}} \quad (8.5)$$

where f_c and d_{uf} are the cylinder compressive strength of concrete and distance from the FRP U-jacket curtailment to the centre of steel tension bars, respectively.

8.4.2 Concrete Society guideline

In the Concrete Society (2012) guideline, an equation, which is similar form to but different in coefficients from that in ACI 440.2R (2008) is adopted to determine the

area of vertical FRP U-jacket(s) for the suppression of concrete cover separation. The equation is given by

$$A_{uf} = \frac{A_{tf}\sigma_{tf,max}}{E_{uf}\varepsilon_{ue}} \tag{8.6}$$

where $\sigma_{tf,max}$ is the maximum stress in the FRP tension plate (i.e. at the maximum moment section in the beam); and ε_{ue} is the effective strain in the FRP U-jacket given by:

$$\varepsilon_{ue} = 0.5\sqrt{\frac{f_t}{E_{uf}n_{uf}t_{uf}}} \leq 0.004 \tag{8.7}$$

where f_t is the tensile strength of concrete and can be related to the cylinder compressive strength of concrete using Eq. 8.8 (CEB-FIP 1990).

$$f_t = 1.4\left(\frac{f_c - 8}{10}\right)^{\frac{2}{3}} \tag{8.8}$$

In addition to requiring the area of FRP U-jacket(s) to satisfy Eq. 8.6, the Concrete Society guideline also requires that the radius of beam corners should be greater than 25mm and the FRP U-jacket(s) should extend up the beam sides with the minimum length being:

$$l_{uf} = 0.7\sqrt{\frac{E_{uf}n_{uf}t_{uf}}{f_{ct}}} \tag{8.9}$$

8.4.3 Chinese National Standard

GB-50608 (2010) specifies a design detailing to suppress concrete cover separation: two FRP U-jackets with their net spacing not greater than the beam height are required to be installed at the end of the FRP tension plate, and the area of each FRP U-jacket should satisfy Eq. 8.10.

$$\begin{cases} \text{for wet lay} - \text{up FRP soffit plate: } b_{uf} \geq \frac{1}{2} b_{tf} \text{ and } t_{uf} \geq \frac{1}{2} t_{tf} \\ \text{for purtruded FRP soffit plate: } b_{uf} \geq 100\ mm \text{and } A_{uf} \geq \frac{1}{4} A_{tf} \end{cases} \quad (8.10)$$

in which b_{uf} and b_{tf} are the widths of the FRP U-jacket and the tension plate, respectively; and t_{uf} and t_{tf} are thicknesses of the FRP U-jacket and the tension plate, respectively.

In addition, the FRP U-jackets are required to extend up to the top surface of the beam and the radius of the beam corners should be greater than 20 mm.

8.4.4 Evaluation of existing provisions

Table 8.2 gives the evaluation results of the provisions of the guidelines reviewed above. As indicated by Table 8.2 and Figure 8.2, the provisions in these guidelines do not seem to predict well the required amount of U-jacket for suppressing/mitigating concrete cover separation, and the predicted amounts show a large degree of scatter.

The provision in ACI 440.2R (2008) seems to be the most conservative, with the average predicted-to-test ratio of the cross-sectional area of the U-jacket 6.9, and all the predicted cross-sectional areas of the U-jacket are larger than those actually used in the tests. An FRP U-jacket, which satisfies the requirement in ACI 440.2R (2008) may be sometimes too voluminous to install in practice. Moreover, the degree of scatter is very large: the predicted-to-testcross-sectional area ratios have a coefficient of variation of 122.2%. The maximum predicted-to-test cross-sectional area ratio of the ACI provision is 27.1 for Specimen V1L1W120 in Chapter 7 of the present

research project, while its minimum value is1.7 for Specimen 5B in Smith and Teng (2003); both test specimens are cases where the amounts of U-jackets used are close to the lower-bound value.

Based on the provision in the Concrete Society guideline (2012), the average predicted-to-test cross-sectional area ratio of the FRP U-jacket is 1.3, with the coefficient of variation 96.8%. The maximum ratio is 3.5 for Specimen E3a2 in Pham and Al-Mahaidi (2008), while the minimum ratio is 0.26 for Specimen B5 in Ceroni (2010).

Based on the provision in GB-50608 (2010), the average predicted-to-test cross-sectional area ratio of the FRP U-jacket is 0.6, with the coefficient of variation 81.2%. The maximum ratio is 1.5 for Specimen E3a2 in Pham and Al-Mahaidi (2008), while the minimum ratio is 0.22 for Specimen 5B in Smith and Teng (2003). GB-50608 (2010) seems to provide enough FRP U-jackets to suppress concrete cover separation.

8.5 DESIGN OF VERTICAL FRP U-JACKETS

8.5.1 Design approach

Against the background that not all the existing provisions provide satisfactory predictions for the amount of FRP U-jackets needed to suppress/mitigate concrete cover separation, a new approach for the design of FRP U-jacket to suppress/mitigate

concrete cover separation is developed based on the concrete tooth concept in this section. In the concrete tooth concept, the concrete cover between the initiation crack and the critical crack (i.e. the concrete tooth) controls the failure behaviour of the FRP-plated RC beam and the beam fails when the concrete tooth detaches from the RC beam. The detrimental forces driving the concrete tooth to detach from the RC beam result from the shear stresses at the FRP-to-concrete interface near the end of the soffit plate and the radial stresses as a result of slips between concrete and steel tension bars. An FRP U-jacket used to suppress/mitigate concrete cover separation should provide a resisting force to counterbalance these detrimental forces.

Figure 8.3 illustrates the stress state of the concrete tooth with an FRP U-jacket. The forces driving the concrete tooth to detach from the RC beam are the tension force of the soffit plate and the radial stresses from the slips between the steel tension bars and the surrounding concrete. These detrimental forces are counterbalanced by the tensile force of the U-jacket if the U-jacket can shift concrete cover separation to another failure mode (i.e. IC debonding). It is assumed that the RC beam fails by debonding of U-jacket (following IC debonding or concrete cover separation)when the horizontal crack at the level of the steel tension bars propagates through the inner edge of the U-jacket. For simplification of calculation, it is assumed that the bond strength of the FRP U-jacket is fully developed at failure of the RC beam. The radial stresses are the radial component of the bond stresses having an angle to the bar axis (e.g. 45^{o} in the present study) (Zhang and Teng 2014). The calculation of the radial stresses of steel-to-concrete interfaces are conducted using an equivalent stress block with its magnitude being the maximum radial stress multiplied by a reduction factor

of 0.8 to account for the non-uniform distribution. The equation of moment equilibrium can be established with the centre of rotation at the mid-width of the part of the concrete tooth outside the vertical FRP U-jacket and is given by Eq. 8.1.

$$0.5F_{u,db} \cdot W_t = F_{t,db} \cdot d + M_{rad} \tag{8.1}$$

Where $F_{u,db}$ is the total tensile force in the vertical FRP U-jacket (including the contributions of both sides of the U-jacket) at debonding of the U jacket, which signifies beam failure; W_t is the spacing between the initiation crack and the critical crack (i.e. width of the concrete tooth); $F_{t,db}$ is the tensile force in the FRP soffit plate at the critical crack at failure;d is the concrete cover thickness; and M_{rad} is the moment induced by the radial stresses from the wedge effect.

$F_{u,db}$ can be expressed using the stress in the FRP U-jacket, σ_{db}, at debonding by

$$F_{u,db} = 2.0\sigma_{\mathrm{db}} W_{uf} t_{uf} \tag{8.2}$$

where W_{uf} and t_{uf} are the width and the thickness of the FRP U-jacket, respectively; and the σ_{db} can be determined from Chen and Teng's (2001) bond strength model as follows:

$$\sigma_{db} = 0.427\beta_L \sqrt{E_{uf}\sqrt{f_c^{'}}/t_{uf}} \tag{8.3}$$

In the above equation, E_{uf}, t_{uf} and $f_c^{'}$ are the elastic modulus and thickness of the U-jacket and the cylinder compressive strength of concrete respectively; and β_L is the bond length factor (representing the effect of length of U-jacket) given by

$$\beta_L = \begin{cases} 1 & if\ L \geq L_e \\ sin\dfrac{\pi L_{uf}}{2L_{ue}} & if\ L < L_e \end{cases} \tag{8.4}$$

where L_{uf} and L_{ue} are the bond length and the effective bond length of the U-jacket.

The effective bond length, L_e, of a vertical FRP U-jacket is given by

$$L_e = \sqrt{\frac{E_{uf} t_{uf}}{\sqrt{f_c^{'}}}} \tag{8.5}$$

The accurate prediction of the crack spacing between the initiation crack and the critical crack (i.e., the width of concrete tooth) is a challenge. Although all crack spacing models reviewed by the researcher were found to have considerable scatter, the modified *fib's* (2001) model proposed by Aprile and Benedetti (200) was found to perform with relatively good accuracy and is adopted herein. This model is specific for determining the crack spacing in high moment region (e.g. near the mid-span of a simply supported beam); a value of two times the crack spacing given by the *fib's* (2001) model is therefore used to determine the spacing between the initiation crack and critical crack, both of which are generally in a relatively low moment region.

The adopted crack spacing model is given by

$$S_{cr} = \frac{S_{cr,RC}}{\omega} \tag{8.6}$$

where ω is a homogenization factor that includes the contribution of the FRP soffit plate. $S_{cr,RC}$ is the mean crack spacing of un-strengthened RC beams:

$$S_{cr,RC} = \frac{\Phi}{3.6\rho_{b,eff}} \tag{8.7}$$

where Φ is the longitudinal steel bar diameter; and $\rho_{b,eff}$ is the ratio between the total area of all steel tension bars, A_s, and the effective area of concrete in tension $A_{t,eff}$, which can be taken as the minimum of 2.5db and b(h-y)/3, with y being the depth of compression zone (CEB-FIP 1990). The factor representing the contribution of the FRP soffit plate is given by:

$$\omega = \frac{n_b\rho_{b,eff} + n_f\rho_{f,eff}}{n_b\rho_{b,eff}} \tag{8.8}$$

where n_b and n_f are the homogenization factors for steel and FRP reinforcements, and determined by E_b/E_c and E_f/E_c respectively; $\rho_{f,eff}$ is the area ratio between the FRP reinforcement and the effective area of concrete in tension.

In Eq. 8.1, the tensile force in the FRP soffit plate at the critical crack at IC debonding, $F_{t,db}$, is estimated from the moment at the critical-crack section at IC debonding, M_{PE}, using a conventional section analysis. M_{PE} can be easily related to the IC debonding moment of the beam, defined as the maximum moment in the beam at IC debonding. For a beam in three- or four-point bending, the relationship is

$$M_{PE} = \frac{L_{PE}}{L_{SP}} M_{IC} \tag{8.9}$$

in which L_{PE} and L_{SP} are the distance between the plate end, the adjacent support and the shear span of the beam respectively, and the IC debonding moment M_{IC} is calculated using a section analysis presented in Chapter 5 of the present research project and with the IC debonding strain predicted by the IC debonding strength

model proposed by Lu et al. (2007).

The interfacial stress at steel-to-concrete interfaces arises from the slips between steel tension bars and concrete can be divided into three components (e.g. interfacial shear stress and two radial stress components). In the analysis of a concrete tooth model, only the radial stress component perpendicular to the horizontal plane is considered while the other radial stress component is believed to have a marginal effect on concrete cover separation failure and is neglected in the analysis. A simplified equivalent stress block with its magnitude 0.8 times the maximum radial stress is used to determine the detrimental moment of the radial stress of steel-to-concrete interfaces as given by Eq. 8.10

$$\mathrm{F}_{rad} = nD\tau_{rad}L_{rad} = 0.8nD\tau_{max}(W_{uf} + W_t)/2 \quad (8.10a)$$

$$M_{rad} = \mathrm{F}_{rad}C_{rad} = 0.2nD\tau_{max}(W_{uf} + W_t)W_t \quad (8.10b)$$

in which F_{rad} is the total force of the radial stress; τ_{rad} is the magnitude of the equivalent radial stress;L_{rad} is the length of the equivalent stress block of the radial stress;C_{rad} is the distance from the action point of the total force of the radial stress to the rotation centre; D and *n* are the diameter and number of the steel tension bars, respectively;$W_t$is the crack spacing between the initiation crack and the critical crack; and τ_{max} is the peak shear stress of the steel-to-concrete interface and can be determined by Eq. 8.11 (CEB-FIB 1990).

$$\tau_{max} = 2.0\sqrt{f_t} \quad (8.11)$$

8.5.2 Evaluation of the proposed approach

The newly proposed design approach in this chapter is also assessed using the existing test data in Table 8.2. The moment contributed by the U-jacket of each specimen is compared with the sum of moments resulting from both the radial stress and the tensile force in the soffit plate in Table 8.3.For Specimen V1L1W90 in Chapter 7 of the present research project, the sum of the detrimental moments from the steel-to-concrete interface and the soffit plate is larger than the moment from the vertical U-jacket by 2.0 kN.m. This prediction indicates that the vertical U-jacket cannot provide a large enough force to suppress concrete cover separation. This prediction is consistent with the fact observed in the test that Specimen V1L1W90 still failed by concrete cover separation. Specimen V1L1W120 in Chapter 7 of the present research project is the same as Specimen V1L1W90 except that the width of the vertical U-jacket of Specimen V1L1W120 was 120 mm and larger than that of the vertical U-jacket of Specimen V1L1W90 by 30 mm. The predicted results for Specimen V1L1W120 show that the moment provided by the vertical U-jacket is larger than the total detrimental moment by 0.3 kN.m, and indicates that concrete cover separation can be suppressed. The prediction is consistent with the experimental observation that Specimen V1L1W120 failed by IC debonding rather than concrete cover separation.

In all the other specimens, the moment of the vertical U-jacket is always larger than the sum of the two detrimental moments from the radial stress at the steel-to-concrete interface and the tensile force of the soffit plate. This fact indicates that concrete cover separation can be suppressed by the vertical U-jacket. The predictions are thus

consistent with the test observations of all the specimens except that of Specimen 5B in Smith and Teng (2003), which still failed by concrete cover separation initiated at the inner edge of the vertical U-jacket (the edge farther away from the adjacent plate end).

The evaluation presented above indicates that the proposed approach performs well in the design of vertical FRP U-jackets to suppress concrete cover separation. As found in the tests, concrete cover separation tends to initiate at the inner edge of the vertical FRP U-jacket, if a narrow vertical U-jacket is used. The vertical FRP U-jacket should be wide enough to cover the entire concrete tooth. The vertical FRP U-jacket should extend up to the top face of the beam to ensure a long bond length (longer than its effective bond length if possible). A proper vertical U-jacket should also satisfy these detailing requirements.

8.6 DESIGN OF INCLINED FRP U-JACKETS

8.6.1 General

As explained in Chapter 7, an inclined FRP U-jacket is preferable to a vertical FRP U-jacket in mitigating debonding failures of RC beams strengthened in flexure with an FRP soffit plate and can be highly effective in postponing or even suppressing concrete cover separation failure. An inclined FRP U-jacket mitigates concrete cover separation failure by: (1) constraining the widening of the horizontal crack at the level of steel tension bars; (2) constraining the initiation crack at the soffit plate end;

and (3) carrying the force transferred from the FRP soffit plate. The latter two roles cannot be fulfilled by a vertical FRP U-jacket. The initiation crack at the plate end, being a flexural-shear crack, often develops vertically from the beam bottom, and is parallel to the edges of a vertical FRP U-jacket. The initiation crack often intersects the vertical FRP U-jacket at a level much higher than the steel tension bars. As a result, the opening-up of this crack cannot be effectively constrained by the vertical FRP U-jacket. When an inclined FRP U-jacket is used, the initiation crack at the soffit plate end often intersects the U-jacket near the beam bottom, and the opening-up of the initiation crack can be effectively constrained. Therefore, the 'effective' end of the FRP soffit plate will not shift towards the mid-span of the beam. The force in the FRP soffit plate can be effectively transferred to the inclined FRP U-jacket, which substantially reduces the interfacial stresses at the FRP-to-concrete interface near the plate end.

8.6.2 Design approach

A design model based on the concrete tooth concept is presented herein for the design of inclined FRP U-jackets for the mitigation of cover separation failure. The model is similar to that presented above for the design of vertical FRP U-jackets. Figure 8.4 illustrates the proposed model. Unlike the case for a vertical FRP U-jacket, concrete cover separation cannot initiate at the inner edge of the U-jacket, so the detailing requirement on the width of the U-jacket is not needed. An inclined FRP U-jacket can be designed using Eq. 8.13 for the moment equilibrium of the concrete tooth at beam failure: the moment from the inclined FRP U-jacket should balance

moments from the tensile force of the FRP soffit plate and the radial stresses from the steel tension bars.

The same assumptions are made as those for the design approach for vertical U-jackets. They are: (1) The RC beam fails by debonding of U-jacket following IC debonding or concrete cover separation when the horizontal crack at the level of the steel tension bars propagates through the inner edge of the U-jacket.(2) The bond strength of the FRP U-jacket is fully mobilized at failure of the RC beam.(3) A simplified-stress block with its magnitude 0.8 times the maximum radial stress to account for the non-uniform distribution of the radial stress is used to represent the radial stresses. It is difficult to determine accurately the distribution of the radial stress, and therefore the radial stress is estimated using a simplified stress block with an empirical reduction factor (i.e. 0.8). The reduction factor should be further refined if an advanced method to calculate the radial stress is available.(4) The equation of moment equilibrium can be established with the rotation centre at the centre of the part of concrete tooth not under the FRP U-jacket. This implies that the part of the horizontal crack covered by the U-jacket becomes significant at the debonding of the U-jacket, while other parts of the concrete tooth not covered by the U-jacket remains solid or the crack in this part is not significant. Therefore, the rotation centre is reasonable to set at the centre of the part of the concrete tooth not covered by the U-jacket.

$$F_{y,ufrp} \cdot C' = \left(F_{t,db} - F_{x,ufrp}\right) \cdot d + M_{rad} \tag{8.12}$$

where$F_{x,ufrp}$ and $F_{y,ufrp}$are the horizontal and the vertical components of the force resisted by the inclined U-jacket;C' isthe horizontal distance from the centreline of the inclined U-jacket to the centre of rotation;$F_{t,db}$isthe tensile force in the FRP soffit plate at the critical crack at IC debonding;$d$istheconcrete cover thickness; and M_{rad} is the moment induced by the radial stresses arising from the wedge effect of steel tension bars.

The force in the inclined U-jacket at its debonding can be determined by Eq. 8.2, and its components in the horizontal and the vertical directions are simply as follows:

$$F_{y,ufrp} = F_{u,db} \cdot \sin\theta \tag{8.13a}$$

$$F_{x,ufrp} = F_{u,db} \cdot \cos\theta \tag{8.13b}$$

where θ is the angle between the inclined U-jacket and the beam axis. In both this chapter and Chapter 7, only inclined U-jackets with an angle of 45^{o} to the beam axis are considered. The tensile force in the FRP soffit plate is substantially resisted by the horizontal component of the force in the inclined U-jacket so that the interfacial shear stresses near the plate end are largely reduced. The equations for calculating M_{rad} and $F_{t,db}$ are already given earlier. Eq. 8.13 can be re-arranged for the resisting moments to be on the left hand side and the driving moments on the right hand side.

$$F_{y,ufrp} \cdot C' + F_{x,ufrp} \cdot d = F_{t,db} \cdot d + M_{rad} \tag{8.14}$$

8.6.3 Evaluation of the proposed approach

Four full-scale FRP-plated RC beams with an inclined FRP U-jacket as the plate end anchorage were tested as part of this research project as presented in Chapter 7. Three out of the four specimens belonged to Series I and were identical except for the inclined FRP U-jacket. The concrete cover separation, which was the governing failure mode of the control beam for these three specimens, was successfully suppressed by the inclined FRP U-jacket. In Specimen I1L1W90, the FRP U-jacket had the least amount of FRP and can be viewed as the lower limit of an inclined FRP U-jacket to suppress concrete cover separation successfully in these beams. Therefore, the results of Specimen I1L1W90 are analysed herein to verify the design model.

The measured crack spacing between the initiation crack at the plate end and the critical crack is 190 mm. The tensile force in the inclined FRP U-jacket at debonding, F_{ufrp}, was calculated using Eq. 8.2 to be 61.32kN, with both its horizontal and vertical components 43.36kN. The left-hand side of Eq. 8.14, representing the resisting moment from the FRP U-jacket, is 7.15 kN.m. The tensile force in the FRP soffit plate at the critical crack is 147.4kN, which was calculated from the strain gauge reading close to (about 20 mm away from) the critical crack in the test. Therefore, the moment from the first term on the right-hand side of Eq. 8.14, is 4.16 kN.m. The moment induced by the radial stresses of the steel tension bars was calculated using Eq. 8.10to be 2.7kN.m. The moment to drive the concrete cover separation failure (i.e. the right-hand side of Eq. 8.13) is 6.86 kN.m. The moment

resisted by the U-jacket is larger than the driving moment by 0.19 kN.m. It indicates that in Specimen I1L1W90, the inclined FRP U-jacket was strong enough to surpass the cover separation failure, which agrees with the experimental observation. Although the design model proposed in this section has succeeded in providing a reasonable prediction for Specimen I1L1W90, much further verification of the design model is needed and can be achieved through appropriate laboratory testing or accurate finite element modelling. Moreover, the accuracy of the proposed design model depends on the use of an accurate crack spacing model to determine the width of the concrete tooth near the plate end.

8.7 CONCLUSIONS

In this chapter, a database of FRP-plated RC beams with vertical FRP U-jackets to mitigate their concrete cover separation was established and then used to examine the effect of vertical FRP U-jackets on concrete cover separation and to assess the existing guideline provisions. A new approach for the design of both vertical FRP U-jackets and inclined FRP U-jackets to suppress cover separation failure has been proposed based on the concrete tooth concept pioneered by Raoof and Zhang (1997), Raoof and Hassanen (2000) and Gao et al. (2005). This design approach was verified using existing test data or those presented in Chapter 7.

Based on the results and discussions presented in this chapter, the following conclusions can be drawn:

(1) In terms of performance in mitigating concrete cover separation failure, an inclined FRP U-jacket near the plate end is superior to a vertical one and is therefore recommended as the preferred anchorage measure. The superiority of an inclined FRP U-jacket to a vertical one can be attributed to the following factors: (1) the tensile force in the FRP soffit plate can be easily transferred to the inclined FRP U-jacket; and (2) both the initiation crack at the soffit plate end and the horizontal crack at the level of steel tension bars can be effectively constrained by the inclined U-jacket.

(2) Evaluation of existing guideline provisions using the assembled test database indicated that the provisions in these guidelines do not provide good predictions of the amount of U-jacket for suppressing concrete cover separation, and the predictions show a large degree of scatter.

(3) A new design approach, consisting of two models for vertical U-jackets and inclined U-jackets respectively, was proposed based on the concrete tooth concept (Raoof and Zhang 1997; Raoof and Hassanen 2000; Gao et al. 2005). The new approach takes into account the radial stresses arising from the wedge effect of the steel tension bars.

(4) Evaluation of the proposed model for the design of a vertical FRP U-jacket indicates that the proposed model is superior to the existing guideline provisions. In addition, the width of the U-jacket should be not less than the crack spacing between the initiation crack at the plate end and the critical crack within the

strengthened region. This detailing requirement aims at avoiding concrete cover separation failure that initiates at the inner edge of the FRP U-jacket. The vertical U-jacket should also extend to the top face of the concrete beam to ensure a long bond length for a vertical U-jacket (ideally longer than the effective bond length).

(5) The proposed model for the design of an inclined FRP U-jacket has been verified by tests presented in Chapter 7 although much more verification by laboratory tests or accurate finite element modelling is needed. The accuracy of the model depends on the accuracy of the chosen crack spacing model.

8.7 REFERENCES

ACI 440.2R (2008). *Guide for the design and construction of externally bonded FRP systems for strengthening concrete structures*, ACI Committee 440, American Concrete Institute, Farmington Hills, MI, USA.

Aprile, A. and Benedettim, A. (2004). "Coupled flexural-shear design of R/C beams strengthened with FRP", *Composites Part B:Engineering*, Vol. 35, No. 1, pp. 1-25.

CEB-FIP MC90 (1993). *CEB-FIP model code 1990*, Thomas Telford, London, 1993.

Ceroni, F. (2010). "Experimental performances of RC beams strengthened with FRP materials", *Construction and Building Materials*, Vol. 24, No. 9, pp.1547-1559.

Chen, J.F. and Teng, J.G. (2001). "Anchorage strength models for FRP and steel plates bonded to concrete", *Journal of Structural Engineering-ASCE*, Vol. 127, No. 7, pp.784-791.

Chen, J.F., Yuan, H. and Teng, J.G. (2007). "Debonding failure along a softening FRP-to-concrete interface between two adjacent cracks in concrete members", *Engineering Structures*, Vol. 29, No. 2,pp. 259-270.

CNR DT 200/2004 (2004). *Guidelines for design, execution and control of strengthening interventions by means of fibre-reinforced composites – materials, reinforced concrete and prestressed concrete structures, masonry structures*, National Research Council, Advisory Committee on Technical Regulations for

Constructions, Rome, Italy.

Demakos, C. and Koutsoukos, D. (2003). "Effective strengthening of reinforced concrete beams with anchored FRPs", *Recent Advances in Composite Materials*, Springer.

fib. (2001). *Externally bonded FRP reinforcement for RC structures*, International Federation for Structural Concrete, Lausanne, Switzerland.

Gao, B., Leung, C. K. Y. and Kim, J. K. (2005). "Prediction of concrete cover separation failure for RC beams strengthened with CFRP strips", *Engineering Structures*, Vol. 27, No. 2, pp. 177-189.

GB-50608 (2010). *Technical code for infrastructure application of FRP composites*, China Planning Press, Beijing.

Pham, H. B. and Al-Mahaidi, R. (2006). "Prediction models for debonding failure loads of carbon fiber reinforced polymer retrofitted reinforced concrete beams", *Journal of Composites for Construction*, ASCE, Vol. 10, No. 1,pp. 48-59.

Pimanmas, A. and Pornpongsaroj, P. (2004). "Peeling behaviour of reinforced concrete beams strengthened with CFRP plates under various end restraint conditions", *Magazine of Concrete Research*, Vol. 56, No. 2, pp. 73-81.

Raoof, M. and Hassanen, M.A.H. (2000). "Peeling failure of reinforced concrete beams with fibre-reinforced plastic or steel plates glued to their soffits", *Proceedings of the Institution of Civil Engineers-Structures and Buildings*, Vol.

140, No. 3, pp. 291-305.

Raoof, M. and Zhang, S. (1997). “An insight into the structural behaviour of reinforced concrete beams with externally bonded plates”, *Proceedings of the Institution of Civil Engineers-Structures and Buildings*, Vol. 122, No. 4, pp. 477-492.

Smith, S.T. and Teng, J.G. (2003). “Shear-bending interaction in debonding failures of FRP-plated RC beams”, *Advances in Structural Engineering*, Vol. 6, No. 3, pp. 183-199.

Teng, J.G., Yuan, H. and Chen, J.F. (2006). “FRP-to-concrete interfaces between two adjacent cracks: Theoretical model for debonding failure”, *International Journal of Solids and Structures*, Vol. 43, No.18-19, pp. 5750-5778.

Yuan, H., Teng, J. G., Seracino, R., Wu, Z. S. and YAO, J. (2004). “Full-range behavior of FRP-to-concrete bonded joints”. *Engineering Structures*, Vol. 26, No. 5, pp. 553-565.

Zhang, S.S. and Teng, J.G. (2014). “Finite element analysis of end cover separation in RC beams strengthened in flexure with FRP”, *Engineering Structures*, Vol. 75, pp. 550-560.

8.8 TABLES AND FIGURES

Table 8.1 Geometrical and material properties of beams with vertical FRP U-jackets (to be continued)

Data source		Ceroni(2010)				Demakos and Koutsoukos(2003)				Pimanmas and Pornpongsaroj(2004)				Pham and Al-Mahaidi(2008)		Smith and Teng (2003)	
Pair no.		1		2		3		4		5		6		7		8	
Specimen name		B2	B5	B2	B7	B1/GFRP	B1/GFRP/CMAS	B1/CFRP	B1/CFRP/CMAS	A-420-P	A-420-U	B-200-P	B-200-U	E3b2	E3a2	2B	5B
Beam height (mm)		180	180	180	180	150	150	150	150	220	220	220	220	260	260	250	250
Beam width (mm)		100	100	100	100	100	100	100	100	120	120	120	120	140	140	151	151
Effective depth (mm)		150	150	150	150	120	120	120	120	169	169	169	169	220	220	205	205
Test span (mm)		1800	1800	1800	1800	900	900	900	900	2000	2000	2000	2000	1600	1600	1500	1500
Shear Span (mm)		780	780	780	780	300	300	300	300	1000	1000	700	700	700	700	500	500
Concrete cylinder compressive strength (MPa)		26.9	26.9	26.9	26.9	16.0	16.0	16.0	16.0	44.0	44.0	44.0	44.0	53.7	53.7	48.6	36.4
Tension steel	Bar size (mm)	12	12	12	12	8	8	8	8	12/16	12/16	12/16	12/16	12	12	10	10
	No.	2	2	2	2	2	2	2	2	2/2	2/2	2/2	2/2	2	2	2	2
	Yield stress (MPa)	441	441	441	441	550	550	550	550	480/554	480/554	480/554	480/554	551	551	506	506
Compre	Bar size (mm)	8	8	8	8	8	8	8	8	16	16	16	16	12	12	10	10

ssion steel	No.	2	2	2	2	2	2	2	2	4	4	4	4	2	2	2	2
	Yield stress (MPa)	537	537	537	537	550	550	550	550	554	554	554	554	551	551	506	506
Shear Steel	Bar size (mm)	8	8	8	8	8	8	8	8	6	6	6	6	10	10	10	10
	Spacing (mm)	150	150	150	150	50	50	50	50	50	50	50	50	125	125	100	100
	Yield stress (MPa)	537	537	537	537	550	550	550	550	399	399	399	399	334	335	506	507
FRP soffit plate	FRP type	CFRP	CFRP	CFRP	CFRP	GFRP	GFRP	CFRP	CFRP	CFRP	CFRP	CFRP	CFRP	CFRP	CFRP	CFRP	CFRP
	Elastic modulus (GPa)	230	230	230	230	27.5	27.5	75	75	150	150	150	150	209	209	271	271
	Rupture strain ($\mu\varepsilon$)	15000	15000	15000	15000	20000	20000	15000	15000	14667	14667	14667	14667	10526	10526	13726	13726
	Ply thickness (mm)	0.167	0.167	0.167	0.167	1.300	1.300	0.450	0.450	1.000	1.000	1.000	1.000	0.176	0.176	0.165	0.165
	No. of plies	1	1	1	1	1	1	1	1	1	1	1	1	6	6	2	2
	Width (mm)	100	100	100	100	100	100	100	100	100	100	100	100	100	100	147	147
	Length (mm)	1000	1000	1000	1000	890	890	890	890	1160	1160	1600	1600	1000	1000	1250	1250
FRP U-jacket	FRP type		CFRP		CFRP		GFRP		CFRP		CFRP		CFRP		CFRP		CFRP
	Elastic modulus (GPa)		230		230		27.5		75.0		230.5		230.5		209		257
	Rupture strain ($\mu\varepsilon$)		15000		15000		20000		15000		15108		15108		18660		17538
	Ply thickness (mm)		0.167		0.167		1.300		0.450		0.111		0.111		0.167		0.165

	No. of plies		1		1		1		1		1		1		2		1
	Width (mm)		80		80		100		100		371		371		50		125
	No. of U-jackets**		1		3		1		1		1		1		1		1
Performance	Shear force at soffit plate end (kN)	24.6	26.0	24.6	27.5	33.8	36.3	37.1	43.3	47.8	74.7	58.9	73.4	26.3	33.2	57.6	62.4
	Moment at soffit plate end (kN.m)	9.8	10.4	9.8	11.0	0.17	0.18	0.19	0.22	20.1	31.4	11.8	14.7	3.9	5.0	3.6	3.9
	Moment at mid-span (kN.m)	19.2	20.2	19.2	21.4	10.1	10.9	11.1	13.0	47.8	74.7	41.2	51.5	23.6	29.9	28.8	31.2
	Deflection at loading point (mm)	18.6	24.8	18.6	21.2	5.6	10.2	6.5	12.7	10.3	16.2	10.1	15.9	5.61	7.64	3.51	5.27
	Maximum strain of soffit plate at failure ($\mu\varepsilon$)	1841	2400	1841	2352	N/A#	N/A	N/A	N/A	3420	8760	2890	3750	N/A	N/A	2621	4231
	Failure mode	PE	FR	PE	FR	PE	IC	PE	IC	PE	CC	PE	CC	PE	IC	PE	PE
	Load increase	5.5%		11.6%		7.6%		16.7%		56.2%		24.9%		26.5%		36.2%	
	Deflection increase	33.3%		14.0%		83.3%		95.7%		57.5%		58.2%		8.4%		50.1%	

Note:*: Starting point is determined from the end of the FRP soffit plate. **: In Specimen B5 of Ceroni 2010, the second FRP U-jacket of 100 mm and 0.167 mm in width and thickness respectively was installed at 450 mm from the end of the FRP soffit plate.

#: N/A=data not available in the source reference.

Table 8.2 Evaluation of existing design approaches for beams with vertical FRP U-jackets

Resource	Specimen name	Failure mode*	Area of the cross section of FRP U-jacket (mm^2)			
			Actually used in test	ACI 440	TR55	GB-50608
Ceroni(2010)	B5	FR	26.8	88.7	7.0	8.35
Demakos and Koutsoukos(2003)	B1/GFRP/CMA	IC	260.0	1480.5	152.4	65
	B1/CFRP/CMAS	IC	90	382.1	31.1	22.5
Pimanmas and Pornpongsaroj(2004)	A-420-U	CC	82.4	205.4	109.7	50
	B-200-U	CC	82.4	205.4	107.4	50
Pham and Al-Mahaidi(2008)	E3a2	IC	33.4	267.5	117.0	51
Smith and Teng (2003)	5B	PE	91.2	157.8	25.4	20.5
Chapter 7 of the present thesis	V1L1W120	IC	80.0	2165.5	255.0	109.9

*FR = FRP rupture; IC = IC debonding; CC = concrete crushing; CS=concrete cover separation.

Table 8.3Evaluation of the proposed approach for beams with vertical FRP U-jackets

Resource	Specimen name	Failure mode*	Moment from U-jacket (kN.m)	Moments from the steel-to-concrete interface and soffit plate (kN.m)	Difference of moments
Ceroni(2010)	B5	FR	2.1	0.8	1.3
Demakos and Koutsoukos(2003)	B1/GFRP/CMA	IC	1.8	0.6	1.2
	B1/CFRP/CMAS	IC	1.7	0.5	1.2
Pimanmas and Pornpongsaroj(2004)	A-420-U	CC	2.1	1.3	0.8
	B-200-U	CC	2.1	1.2	0.9
Pham and Al-Mahaidi(2008)	E3a2	IC	3.2	2.0	1.2
Smith and Teng (2003)	5B	CS	4.4	1.3	3.1
Chapter 7 of the present thesis	V1L1W90	CS	6.9	8.9	-2.0
	V1L1W120	IC	9.2	8.9	0.3

*FR = FRP rupture; IC = IC debonding; CC = concrete crushing; CS=concrete cover separation.

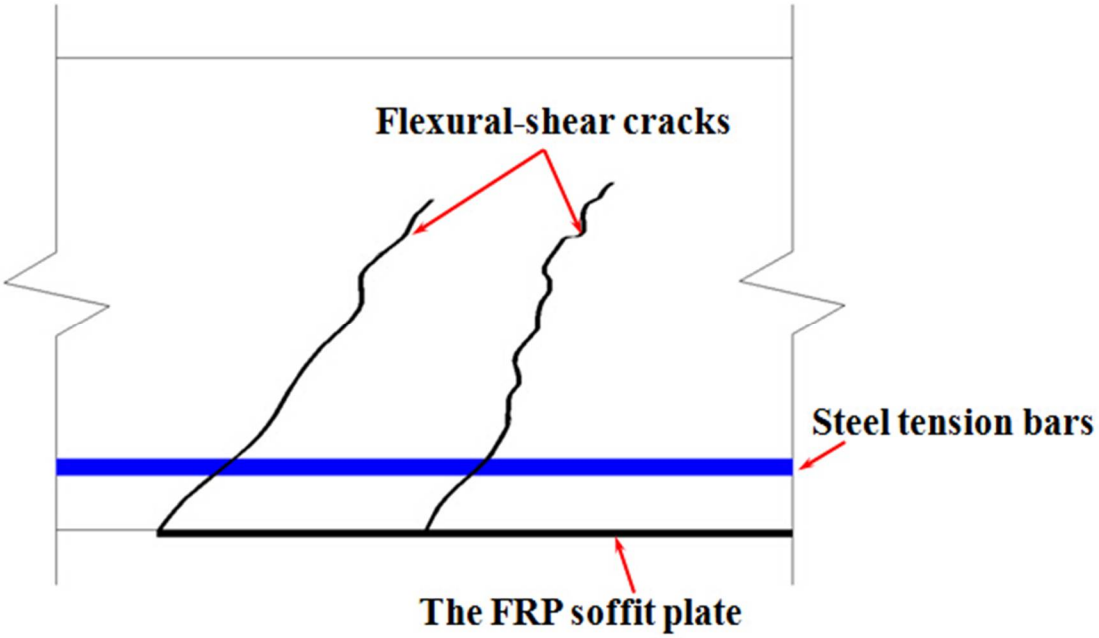

(a) Stage I: formation of flexural-shear cracks near the FRP plate end

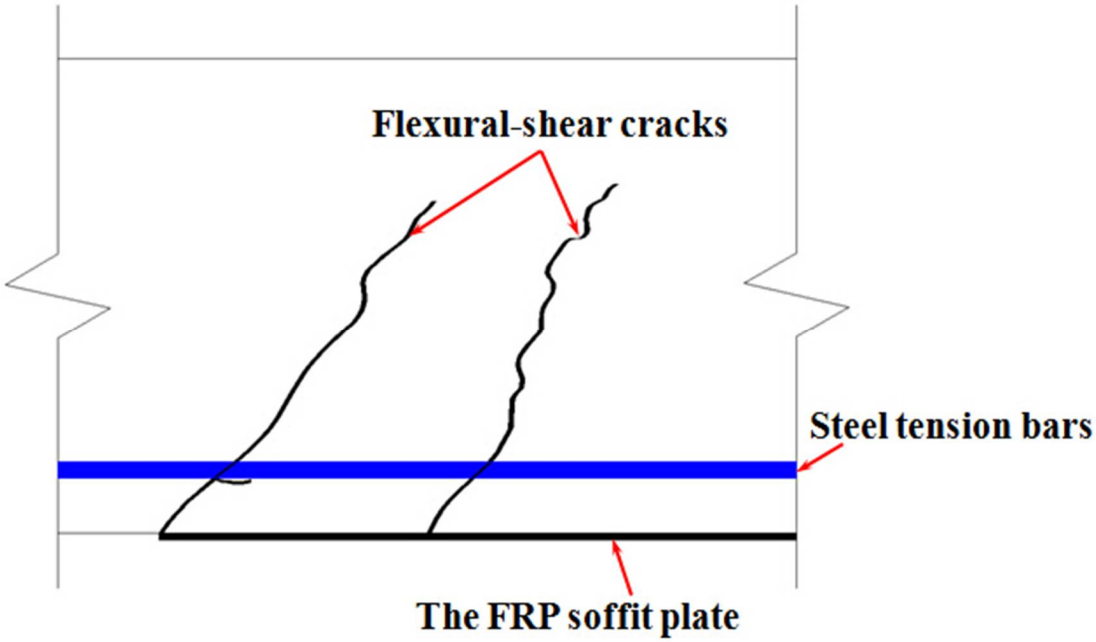

(b) Stage II: appearance of a horizontal crack at the height of steel tension bars

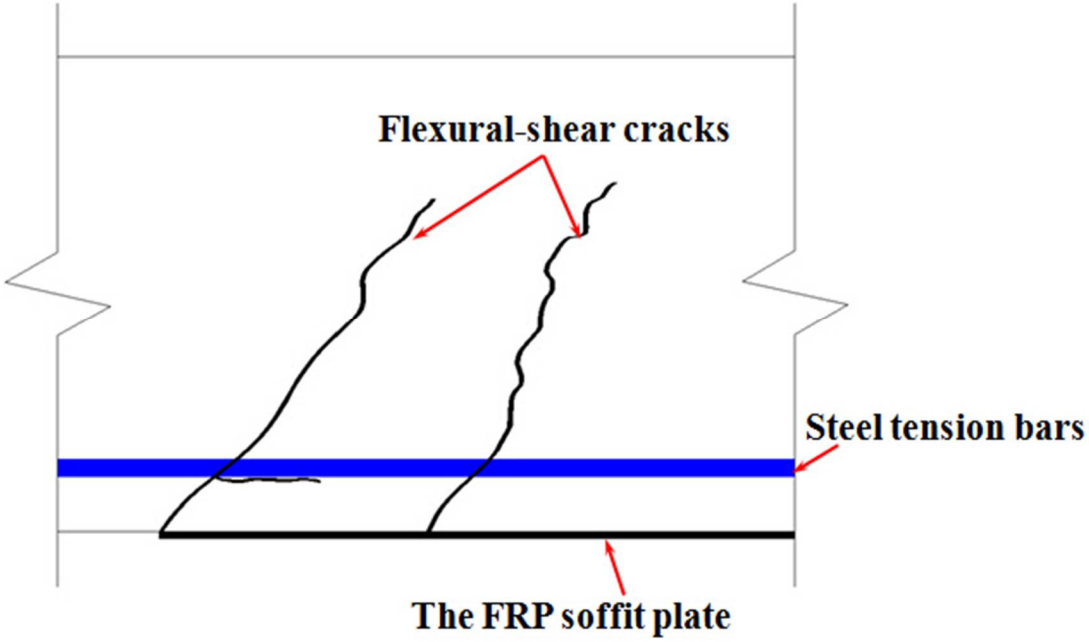

(c) Stage III: propagation of the horizontal crack towards the mid-span

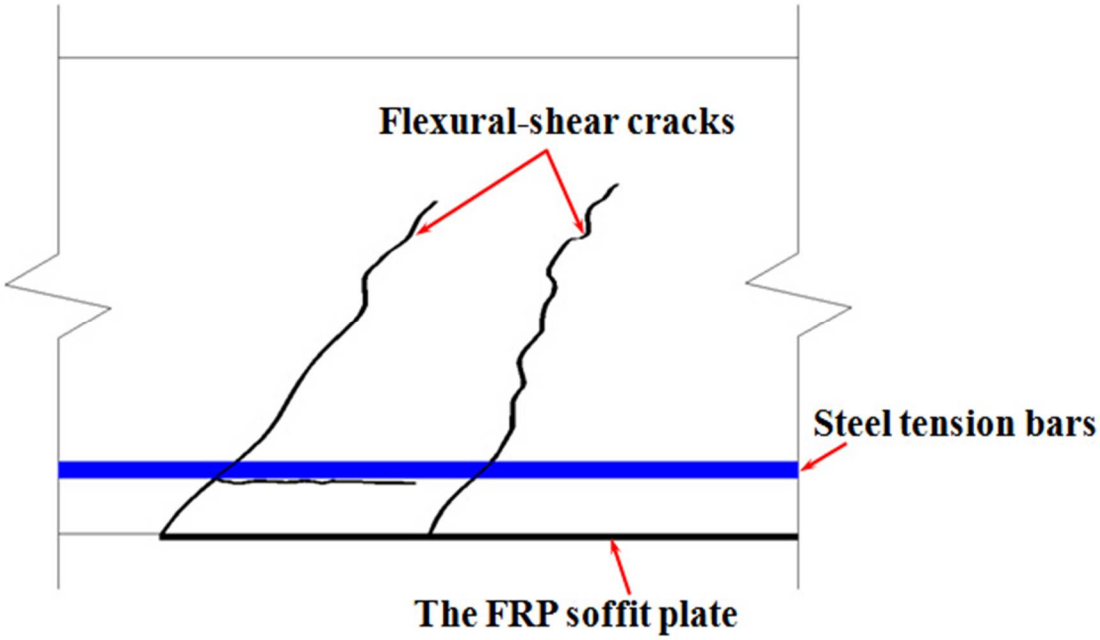

(d) Stage IV: Concrete cover separation failure

Figure 8.1 Concrete cover separation: illustration of failure process

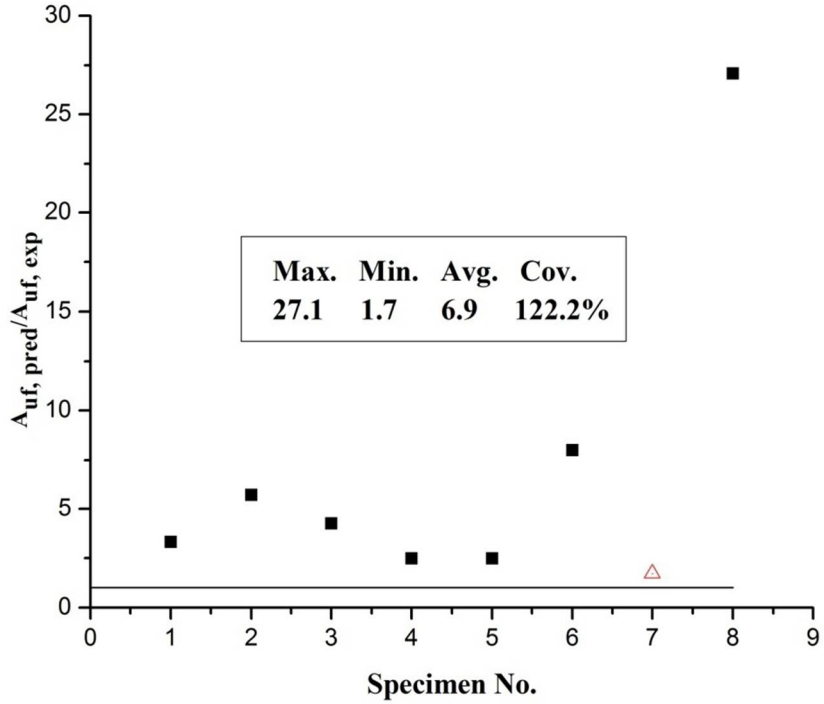

(a) Provision of ACI 440.2R

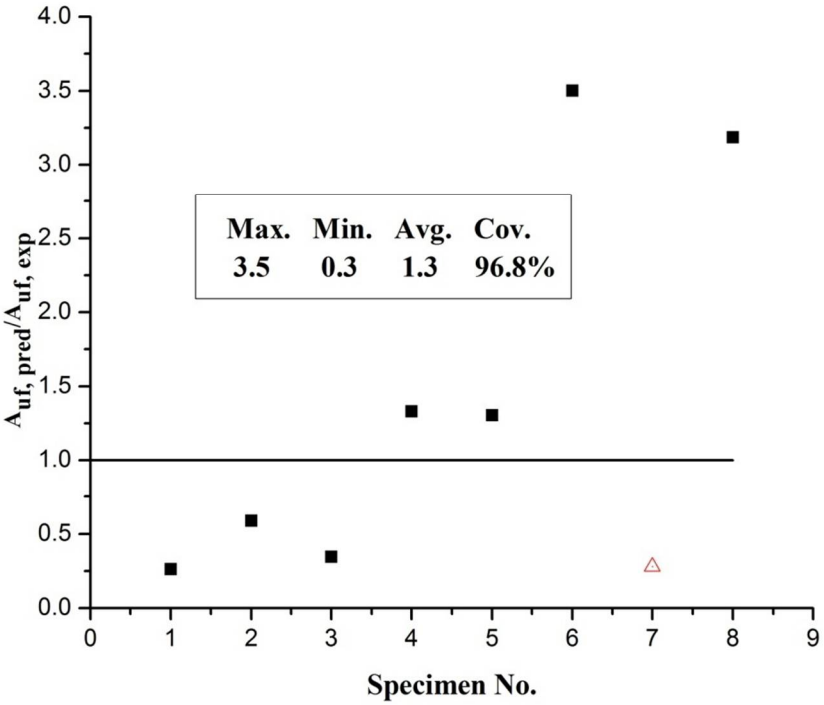

(b) Provision of Concrete Society

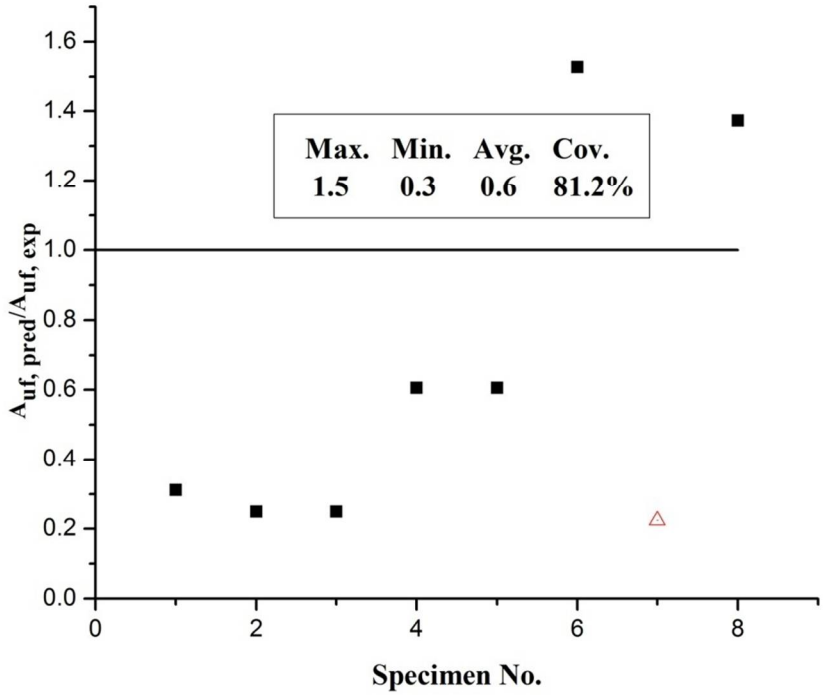

(c) Provision of GB-50608

Figure 8.2 Comparison between provision and tests with a vertical FRP U-jacket

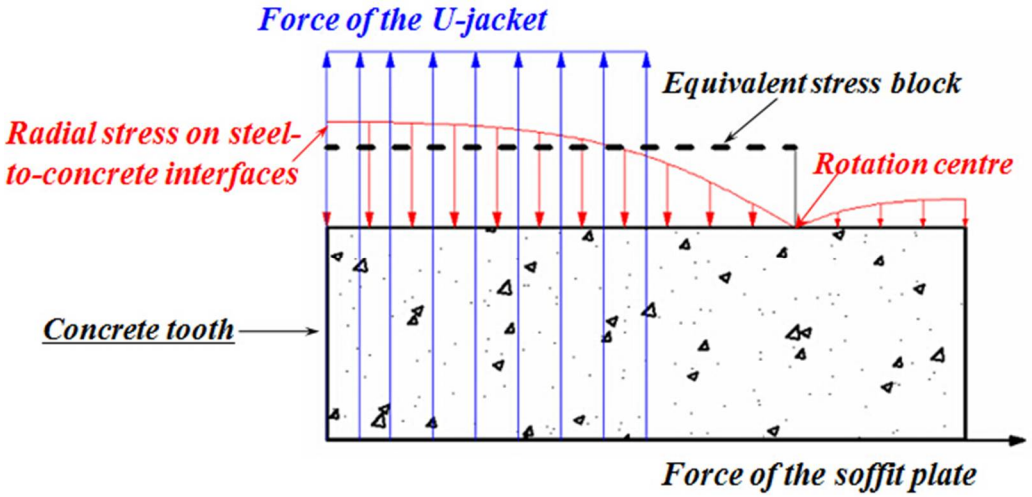

Figure 8.3 Illustration of design model for a vertical U-jacket

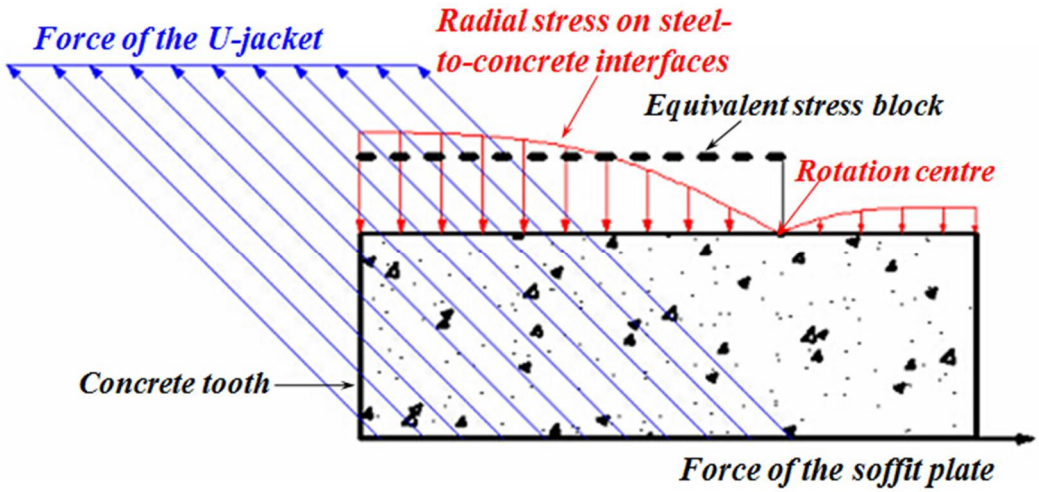

Figure 8.4 Illustration of design model for an inclined U-jacket

CHAPTER 9

CONCLUSIONS

9.1 INTRODUCTION

FRP-plated RC beams are vulnerable to FRP debonding failures of various forms, and their load-carrying capacity is often controlled by these debonding failures. Although knowledge on debonding failures of FRP-plated RC beams has been advanced by previous studies, there are still two major deficiencies in existing knowledge on debonding failures in FRP-plated RC beams. They are (1) the effect of load distribution on intermediate crack (IC) debonding; and (2) the effect of FRP U-jackets on both IC debonding and concrete cover separation. This thesis has presented the results of a research project aimed at addressing the above two knowledge deficiencies.

Almost all the existing laboratory tests on IC debonding of FRP-plated RC beams [i.e. except the studies by Pan et al.(2009) and Mazzottiand Savoia (2009)] were conducted under one- or two-point loading (i.e., three- or four-point bending) for ease of application in the laboratory. However, as indicated by a limited number of tests on

small-scale FRP-plated RC beams by Pan et al. (2009), different load distributions can result in different debonding behaviours of FRP-plated RC beams. Existing IC debonding strength models were proposed and verified using tests under one- or two-point loading only, and did not appropriately consider cases under other loading distributions. Some of these existing IC debonding strength models have the potential to predict IC debonding under UDL; however they needs to be carefully examined using reliable experimental and numerical data. The first part of this research project is intended to clarify this issue, and consists of an experimental programme, finite element (FE) modelling of full-scale FRP-plated RC beams under different load distributions and the evaluation of of existing IC debonding strength models, which have potential to accurately reflect this effect.

The second part of this research project has been carried out to clarify the effects of FRP U-jackets on both IC debonding and concrete cover separation. As revealed by the review given in Chapter 2, premature debonding failures limit the utilization of expensive FRP materials. For example, the maximum strain in the bonded FRP soffit plate at debonding failure in an FRP-plated RC beam, in some cases, is only about 30% of the rupture strain of the FRP material (Kalfat et al. 2013). Moreover concrete cover separation often occurs prior to the yielding of the tension steel bars and in a brittle form with little advance warning. FRP U-jackets have been commonly specified in design guidelines to suppress debonding failures of FRP-plated RC beams and to improve the utilization of the FRP material, but these design provisions are rather empirical and preliminary with a very limited experimental basis. In the second part of this thesis, two experimental studies were conducted to investigate the effect of FRP

U-jackets on IC debonding and concrete cover separation respectively. Based on the concrete tooth concept, an approach for designing FRP U-jackets against concrete cover separation was proposed. The main conclusions of the studies presented in this thesis are summarised below, which are followed by a discussion of future research needs.

9.2 EFFECT OF LOAD DISTIBUTION ON IC DEBONDING

An experimental study was conducted to investigate the effect of load distribution on IC debonding. This experimental programme consisted of five full-scale FRP-plated RC beams, which were divided into two series—one to examine the effect of shear span and the other to examine the effect of load uniformity on IC debonding. The loading system was carefully designed to ensure equal loading at all loading points, and this was achieved by connecting all individual jacks at different loading points to a single manually-operated pump. All five test beams failed by IC debonding. It was found that the maximum moment in the beam at IC debonding (i.e., debonding moment) increased by about 9%, and the debonding strain in the FRP plate (maximum strain in the FRP soffit plate at debonding) increased by 15% when the load uniformity increased from two-point loading to eight-point loading with the same shear span of 1000 mm. This observation means that existing IC debonding strength models based on beams under three- or four- point bending can be over-conservative for use in the design of beams under more uniform loading such as UDL.

The tests presented in Chapter 3 together with beams tested under different load distributions from two other independent sources (Pan et al. 2009; Mazzotti and Savoia 2009) were used to verify a finite element (FE) approach for modelling IC debonding under different load distributions. In this FE approach, three key factors (i.e., constitutive modelling of cracked concrete, bond modelling of FRP-to-concrete interfaces, and steel bar-to-concrete interfaces) are appropriately considered to capture localized flexural cracks, thus leading to accurate predictions of IC debonding in FRP-plated RC beams. In addition, a novel displacement-based load control technique, which was implemented using an imaginary rigid beam system, was devised for imposing multi-point loading in FE simulations to capture the entire debonding process. It was found that the augmented FE approach could produce very close predictions of test results in terms of not only the moment-deflection curves but also the cracking behaviour; that is, this FE approach is capable of accurate modelling of IC debonding in FRP-plated RC beams under different load distributions. An FE parametric study was then conducted to extrapolate the test results. Results from the parametric study indicated that the effect of load distribution on IC debonding could be significant especially when the beam hasa relatively large span-to-heightratio (i.e., beams with a smaller height in the parametric study).

Three existing IC debonding strength models [i.e., the second approach in *fib*(2001); Chen et al. (2006) and Rosenboom and Rizkalla (2008)] have the potential to predict the strength of IC debonding under different load distributions. They were assessed using both the available test data and the numerical results from the present research project. The following conclusions may be drawn from the assessment:

(1) Both *fib*'s (2001) model and Chen et al.'s (2006) model tend to exaggerate the effect of load distribution on IC debonding while Rosenboom and Rizkalla's (2008) model can closely capture the difference in IC debonding strength between two-point loading and UDL;

(2) Rosenboom and Rizkalla's (2008) model produces some questionable trends of how different factors affect the effect of load distribution on IC debonding. For example, the FE approach predicts that the effect of load distribution becomes more significant with an increase in the span-to-depth ratio, width of the FRP plate, concrete strength and steel yield stress, but Rosenboom and Rizkalla's (2008) model produces the opposite trends. Therefore, the reliability of Rosenboom and Rizkalla's (2008) model is still questionable. Further research is therefore needed to develop a more rational and accurate IC debonding strength model for RC beams subjected to diffident load distributions.

9.3 EFFECT OF FRP U-JACKETS ON BOTH IC DEBONDING AND CONCRETE COVER SEPARATION

Two series of tests on FRP-plated RC beams with vertical FRP U-jackets and inclined FRP U-jackets respectively were conducted to investigate their effect on IC debonding. About a 10% increase in the ultimate load was observed in all three FRP-plated RC beams with vertical (i.e. perpendicular to the beam axis) U-jacket anchorage or with parallel side strips compared with that of the control beam strengthened with an FRP soffit plate only. It was found that the vertical restraints imposed by vertical FRP

U-jackets on the FRP soffit plate might result in significant bending strains in the FRP soffit plate and hence lead to premature rapture of the soffit plate. Results of tests on specimens with 45^{o} inclined FRP U-jackets indicated that inclined U-jackets near the mid-span (e.g. Specimen B2S2) and in low moment region (e.g. SpecimensB3S2 and B4S2) had different effects on IC debonding. Inclined U-jackets near the mid-span can be highly tensioned by the widening of major cracks, and the resulting forces in the inclined U-jackets need to be transferred to the FRP soffit plate, which may result in the premature rupture of the FRP soffit plate with only a slight increase in the load-carrying capacity of the beam. Inclined FRP U-jackets in low moment regions can significantly increase both the load-carrying capacity and ductility of the FRP-plated RC beam as they can carry forces transferred from the FRP soffit plate; they can even carry the FRP soffit plate when the soffit plate has otherwise completely debonded from the concrete substrate. Therefore inclined FRP U-jackets in low-moment regions (e.g. near the support of a simply-supported beam) is an attractive option to mitigate IC debonding of FRP-plated RC beams.

FRP U-jackets are also often used to mitigate the brittle concrete cover separation failure as recommended by a number of design guidelines (e.g. ACI 440.2R 2008; Concrete Society2012; GB-506608 2010). However, the provisions in these guidelines lack a solid research basis. Chapter 7 therefore presented a systemic experimental study on the effect of FRP U-jackets on concrete cover separation failure. This experimental programme consisted of ten full-scale FRP-plated RC beams, among which the two control specimens were strengthened only with an FRP soffit plate, and the other eight specimens were strengthened with both an FRP soffit plate and FRP U-jackets of

different forms. The following conclusions can be drawn from this experimental study:

(1) Vertical FRP U-jackets are capable of postponing or suppressing concrete cover separation failure. With an increase in the width of the vertical FRP U-jacket, both the ultimate load and ductility of the beam increase. In beams with an FRP U-jacket that is narrower than the crack spacing near the plate end, the beam will still fail by concrete cover separation, but the failure will start at the inner side of the FRP U-jacket (i.e. the side of the FRP U-jacket closer to the mid-span).

(2) Inclined FRP U-jackets near the support perform better than their vertical counterparts do in suppressing concrete cover separation failure as the tensile force in the FRP soffit plate can be more easily transferred to an inclined FRP U-jacket than a vertical FRP U-jacket.

(3) Existing provisions for the design of vertical FRP U-jackets against concrete cover separation failure have not been established with a solid research basis, and the amount of vertical FRP U-jacket anchorage required by these provisions is more than that is actually needed.

Further to the experimental study on the effect of FRP U-jackets on concrete cover separation failure, an approach for the design of FRP U-jackets for mitigating concrete cover separation failure was developed based on the 'concrete tooth' concept and verified using the test results obtained in the present research project. It was found that:

(1) In terms of performance in mitigating debonding failures, inclined FRP U-jacket anchorage is superior to its vertical counterpart and is therefore recommended as the preferred anchorage measure. The superiority of inclined FRP U-jacket anchorage can be attributed to the fact that: (1) the tensile force in the FRP soffit plate can be much more easily transferred to the U-jacket; (2) both the initiation crack at the soffit plate and the horizontal crack at the level of the steel tension bars can be effectively constrained by an inclined FRP U-jacket; while only the widening of the horizontal crack can be constrained by a vertical FRP U-jacket.

(2) The design approach for plate-end U-jacket anchorage was proposed based on the concrete tooth concept, and should take into account the effect of radial stresses arising from slips between the steel tension bars and the concrete, as the radial stresses play an important role in concrete cover separation failure.

(3) An additional detailing requirement that the vertical FRP U-jacket should cover a horizontal distance of at least 1.5 times the critical crack spacing at the soffit plate end was established to avoid the initiation of a concrete cover separation failure at the inner side of FRP U-jacket. This detailing requirement was established based on experimental observations in some of the specimens in the assembled test database and those presented in Chapter 7.

(4) The proposed design model for inclined FRP U-jacket anchorage at plate end was verified using tests presented in Chapter 7.Although further verification by additional tests or accurate finite element predictions is needed and its accuracy

depends on the choice of the crack spacing model, the proposed model forms a solid basis for future work.

9.4 FUTURE RESEARCH

This thesis has been concerned with debonding failures in FRP-plated RC beams. The research presented in the thesis was conducted to address two knowledge deficiencies in this research area: the effect of load distribution on IC debonding; and the effect of FRP U-jacket anchorage on both IC debonding and concrete cover separation. While the present research has addressed these two knowledge deficiencies to a large extent, a great deal of research is still required to advance our current knowledge on debonding failures in FRP-plated RC beams for the more confident use of FRP materials in the strengthening of RC structures. Some of these issues are discussed below.

An IC debonding strength model, which can accurately reflect the effect of load distribution, is still needed. As indicated by both the experimental study presented in Chapter 3 and FE study presented in Chapter 4, the effect of load distribution on IC debonding can be significant, especially when the beam span-to-depth ratio is large. Results presented in Chapter 5 showed that no existing IC debonding strength model could appropriately consider the effect of load distribution although some existing models (e.g. *fib* 2001; Chen et al. 2007; Rosenboom and Rizkalla 2008) have the potential to provide reasonably accurate predictions of IC debonding under different load distributions. This is because existing IC debonding strength models were proposed and verified using either experimental or numerical studies on FRP-plated RC beams or

slabs under one- or two-point loading (i.e. three- or four-point bending), and sufficient data for IC debonding under different load distributions were not available. The verified FE approach for IC debonding under different load distributions can be used to generate more numerical data as the basis for the development of a new IC debonding strength model that properly reflects the effect of load distribution.

An approach for designing inclined FRP U-jacket anchorage to mitigate IC debonding was required. As indicated by results of the experimental study presented in Chapter 6, inclined FRP U-jacket anchorage in a low moment region of an FRP plated RC beam is highly effective in mitigating IC debonding. Moreover, it can significantly improve both the load-carrying capacity and ductility of the beam as part of the tensile force in the FRP soffit plate, which can be easily transferred to the U-jacket anchorage. However, the mechanism of how the force is transferred between an FRP soffit plate and an inclined FRP U-jacket needs further clarification. This clarification is important for the development of a design approach for inclined U-jackets for the mitigation of IC debonding.

A new approach for the design of FRP U-jackets to mitigate concrete cover separation was presented in Chapter 8, which includes two design models: one for vertical FRP U-jackets and one for inclined FRP U-jackets. The approach was developed based on the concrete tooth concept, and was verified using the limited test data from the present research project. Although the approach was based on a rigorous mechanism basis, more reliable data are needed to verify further the design approach.

A comprehensive, safe and economical design procedure, which accounts for the significant effects including those of FRP U-jackets and load distribution on IC debonding as well as the effect of FRP U-jackets on concrete cover separation, is needed for the flexural design of FRP-plated RC beams against debonding failures. In such a design procedure, the highly brittle failure mode of concrete cover separation should be prevented from becoming the controlling failure mode of an FRP-plated RC beam using FRP U-jackets so that the less brittle IC debonding failure mode controls the failure behaviour of an FRP-plated RC beam. In addition, the effects of both FRP U-jackets and load distribution on IC debonding should be accurately captured in the IC debonding strength model to enable a reliable design of the FRP strengthening system.

9.5 REFERENCES

Chen, J.F., Teng, J.G. and Yao, J. (2006). "Strength model for intermediate crack debonding in FRP-strengthened concrete members considering adjacent crack interaction", *Proceedings, Third International Conference on FRP Composites in Civil Engineering (CICE 2006)*, Miami, Florida, USA,, 67-70.

Féderation International du Béton (*fib*). (2001). *Externally bonded FRP reinforcement for RC structures*, *fib* Bulletin 14, fib Task Group 9.3, fib, Lausanne, Switzerland.

Kalfat, R., Al-Mahaidi, R. and Smith, S.T. (2013). "Anchorage devices used to improve the performance of reinforced concrete beams retrofitted with FRP composites: state-of-the-art review", *Journal of Composites for Construction, ASCE*, Vol.17, No. 1, pp. 14-33.

Mazzotti, C. and Savoia, M. (2009). "Experimental tests on intermediate crack debonding failure in FRP-strengthened RC beams", *Advances in Structural Engineering*, Vol. 12, No. 5, pp. 701-713.

Pan, J.L., Chung, T.C.F. and Leung, C.K.Y. (2009). "FRP debonding from concrete beams under various load uniformities", *Advances in Structural Engineering*, Vol. 12, No. 6, pp.807-819.

Rosenboom, O. and Rizkalla, S.H. (2008). "Modeling of IC debonding of FRP strengthened concrete flexural members", *Journal of Composites for Construction*, ASCE, Vol. 12, No. 2, pp. 168–179.